Quantifying uncertainties of aspects of the neutronics modelling of the Kozloduy-6 system using SCALE 6.2.1

GP Nyalunga

orcid.org/0000-0003-3199-4100

Thesis submitted in fulfilment of the requirements for the degree *Doctor of Philosophy in Nuclear Engineering* at the North-West University

Supervisor: Dr V.V. Naicker

Co-supervisor: Prof K. Ivanov

Graduation: May 2019

Student number: 25449753

DECLARATION

I, Gezekile Portia Nyalunga hereby declare that this thesis represents my work in my own words. I hereby confirm that where others work, or words have been used, I have adequately cited and referenced the original sources. I declare that I have adhered to all the university's policies on plagiarism and have not misrepresented or fabricated any work in my submission.

_____

G.P. Nyalunga

ABSTRACT

This work is based on the benchmark for Uncertainty Analysis in Modelling (UAM) of light water reactors compiled by the Nuclear Energy Agency within the Organisation for Economic Cooperation and Development (OECD/NEA). The objective of the OECD/NEA benchmark is to form uncertainty bounds of results for calculations of LWRs based on operating data using best-estimate (BE) transport codes. The main contribution of this thesis to the OECD/NEA benchmark is the quantification of uncertainties in the Kozloduy-6 VVER-1000 reactor system using SCALE-6.2.1 methodology.

The OECD/NEA benchmark consists of three phases, each with three exercises. Three reactor systems are also studied, viz. the PWR, VVER and BWR reactors. In this study, the first phase of the OECD/NEA benchmark was considered for the uncertainty quantification of the Kozloduy-6 VVER-1000 reactor system. The sources of uncertainties are classified into three groups, namely uncertainties due to nuclear data, uncertainties due to manufacturing tolerances and uncertainties due to numerical methods implementations. In order to identify the source of uncertainties in the system, as a first step, a local sensitivity analysis was performed for certain input data to obtain the input uncertainties that requires propagation. Thereafter, an uncertainty quantification was performed on the input data that showed substantial effect on the results.

The calculations are performed using BE codes obtained from the SCALE 6.2.1 code system, i.e. KENO-VI and NEWT to perform the neutronics calculations and TSUNAMI-2D/3D and SAMPLER to perform the sensitivity and uncertainty analysis. The identified uncertain input data were further propagated on a fuel depletion analysis of the VVER-1000 system. The fuel depletion analyses were performed using TRITON of the SCALE 6.2.1 code. To validate the KENO-VI neutronics calculations, LR-0 benchmark tests were considered. Uncertainty quantification analysis was extended to this LR-0 system's neutronics calculations. As an addition, a verification of the LR-0 model was performed using NWURCS code. The principal input data related to the physical models and to the system description such as geometry, materials properties, etc. are characterised by their uncertainty ranges and probability distributions based on state-of-the-art knowledge (Blanchet, et al., 2007).

The uncertainty due to nuclear data was obtained for both the OECD/NEA benchmark and the LR-0 benchmark models. The uncertainty due to nuclear data will vary, depending on the size and material of the system. Furthermore, it was shown that, although other parameters had an influence on the uncertainty, the nuclear data still remain as the highest contributor of uncertainty of a reactor system in terms of all input parameters considered in this study. Although this is true, the uncertainty due to other parameters must always be considered and be analysed together with the uncertainty due to nuclear data, since some of them could be significant.

KEYWORDS: *Best-estimate, neutronics, uncertainty quantification, nuclear data, manufacturing tolerances, method and modelling uncertainties*

DEDICATION

To my son, Khayalethu Angelo Vuyo Rana.

ACKNOWLEDGEMENTS

This work was performed at the School of Mechanical and Nuclear Engineering at the North-West University, between 2016 and 2018. The research work is based upon research supported by the South African Research Chairs' Initiative of the Department of Science and Technology and National Research Foundation of South Africa with Grant No: 61059. However, any opinion, finding and conclusion or recommendation expressed in this material is that of the author (s) and the NRF does not accept any liability in this regard.

Firstly, I would like to thank God for giving me this opportunity, the courage, perseverance and wisdom to begin and complete this research work.

I want to express my deepest gratitude to my supervisor Dr Vishana Vivian Naicker for her extraordinary guidance and helpful instructions over the past three years of this PhD work, allowing me to enhance my understanding of Nuclear Engineering and Safety.

I would like to express my sincere appreciation to my co-supervisor, Professor Kostadin Ivanov for his proficient comments and valuable suggestions on this study. I especially appreciate his capability to get involved in the study even in his very tight schedule.

An appreciation goes to the OECD/NEA-UAM community for initiating the research work on uncertainty propagation and development of methods.

Finally, I wish to thank my parents, siblings and close friends for their love and support and also having faith in my endeavour.

Gezekile Nyalunga

TABLE OF CONTENTS

LIST OF FIGURES

LIST OF TABLES

LIST OF ACRONYMS

2D	Two-Dimensional
3D	Three-Dimensional
AMPX	Cross-section processing code
BE	Best-Estimate
BEPU	Best-Estimate Plus Uncertainty
BONAMI	BONdarenko AMPX Interpolator
CBC	Critical Boron Concentration
CE	Continuous Energy
CENTRM	Continuous ENergy TRansport Module
CSAS	Criticality Safety Analysis Sequence for KENO
EFPD	Effective Full Power Days
ENDF	Evaluated Nuclear Data File
ESC	Extended Step Characteristic method
FA	Fuel Assembly
FC	Full Core
FP	Fuel Pin
g/cm^3	Grams per cubic centimetre
H_{cr}	Critical moderator Height
HMA	Homogeneous model
HMB	Homogeneous Band model
HTB	Heterogeneous Band model
HFP	Hot Full Power
HZP	Hot Zero Power
K	Kelvin
k_∞	Eigenvalue multiplication factor
KENO-VI	Monte Carlo Criticality Program
LWR	Light Water Reactor
MG	Multi-Group energy
MCNP6	Monte Carlo N-Particles, version 6
NEWT	New ESC-based Weighting Transport code
NWURCS	North-West University Reactor Code Suite
OECD	Organisation for Economic Corporation and Development
PCM	Per cent mille
PDF	Probability Distribution Function
PMC	Produce Multi-group Cross-sections
PWR	Pressurised Water Reactor
SA	South Africa
SAMS	Sensitivity Analysis Module for SCALE

SCALE	Standardised Computer Analyses for Licensing Evaluation
SDF	Sensitivity Data Files
TRITON	Transport Rigor Implemented with Time-dependent Operation for Neutronic
TSUNAMI	Tools for Sensitivity and Uncertainty Analysis Methodology Implementation
UAM	Uncertainty Analysis in Modelling
XSProc	Cross-section processing

1. BACKGROUND AND OVERVIEW

1.1 INTRODUCTION

In a nuclear reactor system, the quality of neutronics results is widely determined by the accurate solution of the neutron transport equation through transport codes. Neutronics results are used to derive and explain the safety and reliability of a nuclear reactor system to produce nuclear energy. This can be done based on a good understanding of the related neutronics backgrounds, which can be obtained via nuclear reactor physics analysis. Reactor analysis includes the understanding of the design of the reactor; the interactions between neutrons and materials; the physical definition of cross-section; and the definitions of the neutron flux and reaction rates.

The nuclear physics of the reactor analysis is divided into three important forms which are: theoretical, experimental and computational physics. In theoretical physics, mathematical models based on fundamental principles are employed to explain known phenomena and to predict natural phenomena. For experimental physics, practical techniques and methods are used and experimental devices are constructed to check the theoretical predictions, identify new phenomena and measure various physical quantities. Computational physics focusses on developing and implementing fast, efficient and accurate numerical algorithms to solve the mathematical equations that describes the behaviour of a physical system (Perko, 2015).

In the fields of science and engineering, experimental physics are expensive, since it requires the construction of experimental facilities, complex measurement devices and prototypes which can pose real safety risks to the experimenters. Most experimental results are irreproducible and may not yield the same results when the calculations are repeated. This is due to continuously changing environment variables and measurements error. Computational physics has therefore become a “go to” tool across the nuclear fields, supplementing and sometimes replacing experimental physics when performing nuclear safety analysis. Neutron transport computer codes along with other codes are employed through mathematical models to accurately describe the underlying physics and behaviour of the natural or engineered systems of a nuclear reactor. The mathematical models can be derived from first principles, theory, semi-empirical and/or empirical methods. Computational physics performed by computer simulations are usually repeatable which allows a certain fidelity of the computer models to produce reliable results (Perko, 2015). With a research environment, these studies can be classified as computational experiments.

The use of computational experiments implies that the system studied is simplified or approximated by the assumptions made in the solution techniques of the neutron transport code. The current assumptions made in computer codes make every computer simulation an estimate of the system modelled. The simulated results are called an estimate and are therefore subjected to an

uncertainty irrespective of the desired output. The uncertainty of a computer experiment is a measure of the precision of the models and its input data parameters used for the simulation. The input data parameters are external data supplied to the model and parameters that defines the operating envelope of the system. The sources of uncertainties in neutronic calculations can be categorized into three classes, viz. those due (1) nuclear data uncertainties, (2) methods and modelling and (3) manufacturing uncertainties. The uncertainty of a computer experiment for a reactor system model requires quantification.

The importance of uncertainty quantification has been highlighted over the last few years in the nuclear reactor analysis field with much attention being paid to light water reactors (LWR). Uncertainty analysis has now become part of any physical modelling and code development task. Uncertainty quantification of calculated results is required to improve knowledge and understanding of a considered model for nuclear reactor behaviour.

Uncertainty analysis in modern nuclear reactor safety analysis also assists with minimising unnecessary conservativism. Previously, conservative assumptions were adopted in computer codes to perform nuclear safety analysis. However, with the large margins that exist between the conservative calculations and the real values, the conservative calculations are amplified to or substituted by best-estimate calculations (BE). Because BE calculations are subject to uncertainties, the estimated results are expressed with an uncertainty range of possible values as shown in Figure 1-1. In Figure 1-1, the real value, the conservative value, the acceptance criteria and the safety limit are also shown together with the margins.

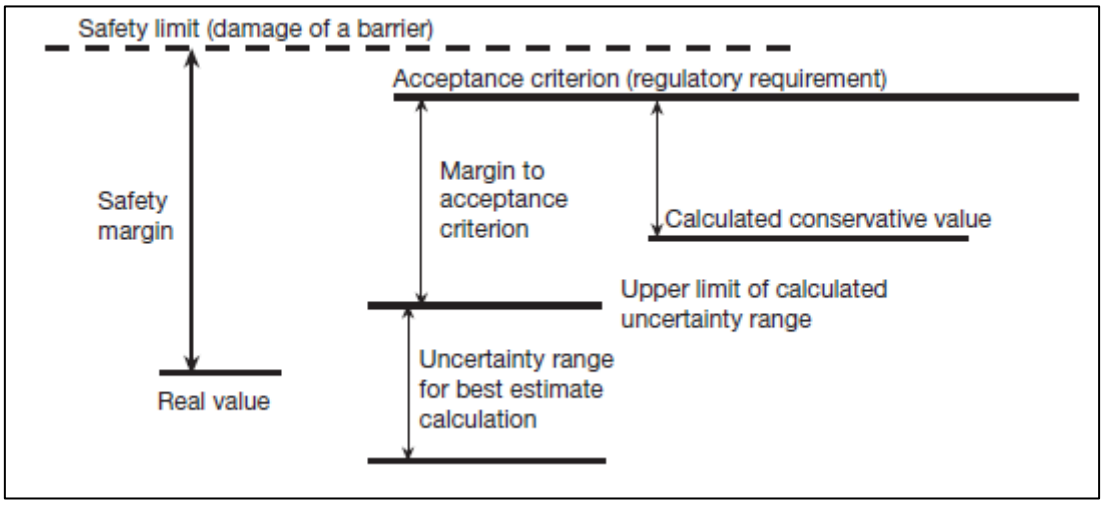

FIGURE 1-1: CONCEPT OF SAFETY MARGINS (IAEA, 2008)

Uncertainty quantification determines the uncertainty in the calculated results based on the uncertainty in the input data uncertainties. Although most input data are available, their accuracy and validation are still a major concern, particularly if their uncertainties lead to large errors in predicting the criticality parameters.

A sensitivity analysis of the factors that might be contributing to the uncertainties assists in obtaining the uncertainties in the output. Sensitivity analysis is performed prior and after uncertainty quantification. A sensitivity analysis prior to uncertainty analysis can be classified as a local sensitivity analysis, while the latter is referred to as a global sensitivity analysis.

1.2 OVERVIEW OF THE STUDY

This work is based on the benchmark for Uncertainty Analysis in Modelling (UAM) for the Design, Operation and Safety Analysis of LWRs compiled by the Nuclear Energy Agency within the Organisation for Economic Cooperation and Development (OECD/NEA) (Ivanov, et al., 2013). The objective of the OECD/NEA benchmark is to develop uncertainty analysis methodologies to assist in the uncertainties analysis in best-estimate (BE) modelling for design, operation and safety analysis of Light Water Reactors (LWRs).

The OECD/NEA benchmark comprises of 3 phases, each with three exercises: Phase 1 (neutronics phase), Phase 2 (core phase) and Phase 3 (system phase). These phases establish a set of best-practices and procedures for performing comprehensive analyses to define, coordinate, and report an international benchmark for the uncertainty in best-estimate code calculations of LWRs. They also foster the development of computer tools that facilitate uncertainty and sensitivity analysis. The use of BE neutron transport codes requires propagation of input data uncertainties to quantify the uncertainties in the results as calculated by the codes (IAEA, 2008). The source of input data uncertainties in the BE code calculations can be classified into three groups, viz. nuclear data uncertainties, modelling uncertainties and manufacturing uncertainties.

In this work, the propagation of uncertainties associated with the three groups has been investigated on Exercise I-2 of Phase 1 of the OECD/NEA benchmark. The study was performed using BE codes, obtained from SCALE-6.2.1 as functional modules (Rearden & Jesse, 2016), on a fuel assembly (FA) model of the Kozloduy-6 VVER-1000 reactor system. The criticality calculations are performed using KENO-VI which applies Monte Carlo (MC) methods and a 2D deterministic code NEWT. The criticality calculations performed using KENO-VI reports a best-estimate eigenvalue with a standard deviation that is computed as the minimum variance of the eigenvalue. The uncertainty analysis is performed using TSUNAMI-2D/3D which uses general perturbation theory (GPT) and SAMPLER which uses the stochastic sampling method of input data perturbations.

The nuclear data uncertainties can be propagated by TSUNAMI-2D/3D using covariance matrices available in the nuclear data file (NDF), or/and by SAMPLER using a set of nuclear data files, with each data file in the set containing a perturbed set of data based on the nominal data file.

Modelling and method uncertainties are mainly due to the numerical implementation of the mathematical formalism used and the stochastic nature of the Monte Carlo code, KENO-VI. There are two ways to quantify this type of uncertainty. One way would be to modify the source code to test various possibilities of appropriate algorithms in the source code. However, access to source codes are usually restricted. Therefore, the second option is to quantify these uncertainties via the input deck by choosing various options with respect to numerical implementation in the code. The sensitivity of parameters associated with inherent code methodologies are tested to eliminate any inaccuracies due to code inherent methodologies as well as to keep computation time reasonable.

Manufacturing uncertainties can be defined to include both geometrical dimensions and material properties. There are many such parameters in a nuclear system and propagating the uncertainties due to all these parameters is a formidable task. The one method that can be used is to isolate those parameters which the investigator deems to be important, and to perform sensitivity studies to further pick out those parameters which would contribute significantly to the uncertainty. The danger of this approach is that important parameters can be overlooked. Nonetheless, this study aims to ensure that the most important input parameters are assessed, and their uncertainties quantified.

The results that are presented in the study are:

- The infinite eigenvalue multiplication factor with its uncertainty;
- The top neutron-nuclide reaction contributors to the uncertainty in the multiplication factor;
- One-group homogenised microscopic cross-sections and their uncertainties for a fuel pin with their corresponding covariance and correlation coefficients;
- Few-group homogenised macroscopic cross-sections and fuel region parameters such as diffusion coefficients, nu-fission, neutron flux and assembly discontinuity factor for the fuel assembly; and
- Fuel depletion analyses on the infinite eigenvalue multiplication factor with its uncertainty and the calculation of nuclide concentration of major actinides and fission products.

1.3 PROBLEM STATEMENT

Nowadays, many countries, including South Africa are in the process of/or considering increasing their nuclear energy production due to the depletion of coal (du Toit, 2017). Nuclear energy is a vital option for most countries, therefore, it is important that a thorough study first be performed on the safety operation of nuclear reactors. A significant part of the study is performed using computer codes. One class of these codes are neutronic codes which yields neutronics results such as the multiplication factor and the neutron flux. These codes can also be further classified as best-estimate (BE) and conservative codes.

The quality of the neutronics results strongly rely on the accuracy of the input data provided to the BE codes and the reliability related to the uncertainty information retrieved from the provided data. Unfortunately, current information of such uncertainties is rather scarce in some cases, especially when measured against evolving requirements. Therefore, it is crucial to continue to generate more comprehensive and reliable uncertainty information, something which then becomes more critical in the neutronics models. In previous studies, more attention has been on the uncertainty and sensitivity analysis concerning the nuclear data evaluation of the best-estimate codes for the neutronics models. However, other parameters such as method and modelling uncertainties and manufacturing uncertainties of the model also require evaluation. Each of these classes of uncertainties have been studied to various degrees of rigour, but composite studies including all the classes are lacking, especially in terms of the VVER-1000 reactor system.

The current work is based on the Kozloduy-6 VVER-1000 reactor system therefore presents a study of the propagation of uncertainties associated with nuclear data uncertainties, method and modelling uncertainties and manufacturing uncertainties.

1.4 RESEARCH AIM AND OBJECTIVES

The aim of this study is to formulate an uncertainty quantification of the Kozloduy-6 VVER-1000 models specifically on the neutronics analyses. This study will serve as a contribution to the OECD/NEA benchmark. Although the OECD/NEA benchmark includes the full core quantification, this study propagates the uncertainty of the neutronics parameters up to the FA lattice level, specified as exercise I-2 of Phase I of the OECD/NEA benchmark. A study on the validation of the neutronic calculations on the LR-0 VVER-1000 core is also performed.

The objectives of this study are:

- Build base models for the simulations of this study;
- Obtain neutronics results using either NEWT or KENO-VI depending on the model requirements;
- Perform a sensitivity analysis on the modelling and method parameters and manufacturing tolerances by modifying the base model to show better understanding of the VVER-1000 system uncertainties;
- Create a table that ranks the input data based on their contribution to the base results;
- Perform an uncertainty analysis on nuclear data, method and modelling parameters and manufacturing tolerance using either TSUNAMI or SAMPLER;
- Develop a validation model of the LR-0 core;
- Verify this model by comparing it with a NWURCS generated model;
- Compare the KENO-VI results with results given in the validation specification;

- Test sensitivities due to input data;
- Propagate the input data uncertainties to quantify the overall output uncertainty;
- Analyse the trend in the results obtained for the OECD/NEA VVER-1000 FA and the LR-0 VVER-1000 FA and core; and
- Perform a fuel depletion analysis on the OECD/NEA benchmark and the uncertainty analysis of the fuel depletion analysis.

1.5 CONTRIBUTION OF THIS THESIS

The OECD/NEA benchmark has been established over recent years to satisfy an increasing demand from the nuclear community for best-estimate predictions accompanied by uncertainty and sensitivity analysis. The main objectives of the OECD/NEA benchmark activity are to determine uncertainties in modelling for reactor systems using best-estimate codes under steady state and transient conditions, and to quantify the impact of these uncertainties for each type of calculation in Multiphysics analysis which involves the following:

- Neutronics,
- Thermal-hydraulics, and
- Fuel behaviour.

The structure of the OECD/NEA benchmark consists of three phases each with three exercises for the three main LWRs types (BWR, PWR, VVER-1000). The reactor types were selected based on previous benchmark experience and available data.

One of the responsibilities of each participant in the benchmark is to produce and submit results to be included in the benchmark report, for a system chosen by each participant. Currently, the participants involved in the benchmark are conducting analysis on Phase I. This thesis lists and discusses the results that were forwarded by the author to the benchmark co-ordination team on April 2017 and April 2018. The results submitted for Exercise I-1 and Exercise I-2 were:

- The infinite eigenvalue multiplication factor with its uncertainty;
- The top neutron-nuclide reaction contributors to the uncertainty in the multiplication factor;
- One-group homogenised microscopic cross-sections and their uncertainties for a fuel pin with their corresponding covariance and correlation coefficients; and
- Two-group homogenised macroscopic cross-sections and fuel region parameters such as diffusion coefficients, nu-fission, neutron flux, inverse neutron velocity and assembly discontinuity factor for the fuel assembly.

Optimisation is a vital component of model development. There are parameters that need to be treated with caution to produce accurate results using deterministic codes. In particular, the

hexagon configuration of the VVER-1000 has caused challenges with defining parameters such as the grid discretisation in a NEWT calculation. An approach to treat this parameter has been developed in this study. Other parameters were also included to enhance the accuracy of the neutronics results obtained. This contribution was published as a conference paper in the BEPU2018 international conference (Nyalunga, et al., 2018).

Not enough information was given on how the spacer grids must be modelled in the OECD/NEA benchmark specification for the VVER-1000. Methods for modelling the spacer grids for light water reactors have been developed and analysed in previous studies. Although the impact of each method has been provided in these studies, no uncertainty quantification of these methods was performed. An uncertainty analysis relating to the spacer grids is provided as a contribution by this study.

The main part of this work is to quantify the global influence of the combination of all input uncertainties on the neutronics output. This contribution will provide the global uncertainties due to all the considered uncertain input data for the VVER-1000 system.

Fuel depletion analyses have been performed for light water reactors over the years. There is a lack of uncertainty analysis of depletion calculation for the VVER-1000, however. This study uses the available tools in SCALE-6.2.1 to obtain the uncertainty analysis of the fuel depletion.

As it was mentioned in the introduction, previously, conservative assumptions were adopted in computer codes to perform nuclear safety analysis. With the current trend moving towards best estimate plus uncertainty analysis, this work contributes towards this endeavour in Nuclear Engineering analysis.

1.6 ORGANISATION OF THE THESIS

The thesis is organised so that Chapter 2 provides a literature review and theoretical background. Aspects of neutronics calculations and sensitivity/uncertainty analysis are described. The aim of Chapter 2 is to enable a wider understanding of the topic and to put the work presented in this thesis into the proper context.

Chapter 3 presents a description of the different codes used for the neutronics and sensitivity and uncertainty analysis. This chapter also provides the structure that is used to define the input files of the codes and methods for testing the convergence of the desired results.

Chapter 4 focuses on the description of the VVER-1000 in terms of geometry and materials. It provides the assumptions and instructions that assist with developing the neutronics model of this system studied for the SCALE-6.2.1 calculation.

Chapter 5 discusses the neutronics results of the VVER-1000 calculation as well as the analyses of the uncertainty quantification. The performance of the codes used, and the underlying uncertainty mechanisms are also discussed.

Chapter 6 focuses on the description of the VVER-1000 reactor system used for the validation analysis of the different codes used in this study. A verification method used that was used to verify the models was also provided in this section.

Chapter 7 covers the results of the validation calculation cases and the uncertainty quantification associated with these calculations. Insights relevant to uncertainty identification and quantifications are discussed as well.

Chapter 8 summarises all the results of the work presented herein and some recommendations for future work are proposed.

2 LITERATURE STUDY

This chapter provides the background and an overview of the general aspects of neutronics calculations and the numerical methods available to solve the neutron transport equation. It provides a brief discussion of the sources of uncertainty and uncertainty quantification methodologies currently used for sensitivity and uncertainty analysis. The importance of the verification and validation of neutronics is also discussed.

2.1 BACKGROUND OF NUCLEAR DATA

An efficient characterisation of a nuclear system's neutronic calculations requires high quality nuclear data and accurate information regarding nuclear reactions. In reactor physics analysis, the neutronics parameters such as the effective multiplication factor (k), neutron flux, and safety coefficients are calculated from mathematical equations which make use of nuclear data. This nuclear data is required for all reactor materials over the whole energy range covered by the reactor neutron energy spectrum. Depending on the physics they represent, this data can be divided into three types, namely neutron transport data, fission yield data and decay data.

Neutron transport data are usually associated with cross-sections, angular and energy distribution of outgoing particles upon interactions, resonance parameters etc., which are necessary for a transport code. Fission yield data are used for the calculation of waste disposal inventories and decay heat, depletion calculations, and beta and gamma ray spectra calculations of fission-product inventories. Decay data describes the nuclear levels, half-lives, Q-values and decay schemes etc., used for dosimetry calculations and decay heat estimation in nuclear repositories (Alhassan, 2015).

As a starting point for a nuclear system calculation, nuclear data are usually stored in an evaluated nuclear data file (ENDF). The evaluated nuclear data reflects the best representation of the true cross-sections. The evaluated nuclear data are available for incident neutron energies in the range from $10^{-5} eV$ to $20\ MeV$, and are given for nuclear reactions of more than 400 nuclides. The ENDF includes general information of neutron interactions such as the average number of neutrons (nubar) produced per fission, fission spectrum of neutrons (χ) and delayed neutron data, resonance parameters, reaction cross-sections and nuclear data covariance information.

2.1.1 TYPES OF NEUTRON INTERACTIONS

The theory of neutronics involves the determination of the type of nuclear reaction that take place in the reactor system together with their cross-sections to achieve the desired outputs. In nuclear engineering, the nuclear cross-sections as obtained from evaluated nuclear data files are referred to as microscopic cross-sections. The microscopic sections can be understood as inherently

positive energy dependent continuous random variables. The microscopic cross-section is defined as (Taavitsainen, 2016):

$$\sigma(E) = \frac{number\ reactions/nucleus/second\ with\ energy\ E}{Number\ of incident\ neutrons/cm^2/second\ with\ energy\ E} = [m^2] \quad (1)$$

and are traditionally given in barns $(1b = 10^{-28}m^2)$, with one of its interpretations being the effective cross-section area of the nucleus, hence the name.

The microscopic cross-sections are reaction-wise and may have summation rules related to them. The total neutron cross-section is the sum of its partial reactions which, in turn, are the sum of their respective partial reactions:

$$\sigma_t(E) = \sigma_s(E) + \sigma_a(E) = \sigma_e(E) + \sigma_{in}(E) + \sigma_\gamma(E) + \sigma_f(E) + \cdots \quad (2)$$

The classification of some of the nuclear reactions is summarised in Table 2-1 and their behaviour in the energy range of $10^{-5}MeV$ to $10\ MeV$ is demonstrated in Figure 2-1.

TABLE 2-1: KEY NUCLEAR REACTIONS (OKUMURA, ET AL., 2014)

Classification	Reaction	Transcription	XS symbol
Scattering (σ_s)	Elastic scattering	(n,n)	σ_e
	Inelastic	(n,n')	σ_{in}
Absorption (σ_a)	Radiative capture	(n,γ)	σ_γ
	Fission	(n,f)	σ_f
	Charged particles	(n,p)	σ_p
	Emission	(n,α)	σ_α
	Neutron emission	$(n,2n)$	$\sigma_{(n,2n)}$

The elastic scattering cross-section is mostly constant in all the energies except at the MeV region. Meanwhile, the in-elastic scattering requires the incident neutron to have enough kinetic energy to place the target nucleus in its excited state. Hence, the inelastic scattering XS is zero up to some threshold energy. Fast neutrons can be moderated by inelastic scattering with heavy nuclides, and by elastic scattering with light nuclides or with heavy nuclides below threshold energies. Most absorption XS including the fission XS appear as a straight-line with a slope of $-1/2$ on a log-log scale.

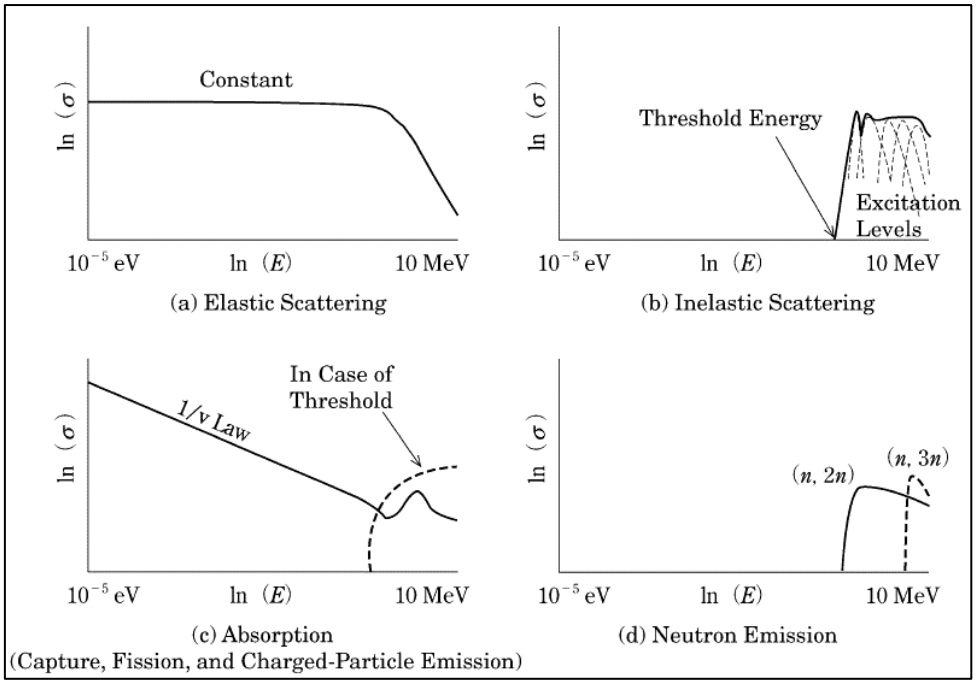

FIGURE 2-1: ENERGY DEPENDENCE OF CROSS-SECTION (OKUMURA, ET AL., 2014)

This implies that the absorption XS are inversely proportional to the neutron speed and therefore increase as the neutron energy decreases. Such large fission XS's at low neutron energies and thermal neutrons in the Maxwellian distribution make it possible for a natural or low-enrichment uranium fuelled reactor to reach a critical state (Okumura, et al., 2014). In a thermal reactor, the neutron interactions are centred between 0.01 and $1eV$; while in a fast reactor, neutrons are spread over a much larger energy range extending from eV energies to about 10 MeV, with an emphasis on energies between keV and several MeV.

There are several evaluated nuclear data libraries currently available from various nuclear data centres and these are listed in Table 2-1 (Alhassan, 2015).

TABLE 2-2: EVALUATED NUCLEAR DATA FILE

File name	Transcription
JENDL	Japanese
ENDF/B	USA
TENDL	Netherlands
CENDL	Chinese
JEFF	OECD/NEA data bank
BROND	Russia

The nuclear data information stored in the ENDF are converted to multi-group cross-section data through energy discretisation in formats suitable for most nuclear codes as shown in Figure 2-2 (Okumura, et al., 2014):

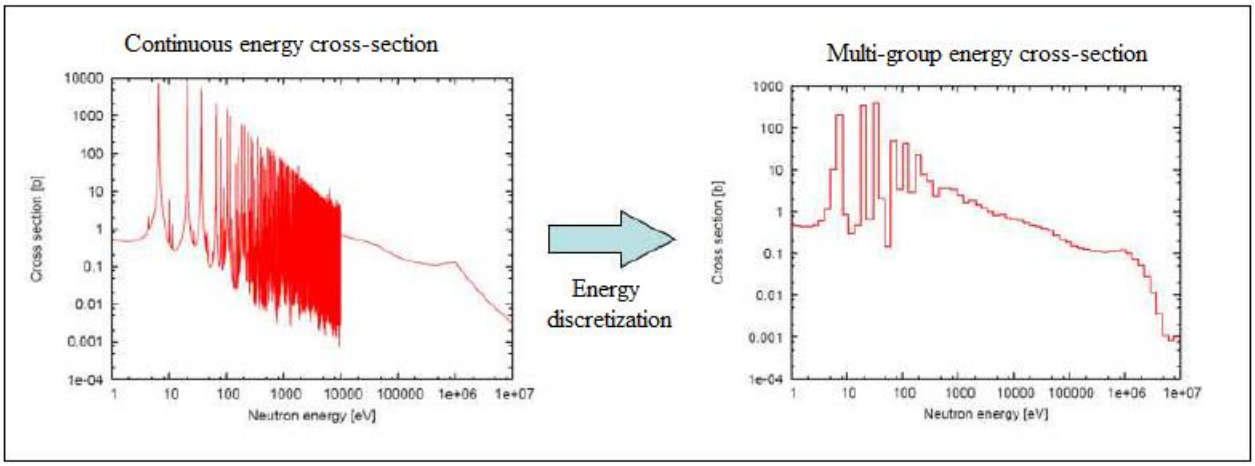

FIGURE 2-2: ENERGY DISCRETISATION OF THE CE DATA (OKUMURA, ET AL., 2014)

The first step in the calculation of a nuclear system consists of generating cross-section libraries in the multi-group (MG) or continuous-energy (CE) form that is suitable for use in the transport code. The covariance matrices specify nuclear data uncertainties and its associated correlations. These data are necessary for the assessment of uncertainties of design and safety parameters in nuclear applications which will be discussed in more detail in Section 2.3 (Alhassan, 2015).

2.1.2 EFFECTS OF RESONANCE SELF-SHIELDING

With neutron interactions, the nuclei interacting with neutrons exhibit resonances in the epithermal region of the reactor neutron spectrum. The use of the $1/E$ form of the slowing-down flux assumes that there is no substantial absorption taking place at those energies. In practice, neutrons in the epithermal region are likely to be absorbed by materials in narrow intervals of energies that correspond to sharp peaks in absorption cross-section called the resonances. Due to this, the neutrons will be absorbed, resulting in a flux depression as seen in Figure 2-3. The magnitude of the depression is a function of the dilution of the nuclide within a material mixture. The less dilute the nuclide, the larger its contribution to the total cross-section and the larger the flux depression results. The complex cross-section structure of the resonances can be observed between the energies of $1\ eV$ and $10\ keV$ (Ball, 2011).

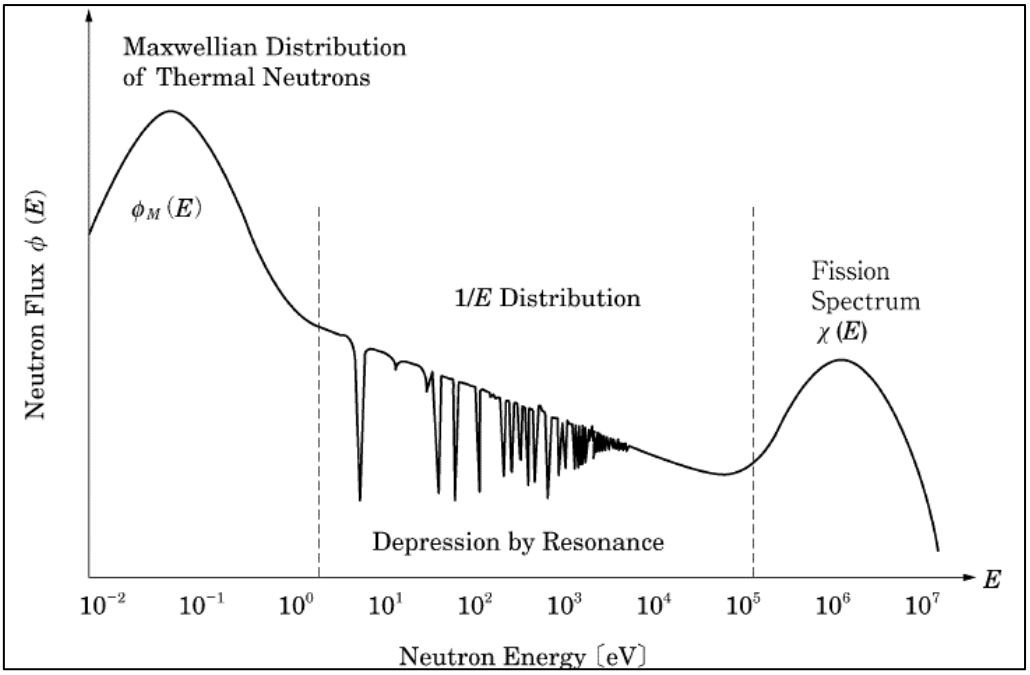

FIGURE 2-3: NEUTRON SPECTRUM OF A THERMAL REACTOR

The effect of flux depression influences the group constants that contains resonances. In Figure 2-4, the flux depression that has formed due to the presence of a strong cross-section resonance is observed (Ball, 2011). The process of correcting the multi-group cross-sections to new values that reflect the flux depressions is an initial step of any lattice calculation.

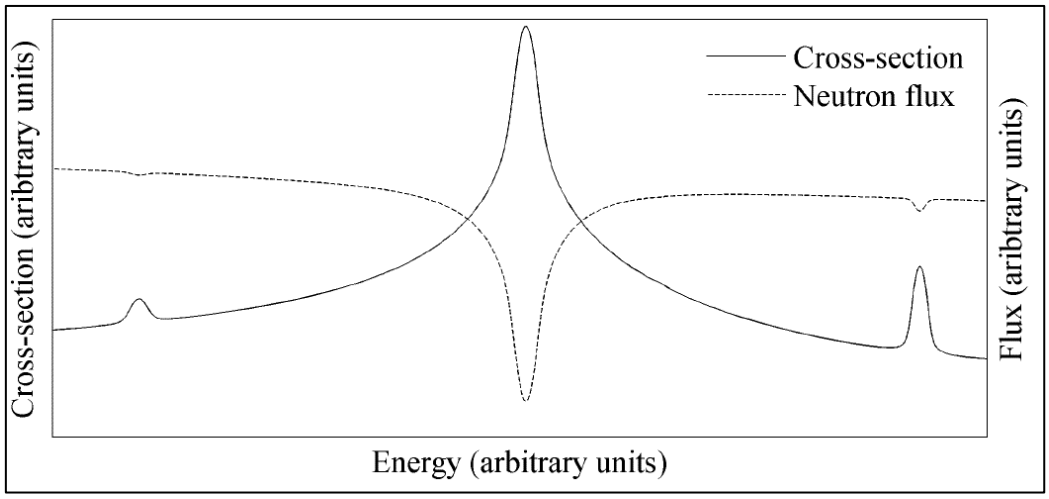

FIGURE 2-4: NEUTRON FLUX DEPRESSION IN RESONANCE

2.2 NUMERICAL METHODS FOR NEUTRON TRANSPORT

To simulate the neutronics of a reactor system using BE codes, two numerical approaches are considered for this study. The two numerical approaches are the Monte Carlo methods applied in KENO-VI and MCNP6 codes and the deterministic techniques applied in the NEWT code. The Monte Carlo method is extremely effective for problems with complex geometries where

calculations of integral quantities such as the neutron multiplication eigenvalue factor is desired. However, obtaining accurate differential information such as the neutron flux as a function of space and energy can be inefficient and prone to inaccuracy even with correct integral quantities when the Monte Carlo Method is used. The deterministic methods are therefore more suitable for problems that require the neutron flux as a function of space (DeHart, 2006). In the deterministic methods, the neutron transport equation is discretised and solved directly with numerical methods. The neutron transport equation represents the description of the transport process with cross-sections that are defined sufficiently well (Tuttelberg, 2014).

2.2.1 NEUTRON TRANSPORT EQUATION FOR NEUTRONICS SOLUTIONS

To derive the solution of the neutronics calculations, the time-dependent Boltzmann equation given in Eq (3) is solved:

$$\underbrace{\frac{1}{v}\frac{\partial}{\partial t}\psi(\vec{r},\hat{\Omega},\mathrm{E},\mathrm{t})}_{time-rate\ of\ change} + \underbrace{\hat{\Omega}\cdot\nabla\psi(\vec{r},\hat{\Omega},\mathrm{E},\mathrm{t})}_{streaming\ term} + \underbrace{\Sigma_t(\vec{r},E)\psi(\vec{r},\hat{\Omega},\mathrm{E},\mathrm{t})}_{total\ removal\ term} = q\underbrace{(\vec{r},\hat{\Omega},\mathrm{E},\mathrm{t})}_{source\ term} \tag{3}$$

where the source term $q(\vec{r},\hat{\Omega},\mathrm{E},\mathrm{t})$ consists of a scattering source S, an external source Q and a fission source F. The independent variables of the Boltzmann equation, $\vec{r},\hat{\Omega},\mathrm{E},\mathrm{t}$, represents the following: $\vec{r}$ represents the 3 spatial coordinates (x,y,z), $\hat{\Omega}$ the two directional ordinates (α,μ), E the energy and t the time. The scattering source describes the scattering to the neutron density phase space element from other energies and directions. It can be written with a double-differential scattering cross-section (Taavitsainen, 2016):

$$S(\vec{r},\hat{\Omega},\mathrm{E},\mathrm{t}) = \int_{4\pi}\int_{E}\Sigma_s(\vec{r},\hat{\Omega}'\to\hat{\Omega},E'\to E,t)\psi(\vec{r},\hat{\Omega}',E',t)d\hat{\Omega}'dE' \tag{4}$$

The fission source, in turn, can be written with the help of the scalar flux as the fission neutrons are emitted isotropically as shown in Eq (5).

$$F(\vec{r},E,t) = \frac{1}{4\pi}\int_0^\infty \chi(E)\nu\Sigma_f(\vec{r},E')\phi(\vec{r},E',t)dE'. \tag{5}$$

Here, the $\chi(E)$ term is the fission spectrum describing the probability for fission neutron to be emitted with an energy dE about E, while ν is the fission neutron yield per fission. The scalar counterpart of the neutron flux is given in Eq (6) as:

$$\phi(\vec{r},E,t) = \int_{4\pi}\psi(\vec{r},\hat{\Omega},\mathrm{E},\mathrm{t})\,d\hat{\Omega} \tag{6}$$

Finally, the external source term does not depend on the flux and describes the effect of possible external sources.

The neutron flux ψ, is a solution of the neutron transport equation and is useful for calculating the physical neutronics results. The problem of solving the neutron transport equation can be modified into a steady-state problem by assuming a stational pseudo-critical equation and ignoring the time-dependence of Eq (3) to yield Eq (7):

$$\underbrace{\hat{\Omega} \cdot \nabla \psi(\vec{r}, \hat{\Omega}, \mathrm{E})}_{streaming\ term} + \underbrace{\Sigma_t(\vec{r}, E)\psi(\vec{r}, \hat{\Omega}, \mathrm{E})}_{total\ removal\ term} = \underbrace{q(\vec{r}, \hat{\Omega}, \mathrm{E})}_{source\ term} \tag{7}$$

By introducing the multiplication factor k, the fission source in the source term is scaled to exactly balance the loss rate in Eq (8):

$$q(\vec{r}, \hat{\Omega}, \mathrm{E}) = S(\vec{r}, \hat{\Omega}, \mathrm{E}) + \frac{1}{k} F(\vec{r}, \hat{\Omega}, E,) \tag{8}$$

This k eigenvalue can also be defined as the ratio of the number of neutrons produced in the current generation to the number of neutrons produced in the preceding generation. The k-eigenvalue is related to criticality so that $k = 1$ implies that the system is critical, $k < 1$ shows sub criticality and $k > 1$ means the system is supercritical (Tuttelberg, 2014).

2.2.2 MONTE CARLO (MC) METHODS

The Monte Carlo method is widely used in reactor systems to solve neutron transport problems. The Monte Carlo methods as applied to the KENO-VI code used in this study solves the Boltzmann neutron transport equation given in Eq (3) by modifying it for the continuous and multi-group energy mode solution methods (DeHart, et al., 2015).

In a neutronics calculation, a Monte Carlo method solves a neutron transport problem by simulating individual neutron histories to obtain criticality results such as the multiplication factor and the neutron flux. A criticality problem is specified by defining the geometry of a reactor system, materials involved, quantities to be tallied and free parameters. The free parameters are the number of skipped generations (inactive cycles), active generations (active cycles) and neutron source per generation. For criticality calculations, a generation is the life of a neutron from birth in fission until the history is terminated. In MCNP, termination can be caused by either, absorption or leakage from the system. In KENO-VI, each neutron is tracked until the history is terminated via leakage from the system or the particle is killed via Russian Roulette.

To summarize the history of the neutron, the neutron's starting position, energy and direction of motion are determined from a given cumulative distribution function. The cumulative distribution function is explained below. The distance to a collision site is determined, and the nature of the

collision (reaction type) is then determined. Should the reaction type be absorption, then the neutron history is terminated. If the absorption was fission, then the fission neutrons produced become the source neutrons for the next generation at the point where they were created. Should the reaction type be a scatter cross-section, then the neutron history is continued to the next stochastically determined collision site where the process is repeated. Should the neutron reach the boundary of the problem, then the history is terminated. More detailed descriptions of these processes are found in the SCALE 6.2 (Rearden & Jesse, 2016) and the MCNP6 (Pelowitz, 2013) manuals.

Each part of the process is determined stochastically using probability and cumulative distribution functions (PDFs and CDFs, respectively) and random numbers.

The PDF is a function f(x) which defines the probability that a variable x will have for a given value of the variable in the given interval. This function can be normalized as shown in Eq (9) where $a \leq x \leq b$ defines the range of x:

$$\int_a^b f(x)\,dx = 1 \tag{9}$$

The PDF can be used to define the cumulative density function (CDF), which is calculated from Eq (10) by direct integration (Abbasi, 2016):

$$F(x) = \int_0^x f(x')dx' \tag{10}$$

The relationship between $f(x)$ and $F(x)$ is defined as:

$$f(x) = \frac{dF(x)}{dx} \tag{11}$$

All CDFs arising from a properly defined PDF are numerically invertible. Therefore, x can be determined by setting a random number r to be F. With each physical process defined by CDF, the random walk of the neutron can then be defined using a random number generator.

The multiplication factor k may be given as the ratio of the number of neutrons produced in $(n+1)^{th}$ generation to the number of neutrons produced in the n^{th} generation, which is the case for MCNP.

In the case of KENO-VI, an integral form of the transport equation in Eq (7) is obtained, in which k is an eigenvalue of the integral of the equation. The solution strategy is then to use an iterative procedure. The integral equation then contains flux expressions Φ_{n-1} and Φ_n for generations $n-1$ and n. The integral form of the transport equation is solved both in continuous energy form and

multi-group energy form in KENO-VI. Detailed explanation regarding the integral transport equation as applied in KENO-VI can be obtained in the SCALE manual (Rearden & Jesse, 2016).

Figure 2-5 shows a sampled neutron track with respect to the reactions it undergoes. Following the first generation of neutron histories, the information stored from the source obtained from the previous generation is used as the starting points of the neutron source distribution for the next generation. The neutron transport is continued from generation to generation until the required number of generations is completed.

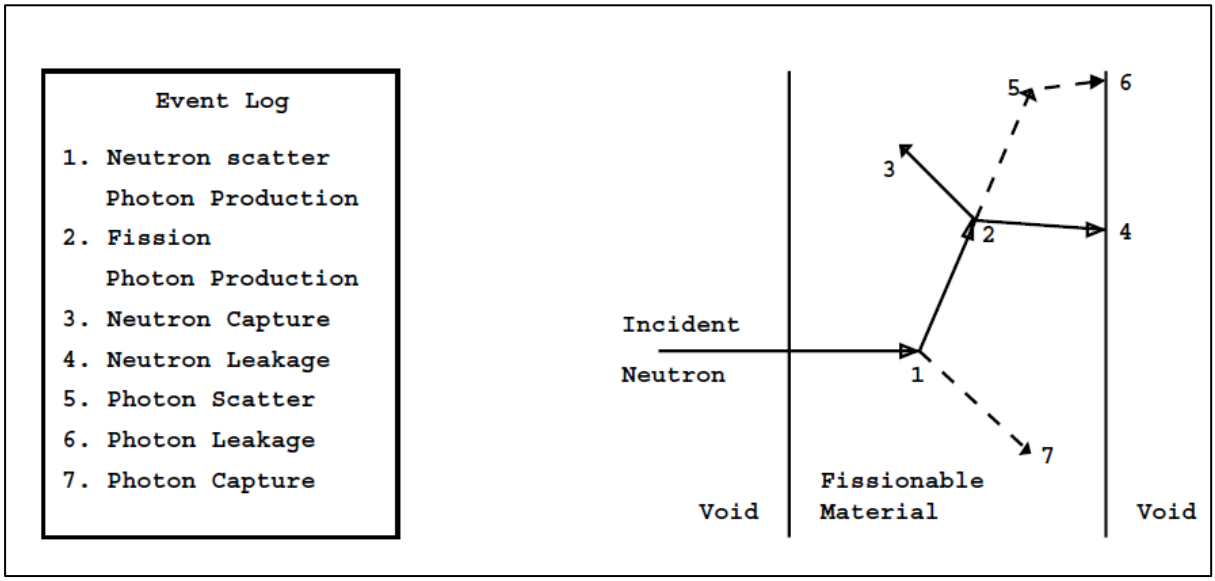

FIGURE 2-5: NEUTRON PATH (BRIESMEISTER, 2000)

Since Monte Carlo methods generate the samples $x_1 \dots x_N$ of x over N neutron histories, the sample mean value is calculated by:

$$\bar{x} = \frac{1}{N}\sum_{i=1}^{N} x_i \tag{12}$$

An example of x could be the multiplication factor k. Good statistics are not possible in the first few generations because not enough historical data has been collected to develop a well distributed source definition. The first few generations (number of skipped generations) are used to converge the neutron source only. The number of active generations are used to develop the statistical bounds of the desired results. The statistical bound can be obtained as the variance of the N number of histories, which measures the spread in a set of numbers. This is shown in Eq (13):

$$\sigma = \sqrt{\frac{\sum_{i=1,N}(x_i - \bar{x})^2}{N-1}} \tag{13}$$

Using more skipped and active generations would yield better results, however, this comes at the cost of computation time and memory requirements. Therefore, the user must ensure a source convergence and statistical accuracy based on time and the computer system available (Abbasi, 2016). The estimated variance of the mean value also known as the standard deviation is determined by:

$$\sigma_{\bar{x}} = \frac{\sigma}{\sqrt{N}} \tag{14}$$

To obtain a good statistical accuracy of the results, the N number of active generations must be large such that 68.27% of the sample points will fall within one standard deviation of the mean value. The sample will then display characteristics of a normal distribution as shown in Figure 2-6. Further properties of a normal distribution are that approximately 95% of the normal distribution population will fall within two standard deviations and 99.7% of the population will fall within three standard deviations of the mean value as seen in Figure 2-6. This characteristic of the normal distribution is critical in assisting scientist and engineers with stabling a level of confidence in their results (Wyant, 2012).

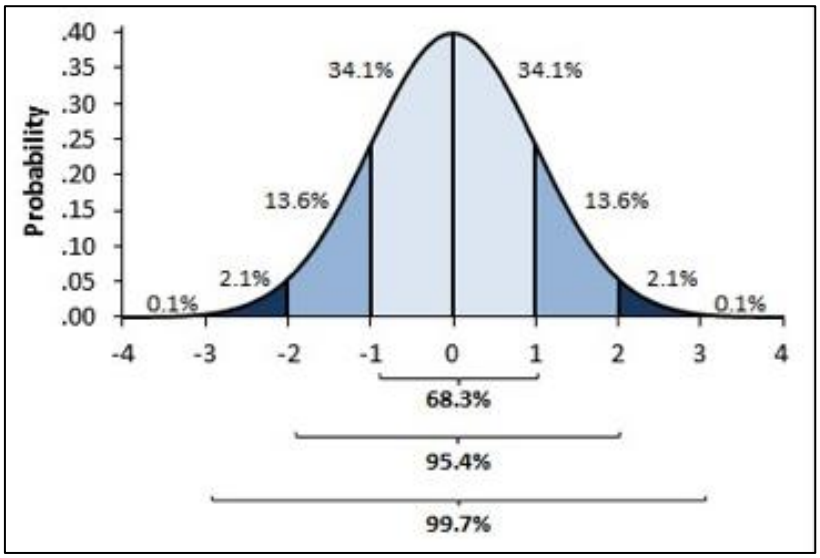

FIGURE 2-6: NORMAL DISTRIBUTION

2.2.3 DISCRETE ORDINATES (S_N) APPROXIMATION OF THE TRANSPORT EQUATION

As it is well-known that the neutron transport equation can be solved in various forms, and simplifications are often made to adapt the equation to the requirements of a specific application. Deterministic transport methods allow the discretisation of all the variables (energy, space and angular variables) in the equation. When energy is discretised, the transport equation in Eq (7) becomes a set of linear equations for each energy group g as can be shown in Eq (15):

$$\hat{\Omega} \cdot \nabla \psi_g(\vec{r}, \hat{\Omega}, \mathrm{E}) + \Sigma_{t,g}(\vec{r}, E)\psi(\vec{r}, \hat{\Omega}, \mathrm{E}) = q_g(\vec{r}, \hat{\Omega}, \mathrm{E}) \quad (15)$$

The coupling between energy groups is managed by group-specific scattering cross-section as shown in Eq (16).

$$\Sigma_{s,}(\vec{r}, g' \to g, \hat{\Omega}' \cdot \hat{\Omega}) = \frac{\int_{E_{g+1}}^{E_g} dE \int_{E_{g'+1}}^{E_{g'}} \Sigma_s(\vec{r}, E' \to E, \hat{\Omega}' \cdot \hat{\Omega})\phi(\vec{r}, E')\, dE'}{\int_{E_{g'+1}}^{E_{g'}} \phi(\vec{r}, E')} \quad (16)$$

Spatial discretisation involves the discretisation of the simulation geometry in space such that the simulation is composed of N_v volumes with the material properties assumed to be homogeneous within each volume. For the angular variables, a discretisation of the outgoing angular distributions of the particle interactions is performed. Hence, the angular distributions are reduced to a set of directions, $\hat{\Omega}_n$, where $n = 1, \dots, N$ chosen to be normal to the surfaces created by the spatial discretisation. Subsequent integration is then performed using the appropriate quadrature scheme as discussed later.

For a given set of pair (α, μ) of the unit vector $\hat{\Omega}$ in several fixed directions and a set of spatial points, the transport equation for lattice calculations with appropriate boundary conditions is solved using the discrete ordinates method. Further details regarding (α, μ) are provided in Section 2.2.3.2.

2.2.3.1 *Step characteristic approximation*

Usually discrete ordinates are based on a finite-difference approximation to solve the flux streaming term. Such a differencing scheme becomes difficult when complex non-orthogonal geometries are desired because of the nature of finite difference approximations for spatial derivatives. This method can be substituted by the method of characteristic which solves the transport equation analytically along characteristic directions within a computational cell (Rearden & Jesse, 2016).

The method of characteristic is used for 2-D cell and assembly transport problems in which streaming dominates scattering. Since the angular flux $\psi(\vec{r}, E, \hat{\Omega})$ in direction $\hat{\Omega}$ is the required, the streaming term is then written along the s-axis oriented along the characteristic direction $\hat{\Omega}$ to produce:

$$\hat{\Omega} \cdot \vec{\nabla} \psi(\vec{r}, E, \hat{\Omega}) = \frac{d\psi(s, E)}{ds} \quad (17)$$

Hence Eq (17) can be written in the characteristic form as:

$$\frac{d\psi(s)}{ds} + \Sigma_t(s)\psi(s) = q(s) \tag{18}$$

E is emitted from the equation for brevity. This then has a solution of the form:

$$\psi(s) = \psi_0 e^{-\Sigma_t s} + e^{-\Sigma_t s}\int_0^s q e^{\Sigma_t s'} ds' \tag{19}$$

where ψ_0 is the known angular flux at $s = 0$ given from boundary conditions for known cell sides. One of the schemes that use the method of characteristic is the step characteristic (SC) method developed by Lathrop (Rearden & Jesse, 2016). This approach assumes that the source q and macroscopic total cross-section Σ_t are constant within a computational cell and that the angular flux is constant on the cell boundaries of the incoming direction. The integration term of Eq (19) is then performed to obtain:

$$\psi(s) = \psi_0 e^{-\Sigma_t s} + \frac{q}{\Sigma_t}(1 - e^{-\Sigma_t s}) \tag{20}$$

Although this method described above is based on rectangular cells, the derivation of Eq (20) makes no assumptions about the shape of the cell. It merely requires knowledge of the relationship between cell edges along the direction of the characteristic. When applied to generalized geometries, the method is referred to as the Extended Step Characteristic (ESC) method.

Figure 2-7 represents a sample computational cell in which SC method is applied. Assume that Ψ_L and Ψ_B are known and evaluating Eq (17) along the direction $\hat{\Omega}$. Then, Ψ_T will have a weighted contribution from Ψ_L and Ψ_B and Ψ_R will have a contribution only from Ψ_B. If the sides L and B are at the boundary of the problem, then these values will be boundary conditions. If not, then Ψ_L would have been evaluated in a previous calculation where cell would have been to the left of the current cell, and Ψ_B would have been evaluated in a previous calculation where the cell would have below the current cell.

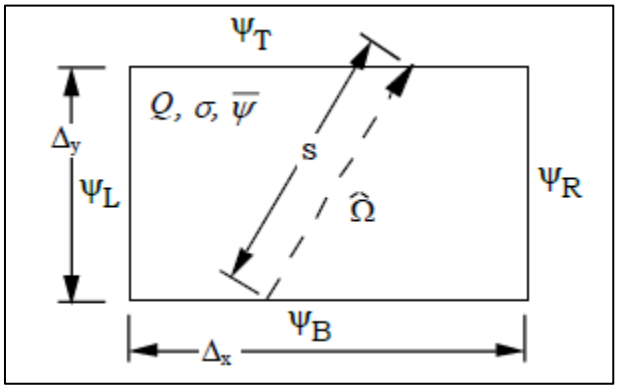

FIGURE 2-7: TYPICAL RECTANGULAR CELL USED IN SC

When a non-Cartesian cell is considered, the 2D space can be approximated by an irregular mesh comprising of arbitrary polygons where a unit cell is divided into zones consisting of polygonal meshes as shown in Figure 2-8 (Oberle, et al., 2006).

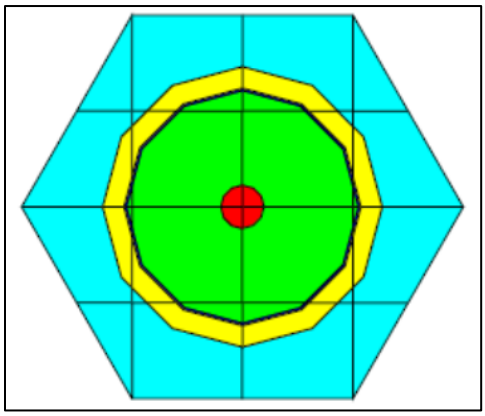

FIGURE 2-8: PIN CELL MESHES

2.2.3.2 *Angular dependence*

In terms of the representation of the unit vector $\hat{\Omega}$, α is defined as the azimuthal angle of the unit vector $\hat{\Omega}$ projected onto the x-y plane with respect to the x-axis; and μ denotes the cosine of the polar angle θ, needed to rotate the z-axis to unit vector $\hat{\Omega}$ as illustrated in Figure 2-9. The angular variables in x, y, z are represented as follows (Young, 2016):

$$\begin{aligned} \Omega_x i &= \eta = \sqrt{1-\mu^2}cos\alpha \\ \Omega_y j &= \varepsilon = \sqrt{1-\mu^2}sin\alpha \\ \Omega_z k &= \mu = cos\theta \end{aligned} \tag{21}$$

The angular variables α and θ ranges between $0 < \alpha < 2\pi$ and $0 < \theta < \pi$ respectively.

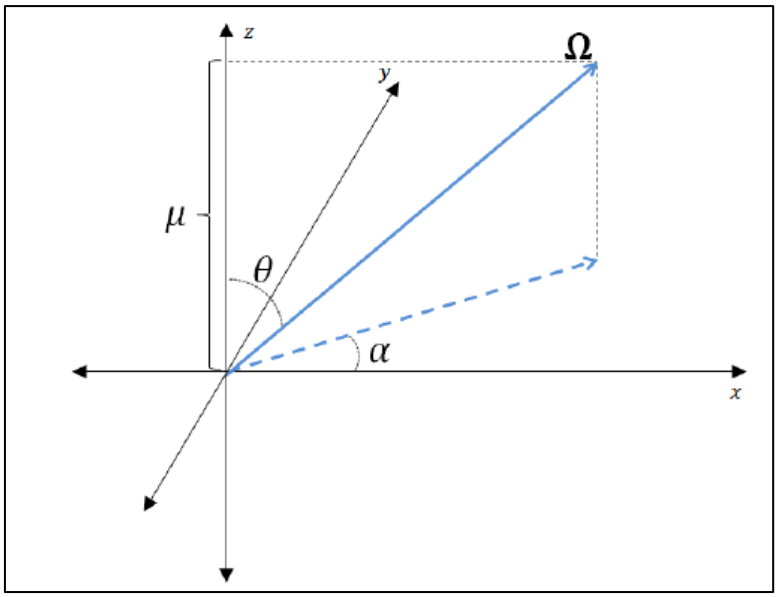

FIGURE 2-9: ILLUSTRATION OF THE ANGULAR VARIABLES IN x, y, z AXIS

To discretise the angular variables, a set of discrete angles is chosen as:

$$\widehat{\Omega}^n = \widehat{\Omega}(\alpha^n, \theta^n), for\ n = 1,2, \dots, N \tag{22}$$

along with corresponding weights, w_n. The combined set of the angles and weights is known as a quadrature set. A quadrature set is a set of weights and directions (ordinates), with the ordinates conveniently described using the direction cosines in Eq (21) (Jarrel & Adams, 2011). The quadrature of angles, $\widehat{\Omega}_n$ and weights, w_n is chosen such that angular integrals are approximated as (Young, 2016):

$$\int_{4\pi} f(\widehat{\Omega}) d\Omega \approx \sum_{n=1}^{N} w_n f(\widehat{\Omega}^n) \tag{23}$$

The angular flux variable is then restricted to these discrete angles:

$$\psi_n(\vec{r}) = \psi(\vec{r}, \widehat{\Omega}^n) \tag{24}$$

Then, angular integrals such as the scalar flux in the transport equation in Eq (24) can be approximated using a quadrature summation as shown in Eq (25):

$$\phi(\vec{r}) = \int_{4\pi} \psi(\vec{r}, \widehat{\Omega})\, d\Omega \approx \sum_{n=1}^{N} w_n \psi_n(\vec{r}) \tag{25}$$

Employing this quadrature treatment to Eq (25) give rise to the discrete ordinates form of the multi-group transport equation shown in Eq (26):

$$\widehat{\Omega}^n \cdot \nabla \psi_g^n(\vec{r}) + \Sigma_{T,g}(\vec{r}) \psi_g^n(\vec{r}) = \sum_{g'=1}^{G} \sum_{n'=1}^{N} w_n \Sigma_{s,g'\to g}^{n'\to n}(\vec{r})\, \psi_g^n(\vec{r}) + \frac{\chi_g(\vec{r})}{4\pi k} \sum_{g'=1}^{G} \nu\Sigma_{f,g'}(\vec{r}) \sum_{n=1}^{N} w_n \psi_{g'}^{n'}(\vec{r}) \tag{26}$$

The discrete form of the scattering cross-section used in the Eq (16) is defined as:

$$\Sigma_{s,g'\to g}^{n'\to n}(\vec{r}) = \Sigma_{s,g'\to g}(\vec{r}, \mu_0) \tag{27}$$

where $\mu_0 = \widehat{\Omega}^{n'} \cdot \widehat{\Omega}^n$.

In principle, a wide variety of quadrature sets can be used with the deterministic method in lattice physics codes for angular discretisation. In NEWT, level symmetric quadrature and product quadrature set are utilised.

The level symmetry quadrature is defined by S_N orders of approximation available in $S_2, S_4, S_6, S_8, S_{10}, S_{12}, S_{14}$ and S_{16}.The level symmetric quadrature exhibits octant symmetry as seen in Figure 2-10. The number of azimuthal angles corresponding to each polar angle in the quadrature can vary. The specific directions and corresponding weights are chosen such that they properly integrate polynomial functions as accurate as possible (Young, 2016). The symmetry of the quadrature imposes equal weights for all directions belonging to a set of positions invariant with respect to $\pi/2$ rotations. For instance, the quadrature in Figure 2-10 is S_8, with four levels in the positive-z half space as shown. However, the LSQ method does not insist that the angles take on any direction. Hence they tend to be used for general reactor problems.

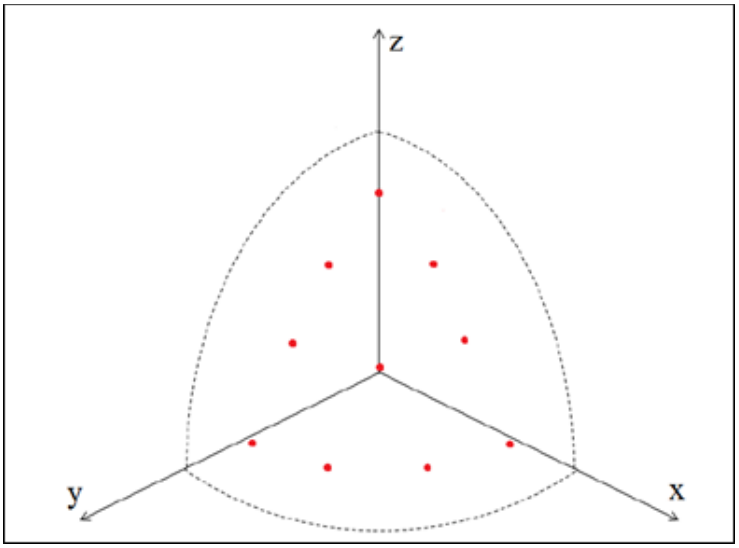

FIGURE 2-10: ILLUSTRATION OF LSQ SET

In some instances, it is important to construct a quadrature that treats different directions in space differently. To construct this quadrature, a product quadrature (PQ) is assigned to align the pole of an angular coordinate system with the axes of the cylindrical structures (Young, 2016). The product quadrature (PQ) is defined as the combination of a one-dimensional quadrature set along the polar axis and a one-dimensional quadrature set in the azimuthal plane. This method yields a set whose weights are products of the weights from the two sets. Figure 2-11 shows a PQ with four azimuthal angles and three polar angles per octant. It must be noted that each polar angle contains the same four azimuthal angles.

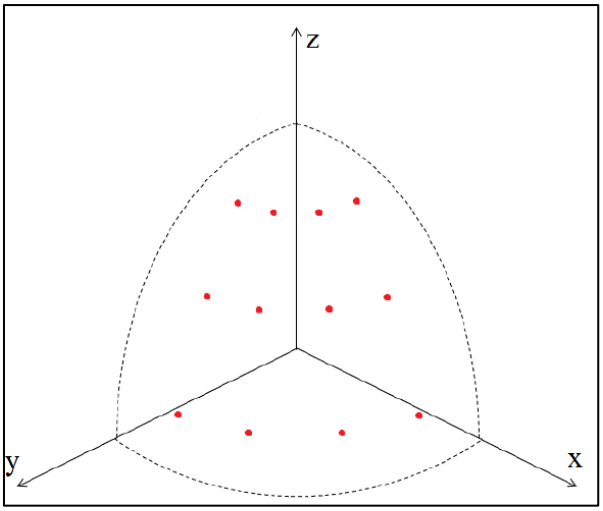

FIGURE 2-11: ILLUSTRATION OF PQ SET

As an example, to obtain the scalar flux, $\phi(\vec{r})$, the following summation would be used:

$$\phi(\vec{r}) = \sum_{n=1}^{N_{polar}} \sum_{m=1}^{N_{azi}} \psi(\vec{r}, \theta^n \alpha^m) w_n w_m \tag{28}$$

The benefit of using PQ sets is the ability to have an arbitrary number of directions without limitations from potentially problematic negative weights (Jarrel & Adams, 2011). The PQ method is more efficient for angular discretisation and allow several computation optimisations. It has been stated that LSQ sets should be used for general analysis, and in a real-world reactor analysis, a higher quadrature using the PQ sets should be employed (Wang, 2009).

2.2.3.3 *Homogenisation and the collapse of nuclear cross-sections*

Using the methods discussed in the previous section, the solution to the neutron flux contains space-dependent data. This, together with the energy dependency, can make the dimensions of the matrices used in the numerical solution extremely large. Homogenisation of cross section to lessen the space-dependent information and group-collapsing of cross-section to reduce the energy-dependent information is therefore considered to make the solution more tractable (Okumura, et al., 2014). The analytical derivations from Eq (29) to (31) are useful to get a general understanding of the energy dependence of the neutron flux when solving the neutron-transport equation.

The basic idea of performing these two methods is to conserve neutron reaction rate in the system. In the homogenisation, a homogenised neutron flux ϕ_g^{homo} is first defined as an averaged flux weighted by volume V_k of region (k) using Eq (29).

$$\phi_g^{homo} = \sum_k \phi_{g,k} V_k \Big/ \sum_k V_k = \sum_k \phi_{g,k} V_k / V^{homo} \tag{29}$$

To represent the reaction rate in the homogenised whole region of volume V^{homo}, a homogenised XS $\Sigma_{x,g}^{homo}$ is determined as:

$$\Sigma_{x,g}^{homo} \phi_g^{homo} V^{homo} = \sum_k \Sigma_{x,g,k} \phi_{g,k} V_k \tag{30}$$

The term: $\phi_{g,k}$ in Eq (30) is defined as the fine-group neutron flux. Therefore, the homogenised cross-section is calculated as:

$$\Sigma_{x,g}^{homo} = \sum_k \Sigma_{x,g,k} \phi_{g,k} V_k / \phi_g^{homo} V^{homo} \tag{31}$$

The methods described above, can easily be observed in Figure 2-12.

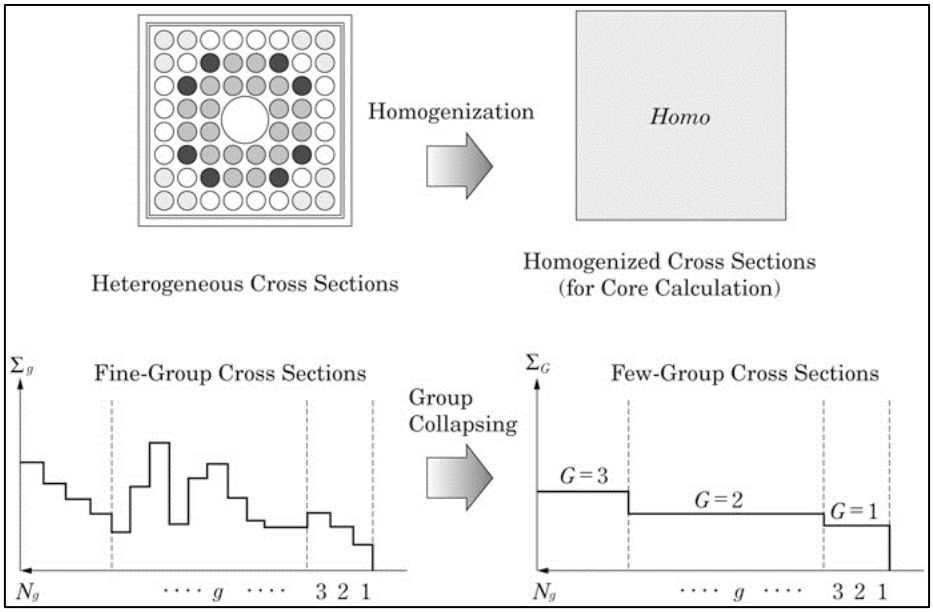

FIGURE 2-12: HOMOGENISATION AND GROUP COLLAPSING OF XS

Deterministic methods can generate the few group homogenised cross-sections provided there are energy boundaries for the few-group structure. The few-group structure is often determined based on the problems' reactor design, fuel type, coolant and moderator properties and based on experience (Moghrabi & Novog, 2018).

Two groups are adopted for the nuclear core calculation of the LWRs and the energy cut-off point of 0.625 eV for the few-group structure is used for collapsing the cross-sections into two groups (Ivanov, et al., 2013). It must be noted that the energy boundary is not universally fixed and can vary depending on the problem or model specifications.

2.2.4 COMPARISON OF DETERMINISTIC AND MONTE CARLO METHOD

The comparison between a deterministic model and a Monte Carlo model is shown in Table 2-3.

TABLE 2-3: DETERMINISTIC VS MONTE CARLO

Deterministic	Monte Carlo
2D method based on multi-group treatment of energy Some 3D problems can be solved.	3D method based on CE but can also use MG
Can handle a simplified geometry	Can handle complex geometries consisting of discrete material regions
Avoids statistical uncertainty	Produces statistical uncertainty
Computationally less demanding	High computational cost

Whilst most of the deterministic codes are solving 2D, some 3D problems can be solved using deterministic codes such as e.g. PARTISN, DOORS.

The KENO-VI which uses the Monte Carlo methods allows a continuous energy (CE) mode and multi-group (MG) mode, while the NEWT code which is based only on multi-group mode. In general, continuous energy (CE) methods are preferred because the CE treatment avoids many of the assumptions and approximations inherent in multi-group (MG) methods (Dunn, et al., 2004). A CE cross-section library includes almost all the details of the evaluated nuclear data file and is more accurate. However, Monte Carlo transport calculations using continuous energy cross-sections libraries are extremely time consuming.

The main advantages of using Monte Carlo CE method are as follows (Cai, 2014):

- The exact simulation of the interactions between a neutron and material are performed;
- Exact 3-D geometries are calculated; and
- Point-wise library data are directly used, and no self-shielding approximation are necessary.

Although CE Monte Carlo is the most accurate method, there are many applications where the MG Monte-Carlo method is required. Effective use of the MG method requires the availability of appropriate MG cross-sections. The MG option in the Monte Carlo method is a powerful method for several important applications (Wagner, et al., 1994):

- Comparison of deterministic transport codes to Monte Carlo codes;

- Utilisation of adjoint calculations in problem where it is more efficient than forward transport calculations;
- Generation of adjoint importance functions to enhance calculation efficiency in forward multi-group or continuous energy MC calculations;
- Cross-section sensitivity studies; and
- Solution of problems with multi-group cross-sections when continuous energy cross-sections are unavailable.

2.3 SENSITIVITY AND UNCERTAINTY METHODOLOGIES

2.3.1 IMPORTANCE OF UNCERTAINTY QUANTIFICATION

Uncertainty analysis refers to the determination of the uncertainty in the input data of a system and the propagation of these uncertainties in the calculation chain to yield the uncertainties of the results in the output. Uncertainty quantification assists in giving confidence in the results of interest and confidence in the accuracy of best-estimate code. Uncertainty quantification of a model output is required to improve knowledge and understanding of a considered model for nuclear reactor behaviour.

In the IAEA report for safety standards, the use of BE codes with realistic input data combined with evaluation of uncertainties in the calculations results was recommended to demonstrate the inclusion of adequate safety margins (IAEA, 2008). This implies that use of BE neutron transport codes requires propagation of input data uncertainties to quantify the uncertainties in the results as calculated by the codes. The sources of uncertainties in numerical simulation calculations can be categorized into three classes, viz. those due to nuclear data uncertainties, those due to methods and modelling, and those due to manufacturing uncertainties. These are discussed Section 2.3.2.

The propagation of uncertainty involves quantification of the effects of the uncertain input data on the model outputs. An initial sensitivity test is done to identify the model inputs that cause significant uncertainty in the output and the relationship between the input, the model and the output data.

Sensitivity analysis refers to the determination of the contributions of the individual uncertainty inputs to the uncertainty in the analysis results and shows how they influence the results (Helton, et al., 2006). There are two different types of sensitivity analysis that are considered in this study: 1) local sensitivity analysis; and 2) global sensitivity analysis. Local sensitivity analysis focuses only on a specific input, to identify the input parameters that requires propagation. A global sensitivity analysis considers the whole input data using the integrated mean (Mesado, 2017). The specific number of input data to consider in uncertainty quantification is chosen based on the parameters that have the greatest uncertainty or the most influence on the output observed from

the initial sensitivity analysis. Uncertainty and sensitivity analyses are essential for quantifying the uncertainties in complex systems' results.

2.3.2 SOURCE OF INPUT DATA UNCERTAINTIES

2.3.2.1 *Nuclear data uncertainties*

Nuclear data are the basis of all neutron transport calculations and include information on cross-section data, decay data and fission yields. As discussed in Section 2.1, nuclear data are important for the development of nuclear reaction models in transport codes for reactor system calculations. Thus, the quality of nuclear data used in BE codes are significant for obtaining reliable and accurate results. For every element and isotope which appear in a transport problem, a cross-section must exist to achieve a solution of that problem (Fisher, 1989). In every cross-section, a slight inherent inaccuracy exists, and the uncertainty of the inaccuracy is propagated throughout the calculations.

The first step in the calculation of a nuclear system consists of generating cross-section libraries in the multi-group (MG) or continuous-energy (CE) form that is suitable for use in the transport code. These libraries are derived from general purpose libraries, named evaluated nuclear data (ENDF) libraries. The cross-sections obtained from the ENDF/B libraries are derived from a combination of experimental measured cross-sections and nuclear model calculations. Both sources inevitably give rise to uncertainty; therefore, their accuracy and validation is still a major concern. The uncertainty in experimental data arises from statistical and systematic errors or biases as well as variables in the experimental systems that are difficult or impossible for the experimenter to control. The uncertainty in nuclear models derives from the differences between the model's approximation and the physical reality of the nuclear systems (Leal, 2016). Therefore, nuclear data uncertainty helps in showing the accuracy of the results that one can expect from a BE code. Nuclear data covariance information which come with nuclear data libraries are often used to quantify the impacts of these uncertainties on the neutronic results (Alhassan, 2015).

2.3.2.2 *Method and modelling uncertainties*

The sources of uncertainties in modelling can generally be classified into three categories:

- Code methodology and its numerical implementation;
- Modelling of a real system with a mathematical formalism; and
- Statistical uncertainties, which arise from the statistical nature of Monte Carlo method if used.

In terms of the first category, the code developer uses specific mathematical formalisms (which can include stochastic models) to represent the real system, and subsequent numerical algorithms to implement these formalisms. For many parts of the mathematical formalisms, multiple algorithms may be programmed giving different ways to solve the same part of the code.

The user can then choose any particular algorithm or part thereof by setting a parameter in the input file. However, in most cases, the code developer sets these parameters to default parameters and the computer codes can run very detailed calculations using these default values. These input code parameters that are associated with the inherent methodologies of the code and with default values provided by the code developer can be classified as inherent input parameters. Without the default values of these parameters changed, the code is forced to output a more general solution that may lack some of the complexity found in the measured data (Blyth, 2012). The mathematical formalisms used together with subsequent numerical algorithms implemented can therefore lead to uncertainties in the calculated results.

There are two ways to quantify this type of uncertainty. One way would be to modify the source code to test various possibilities of appropriate algorithms in the source code. However, access to source codes are usually restricted. Therefore, the second option is to quantify these uncertainties via the input deck by choosing various options with respect to numerical implementation in the code. However, these sensitivity tests must also consider keeping the computation time reasonable. To keep the computation time reasonable, it is therefore important to find a balance between a small convergence value for the calculations which indicates the required accuracy of the solution and the time expenditure. In this instance, the sensitivity analysis is not limited to propagating uncertainties, but also done as a tool for optimisation.

In terms of the second category, it may be difficult to quantise a model that may have been observed experimentally, into a series of inputs that are suitable and realistic to model. It requires some simplifications that stray from the exact scenario to make the input more general. Usually some generalisations are made to simplify the input enough for practical use. During the process of simplifying, some uncertainties are introduced, and the produced results will be slightly different than the measured one.

In terms of the third category, the stochastic nature of a Monte Carlo estimates will always include some degree of statistical uncertainty. According to the central limit theorem, the statistical uncertainty is proportional to $1/\sqrt{n}$, where n is the number of events that contributes to the estimated results. The precision of the estimated results depends upon the quality of the statistics, which is determined by the total number of neutron histories. This implies that, a large enough number of neutron histories will result in a small statistical uncertainty. However, achieving a small statistical uncertainty comes at a cost of computational time.

The major disadvantage of the Monte Carlo method is its requirement of significant computational resources to minimise the statistical uncertainties (Liu, 2015). To reduce the statistical uncertainties by a factor of 10, it is necessary to use 100 times more neutrons, so that the computational cost increases by a factor of about 100 (Helgesson, 2013).

2.3.2.3 *Uncertainty due to manufacturing tolerances*

The neutronics results rely on a nominal representation of the physical parameters such as the geometry dimensions and material compositions of the evaluated reactor system. However, components are not produced with the exact nominal values. Rather, they are manufactured within a tolerance about the nominal value. Each individual parameter is manufactured within a specified tolerance to ensure quality control, fabricability, etc. (NEI, 2017). The impact of tolerances of the physical parameter on the neutronics results therefore needs to be evaluated.

A sensitivity analysis using either the upper or lower tolerance limit of an individual parameter shows the effects of the specified tolerance on the neutronics results (Frosio, et al., 2017). This analysis assists with isolating those parameters which shows insignificant effects in the results. For the uncertainty propagation of an individual parameter, the tolerance limit is used as statistical interval, for which a specified distribution must be obtained or defined.

2.3.3 UNCERTAINTY AND SENSITIVITY METHODS

The UQ methodologies used in this study are classified as perturbation theory and statistical sampling based (SS) methods. The perturbation theory methods require looking into where and how the input parameters appear in the mathematical models embedded within the code and how the numerical methods solve the equations to calculate derivative information. The statistical sampling method is used mainly when few input parameters are considered, and many outputs are desired. Before applying the two methods, the sensitivity in the calculated results can be obtained by comparing the results of a varied parameter.

2.3.3.1 *Uncertainty analysis using perturbation theory*

The perturbation theory method estimates the impact of cross-section uncertainties in a reactor system's multiplication factor k, by propagating uncertainties using sensitivity coefficients and the first order perturbation theory. The sensitivity coefficient shows the change in the system's response k due to a change in the nuclear data parameters (e.g. capture, nubar) as defined in Eq (32):

$$S_{k,\Sigma_x} = \frac{dk/k}{d\Sigma_x/\Sigma_x} \tag{32}$$

where Σ_x is the macroscopic cross-section for reaction x. This term can be classified as an explicit sensitivity coefficient. To provide an accurate estimation of the sensitivities in a system where resonance self-shielding is important, the sensitivity coefficients as computed in Eq (32) require an additional term called implicit sensitivity coefficient. The implicit term accounts for the first-order implicit effect of perturbations in the material number densities or nuclear data upon the self-shield

group-wise macroscopic cross-section data (Rearden, 2004). Eq (33) gives the implicit term definition:

$$\left(S_{k,\Sigma_{x,g}}\right)_{implicit} = \frac{\omega_i}{\Sigma_{x,g}} \frac{d\Sigma_{x,g}}{d\omega_i} \tag{33}$$

where ω_i represents either the number density of a material or a certain nuclear data component or a physical dimension of a system. The complete sensitivity coefficient for reaction x in energy group g is calculated as the total of the explicit and implicit sensitivities as shown in Eq (34):

$$S_{k,\Sigma_x} = \left(S_{k,\Sigma_{x,g}}\right)_{implicit} + \left(S_{k,\Sigma_{x,g}}\right)_{explicit} \tag{34}$$

In terms of the group-wise cross-section data, the desired results are the effect on k of perturbing one cross-section that affects the resonance-shielded values of all cross-section data. If ω_i is a cross-section data component for process y of nuclide j in energy group h expressed as $\Sigma_{y,h}^{j}$, which is sensitive to the perturbations in process x in energy group g for nuclide i expressed as $\Sigma_{x,g}^{i}$, the implicit sensitivity coefficient of k due the perturbations in $\Sigma_{x,g}^{i}$ using the chain rule becomes (Rearden, 2004):

$$\left(S_{k,\Sigma_{x,g}^{i}}\right)_{implicit} = \sum\sum \frac{\Sigma_{y,h}^{j}}{k} \cdot \frac{dk}{d\Sigma_{y,h}^{j}} \times \frac{\Sigma_{x,g}^{i}}{\Sigma_{y,h}^{j}} \cdot \frac{d\Sigma_{y,h}^{j}}{d\Sigma_{x,g}^{i}} \tag{35}$$

The response uncertainty is then obtained by summing all the contributions to the system response from the uncertainties through the sensitivity coefficients and covariance data (Ferrer, et al., 2012). The vector S_k contains the sensitivities of the calculated k due to the nuclear data parameters.

In TSUNAMI, a module called SAMS uses the relative sensitivity vector S_k defined above as well as the SCALE 6.2.1 nuclear data covariance matric $COV_{\Sigma\Sigma}$ to calculate the relative uncertainty of the response k through a mathematical representation:

$$\left(\frac{dk}{k}\right)^2 = \mu_i = S_{k,\Sigma_{x,g}^{i}}^{T} COV_{\Sigma\Sigma} S_{k,\Sigma_{x,g}^{i}} \tag{36}$$

where $COV_{\Sigma\Sigma}$ is a covariance matrix in relative units of $(\%)^2$ and the superscript T denotes a transpose of a matrix (Sabouri, 2013). The covariance matrix $COV_{\Sigma\Sigma}$ contains the cross-section relative covariance data evaluated for all reactions Σ (in all energy groups). This matrix is symmetric; diagonal terms are relative variance and off-diagonal terms are relative covariance (Rearden & Jesse, 2016). A brief description of the SAMS module will be provided later in Section 3.6.1. The TSUNAMI covariance data file is composed of a combination of high and low fidelity nuclear data uncertainties (Cardoso, et al., 2015).

In general perturbation theory (GPT), the response uncertainty is extended to include other system responses in addition to the multiplication factor.

2.3.3.2 *Statistical sampling method*

The statistical sampling (SS) method is based on sampling probability distribution functions (PDFs) of uncertain input parameters to create a number, N, of input files. The PDFs are based on the knowledge of the actual distribution of the given parameter or are assumed when not available. For N input files created, the model is run N times with the N input files and N outputs files are generated. The overall output is then obtained, i.e. the mean and standard deviation are calculated from the N individual output values of the response required.

The uncertainty in the response k due to uncertainties in the input data is interpreted from the standard deviation estimated using Eq (37) as:

$$dk = \sqrt{\frac{\sum_{n=1}^{N}\left(k_n - \overline{k_n}\right)^2}{N-1}} \tag{37}$$

where k_n is the n^{th} sample. Consequently, the relative uncertainty in the response k can be obtained using Eq (38) as:

$$\mu_i = 100\% \times \frac{dk}{\bar{k}} \tag{38}$$

2.3.3.3 *Quantifying sensitivity coefficients*

To complete an uncertainty quantification using SS method, it is of interest in nuclear reactor physic and criticality analysis to include the inter-dependencies between the output response and the uncertain input, to establish whether a clear statistical correlation exists between these variables. The relationship between the output response and an uncertain input parameter is assessed by obtaining the correlation coefficients to quantify the association between the two variables. The output response is often referred to as the dependent variable, and the input data used in predicting the uncertainty are referred to as the independent variables. Using a set of random samples for a specific perturbed input x to obtain output y, the correlation coefficient is calculated using Eq (39) (Alhassan, 2014):

$$c_{x_i y_i} = \frac{\sum_{i=1}^{n}(x_i - \bar{x})(y_i - \bar{y})}{(n-1)\sigma_{x_i}\sigma_{y_i}} \tag{39}$$

where $\bar{x}$ and $\bar{y}$ are the sample means and σ_x and σ_y are the standard deviations for input x and output y. The correlation coefficient between the two variables varies between +1 and -1. The +1

value indicates that input variable and the output variable tend to increase together, and -1 value indicates that input variable and the output variable tend to move in opposite directions.

For several inputs x, s, t, …, the correlation coefficients can be calculated among them using Eq (40):

$$c_{x_i s_j} = \frac{\sum_{i=1}^{n}(x_i - \bar{x})(s_i - \bar{s})}{(n-1)\sigma_{x_i}\sigma_{s_i}} \quad (40)$$

where $\bar{x}$ and $\bar{s}$ are the sample means and σ_x and σ_s are the standard deviations for inputs x, s. By collecting all the correlation coefficients for all the variable, a correlation matrix can be constructed (Mesado, 2017).

2.4 NUMERICAL VERIFICATION AND VALIDATION

To classify a code as best-estimate, it is crucial to ensure that the reactor system models defined in the BE codes are representative of a real-scale reactor to obtain accurate simulation results.

Verification ensures that mathematical models are accurately programmed and solved in a computer code. The fundamental tools of verification are the method of produced solutions, compared with known analytic solutions or compared with highly accurate solutions of special or simplified cases. In this study, verification was done by using a previously tested method, NWURCS, that is used to generate the input of the model. This method requires verification of its accuracy by comparing its results to ensure that it represent the actual definition of the model. A brief description of NWURCS is given in Section 6.4 and a detailed description of this method can be obtained from (Nyalunga, 2016).

The accuracy of the code results can be proven through validation against experimental measured data, plant data and other similar real physical systems. In the interest of brevity, for the rest this section “experimental measured data” will be used to refer all these types of data collectively. Validation is the process in which a code’s outputs are compared to experimental results to assess the code accuracy. Validation ensures that the computational model is physically accurate. Validation ensures that the used mathematical simplifications and correlations are valid (Perko, 2015).

Verification and validation applications are important because of the impact of uncertain input parameters, numerical imprecisions and hidden physical processes.

The necessity of validation is identified in many state-of-the-art neutron transport codes such as KENO, MCNP, etc. These codes can predict the response k with a high degree precision, or with repeatability and reproducibility (Perko, 2015). However, problems exist with the codes’

accuracies, that is, there is always a difference between the calculated and the experimental measured data. The difference between the calculated value and experimental measured data is due to different contributions, as stated below:

- Uncertainties of input parameters (e.g. nuclear data, geometry, compositions)
- Computational methods (e.g. deterministic and Monte Carlo methods)
- Modelling approximations (e.g. homogenising regions or simplifying geometry)

Thus, when comparing computational results with experimental data, the imprecise knowledge about the input data parameters must be considered by propagating the input uncertainties to the computed outputs. In an instance where experimental data for a given application does not exist, validation can be done by comparing computed results with critical benchmarks, which are based on experimental data from critical systems. A benchmark for validation is chosen based on similar physical characteristics between the benchmark and the application of interest. The physical characteristics can be a fissile element and its concentration, moderator type, or geometrical configuration.

In this study, validation of the neutronics results of this study are performed using the LR-0 benchmark measured data for the experimental zero-power reactor LR-0. The LR-0 benchmark measured data were obtained from the experiment performed out at Nuclear Research Institute Rez plc in Czech Republic. The LR-0 benchmark specifications are discussed further in Section 6.

2.5 SUMMARY

Chapter 2 has outlined the background of neutronics and numerical approaches available to obtain the neutronics results of this study. The sources of uncertainties of the neutronics results were discussed as well as the methods available to quantify these uncertainties. The importance of verification and validation for the neutronics results was also provided.

3 APPLICATION OF THE COMPUTATIONAL CODES

This chapter provides a brief description of the computational codes used for this research work to generate best-estimates and associated uncertainties. As mentioned in Section 2.2, neutronics calculations can be performed using either a Monte Carlo or deterministic techniques. The uncertainty quantification can be performed using generalised perturbation theory or statistical sampling techniques. See below for the practical overview of the methodologies of these codes.

3.1 INTRODUCTION

Reactor analyses often require numerous calculations to compute quantities of interest. The availability of tools that can produce sufficiently accurate results with moderate computational requirements is crucial (Hamilton, et al., 2016). Several modules from the SCALE-6.2.1 code were used to perform the reactor physics calculations for the Kozloduy-6 VVER-1000 and LR-0 VVER-1000 systems. The inputs and results presented in this work have been provided using deterministic and Monte Carlo transport codes.

The Monte Carlo calculations were performed using version VI of the KENO code and the deterministic calculations were performed using the discrete ordinates (S_N) code NEWT (New ESC-based Weighting Transport code) that falls under TRITON sequences. The main intended use of TRITON is the generation of homogenised multi-group constants using NEWT for core analysis. Furthermore, TRITON has a built-in decay and burn-up routine (T-DEPL) which can generate time-dependent nuclide concentrations and spent-fuel characteristics including radioactivity and decay heat. This version of TRITON extends the burn-up capability to 3D problems. The sensitivity and uncertainty analyses were performed using TSUNAMI and SAMPLER of SCALE-6.2.1.

The sections that follows discuss the methods that were used in the above-mentioned codes. In general, the reactor physics calculations are performed in three stages. First, nuclear data from an established nuclear data library are obtained and processed using a code to generate a large number of cross-sections based on energy group discretisation. These structures are referred to as multi-group libraries. Secondly, transport simulations are performed utilising this multi-group nuclear data for a specific lattice geometry. Lastly, the nuclear data obtained from the transport code are supplied to nodal-diffusion codes for full core analysis.

3.2 TRANSPORT NUCLEAR DATA LIBRARIES

For obtaining the results of this study, the ENDF/B nuclear cross-section libraries (XSLIB) have been used for accurate and realistic calculations of the criticality results for the VVER-1000. The

XSLIB contain nuclides for actinides, structure materials, neutron poison, moderators, and fission products necessary for LWR problems with fresh or irradiated fuel for the temperature range from 293K up to 2400K. The information retrieved from the XSLIBs are used in this study to calculate the criticality safety parameters, considering all the relevant nuclear reactions within the total energy range. There are two versions of the ENDF/B available in SCALE-6.2.1: ENDF/B-V.II.0 (CE and 238-MG) and ENDF/B-VII.1 (CE, 56- and 252-MG).

The 252-group library provides a more detailed representation of the ^{238}U resonance structure, improved resonance self-shielding parameters and an increase in the thermal scattering cut off to improve performance for light water reactor systems. The 56-group was collapsed from the 252-group using an LWR flux spectrum and has been optimised for LWRs to allow shorter execution times in criticality and transport depletion calculations. Although this library does well in predicting LWR lattices, it is not able to calculate homogeneous thermal, epithermal, and intermediate-energy systems as accurately as the 252-group (Rearden & Jesse, 2016). The MG libraries are available for use in NEWT and KENO-VI calculations and CE library is available for use in KENO-VI calculations only.

3.3 NUCLEAR CROSS-SECTION PROCESSING

The nuclear cross-sections (XS) used for the solution of the neutronics calculations are generated using the XSProc nuclear data processing system of the SCALE-6.2.1. Most materials used in reactor analysis exhibits resonances in the epithermal region of the reactor neutron spectrum. This implies that, due to self-shielding effects, the neutron flux experiences significant perturbation inside the material (Goncalves, et al., 2001). As a result, the application of resonance self-shielding must be applied for cross-section processing to create applicable multi-group constants for lattice physics (Ball, 2011). The XSProc module was therefore designed to allow for the treatment of self-shielding and cross-section temperature correction.

The first process in using a multi-group energy structure involves processing neutron cross-section data to generate a fine structure of the multi-group cross-sections that are a function of dilution and temperature. This cross-section characterises the self-shielding of isotopes and must be generated specifically for isotopes that are contained in the unresolved resonance region. In the resolved resonance region, energy self-shielding is considered with a continuous energy representation of resonances. The cross-sections are generated for a range of dilution cross-sections and temperatures of the actual geometry (Herman & Trkov, 2009).

The XSProc module calls BONAMI, CENTRM and PMC to compute the self-shielding cross-sections. The section of the input file that calls XSProc is the CELLDATA block that is provided for a given unit cell. During the XSProc execution, the multi-group (MG) library specified in the input

file is processed by BONAMI prior to the CENTRM calculations. This is done so that BONAMI provides self-shielded data for the MG component of the CENTRM solution.

BONAMI (BONdarenko AMPX Interpolator) performs resonance self-shielding calculations based on the Bondarenko method. It reads the Bondarenko shielding factors ("f-factors") and infinitely dilute microscopic cross-sections from a problem-independent nuclear data library. It also interpolates the tabulated shielding factors to allocate temperatures and background cross-sections for each nuclide in the system, and lastly produces a self-shielded problem dependent data set (Rearden & Jesse, 2016).

The essence of the Bondarenko method is to parameterize the flux spectrum that corresponds to the varying degrees of self-shielding in terms of a background cross-section parameter σ_0. The background cross-section σ_0 is also known as the diluted cross-section (Herman & Trkov, 2009). With this method, it is possible to pre-process the MG data for different σ_0 representing the varying degrees of resonance self-shielding. The code performs self-shielding for arbitrary number of mixtures using either the narrow resonance (NR) or the intermediate resonance (IR) approximation.

CENTRM (Continuous ENergy TRansport Module) utilises a combination of MG and pointwise (PW) solution methods to solve the neutron transport equation over the energy range ~ 0 to $20\ MeV$. The energy range of interest is divided into three intervals called the upper multi-group range (UMR), the pointwise range (PW) and the lower multi-group range (LMR) respectively which are defined by input. Several transport computation methods are available for both MG and PW calculations. These include a space-independent slowing down calculation for infinite homogeneous media, 1D discrete ordinates or P1 methods for slab, spherical, and cylindrical geometries, and a 2D method of characteristics (MoC) method for lattice unit cells. The MoC calculation is presently limited to square lattices (Rearden & Jesse, 2016).

For the PW transport calculation, an energy range is usually chosen to include the interval where the important absorber nuclide has a resolved resonance. The MG calculations are performed where the cross-sections usually have a smoother variation or where the shielding is insignificant. The shielded MG cross sections processed by BONAMI are then used in CENTRM to correct infinitely dilute CE data in the unresolved resonance range.

CENTRM can be a rigorous cross-section treatment since it avoids inherent assumptions by calculating a problem-dependent flux. It enables problem-dependent MG cross-sections to have the flexibility and accuracy of PW continuous energy cross-sections for criticality analyses (Kriangchaiporn, 2006).

PMC (Produce Multi-Group Cross-sections) calculates MG cross-sections for each material mixture in each CENTRM calculation by using the PW neutron spectra within the mixture to weight the cross-sections in a continuous energy library file. This provides problem-dependent, self-shielded MG data representative of the fine-structure due to resonance reactions in the neutron energy spectrum for the system of interest. The self-shielded cross-sections obtained from PMC are calculated within the energy interval of the CENTRM PW flux calculation, defined by the energy limits DEMIN and DEMAX. Outside of this energy interval, the shielded cross-sections previously calculated with the Bondarenko method in BONAMI are retained (Rearden & Jesse, 2016).

XSProc automatically calls PMC during execution of a SCALE sequence, and the resulting zone-averaged, problem-dependent cross-sections can be passed to MG transport solvers such as KENO, NEWT, etc. called by the sequence.

The XSProc results are achieved by defining the CELLDATA block and including parameters relevant to the problem of interest. The parameters of interest that were defined for BONAMI are SZF (spatial mesh size factor) and IROPT (to choose the intermediate resonance or narrow resonance for background cross-sections). For CENTRM, the parameters are ISN (order of SN angular quadrature), ITERP (temperature interpolation method), ALUMP (mass lumping fraction) and DEMAX and DEMIN (highest and lowest energy range to calculate PW fluxes). The description of the parameters that were defined for BONAMI and CENTRM are given in the Table 3-1.

TABLE 3-1: XSPROC PARAMETERS

Parameter	Description	Values
SZF	This is a spatial mesh size factor. A value between 0.0<SZF<1.5 gives a finer mesh, while SZF>1.5 gives a coarser mesh.	>1.5
IROPT	Allows BONAMI to use intermediate resonance approximation (IR) if IROPT=1 and narrow resonance (NR) approximation for IROPT=0 (default is 0).	0/1/2/3
ISN	Defines the quadrature sets for geometry-dependent quantities.	2/4/6/…
ITERP	Introduces the use of the CRAWDAD (Code to Read and Write DAta for Discretised solution) temperature interpolation method for CE cross section. The CRAWDAD method generates CE cross-sections and thermal kernels. It reduces the energy range to interval of CENTRM PW calculation i.e. DEMIN>DEMAX.	0/1/2

ALUMP	This means that the fuel is lumped into one or more masses such that their masses are within the effective mass to shield its interior from resonance energy neutrons (CNSC, 2003).	0 - 1
DEMIN	This value is the lowest energy (eV) for which CENTRM calculates PW fluxes.	>0.001 eV
DEMAX	This value is the highest energy (eV) for which CENTRM calculates PW fluxes.	<500 keV

The parameters in Table 3-1 were chosen according to the contributions they introduced in the results when varied. Other parameters for BONAMI and CENTRM have been used at default values in this study. These parameters can be obtained in the SCALE manual. Although the parameters showed very low to no change in the results when varied, it is quite possible that some parameters could have been overlooked that should have been included. If such is found to be the case, the current investigation can be further refined.

The parameters defined in Table 3-1, were considered for all neutronics calculations that desired the use of MG libraries. XSProc processes the materials prior to execution of the NEWT and KENO codes and are thus processed parameters are the same for the FP model and the FA model.

3.4 NEUTRONICS CALCULATION CODES

For the subsequent transport calculation, there are two modules from SCALE-6.2.1 that are considered in this study, namely NEWT and KENO-VI, and the results were compared. The comparison of results between codes is very valuable in providing a basis for verification as well as code validation against an experimental benchmark (Goluoglu, et al., 2007).

3.4.1 NEWT MODULE

NEWT (New ESC-based Weighting Transport code) is a two-dimensional multi-group transport code that uses deterministic methods. NEWT uses the discrete ordinate approach to solve the neutron transport equation on a unit cell or lattice geometry level. The NEWT algorithm for solving the transport equation is based on the Extended-Step Characteristic (ESC) (Moghrabi & Novog, 2018). The ESC method was described in Section 2.2.3.1. The two important assumptions of the ESC method are that: all the properties within each cell are uniform and that cell boundaries are defined by straight lines (Grgic, et al., 2010). NEWT's solution grid is based on arbitrary polygons for the accurate representation of non-orthogonal geometries such as a fuel assembly lattice (Hartmann, 2016). The NEWT code can calculate homogenised multi-group, scattering matrixes, kinetic parameters, etc. for any group structure and region of interest (Ghasbyan, 2013).

The problem-specific flux calculated in a NEWT calculation is used to collapse a multi-group structure to a few-group structure, which for LWRs is typically a single thermal group and a single fast group. After the flux solution is obtained, an energy condensation is performed to derive equivalent macroscopic cross-sections for collapsed energy groups in the region being homogenised. The few-group homogenised cross-sections are passed to core calculations in further studies.

3.4.2 KENO-VI MODULE

KENO-VI is a three-dimensional Monte Carlo code that allows the geometrical model to consist of arbitrarily shaped bodies for nuclear criticality safety analyses (Rearden, 2004). KENO-VI has convenient geometry input, including the treatment of lattice arrays of materials. The principal result from KENO-VI for this study is an estimate of the multiplication eigenvalue k, and is calculated for each active generation. KENO-VI can also be used to calculate quantities such as neutron flux distributions, reaction rates, etc. The theoretical consideration underlying the KENO-VI code was discussed in Section 2.2.2.

The listed eigenvalue k is then an average over all the active generations. The statistical nature of a Monte Carlo solution implies that the statistical uncertainty in k is an equally important quantity in terms of the actual results and should be considered as part of the answer. Numerical analyses are done to ensure a small statistical uncertainty of the KENO-VI calculations and these are described in described in an upcoming Section 3.8.

3.5 FUEL DEPLETION CALCULATIONS

To improve the performance of reactors, it is important to have high-fidelity computer models to predict and assess the isotopic depletion of nuclear fuel in reactors. Isotopic concentration analysis of a fuel is important for improving performance and assessing security risks. Fuel depletion calculations refer to the analysis of the change in the reactor's isotopic composition and the associated effects in operating characteristic during the operation cycle.

In this study, the TRITON control module was used to perform burn-up calculations of the VVER-1000 reactor system. The TRITON module in SCALE-6.2.1 employs NEWT in 2D or KENO in 3D to solve the neutron transport equation and to calculate neutron flux, and for depleted nuclide concentrations calculations, TRITON employs ORIGEN-S.

In general, the fuel burn-up is calculated as:

$$Burn - up = \frac{P(GW) \times T_c(days) \times n}{M(MTU)} \tag{41}$$

where P is the power density, T_c is the cycle-length, n is the number of batches seen by fuel assembly and M is the total mass of the fuel (du Toit, 2017).

The ORIGEN-S module solves the Bateman equations using the neutron flux. The atom density of a set of chosen nuclides is calculated as shown in Eq (42) (Barkauskas, et al., 2017):

$$\frac{dN_i}{dt} = \sum_{j=1}^{m} l_{ij}\lambda_j N_j + \phi \sum_{k=1}^{m} f_{ik}\sigma_k N_k - (\lambda_i + \phi\sigma_i) \tag{42}$$

where:

N_i is the atom density of nuclide i,
λ_i is the radioactive disintegration constant of nuclide i,
σ_i is the spectrum-averaged microscopic neutron absorption cross-section of nuclide i,
ϕ is the space and energy-averaged neutron flux, and
l_{ij} are the branching fractions for neutron absorption by other nuclides k that lead to the formation of species f_{ij}.

The ORIGEN-S module is used in this study to calculate the nuclide concentrations as well as reaction rates for a set of nuclides.

3.6 SENSITIVITY AND UNCERTAINTY ANALYSIS CODES

Sensitivity and uncertainty analyses is performed using TSUNAMI and SAMPLER modules of the SCALE-6.2.1 code.

3.6.1 TSUNAMI - GPT

TSUNAMI contains several codes that can be used in criticality code validations. In TSUNAMI, the sensitivity coefficients required to predict the relative changes in a systems' calculated k value due to changes in the neutron cross-section data are computed using a SAMS sequence. The relative uncertainty in the calculated k value is then computed using these sensitivity coefficients as the method in Section 2.3.3.1 describes. To produce this uncertainty, SAMS folds the sensitivity data with the cross-section covariance data to tabulate the uncertainties in the cross-section data (See Section 2.3.3.1 regarding this implementation).

The value of the relative uncertainty in response k is usually given in $\%\Delta k/k$ or in pcm (10^5), where pcm can be defined as the difference in k (Δk) multiplied by 10^5. An alternative definition would be to use the reactivity instead of k. The sensitivity of k to energy-dependent cross-section data for each neutron-nuclide reaction of each nuclide in a system are also computed (Reed, et al., 2014).

These sensitivities can be analysed by visual inspections using the sensitivity data files (SDF) plotted by either FULCRUM or JAVAPENO obtained in SCALE (Rearden & Jesse, 2016).

3.6.2 SAMPLER - SS

As discussed in Section 2.3.3.2, uncertainty analysis can also be quantified by means of a statistical sampling method, provided a range of possible values, for instance, of an input variable given whose exact value is unknown. The uncertainty quantification is done by considering a range for the variable and a probability distribution function (PDF) for the variable that assigns a probability for any value inside the range. In this work, the tolerance limits were used to define the range for each variable. The accuracy of results obtained depends on the number of input parameters based on the sample size and the randomness in the sampling procedure. A large number of samples would yield better results; however, this comes at the cost of computational time and memory requirements. Therefore, sample size is chosen based on the availability of computational time and memory resources that can be used to obtain reasonable results.

For sampling-based uncertainty and sensitivity analysis there are three steps for obtaining the desired results and these are explained below.

- Step 1: Characterisation of input variables uncertainty

The user decides on the input variables of interest, that are sensitive for the output variables. In this work, the input variables of interests are the nuclear data, code parameters associated with modelling and methodology, as well as the manufacturing uncertainties. The uncertainties related to these input variables are defined by providing intervals of possible values and the PDFs associated with them. Uniform distribution is used for the PDFs since it assigns equal probability to each value within the sample space (Ivanov, et al., 2013).

With regards to the nuclear data, the SAMPLER method samples joint PDFs given in the nuclear data covariance library to produce a random sample for the nuclear data cross-section (Rearden & Jesse, 2016). SAMPLER uses a set of nuclear data files, with each data file in the set containing a perturbed set of data based on the nominal data file.

- Step 2: Samples size N

The sample size N is defined as the number of times (N) the simulations are performed. The N that were considered for this study were 150, 300 and 500. Selection of the sample size depends on the desired uncertainty accuracy.

- Step 3: Desired outputs

Each N simulation uses a different set of input values and has its own set of output responses. The output responses that can be obtained at the end of a SAMPLER calculation are listed in Table 3-2. For each of these responses, the average values and standard deviations, covariance and correlation coefficients between responses are printed in the output file.

TABLE 3-2: RESPONSES AND CODES FOR SAMPLER

Output Variables	Codes
$\boldsymbol{k}$ eigenvalue	KENO, NEWT, T-DEPL
Microscopic reactions by nuclide	NEWT, T-DEPL
Homogenised and Collapsed cross-sections	NEWT, T-DEPL
Nuclide composition	T-DEPL

The computational time can be reduced using parallel computations. Running SAMPLER in parallel is currently unavailable in SCALE-6.2.1. Therefore, the parallel computation was achieved by separating the total number of calculations (which is the sample size) into a few groups, with each group executed via a windows batch file on a separate co-processor of the computer. When all the calculations are completed, SAMPLER is then re-run to create the statistical output from the generated individual output files. The SAMPLER input must have $run\_cases = no$ under the parameter block to be able to perform this method.

The input files are created using the following steps in this example:

- Create a folder e.g. named “test”;
- Sampler input “a000.inp” is prepared with command “$run\_case = no$” included in the parameter block in “a000.inp”; and
- To generate N input files, the sampler input “a000.inp” is run by using the command (“scalerte test\a000.inp”). This creates the folder “a000.samplerfiles” with all the N input files for the perturbed input variables as shown in Figure 3-1.

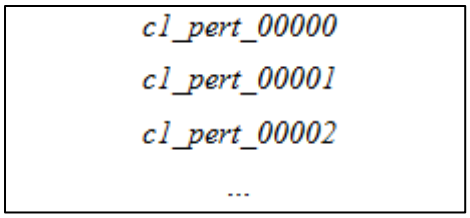

FIGURE 3-1: EXAMPLE OF PERTURBED INPUT FILES

Batch files are required to run SAMPLER in parallel on a windows machine.

- For an example of 11 samples with 3 CPUs, 3 batch files in the folder “mycodes” are created.
  - RUNSAMPLES1.bat
  - RUNSAMPLES2.bat
  - RUNSAMPLES3.bat

- In RUNSAMPLES1.bat the following commands are entered, and the next set of calculations is entered in RUNAMSAMPLES2.bat, until all the N are specified.

```
Cd\
Cd SCALE-6.2.1\bin
Scalerte c:\test\a000.samplerfiles\c1_pert_00000.input
Scalerte c:\test\a000.samplerfiles\c1_pert_00001.input
Scalerte c:\test\a000.samplerfiles\c1_pert_00002.input
Scalerte c:\test\a000.samplerfiles\c1_pert_00003.input
...
```

FIGURE 3-2: EXAMPLE FOR PARALLEL CALCULATIONS

3.7 MODEL DEFINITION IN SCALE

To perform a SCALE calculation, an analytical sequence is selected characterised by the type of analysis (criticality, shielding) to be performed and the geometric complexity of the system being analysed. To use the simulation codes, a model of a nuclear system needs to be represented in a logic that the code can interpret the problem of interest. A single set of input data to define the model is prepared for the control module corresponding to the analytical sequence. The control module uses the input data to derive additional parameters and prepare the input for each of the functional modules in the analytical sequences. The control module input data is specified in a simplified, free-form format, following the steps below:

- Cross-section processing.
- Material definition.
- Geometry definition.
- Boundary condition specifications.

The above-mentioned input data steps are discussed further from Sections 3.7.1 to 3.7.4. The cross-section processing method was discussed in Section 3.3. Among the sequences obtained in SCALE 6.2.1, the NEWT module and the KENO-VI module have been used for the solution of the neutronics of the study, while TSUNAMI-2D/3D and SAMPLER has been used for sensitivity and uncertainty analysis of the study. In addition to nuclear data, the neutron transport calculations require knowledge of the problem geometry, including material compositions, temperatures and densities. Therefore, the definition of these parameters must be treated with care. Appendix C contains examples of how a SCALE input file looks like.

3.7.1 MATERIAL DEFINITION

In the SCALE input file, the material is defined by the material name, mixture number for the mixture, temperature of the material and a termination word (END). The format that was used for most of the materials is as follows:

SC ---- MX ---- VF=0 ---- ADEN ----TEMP ---- END

The following format was considered for the moderator and the fissile material:

SC ---- MX ---- DEN ---- VF=1 ---- TEMP ---- END

where:

SC - indicates the isotopes, nuclide, compound or alloy that will make up the material
MX - is an integer number that represent the mixture number
DEN - is the actual density in g/cm^3 of a material
VF - enters the density multiplier (equals 1 when DEN is defined and 0 for ADEN)
ADEN - is the number density specification in atom / barn-cm
TEMP - defines the temperature of the material
END - terminates the data for a material

The number density for each nuclide in a material or in a mixture of materials is obtained by Eq (43) as:

$$\mathrm{N_i} = \frac{\rho}{M_i} N_A \tag{43}$$

where ρ is the density in g/cm^3 that is occupied by nuclide i, M_i is the molar mass for nuclide i and N_A is the Avogadro's number (0.62214199 x 10^{24}). Each nuclide in a material is accompanied by either a weight percent or an atom percent. The weight percent is converted to atom percent to calculate the number density of each nuclide.

In NEWT calculations, the READ COMP must be accompanied by the READ MATERIAL block to complete the material definition for use in the NEWT calculations. The data defined under READ MATERIAL are the mixture number, the P_N scattering order, embedded comment (com=) and the terminator (END). The materials together with their number densities are listed in Appendix A.

3.7.2 GEOMETRY DEFINITION

In KENO-VI, the geometry of a model consists of units that are constructed by nesting spheres, cylinders, hexprism, etc. oriented along X-, Y-, and Z- axes to construct the desired geometry. The geometry input is based on the SCALE Generalised Geometry Package (SGGP). The units of the geometry can be combined in rectangular/hexagonal arrays or inserted in other units and

completely enclosed by the next larger unit (global unit). This method of defining the geometry of interest in a KENO-VI model allows for very fast particle tracking, while permitting the use of complex geometry models. In this study, the desired geometry consists of hexagonal fuel pins set within fuel assemblies. The system studied is then constructed such that the hexagonal fuel assemblies are stacked together to form a 3D hexagonal array of units with the applicable desired boundary conditions.

As with KENO-VI, the geometry definition in NEWT is also based on SGGP, however, in contrast to KENO-VI geometry, the NEWT geometry is defined in two-dimensional. Therefore, NEWT geometry definition omits the z-axis along with other inherently 3D bodies supported by KENO-VI (Rearden & Jesse, 2016). Furthermore, there are two more considerations in a NEWT geometry definition, i.e. a grid structure associated with each unit and the approximation of curved surfaces such as cylinders using N-sided polygons.

The grid structures dimensions (GD) are integers (≥2) that specify the number of rectangular cells to be placed in a global unit and other units (optional) in the x- and y- directions (Rearden & Jesse, 2016). The GD definition is important since it assists in the convergence of results of interest such as k and the flux. Therefore, constructing an efficient and optimized GD requires balancing accurate results with reasonable execution time (Rearden & Jesse, 2016). The GD in an FA model can be defined in the global unit, with an optimized sub-grid in the unit as an addition to the global GD. However, for a lattice whose pitch is not an even multiple of the unit cell pitch (such as the VVER-1000 FA), only a global unit GD is recommended (Ade, 2012). It must be noted that defining only the global unit GD will produce results that are not of higher solution fidelity. Therefore, the study will present three cases. In case one the global GD is fixed at 2×2 and varied in the unit cell. In case two the GD is defined in the global unit and not defined in the unit cell. In case three the GD is varied in the global unit and kept fixed at 4×4 in the unit cell.

The N-sided polygons are the approximation of a circle using an equilateral polygon to ensure that all cells are straight sided as seen in Figure 3-3. NEWT requires that all cells be straight sided, since its solution grid is based on arbitrary polygons. The default value is $N = 12$. A study was performed by Canuti (Canuti, et al., 2012), on the N-sided polygons to see its effects on multiplication results of VVER-1000 fuel pin (marked as Kozloduy-6 on Figure 3-4), as well as other LWR fuel pins. The analysis was evaluated for the number of sides from 8 to 28, with GD at 2×2 and at 40×40. The results are shown on the graphs in Figure 3-4. When GD = 40×40 is used, the effect of the N-sided polygon was lower to negligible (below 40 pcm) for all the N-sides, whereas, when GD = 2×2 was used, the effects converges from N-sides = 12 (below 30 pcm). The default value of $N = 12$ will therefore be used for all NEWT calculations in the current study.

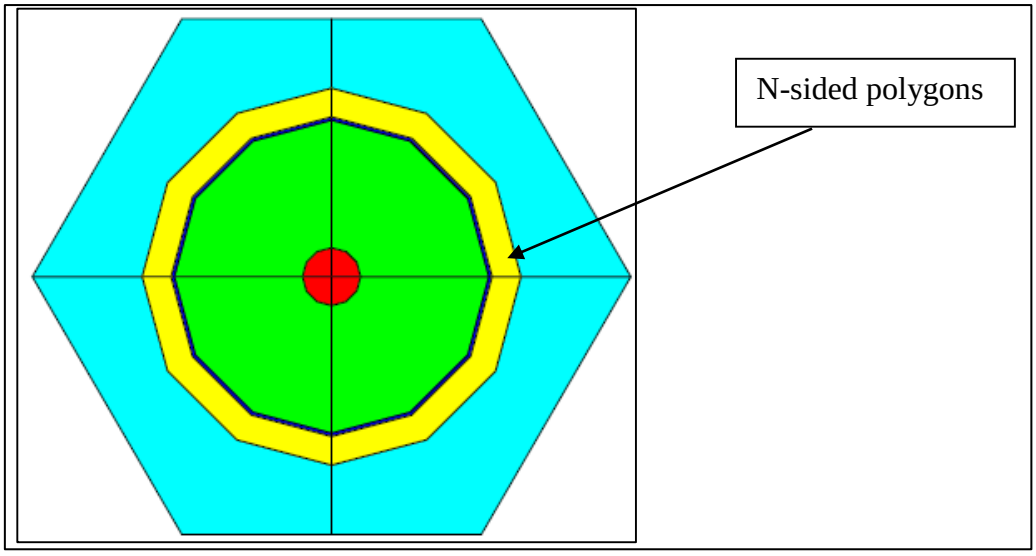

FIGURE 3-3: N-SIDED POLYGONS DEMONSTRATION

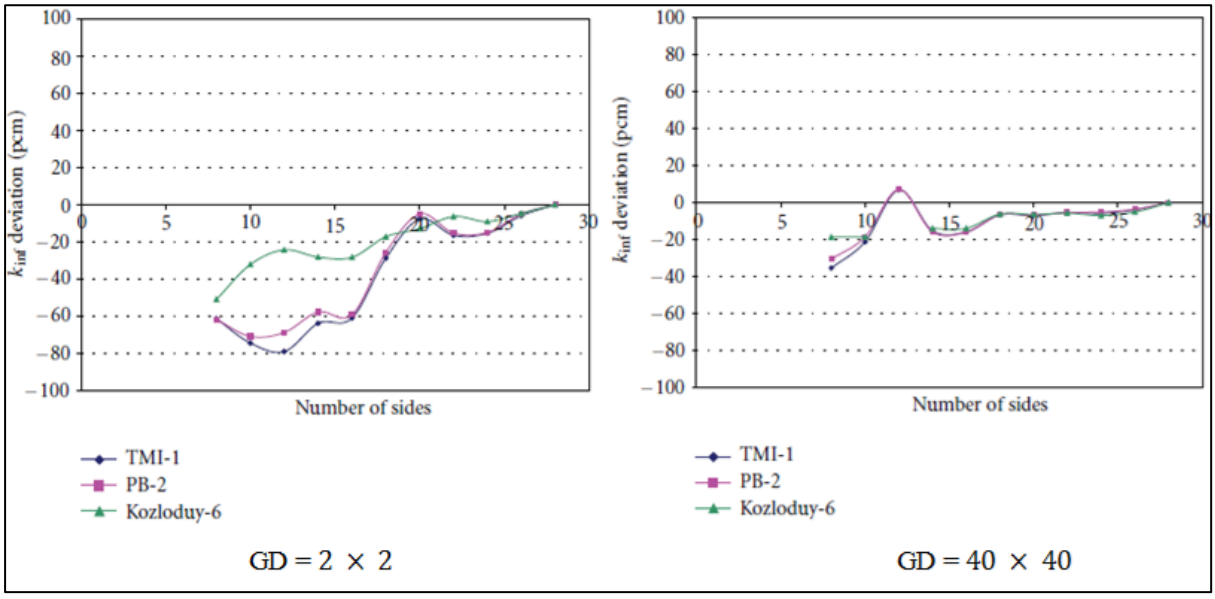

FIGURE 3-4: INFLUENCE OF THE N-SIDES ON k_{∞} (CANUTI, ET AL., 2012)

3.7.3 BOUNDARY CONDITIONS

The use of boundary conditions (BCs) in transport codes assists in reducing the problem to a tractable size by modelling the action of the outside domain on the particles that leave the domain (Sanchez, et al., 2002). The geometry defined for a model is limited to an outer boundary, beyond which no cells exist. The life of a neutron passing this boundary will depend on the boundary conditions. The boundary conditions considered to be used in the VVER-1000's fuel assembly and fuel pins' outer boundaries for this study are the white and reflective boundary conditions abbreviated as WBC and RBC respectively. For RBC also known as mirror boundary conditions, the neutron is reflected back into the geometry at an angle symmetrical with respect to the surface's normal. A WBC will reflect the neutron back into the geometry isotropically. These boundary

conditions can be used to create infinite geometries in which the same structure is repeated over and over again (Leppanen, 2017).

For KENO and NEWT, both the WBC and RBC are available, and the RBC is always recommended for use for accurate results. For a full core calculation performed with a 3D code, the vacuum boundary conditions are desired. This is due to the fact that, a full core's geometry is assumed to be a non-re-entrant, meaning that a neutron will be terminated after it has crossed this boundary (Leppanen, 2017).

3.7.4 ANGULAR QUADRATURE SETS

In this study, the choice of angular quadrature sets in the S_N method not only defines the number of discrete angular directions within the cell, but also determines which BC will be used in terms of NEWT calculations. This is due to the nature of the geometrical configuration chosen for this study. Two quadrature sets were considered for analysis: level symmetry quadrature (LSQ) and the product quadrature (PQ) sets. A more in-depth discussion of the angular quadrature sets was given in Section 2.2.3.2.

The LSQ sets as used in the discrete ordinate method is defined by the S_N orders with even numbers ranging from 2 to 16. In general, N≥6 is recommended, since in LSQ, the symmetry imposes equal weights for all directions belonging to a set of positions invariant with respect to π/2 rotations (Sanchez, et al., 2002). It must be noted that using the LSQ sets for hexagonal FA models will allow the use of white boundary conditions (WBC) only. Reflective boundary conditions (RBC) are not allowed due to the irregular distribution of the unstructured core mesh.

The PQ set is defined as the combination of a one-dimensional quadrature set along the polar axis (NPOLAR) and a one-dimensional quadrature set in the azimuthal plane (NAZIM), yielding a set whose weights are products of the weights from the two sets. Each azimuthal quadrature order (NAZIM) may be applied with a different polar ordinate (NPOLAR) (Wang, 2009). PQ sets allow both reflective (RBC) and white (WBC) boundary conditions.

The benefit of the PQ sets is the ability to have an arbitrary number of directions without limitations from potentially problematic negative weights (Sanchez, et al., 2002). It has been stated that LSQ sets should be used for general analysis, and in a real-world reactor analysis, a higher quadrature using the PQ sets should be employed (Wang, 2009).

3.8 CONVERGENCE TESTS OF THE RESULTS

3.8.1 CONVERGENCE OF FISSION SOURCE DISTRIBUTION

To provide improved confidence in the computed k and tally results, convergence of the fission source distribution is considered. The convergence of the fission source distribution is necessary to ensure that all regions containing fissile material in a model are adequately represented in the final k estimate. It is also useful to avoid the false convergence of the k distribution and tally results that can be caused by insufficient sampling of important parts of the system. In the Monte Carlo simulations, a Shannon entropy test result is used to guarantee that a problems' fission source is converged. The Shannon entropy, denoted by H, is defined as (Rearden & Jesse, 2016):

$$H(S^N) = -\sum_{i}^{M} (S_i^N) log_2 (S_i^N) \tag{44}$$

where (S_i^N) is the fraction of the fission source distribution from the N^{th} cycle tallied in the spatial bin i, and M is the total number of spatial bins (represented using a spatial mesh). By computing H for each generation, the distribution of fission source is used to generate a score for H for each generation, and the convergence of the fission source can be addressed by tracking the convergence and randomness of the values of H over each successive generation. For KENO-VI to compute H, it is important to place a 3D mesh grid on a problem covering all of the fission regions, and then to tally the number of fission events in a cycle that fall into each of the grid boxes. The mesh grid used to determine H can either be specified by the user or automatically determined by KENO-VI.

The posterior relative entropy $D(S^N||T)$ can be developed from the concept of entropy (Chapman, 2010). $D(S^N||T)$ is defined as the measure of the statistical distance between two distributions S^N from the N^{th} cycle and T, where T is the average fission source over the second half of the active generations. $D(S^N||T)$ is written as:

$$D(S^N||T) = \sum_{i}^{M} (S_i^N) \, log_2 \left(\frac{S_i^N}{T_i} \right) \tag{45}$$

where T_i the average fission source over the second half of the active generations in each bin i. The average fission source can be calculated as:

$$T_i = \frac{\sum_{j=N_{1/2}+1}^{N_{max}} S_i^N}{\left(N_{1/2} - N_{max} \right)} \tag{46}$$

where $N_{1/2}$ is defined as the final cycle of the first half of the active cycled and N_{max} as the total number of cycles.

The value of the relative entropy is a nonnegative and can become zero only when $S_i^N = T_i$ for all bins (Ueki, et al., 2003). As the KENO-VI calculation runs through the iterations, the posterior relative entropy will show a general increasing trend since S^N moves away from T. This implies that T becomes less credible (Chapman, 2010).

There are three additional tests that are conducted by KENO-VI to conclude on a converged fission source and all these tests can be examined from the output file of a KENO/TSUNAMI simulation. The following three tests are based on both the Shannon entropy $H(S^N)$ and the posterior relative entropy $D(S^N||T)$ and the description of how to analyze these tests is given in the following statements.

- *Test 1*

As part of this test, a mean square posterior relative entropy $msq\ (D)$ is introduced together with a centered mean square Shannon entropy $cmsq\ (H)$. The quantity $msq\ (D)$ is related to the average source distribution T_i.

This test is analyzed by comparing $msq\ (D)$ and $cmsq\ (H)$ to determine whether the source has converged. When $msq\ (D) \leq cmsq\ (H)$, the test is said to have passed, which implies that an adequate number of skipped cycles was used.

In simple terms, this test is said to have passed when $D(S^N||T)$ does not cross the average of $D(S^N||T)$ over the second half of the active cycles before the first active cycle begins.

- *Test 2*

This test given by Eq (47) verifies that the Shannon entropy H of each generation does not vary significantly from the average H of the system and should be valid over all active generations.

$$D(S^N||T) - \left[H\left(T - H(S^N)\right)\right] \leq \varepsilon \tag{47}$$

The variable ε has been fixed to 0.1 (Rearden & Jesse, 2016).

- *Test 3*

The last test verifies that the average Shannon entropy of all active cycles does not differ significantly from the Shannon entropy of the last half of the active cycles by calculating whether

$$H_\eta = H(S^N) - H_b \leq \eta \tag{48}$$

H_b is the average Shannon entropy over the second half of active cycles, and η has been fixed to 0.1.

More details can be obtained from the SCALE manual on these three tests (Rearden & Jesse, 2016).

3.8.2 ACCURACY OF THE MULTIPLICATION FACTOR (k)

Once the fission source is converged, the active generations are started, and k is obtained as the average of all the k's obtained from each active generation. The standard deviation of k is then obtained as shown in Eq (13) of Section 2.2.2. Since the calculation is a statistical process, the standard deviations decrease as more active generations are run. The total number of active generations are then set in terms of the required standard deviation (Naicker, et al., 2016).

3.8.3 RANDOM NUMBER

Random numbers are used in Monte Carlo codes which are produced by the code using a suitable algorithm. The algorithm requires a random number seed at the start of the calculation, and for different random number seeds, different sets of random numbers are generated. Running several calculations N of the same model with different random number seeds gives insights of the fundamental factors that may lead to the stochastic uncertainties in the results. Therefore, a numerical study of the stochastic uncertainty in Monte Carlo (KENO-VI) simulations was performed as part of this study to gain insight into the statistical uncertainty using random numbers. N calculations were performed using a base case model with different random number seed for each calculation, to quantify the uncertainty in k due to the stochastic nature of KENO-VI.

Due to the statistical nature of the calculation, each calculation i had a standard deviation, σ_i which allowed the definition of the apparent standard deviation:

$$\bar{\sigma}_a = \frac{1}{N}\sum_{i=1}^{N} \sigma_i \tag{49}$$

The true standard deviation was also defined as:

$$\Delta k = \sqrt{\frac{1}{N-1}\sum_{i=1}^{N}\left(k_i - \bar{k}\right)^2} \tag{50}$$

k_i are the individual values for the multiplication constant for each calculation, with the average given as $\bar{k}$.

To determine the factor by which the statistical uncertainty produced for the calculations will be reduced by a Monte Carlo calculation, a ratio between the true standard deviation and an apparent standard deviation is obtained with Eq (51):

$$f = \frac{\Delta k}{\bar{\sigma}_a} \tag{51}$$

As reported in Farkas (2005. Farkas), for a MCNP calculation of a WWER-440 full core, effect of using different random number seeds for a set of calculations yielded a statistical uncertainty of $\Delta k = 0.00022$ in the k compared to the statistical uncertainty of $\bar{\sigma}_a = 0.00033$ for the individual calculations. This limitation can be applied for KENO-VI results since it is a Monte-Carlo code which relies on random number seeds.

3.8.4 CONVERGENCE OF $F^*(r)$

In this study, a TSUNAMI-CE simulation using the CLUTCH method is performed to obtain the eigenvalue sensitivity coefficients. The CLUTCH method calculates the importance of events during a particle's lifetime by examining how many fission neutrons are created by that particle after those events occur. This method uses a weighting function called the $F^*(r)$ function to account for the average importance of fission neutrons at r and is given by the Eq (52).

$$F^*(r) = \iint_{E\Omega} \frac{\chi(r,E)}{4\pi} \phi^*(r,E,\Omega)\, d\Omega dE \tag{52}$$

where $\chi(r,E)$ is the fission neutron emission spectrum and $\phi^*(r,E,\Omega)$ is the adjoint flux created in phase-space (r,E,Ω). The $F^*(r)$ is only a function of space and does not include an energy dependence unless $\chi(r,E)$ is strongly depended on the energy of the neutron initiating the fission event (Perfetti & Rearden, 2016).

For the CLUTCH method to accurately perform the sensitivity coefficient calculation, the $F^*(r)$ function requires convergence. A spatial mesh definition is provided for the CLUTCH method to perform sensitivity calculations and the $F^*(r)$ function must be converged over this defined mesh. The $F^*(r)$ function's convergence is analyzed using the inactive generations (NSK) since the $F^*(r)$ tallies may begin during the inactive generations (NSK) of the Monte Carlo simulations (Perfetti & Rearden, 2016). This implies that the $F^*(r)$ convergence does not require the fission source to be converged for it to converge.

A study by Sihlangu (Sihlangu, et al., 2018) has developed a method examining the convergence in $F^*(r)$ function. The recommendation was that $10 \times 10 \times 10$ spatial mesh, with 5 latent generations (CFP) and below 100 number of skipped cycles be used for accurate results. More details on the methodology is obtained in the reference (Sihlangu, et al., 2018).

3.9 SUMMARY

This section has successfully provided the systematic literature of the codes important for understanding the analysis of the neutronics results and the S/U analysis of this study. The SCALE-6.2.1 input file structure and definition have been provided to give guidance on the input data required to process the simulations of the neutronics analysis. The assessment methods for the convergence test of the KENO-VI calculations were also discussed.

4 SYSTEM SPECIFICATIONS AND MODEL DEVELOPMENT

The current section provides the specifications of the system that was used to obtain the neutronics results of the study obtained from the OECD/NEA Benchmark document (Ivanov, et al., 2013). The specification of the Kozloduy-6 VVER-1000 reactor system is given in terms of geometry dimensions and material definition. In terms of geometry definition, modelling of the spacer grids has been studied by analysing the available methods for spacer grids. The manufacturing tolerances of the geometry and materials of the system are provided. Also, the assumptions that were made in the geometry and material to achieve sensitivity and uncertainty calculations are described under this section.

4.1 KOZLODUY-6 VVER-1000 FUEL ASSEMBLY SPECIFICATIONS

The VVER-1000 FA specifications are given as part of the OECD/NEA benchmark compiled by the OECD/NEA. The VVER-1000 FA has hexagonal symmetry, with a FA pitch of 23.6 cm. The models are studied at the hot zero power (HZP) and hot full power (HFP) states and the temperatures of the materials in the system at these states are given in Table 4-1.

TABLE 4-1: GENERAL REACTOR CONDITIONS

Parameter	Hot Zero Power	Hot Full Power
Fuel temperature (K)	552.15	900
Cladding temperature (K)	552.15	600
Moderator temperature (K)	552.15	560
Moderator density (g/cm^3)	0.7670	0.7525
Reactor power (MWt)	3.000	3000

The VVER-1000 FA contains fuel pins, guide tubes, instrumentation pins and spacer grids. There are 15 spacer grids in which 13 are intermediate spacer grids and two are end grids. The intermediate grids are located in the active fuel region (Tran & Cho, 2016). Figure 4-1 gives a top view of the the FA and it shows the order in which the components are placed in the FA. Figure 4-2 shows the side view of the FA and the location of the spacer grids in the FA.

The spacer grids are an important structural component of the FA which support the FA laterally and vertically to ensure higher rigidity and to maintain the form of the FA. The spacer grids surround the fuel pins and are intact with the guide tubes in the FA. The end grids are located at the end of fuel stack and are there for improved structural support. Although, there are 15 spacer grids in the VVER-1000, in this study the end grids were not included, since the focus will be on the active length of the FA which is where the intermediate grids are located. The spacer grids height and its

location in the FA is shown in Figure 4-2 (Pazirandeh, et al., 2011). The rods and materials of the FA are discussed in the Sections 4.1.1 and 4.1.2.

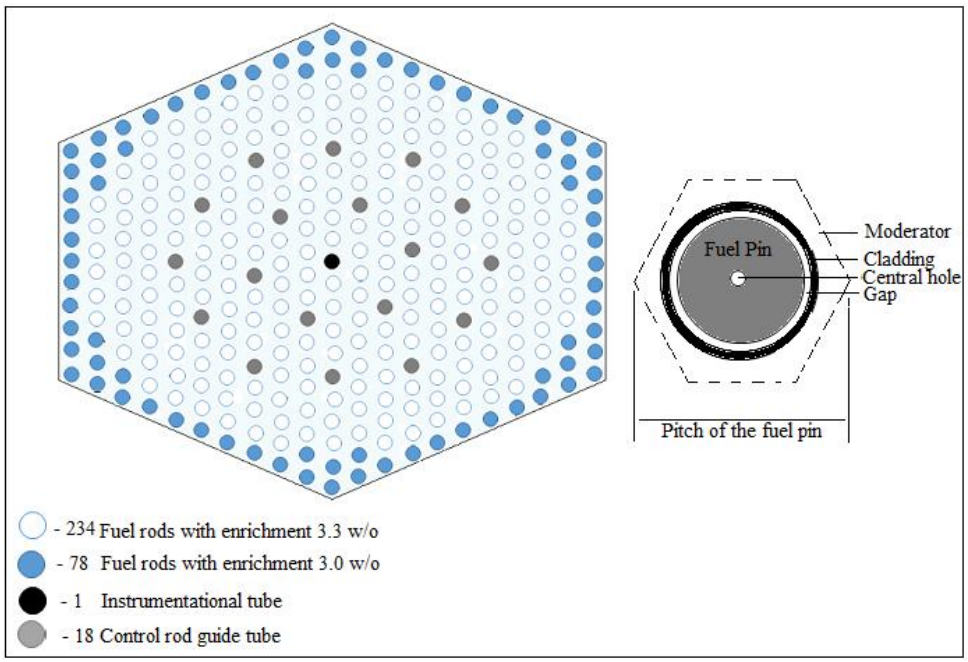

FIGURE 4-1: SCHEMATIC DIAGRAM OF THE FP AND FA OF THE OECD VVER-1000

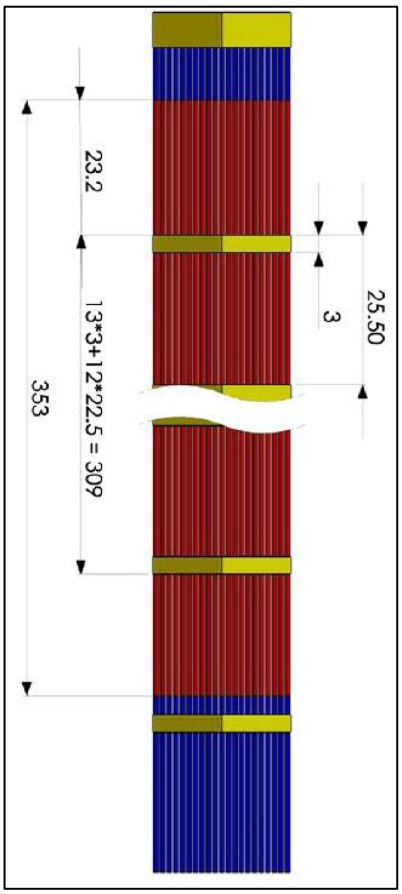

FIGURE 4-2: FA WITH SPACER GRIDS

4.1.1 THE VVER-1000 FA RODS

The VVER-1000 fuel assembly (FA) as seen in Figure 4-1consists of 331 rods of which 312 are fuel pins (FP), 18 are guide tubes (GT) and 1 is an instrumentational pin (IP). The rods and their immediate environment in the FA have hexagonal symmetry, with a pitch of 1.275 cm.

TABLE 4-2: VVER-1000 RODS SYSTEM SPECIFICATION

Diameters	Value (cm)
Inner Hole (IHOD)	0.140
Fuel Pin (FPOD)	0.757
Gap (GOD)	0.773
Clad (COD)	0.910
GT (GTID)	1.100
GT (GTOD)	1.260
IP (IPID)	0.960
IP (IPOD)	1.120

The FP is modelled as concentric cylinders of central void, fuel, gap and clad as shown in Figure 4-3 surrounded by moderator and SGs. The GT and IP are modelled the same way as two concentric cylinders of moderators and clad surrounded by moderator and SGs as shown in Figure 4-3. The outer (OD) and inner diameter (ID) of the cylinders are given in Table 4-2.

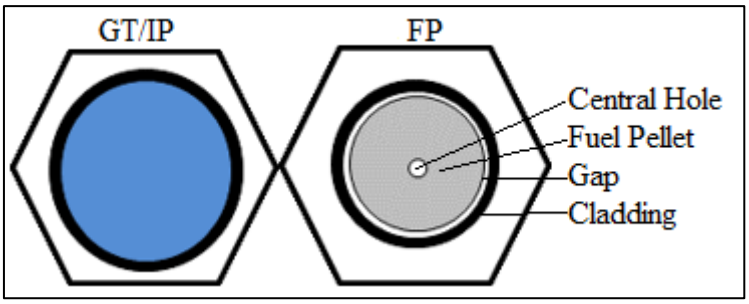

FIGURE 4-3: TOP VIEW OF THE RODS

4.1.2 VVER-1000 MATERIALS

The materials in Table 4-3 were obtained from the OECD/NEA benchmark specification. The composition of the central hole is 79% nitrogen and 21% oxygen. Since the specification document did not specify the units of this composition, it was assumed that these were in wt %. However, these numbers could have been specified in volume percent, in which case the number densities would have been different. Since the contribution from central hole material is considered to be small in terms of the neutronic analysis, this was therefore not investigated further. The UO_2 has 0.0054 wt % of ^{234}U atom density. The enrichment for the UO_2 are 3.0 wt% and 3.3 wt% as specified in the OECD/NEA benchmark specifications.

TABLE 4-3: MATERIALS AND THEIR CORRESPONDING DENSITIES

Fuel cell	Material	Density (g/cm^3)
Central hole	Dry air	0.00124
Fuel pellet	UO_2	10.4
Gap	Helium	0.000164
Clad	Alloy Zr+1%Nb	6.45
Spacer grid/ Guide tube	Steel 08X18H10T	7.90
Central tube	E110 Zr+1%Nb	6.55

4.2 GENERAL OUTLINE OF METHOD

A method was required to perform the sensitivity and uncertainty analysis. The method includes steps where by:

- An infinite height (z-direction) VVER-1000 base model is created for NEWT and KENO-VI.
- Two base criticality calculations are performed using NEWT and KENO-VI.
- Two base nuclear data uncertainty calculations are performed using TSUNAMI-2D and TSUNAMI-3D.
- The XSProc and NEWT parameters that require optimisation analysis are established.
- A re-run of the base NEWT calculation for each parameter to test their sensitivities is done.
- Ranking of the parameters, according to their contribution to the base model result is performed.
- A second model whereby a fixed height 3D base model of the FA is created.
- Two further criticality calculations using KENO-VI (MG) and KENO-VI (CE) are produced.
- A set of sensitivity analysis test for the 3D KENO-VI model is determined.
- The base KENO-VI calculation for sensitivity test is re-run.
- All the sensitivities of the VVER-1000 criticality results are ranked according to their contribution to the base model result.
- Propagation of the all input data uncertainties is performed as the last step using SAMPLER to obtain overall uncertainties in the model.
- An additional fuel depletion test is performed using TRITON/NEWT and TRITON/KENO on the FA.
- Lastly, the results that will be submitted to the OECD/NEA benchmark are collected.

4.3 CRITICALITY BASE MODEL

A NEWT/KENO-VI criticality calculation is achievable when a nuclear data library, geometry, materials, and boundary conditions of the system modelled are specified. The methods used to define the NEWT/KENO-VI input file are given in Section 3.7. As stated in Section 3.2, the nuclear

data libraries are available in two versions, ENDF/B-VII.0 and ENDF/B-VII.1, where by multi-group and continuous energy libraries are obtained.

The MG libraries are available for use in NEWT and KENO-VI calculations, while the CE library is available for use only in KENO-VI. The use of MG libraries in NEWT and KENO-VI requires calculation of resonance self-shielding using XSProc. The default values for parameters that are used by XSProc to perform resonance self-shielding calculations are given in Table 4-4. XSProc employs BONAMI and CENTRM modules to perform those calculations.

The geometry and materials of the system are defined based on the specification given in Section 4.1. The NEWT calculations are performed using the default value of $S_N = 6$ for the LSQ set. P_N scattering was set to 2 for the moderator and 1 for the rest of the materials. GD was 24×24 for the FP. The FA had GD set as 4×4 for the unit cell and 2×2 for the global unit.

TABLE 4-4: XSPROC CODE PARAMETERS

Code	Parameter	Default value	Possible values
BONAMI	SZF	1	>1.5
	IROPT	0	0/1/2/3
CENTRM	ISN	6	2/4/6/…
	ITERP	0	0/1/2
	ALUMP	0.2	0 – 1.0
	DEMIN	0.001 eV	>0.001 eV
	DEMAX	20 keV	<500 keV

It is well known that statistical estimates of k_∞ obtained from Monte Carlo criticality simulations can be affected by fission source distribution and the number of cycles to run the simulations. Therefore, the parameters GEN (number cycles) and NPG (neutrons per generation) as used in KENO-VI to specify the fission source distribution and cycles must be treated with caution. For the KENO calculations, the number of inactive cycles, NSK, was set to 60 and 150, the number of active cycles, GEN, was set to 500 and 1000 and the number of source generations, NPG was set to 25000 and 40000 for the FP and FA respectively. These are chosen to ensure a small stochastic uncertainty that is due to the stochastic nature of KENO-VI. The boundary conditions that are used are reflective (RBC)and white boundary condition (WBC) for KENO and NEWT calculations respectively. Although WBC is allowed in KENO-VI (MG), to accurately evaluated the sensitivities in the NEWT simulations, the KENO-VI (MG) must estimate results of higher accuracy. Hence, the RBCs are used.

For a fixed height model, RBC are defined for all planes parallel to the z-direction, and vacuum boundary conditions are specified in the z-direction. For KENO-VI (MG) to take all the cells of the heterogeneous FA into account in the self-shielding treatment, the input is modified without changing the source code using the methods discussed later in Section 4.5.3.1. Each spacer grid was defined as a homogenised band in its location in the FA. This was done by treating the SG

material and the material between the SG and the clad as one material. The method that was used to define this homogenised material will be discussed later in Section 4.5.3.

4.4 METHOD OF CODE PARAMETER OPTIMISATION

The purpose of performing optimisation is to study the effects of XSProc and NEWT code parameters on the neutronics results of the VVER-1000. The XSProc parameters that were considered for this analysis are given in Table 4-4. The NEWT parameters that were considered for this analysis are the grid dimension (GD) and the choice of angular quadrature sets together with their parameters. For the angular quadrature sets, there were two possibilities: the level symmetry quadrature (LQS) and the product quadrature (PQ). The definitions of these parameters are provided in Section 3.7.

Each calculation used the base model with one modified parameter at a time, thus quantifying the effect of selected parameters. The effect of a modified parameters is established by the effect in k_∞ as well as computational time. In the case where the effect is negligible, the parameter is set at its default value in the final model. The accuracy of the NEWT results is conclusive when the criticality results are in good agreement with KENO-VI criticality results. Therefore, KENO-VI is used to verify the NEWT model that has maximum accuracy after the optimisation of all the desired code parameters has been completed.

The standard resonance self-shielding treatment in NEWT/KENO-VI (MG) does not allow for the direct treatment of annular lattice heterogeneous SGs present in the VVER-1000 FA. The effects of code parameters are independent from the effects of material and geometry. The SGs were therefore excluded in the system for this analysis. In a later study, the SG will be included to test for its sensitivity.

4.5 SENSITIVITY ANALYSIS METHODOLOGY

The sensitivity analysis is performed prior to the propagation of uncertainties in the input data so that insignificant parameters can be left out. The source of input data uncertainties that are analysed in this section are classified into three groups, viz. nuclear data, geometry and material modelling and manufacturing tolerances. The calculations are performed using KENO-VI with the available multi-group (MG) and continuous energy (CE) cross-section libraries based on the ENDF/B-VII evaluation.

4.5.1 EVALUATION OF THE STATISTICAL UNCERTAINTIES DUE TO KENO-VI METHODS

Using the KENO-VI code for neutronics analyses introduces statistical uncertainties in the results due to the Monte Carlo (MC) method solution. To ensure a negligible statistical uncertainty of the

Monte Carlo calculation, the number of source neutrons, the number of in-active and the number of active cycles must be defined such that the fission source converges, and k achieves the required standard deviation. In addition to this, the random numbers generated must also not bias the results. One way to check this would be to repeat the calculations by keeping the number of source neutrons, inactive and active cycles fixed, but changing the random seed used to generate the random numbers for each calculation. This additional numerical analysis was also performed. The method that was used to accomplish this numerical analysis is described in Section 3.8.3.

4.5.2 EVALUATION OF NUCLEAR DATA LIBRARIES

As discussed earlier in Section 3.2, the SCALE-6.2.1 code has nuclear data libraries available in both the MG and CE form for cross-section generation. There are three major factors that affect accuracy of cross-section generation. These include energy group structure, self-shielding method, and collapsing methodology (Alpan & Haghighat, 2000). This implies that the accuracy of the neutronics calculations depend on the type of nuclear libraries chosen to generate the cross-sections of the calculations, therefore it is important to evaluate their uncertainties. In the MG form, the three available group libraries, a 238-group fine group library that is based on the ENDF/B-VII.0 evaluation, a 56-group broad-group structure and a 252-group fine-group library, both of which are based on the ENDF/B-VII.1 evaluation, are each used to obtain criticality results.

It must be noted that a k_∞ estimation for criticality calculations done using a CE method is considered to have a higher accuracy than a MG method. Therefore, the effects of the MG libraries on the k_∞ will be compared against a calculation performed using a CE library. The uncertainties due to nuclear data obtained in each group library are calculated and compared against nuclear data uncertainties obtained from using CE library.

4.5.3 GEOMETRY AND MATERIAL SENSITIVITY OF THE VVER-1000 FA MODEL

The effects on the neutronics results and its uncertainty due to the presence of the SGs in the VVER-1000 system are analysed. In this study, the geometry and material sensitivity of the SGs are investigated considering the following:

- Spacer grids modelling methods in the FA;
- Spacer grids dimension variation; and
- and spacer grid material options.

All the geometric dimensions of the VVER-1000 reactor system are provided as seen in Section 4.1 obtained from the OECD/NEA benchmark specification. The SG volume is given to be 1.2% of the FA volume, as mentioned in the OECD/NEA benchmark specification (Ivanov, et al., 2013).

4.5.3.1 *Spacer grid modelling*

There are three methods of SG modelling that has been considered for analysis, and those are the heterogeneous band (HTB), homogenous band (HMB) and homogenous (HMA) model type. In the heterogeneous model (HTB), the SGs were modelled individually as a band of given width and height; in the homogenous band model (HMB), the SG material and the moderator material between the SG inner width p_{in} and clad outer diameter were homogenously mixed and defined as a band; and in the homogenous model (HMA), the SG material was homogenously mixed with the water moderator throughout the axial length of the FA. The total mass and volume are preserved for all the models.

A homogenous material is a material that results from a dilution of two different materials (V_1 and V_2). The density and number densities of the homogenised material are obtained using the following equations (Tran & Cho, 2016):

$$V_{new} = V_1 + V_2 \tag{53}$$

$$\rho_{new,1} = \frac{m_1}{V_{new}} \tag{54}$$

$$\rho_{new,2} = \frac{m_2}{V_{new}} \tag{55}$$

Therefore, the number densities for each material, where A_1 and A_2 are the molar mass of each material are given as:

$$N_1 = \frac{\rho_{new,1} N_A}{A_1} \tag{56}$$

and

$$N_2 = \frac{\rho_{new,2} N_A}{A_2} \tag{57}$$

There are two major factors that motivated the analysis of the three types of SG modelling in this study. These include the treatment of self-shielding in the KENO-VI (MG) calculations, which can be achievable with the HMB/HMA model for this type of system; and the lattice or core neutronic calculations using deterministic methods, which can be achievable with the HMA model in most cases.

Studies have been performed to analyse the effects of SGs in reactor cores. In a study by Tran (Tran & Cho, 2016), the three types of SGs modelling were analysed on a PWR core using MCNP5, a Monte Carlo based code. The value of k was significantly different when comparing the HMA model with the HTB model, with the difference being 344 pcm, while the difference between the

HTB and HMB model was 117 pcm, which was almost half of the first difference (Tran & Cho, 2016). Another study by Pazirandeh (Pazirandeh, et al., 2011) tested the three models for a full core VVER-1000 system using WIMS and CITATION to obtain the effects of the SGs on excess reactivity and critical boron concentration. The difference in the calculated excess reactivity and critical boron concentration between the HMB and the HMA was 200 pcm and 15 ppm respectively. This difference was reduced by 40 pcm and 3 ppm when the HTB model was used.

However, these studies did not apply the sensitivity due to varying the geometry dimension and material selection of the SG to the broader context of including the uncertainties due to other parameters such as the nuclear data. It is noted that these two studies were completed on full cores, and the current study is based on the FA of the Kozloduy-6 VVER-1000 system. The outcome of homogeneity studies of the SG will be used in future studies using other codes such as NEWT/ NESTLE.

4.5.3.2 *Spacer grid (SG) dimensions*

To get deeper insight into the heterogeneous scheme of the SG, the effects of the multi-dimensional heterogeneity of the SG must be considered using KENO-VI (CE). The KENO-VI (CE) code allows analysis between the three models mentioned above without the self-shielding treatment required for the KENO-VI (MG).

To properly treat the heterogeneity of a SG, the height and the inner and outer width of the SG is required. The outer width p of the SG is equivalent to the pitch of the fuel pin p_{FP}. Since the SG height h and inner width p_{in} were not specified in the OECD/NEA benchmark, the reference height of 3 cm from Pazirandeh (Pazirandeh, et al., 2011) was used for the base model. The width p_{in} of the SG is between the clad of the fuel pin and the inner width of the SG. To calculate the width p_{in}, the following were considered:

- Step 1: Calculation of the volume of SGs in an FA

If the volume of all the spacer grids $V_{all,SGs}$, in a FA is 1.2% of the FA volume, then the volume can be calculated as follows:

$$V_{all,SGs} = V_{FA} \times \frac{1.2}{100} \tag{58}$$

where V_{FA} is the volume of the FA calculated using the pitch of the FA, p_{FA} and its specific height h as shown Eq (59):

$$V_{FA} = \frac{\sqrt{3}}{2} p^2{}_{FA} \times h \tag{59}$$

- Step 2: Obtain volume of each SG in each fuel pin

To obtain the volume of each spacer grid in each fuel pin, Eq (60) is used:

$$V_{each,SG} = \frac{V_{all,SGs}}{\eta_{FPs} \times \eta_{SGs}} \tag{60}$$

where η_{FPs} is the total number of fuel pins and η_{SGs} represents the total number of spacer grids in each fuel pin.

Alternatively, $V_{each,SG}$ can be expressed as:

$$V_{each,SG} = \frac{\sqrt{3}}{2}\left(p^2{}_{FP} - p^2{}_{in}\right)h_{SG} \tag{61}$$

where p_{in} is the inner width between the spacer grid and the clad as defined above.

- Step three: Obtaining the inner width p_{in} of the SG

By equating Eq (60) and (61), the width p_{in} can be calculated as follows:

$$P_{in}^2 = P_{FP}^2 - \left[\frac{2}{h_{SG}\sqrt{3}} \times \frac{1.2V_{FA}}{100\eta_{FPs} \times \eta_{SGs}}\right] \tag{62}$$

A sensitivity analysis of using different values of the SG dimensions was performed by varying h_{SG} and p_{in} and while preserving the height between the top of one spacer grid and to the top of the next spacer grid location. The height of each spacer grid was varied by assuming ± 0.5 cm steps from the initial value of 3 cm as seen in Table 4-5. The dT in Table 4-5 is the thickness between the clad outer surface and the SG inner surface.

TABLE 4-5: SG DIMENSIONS

h_{SG} (cm)	$p_{in}(cm)$	dT
1.5	0.5563	0.1013
2.0	0.5777	0.1227
2.5	0.5901	0.1351
3.5	0.6040	0.1490
4.0	0.6083	0.1533
4.5	0.6116	0.1566

4.5.3.3 *Spacer grid Material parameters*

In the early VVER reactors, the stainless-steel material was used for spacer grids. However, in the 1990s, the Russian VVER fuel manufacturers turned to manufacturing the FA with zirconium SG (IAEA., 2015). This is mainly due to the low thermal cross-section and higher melting temperatures of the Zr alloys (Abe, et al., 2014).

The material specified in the OECD/NEA benchmark specification for the spacer grid is stainless steel. It is therefore informative to compare the results using stainless steel with those using Zr-alloy for the SG material, taking the associated uncertainties into account, including the nuclear data uncertainties.

The sensitivity of SG materials was performed considering three sets of calculations:

- The base model with stainless-steel as SG material was considered;
- No SG material available, meaning the location of the SG was replaced with the moderator; and
- The stainless-steel was replaced by the E110 zirconium alloy material.

4.5.4 MANUFACTURING TOLERANCES

For a material or geometry value of a nuclear system, a tolerance limit should exist. Normally, the tolerance is part of the manufacturing process and would be specified by the manufacturer. However, if there is no data available, then the most common practices would be to allocate some tolerances that seem appropriate based on experience or intuition, and then conduct an analysis to ensure that the allocated tolerances suit the desired design function (Frosio, et al., 2017). The sensitivity with respect to the tolerance limits of geometric and material parameters was also studied, and the methodology used is discussed in this section. In the current study, the manufacturing tolerance for the parameter of interest was obtained mostly from the available specification of the manufacturing tolerance from the OECD/NEA benchmark as shown in Table 4-6.

For each of the parameters considered, calculations were done with the parameters set to either the upper or lower value of the tolerance, to test the sensitivity. If these parameters proved to be significant, then for the later uncertainty quantification, the uncertainty range of the parameters were taken to be the tolerance limits and a uniform distribution is assigned. This uniform distribution was as specified in the OECD/NEA benchmark.

A similar study was done to calculate the manufacturing tolerance sensitivities of a VVER-1000 fuel pin based on the OECD/NEA benchmark (Canuti, et al., 2012). In the current study, this sensitivity analysis is performed for the fuel assembly of the VVER-1000 system. Most of the parameters that are tested in this study are similar to the one that were tested in the referenced study. The results will be compared, to see if the effects of the manufacturing tolerances changes when the system is a fuel assembly.

TABLE 4-6: TOLERANCES OF THE VVER-1000 PARAMETERS

Parameter	Nominal	Bounds
IHOD (cm)	0.140	+0.030

ρ_{fuel} (g/cm^3)	10.400	+0.200
FPOD (cm)	0.753	+0.003
GOD (cm)	0.772	+0.006
COD (cm)	0.910	±0.005
^{235}U w/o (3.3%)	3.300	±0.050
^{235}U w/o (3.0%)	3.000	±0.050
T_{H_2O} (K)	552.150	±2.000
ρ_{H_2O} (g/cm^3)	0.767	±0.002
SG Height (cm)	3.000	±0.005

Although, the study by Canuti has presented the sensitivities due to manufacturing tolerance in a VVER-1000 fuel pin, the quantification of uncertainties of these parameters were not shown. Therefore, the current study intends on performing uncertainty quantifications of the parameters that shows to be significant as discussed above.

4.5.5 MODEL ASSUMPTIONS

Apart from the standard assumptions made in neutronic modelling, there are few assumptions that were made in the system's modelling that requires explanation. As part of this study, a sensitivity analysis of these assumptions for the neutronic models is conducted to assess the impact.

4.5.5.1 *Manufacturing tolerance for fuel diameters*

For a given fuel assembly, it is assumed that the fuel pin dimensions as listed in Table 4-6 differs individually within the tolerance limit. This is because the fuel pin is relatively long, and the manufacturing process would most probably manufacture each pin (rod) as individual elements and not as a single long rod with a single tolerance that later gets cut up. Therefore, perturbation of the clad diameter and fuel diameter is done whereby these parameters are perturbed individually for each fuel pin to propagate their uncertainties.

4.5.5.2 *The dependency of UO_2 density on the enrichment*

On the other hand, the fuel density and fuel enrichment were perturbed as single parameters for the entire fuel assembly rather than for each fuel rod, since it is assumed that in the manufacturing process, the fuel material and fuel enrichment originate from the same batch. The fuel density would change depending on the enrichment since the molar mass of ^{235}U and ^{238}U are different. The fuel enrichment and fuel density were therefore analysed to see if they are dependent on each other. This was done by assuming that the volume of the fuel pellets with different enrichments is the same. For enrichments of 3.25, 3.30, 3.35, and with the density at 3.30 enrichment to be 10.4 g/cm^3, the density was calculated to be 10.3999, 10.40000 and 10.40001 g/cm^3 respectively. By performing two criticality calculations with density of 10.3999 and 10.40000 g/cm^3, the change in

k was in the order of 5 pcm, which is considered negligible. This dependency is shown in detail in Appendix D.

4.5.5.3 *The dependency of moderator-density to its temperature*

The density of water is dependent on the temperature of the water. A specified temperature will have an uncertainty range, and each temperature point in this range will then have a corresponding density. There will thus be a range of density points associated with each temperature point in the range. However, each of these density points in the temperature range will also have its own uncertainty range. The sensitivity due tothe density in this double dependency as a function of the temperature was therefore also investigated.

For the moderator temperature and density sensitivity, the sensitivity due to the tolerances of the temperature were taken to be ±2K about the given temperature 552.15 K, with the resultant temperatures listed in Table 4-7. The tolerances were not given in the OECD/NEA benchmark, however, tolerances of 2K was listed in (Kyncl, et al., 2005).

Each temperature point has a corresponding density which in turn are given sensitivity bounds of ±0.002 (g/cm^3) as listed in the second column Table 4-7. These bounds were also obtained from (Kyncl, et al., 2005).

TABLE 4-7: TEMPERATURE AND DENSITY TOLERANCES

Temperature	Density	Bounds
550.15	0.76994	±0.002
552.15	0.76612	±0.002
554.15	0.76253	±0.002

4.6 UNCERTAINTY QUANTIFICATION

One of the aims of the OECD/NEA Benchmark is to quantify the uncertainty associated with the parameters in the models. The uncertainties due to imprecise knowledge of parameter values in the calculation are quantified by ranges and probability distributions. SAMPLER which uses the statistical sampling method of input data perturbations is used to perform this analysis. Due to the statistical sampling method used in SAMPLER, to propagate the uncertainties due to all the input data, a grouping of the parameters is required. This grouping is necessary to separate the parameters that cannot be statistically sampled to the one than can be and to also cast out the parameters that has insignificant impact on the results.

The first group was defined as those parameters which have definite values or attributes. In terms of the parameters listed in Table 4-4, one such a parameter is ISN. Other parameters belonging to this group were the nominal value of the SG width and the type of SG material. The second group was defined as those parameters which can have continuous or quasi-continuous values. These

were the manufacturing tolerances and code parameters such as SZF listed in Table 4-4. The nuclear data libraries could also be part of this group since the energy group structure is normally introduced from the continuous energy group representation to allow numerical solutions. However, the distinction between using different versions of a library such as ENDF/B-VII.0 and ENDF/B-VII.1 would belong to group one. The grouping is done after all the sensitivity test analyses of all the source of uncertainties have been performed.

All the input data involved in this study are given in Table 4-8 according to their groups. The uncertainty due to the nuclear data was assigned to group two. As it was discussed in Section 3.6.2, SAMPLER provides 1000 perturbed instances of the library for propagation of nuclear data uncertainty.

TABLE 4-8: GROUPING OF THE INPUT DATA

Group 1	**Group 2**
IROPT	SZF
ISN	DEMIN
ITERP	DEMAX
GD	ALUMP
SN	Manufacturing tolerances
NPOLAR	Nuclear data consisting of 1000 perturbed files
NAZIM	
SG $h/\ p_{in}$	
SG material	
SG model	
Random number seeds	
Nuclear data libraries	

To propagate the uncertainty, specific states of the systems were defined using selected values for the parameters from group one. For each state, N stochastic combinations of the parameters were chosen from group two, resulting in the creation of N input files. An alternate description would be to say that N samples were created. KENOVI calculations were then performed for each sample, each yielding a required response R_i. The standard deviation of the N responses for each state then yielded the uncertainty in R for each state. In selecting the parameters of group two, a random sampling method is applied using a uniform probability distribution function (PDF).

4.7 FUEL DEPLETION ANALYSIS

With the TRITON capabilities available from SCALE-6.2.1 code, a fuel depletion calculation was performed on a fuel assembly using both NEWT (2D) and KENO-VI (3D). This analysis is performed at Hot Full Power and the fuel was depleted to 315 effective full power days. The

calculation of burn-up requires time intervals to define the burn-up steps. For more accurate estimation of the depletion parameters, small intervals are required. The time intervals given in Table 4-9 are obtained from Czakoj (Czakoj, et al., 2018).

The time-interval that was used in this study was 1.2 day intervals for the first six days, 6 day long intervals for the next 24 days and 19 day long intervals for the following 285 days. The analysed results are the multiplication factor and nuclide densities as a function of burn-up.

TABLE 4-9: TIME-INTERVALS

#	Time interval	Total time
0	0	0
1	1.2	1.2
2	1.2	2.4
3	1.2	3.6
4	1.2	4.8
5	1.2	6
6	6	12
7	6	18
8	6	24
9	6	30
10	19	49
11	19	68
12	19	87
13	19	106
14	19	125
15	19	144
16	19	163
17	19	182
18	19	201
19	19	220
20	19	239
21	19	258
22	19	277
23	19	296
24	19	315

4.8 UAM CONTRIBUTION

The primary aim of the OECD/NEA benchmark is to study and verify the methods and codes used for sensitivity and uncertainty analysis using best-estimate coupled code calculations. A requirement of the benchmark is an accurate computation of the neutronics and thermal-hydraulics uncertainties. For the current study, thermal-hydraulics uncertainties were not considered due to time constraints. Therefore, as it was mentioned in the beginning, this study is based on Exercise I-1 and I-2 of phase 1, which is entirely based on the analysis of neutronics uncertainties. These set of exercises contained in Phase 1 provide a good verification for the methodology and tools

that have been discussed above in Chapter 3. Pin-cell and fuel assembly problems are specified in the above exercises to which participants provide their results for response uncertainties.

4.9 SUMMARY

The information that was provided in this section forms the basis of the methodology followed to develop the VVER-1000 system and to calculate the results of this study.

5 RESULTS AND DISCUSSIONS

The following chapter contains the results and discussions of the Kozloduy-6 system models as defined in Chapter 4. The results obtained are the criticality results, sensitivity of the criticality calculations to the input data and uncertainty quantification of the criticality results for the VVER-1000 FA system. The results for the contribution to the OECD/NEA benchmark were included and discussed as part of this chapter. The criticality results were performed using KENO-VI and NEWT of the SCALE-6.2.1 code and the uncertainty analysis was performed using TSUNAMI and SAMPLER of the SCALE-6.2.1 code. Fuel depletion calculations were completed for the fuel pin and the fuel assembly of the VVER-1000. For every Monte Carlo calculation, a statistical uncertainty for the computed k was provided. A comparison between a Monte Carlo based code and a deterministic based code was carried out to gain deeper insight on the results of the deterministic code.

5.1 OPTIMISATION OF CODE INPUT PARAMETERS

The following results for the optimisation of code input parameters were obtained to study the effects of code parameters on the eigenvalue for a hexagonal system using NEWT. The NEWT code will be used later, to compute the results for the contribution to the OECD/NEA benchmark. The optimisation of the code parameters is therefore important. Optimising the input code parameters allows the reduction of the uncertainties that might be due to the inherent methodologies of the code. The FA was modelled without spacer grids. The analysis was done to observe the change in the eigenvalue results due to varying certain code input parameters of XSProc and NEWT.

The parameters that are optimised in this study for the XSProc calculations are presented in Section 5.1.3, while Section 5.1.4 and Section 5.1.5 gives the results for NEWT parameters. Optimisation is determined with respect to both the value and the convergence of k_∞. The estimation of k_∞ for criticality calculations were also done using KENO-VI (MG) in this Section. KENO-VI (MG) and NEWT use the same set of cross-sections calculated by XSProc since both are multi-group calculations. However, the flux solver for KENO-VI (MG) is stochastic, and therefore has a higher accuracy than a deterministic code provided that a sufficiently high number of neutron histories are evaluated. KENO-VI results were therefore used as comparison with the results from the NEWT code to verify the optimisation. The nominal results for the NEWT results are displayed in Section 5.1.1. The uncertainties due to nuclear data as presented in Section 5.1.2 for the nominal case were obtained using TSUNAMI-2D which uses NEWT and TSUNAMI-3D which uses KENO-VI.

5.1.1 NOMINAL CRITICALITY RESULTS

The results from KENO-VI (MG) and NEWT are compared for the FP and FA models. The results from NEWT for the FP and FA models are about 150 pcm and 180 pcm away from their corresponding KENO-VI (MG) solutions respectively. As will be shown later, these differences were made smaller as a result of optimizing the input parameters. A similar model of the fuel pin and fuel assembly was given by Venturini (Venturini, 2014). In the study by Venturini, the method for optimising XSProc and NEWT parameters was not shown. The results reported for the FP and the FA were 1.34498 and 1.33818 respectively. The difference between the NEWT results and results by Venturini is shown in Table 5-1. The results from the referenced study were obtained using an older version of the SCALE code namely version 6.2b3 together with the 44 group file (listed as 44GROUPCOV in Venturini). No KENO-VI (MG) calculations were presented in the referred study.

TABLE 5-1: MULTIPLICATION FACTOR FOR THE BASE MODEL

	KENO-VI	NEWT	k_{diff} (pcm)	Venturini
Fuel Pin	1.34764 (6)	1.34610	154	266
Fuel Assembly	1.34160 (15)	1.33982	178	164

5.1.2 UNCERTAINTY IN THE CRITICALITY RESULTS DUE TO NUCLEAR DATA

The uncertainty of k in units of $\%\Delta k/k$ for the TSUNAMI-2D and TSUNAMI-3D are shown in Table 5-2. Table 5-2 shows also ${}^{\%\Delta k}/_{k}$ for the uncertainties produced by Venturini to give an indication of the values that can be expected. ${}^{\%\Delta k}/_{k}$ is the quantity that is supplied in the output of TSUNAMI-2D/3D. However, k_∞ is supplied in the output as the multiplication factor. It is therefore also instructive to consider the uncertainty in k_∞ in terms of Δk. Defining ${}^{\%\Delta k}/_{k}$ as C, the quantity Δk was calculated using Eq (63) as:

$$\Delta k = \frac{kC}{100} * 10^5 \ (pcm) \tag{63}$$

with

$$C = {}^{\%\Delta k}/_{k} \tag{64}$$

The impact of nuclear data uncertainties on the k results in terms of Δk for the FP and the FA were about 780 and 760 pcm respectively using both TSUNAMI-3D and TSUNAMI-2D. The model by Venturini produced uncertainties of about 690 and 670 pcm for the FP and FA respectively. These uncertainties are smaller than the uncertainties produced in the current model by about 90 pcm for both the FP and FA.

TABLE 5-2: UNCERTAINTY IN k DUE TO NUCLEAR DATA $\left(\%\Delta k/_k\right)$

	TSUNAMI-3D	TSUNAMI-2D	Venturini
Fuel Pin	0.576420 (7)	0.57713	0.51300
Fuel Assembly	0.564854 (8)	0.56473	0.50300

The top seven important neutron-nuclide reaction contributors that contribute to the uncertainty of k were obtained and their uncertainties are given in units of $\%\Delta k/k$ from the TSUNAMI code. These contributors are shown in Figure 5-1 and Figure 5-2 for the FP and FA respectively. The contributions to the uncertainty in k_∞ due to the neutron-nuclide reaction are caused by the combination of the highest sensitivities associated with a certain reaction and the highest value of the associated covariances.

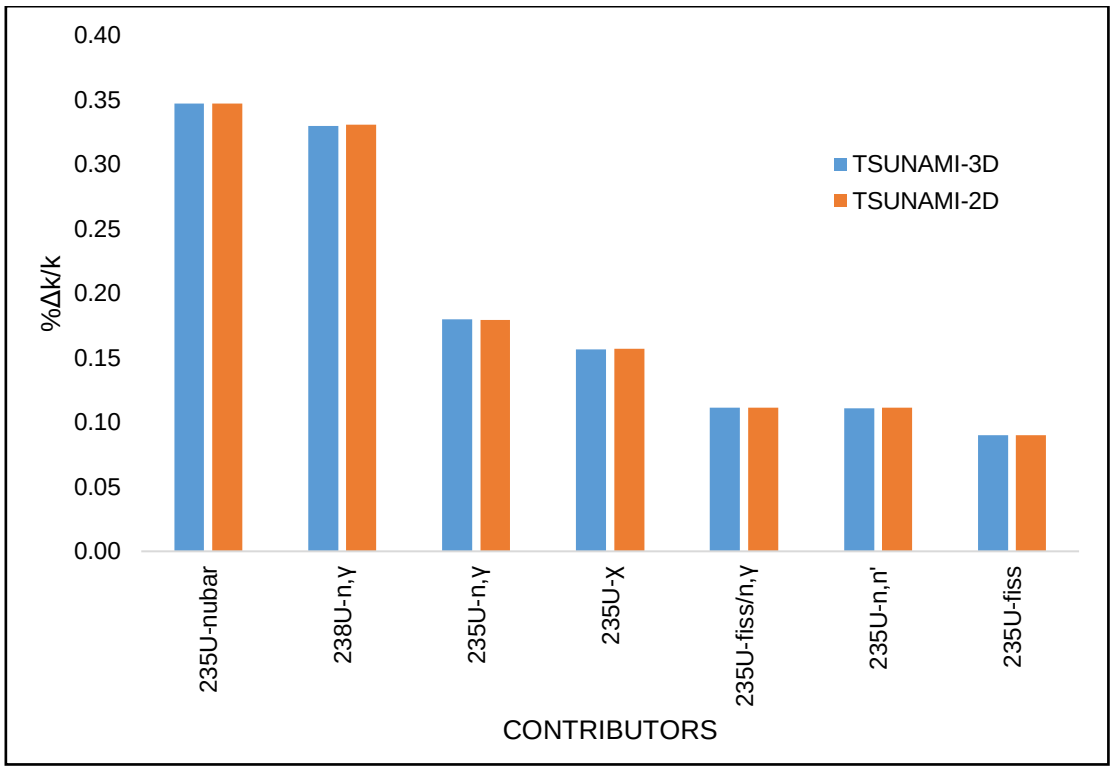

FIGURE 5-1: FPS' SEVEN TOP NEUTRON-NUCLIDE REACTION CONTRIBUTORS

The highest neutron-nuclide reaction contributor was $^{235}U_{nubar}$ with an impact of about 470 pcm for both the FP and FA. The 7^{th} neutron-nuclide reaction contributor was $^{235}U_{fission}$ and $^{235}U_{n,n'}$ with an impact of about 121 pcm and 126 pcm for the FP and FA respectively. The highest neutron-nuclide reaction contributor for the reference results was $^{238}U_{n,\gamma}$ with an impact of about 403 pcm.

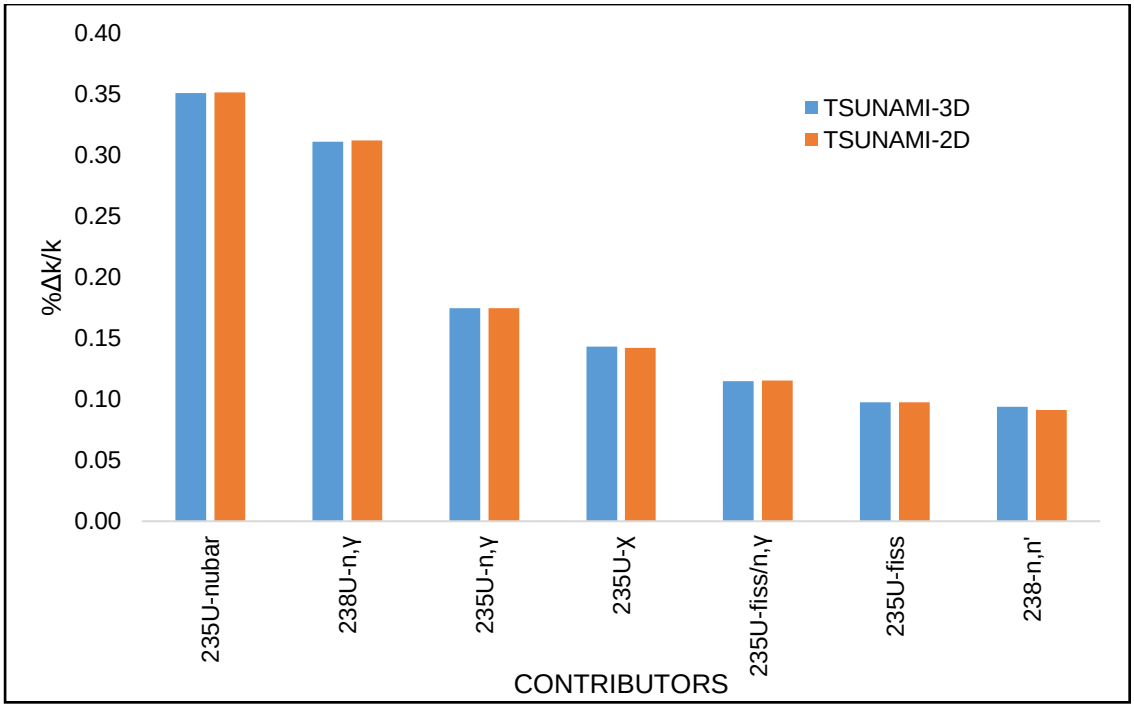

FIGURE 5-2: FAS' SEVEN TOP NEUTRON-NUCLIDE REACTION CONTRIBUTORS

The neutron-nuclide reactions' uncertainties from TSUNAMI-3D and TSUNAMI-2D appear to be in good agreement for FP and FA. The percentage difference $(\%\, diff)$ of these uncertainties between TSUNAMI-3D and TSUNAMI-2D code are shown in Figure 5-3 for both FP and FA. The $\%\, diff$ is given by Eq (65), where A is the uncertainty due to a nuclide obtained with TSUNAMI-2D and B with TSUNAMI-3D. The $\%\, diff$ between uncertainties from TSUNAMI-3D and TSUNAMI-2D were less than 4% as seen in Figure 5-3. The $\%\, diff$ between TSUNAMI-3D and TSUNAMI-2D are largest for neutron-nuclide reaction ${}^{235}U_{n,n'}$.

$$\%diff = 200\% \times \left(\frac{A-B}{A+B}\right) \tag{65}$$

Figure 5-4 shows the $\%\, diff$ between the nuclide reactions' uncertainties calculated for the FP and FA. The $\%\, diff$ between the FP and FP move from 1% to about 17%.

Overall, in terms of nuclear data uncertainties, the uncertainties between TSUNAMI-3D and TSUNAMI-2D are in good agreement.

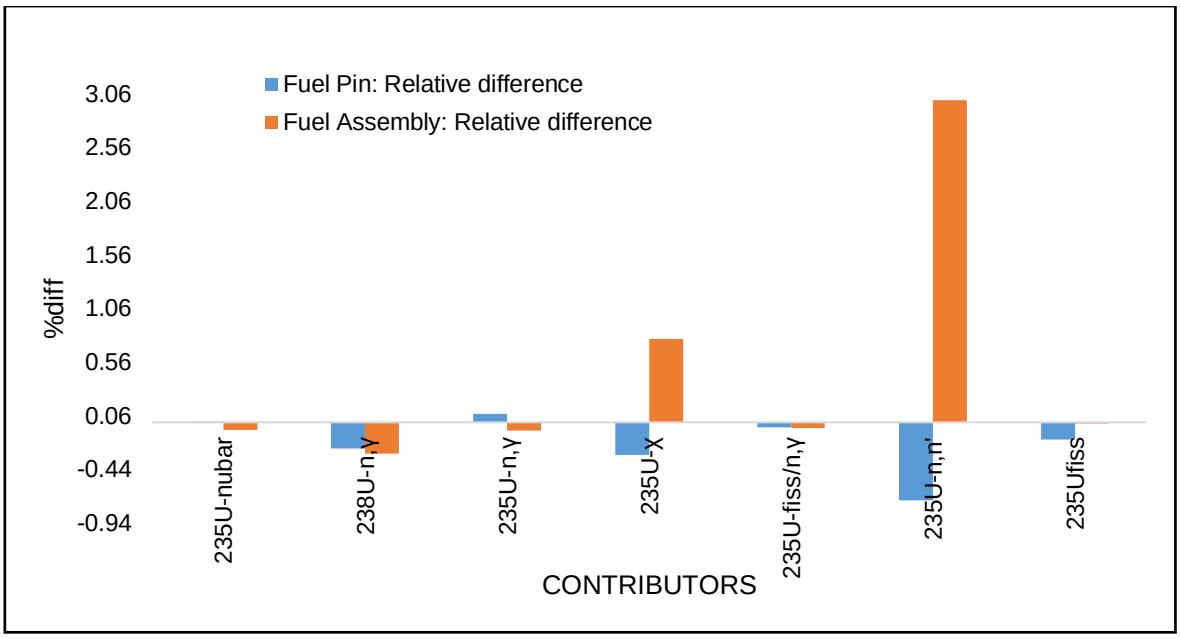

FIGURE 5-3: % $diff$ BETWEEN TSUNAMI-2D AND -3D

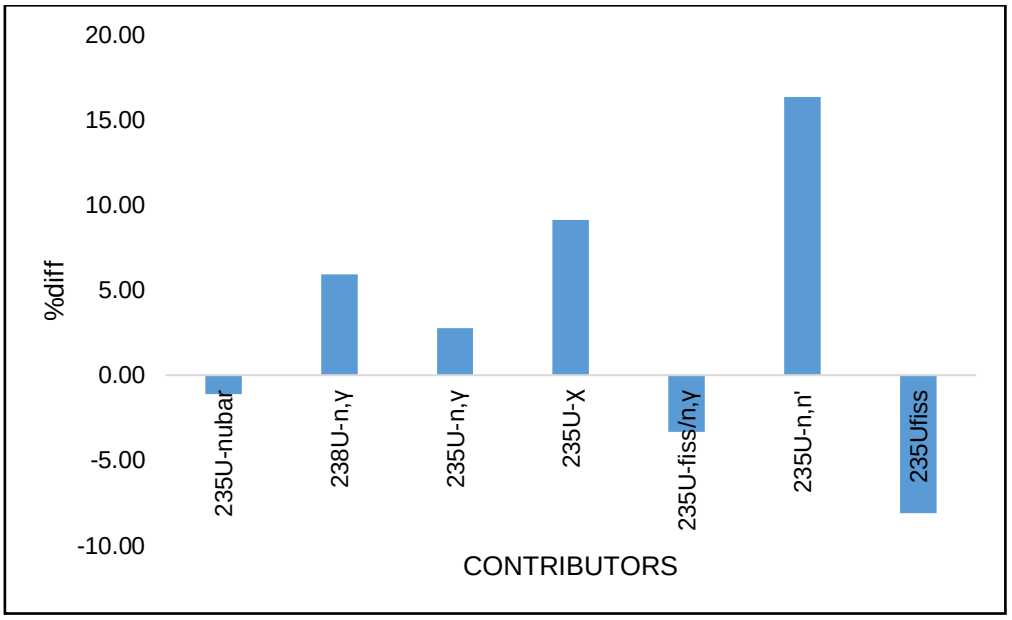

FIGURE 5-4: % $diff$ BETWEEN FP AND FA SYSTEM

5.1.3 OPTIMISED PARAMETERS IN XSPROC

As it has been discussed in Section 3.3, prior to a criticality calculation being performed using NEWT/KENO-VI (MG), the nuclear cross-sections that will be required by these codes are processed using XSProc. This section presents results for the XSProc input parameters that were optimised for the processing of nuclear cross-section and the self-shielding resonance calculations. The parameters that are optimised in this study are defined in Table 3-1 as used in the BONAMI and CENTRM modules under the XSProc calculations.

The first task was to investigate individual parameters described in Section 3.3 that are used in XSProc. For ITERP = 1 and 2, the difference in k_∞ was 23 pcm. ITERP = 0 was equivalent to ITERP = 1 since the temperature was 552.15 K which is below 1200 K. With this difference relatively small, it was decided to use ITERP=1 which is equivalent to the default value, 0. This meant that the square-root interpolation was used.

The behaviour of DEMIN was studied with DEMAX values of $1 \times 10^4\ eV$ and $1 \times 10^5\ eV$. The range of DEMIN was from $1 \times 10^{-5}\ eV$ to $1 \times 10^{-2}\ eV$. For both DEMAX values, k_∞ remains fairly constant below DEMIN in the range $1 \times 10^{-3}\ eV$ until $5 \times 10^{-3}\ eV$ with the difference between the values being 4 pcm. Since this range has the default value of $1 \times 10^{-3}\ eV$ as its lowest limit, it was decided to set DEMIN at $1 \times 10^{-3}\ eV$. With this value for DEMIN, the difference in k_∞ for DEMAX equal to $1 \times 10^4\ eV$ and $1 \times 10^5\ eV$ was 4 pcm. It is recommended in the SCALE manual that the value of DEMAX should be <500 keV. Since DEMAX satisfied this condition for both values, the default of $1 \times 10^4\ eV$ was chosen as this would decrease computational time.

The mass lumping fraction ALUMP was varied from 0.0 to 0.4. The difference between ALUMP = 0.0 and ALUMP = 0.4 is 10 pcm. With this small difference, it was decided to use the default value of 0.2. Although the time decreases as the ALUMP is increased, the factor by which the time is changing is negligible.

For IROPT equal to 0 and 1 the difference in k_∞ was 2 pcm. This meant that the calculation was not sensitive to whether the intermediate resonance approximation or the narrow resonance approximation was used.

In studying the effect of SZF, the value of SZF was changed from 0.1 to 2.0 for ISN values of 16, 32 and 64. Values of SZF greater than 2.0 can be ignored, since for these values there is only one mesh in the unit cell, and k_∞ will then remain constant. Figure 5-5 shows the behaviour of k_∞, as a function of SZF. The value of k_∞ is the same for SZF from 0.1 to 0.5 and then decreases for SZF up to 2.0 for all the ISN values shown. This behaviour is as expected, since a converged value k_∞ should result as the number of meshes increases, i.e. as SZF becomes smaller. In a parallel study based on the fuel compact of the HTGR, it was shown that the value of SZF is 0.3, which compares well with that shown above (Naicker, et al., 2016). It was decided to set SZF at 0.3.

In terms of ISN, k_∞ increases and converges as ISN increases as is shown in Figure 5-6 for SZF = 0.3 and 2.0. The difference in k_∞ for ISN = 24 and 64 is 7 pcm, with time increasing by a factor of 3. If a modelling convergence criterion of 10 pcm is used for k_∞, ISN = 24 is adequate.

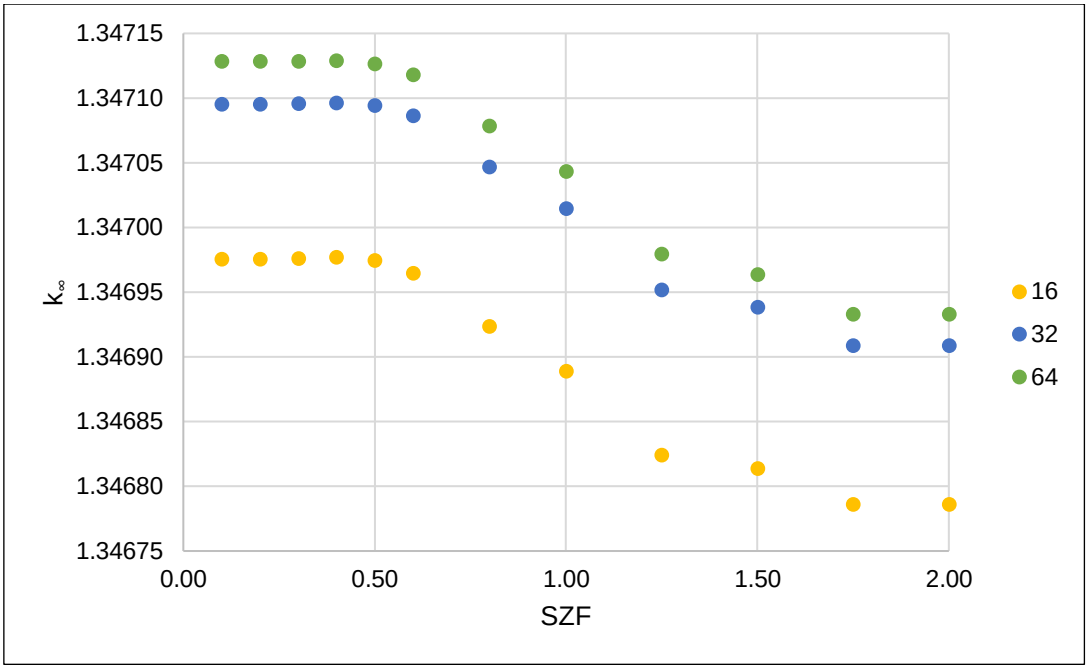

FIGURE 5-5: k_∞ VS SZF

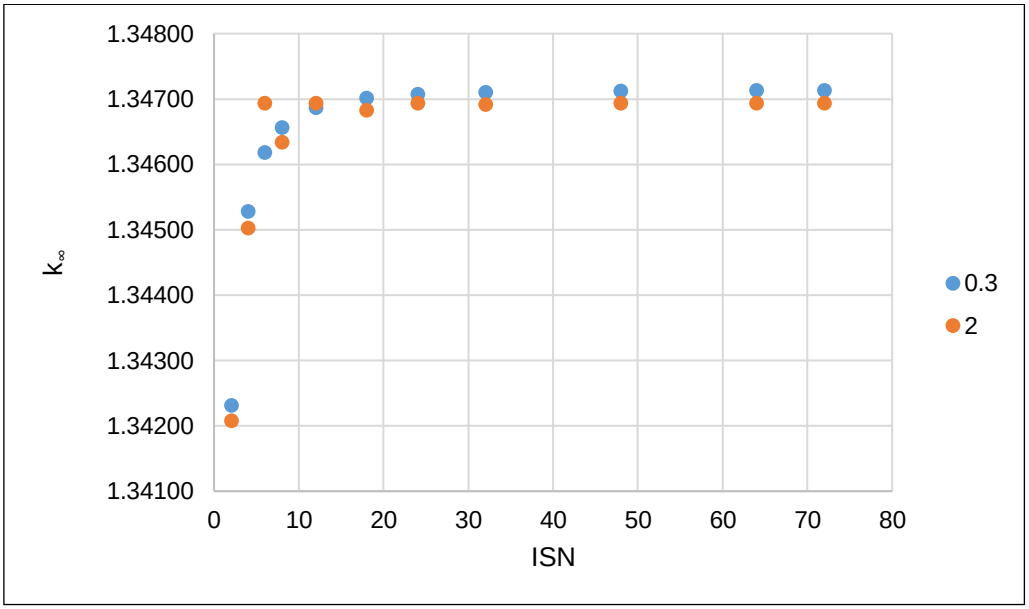

FIGURE 5-6: k_∞ VS ISN

5.1.4 GRID DIMENSIONS (GD) IN NEWT

The default value of S_N = 6 was used for the GD analysis, with P_N set at 2 for the moderator and 1 for the rest of the materials as in the nominal models. Figure 5-7 shows the results for the FP with the default settings for XSProc and with optimized values for XSProc. The GDs were varied using 2, 4, 6…, 40 for the FP.

FP Convergence

Anomalies were observed in k_∞ at values of 20, 40, and 60 (60 is not shown) as it can be seen in Figure 5-7. This is currently not understood and requires further studies. These data points were not considered in the analysis. The difference in k_∞ at GD = 10 and GD = 38 is 24 pcm whilst the difference in k_∞ at GD = 24 and GD = 38 is 3 pcm. Assuming a modelling convergence criterion of 10 pcm then implies that the model can be considered converged with GD = 24. The time taken in seconds for the various GD is shown in Figure 5-8. It must be noted that, although the results converge with finer grids, time for calculations to complete is compromised, since the finer the grid the longer time it would take for calculations to complete.

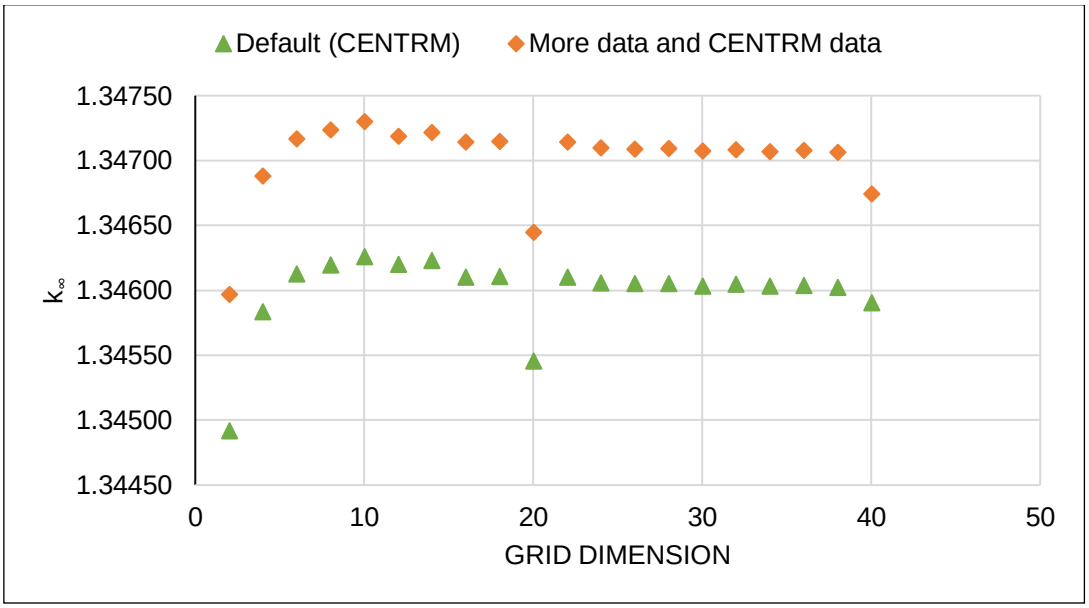

FIGURE 5-7: k_∞ VS GD

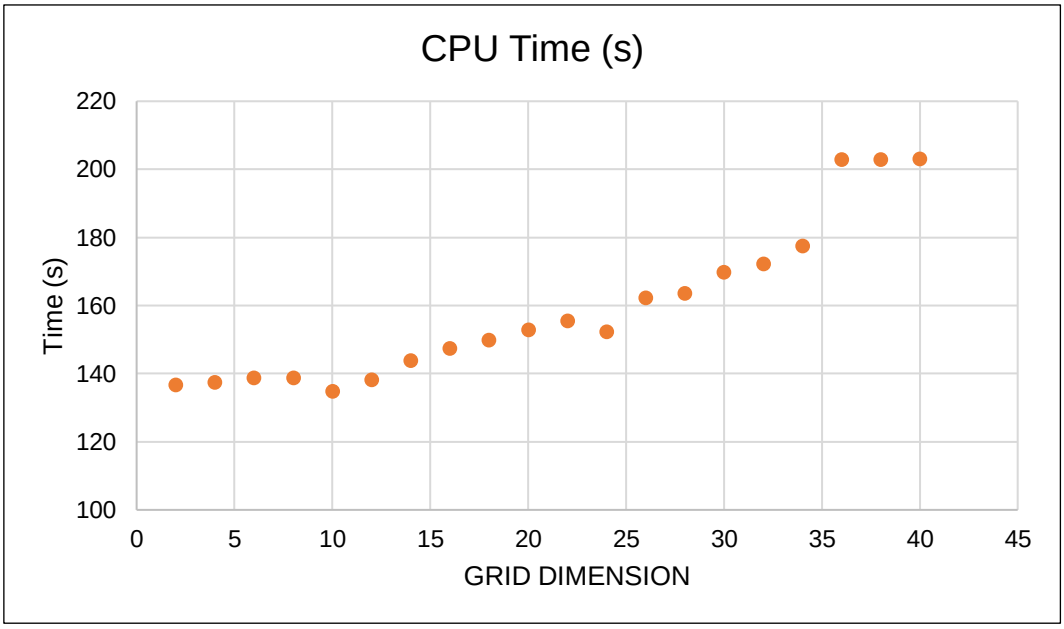

FIGURE 5-8: COMPUTATIONAL TIME FOR FP

FA Convergence

Figure 5-9 shows the results for FA with GD varied using 2, 4, 6…, 40. Not all the chosen GD values were possible for the FA calculation, however. The number of successfully completed calculations were enough to allow for the GD analysis.

For Case One, shown as the blue line in Figure 5-9, the GD was varied in the unit cell, while it was fixed at 2 x 2 for the global unit. k_∞ decreases as GD is increased, with the difference between GD = 38 and 40 being 3 pcm. The time of calculation increases as GD is increased and this is shown by the grey line in Figure 5-9.

In case two, GD was defined only in the global unit with the GD values being 128×128 and k_∞ was found to be 1.33974. The difference of this value with that of Case One for GD = 4 and 40 are 40 pcm and 9 pcm respectively. In Case Two, NEWT could not run for values of GD of 64, 80, 130 and 150. Further investigations would be required to establish that GD = 128 will give a converged solution. In Case Three, shown as the orange line in Figure 5-9, GD was varied only in the global cell and was fixed at 4×4 in the unit cell. The change in k_∞ with the varying GD is small. Case One has depicted a good convergence in the GD analysis compared to Case Three. Therefore, to obtain reliable results at a reasonable computation time, GD = 12 defined in the unit cell is adequate. Defining GD in the unit cell is convenient, since most of the unit cells contain the fissile regions.

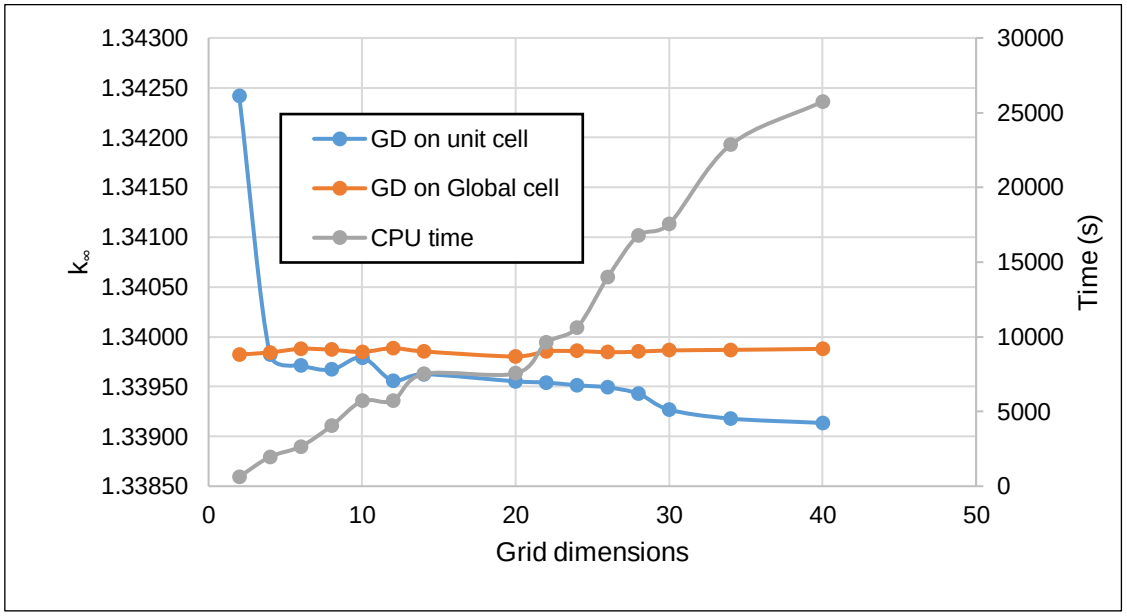

FIGURE 5-9: k_∞ RESULTS AND CPU TIME AS A FUNCTION OF GD FOR FA

5.1.5 THE ANGULAR QUADRATURE SETS

For the level symmetric quadrature set (LSQ), the S_N order is analysed for values of $4 \leq S_N \leq 16$. The difference in k_∞ of the various S_N with $S_N = 16$ is shown in Figure 5-10. The values of k_∞ for $S_N = 16$ are 1.34688 and 1.34136 for the FP and FA respectively. It is preferable to use the lowest value of S_N for a model since this will take the shortest run time.

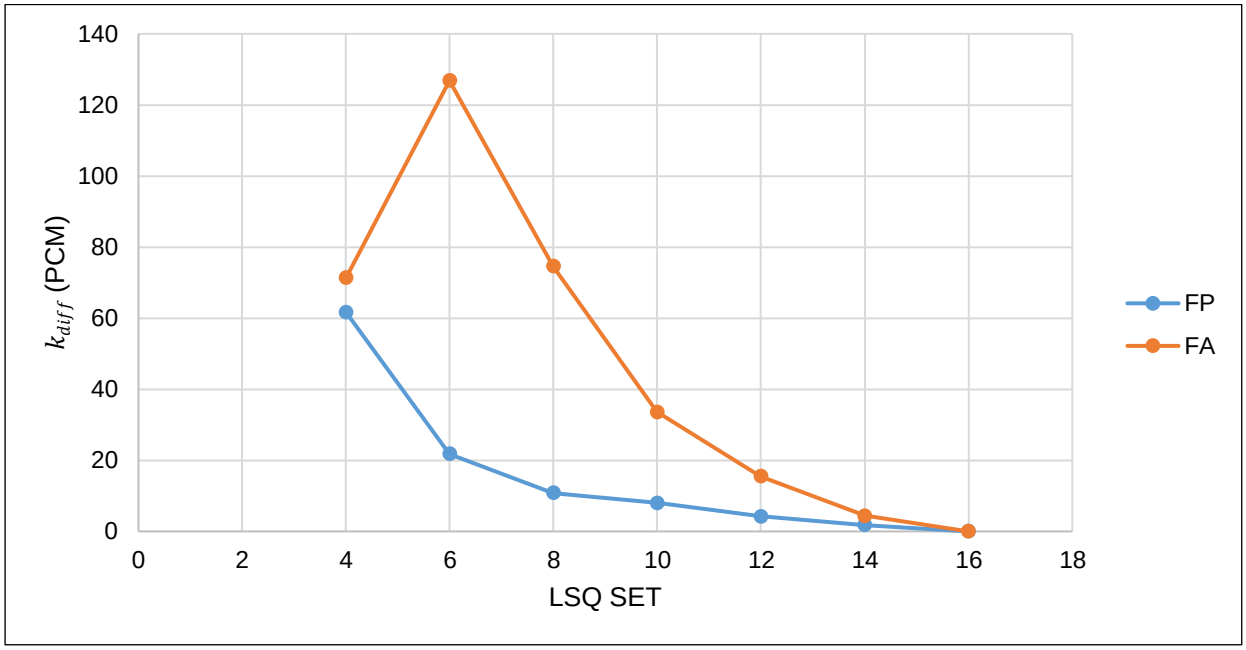

FIGURE 5-10: LSQ SET RESULTS FOR FP AND FA

If the limit for modelling convergence is taken to be 10 pcm, then the lowest values of S_N that can be converged are S_N = 10 and 14 for the FP and FA respectively, where the comparison is taken arbitrarily with S_N = 16. It is noted that for a stricter modelling convergence of 1 pcm, none of the S_N values when compared with S_N =16 will result in a converged solution.

For the product quadrature set (PQ), the values of NAZIM were 6, 9, 12…, 36 and that of NPOLAR were 2, 4, 6…, 24. All possible combinations of (NAZIM, NPOLAR) could be calculated for the FP models, but not all were possible for the FA calculations. In some cases, the calculations terminated because the model was said to be too big and had a problem allocating memory. The number of calculations that completed successfully were enough to allow for an adequate analysis of the modelling convergence criterion.

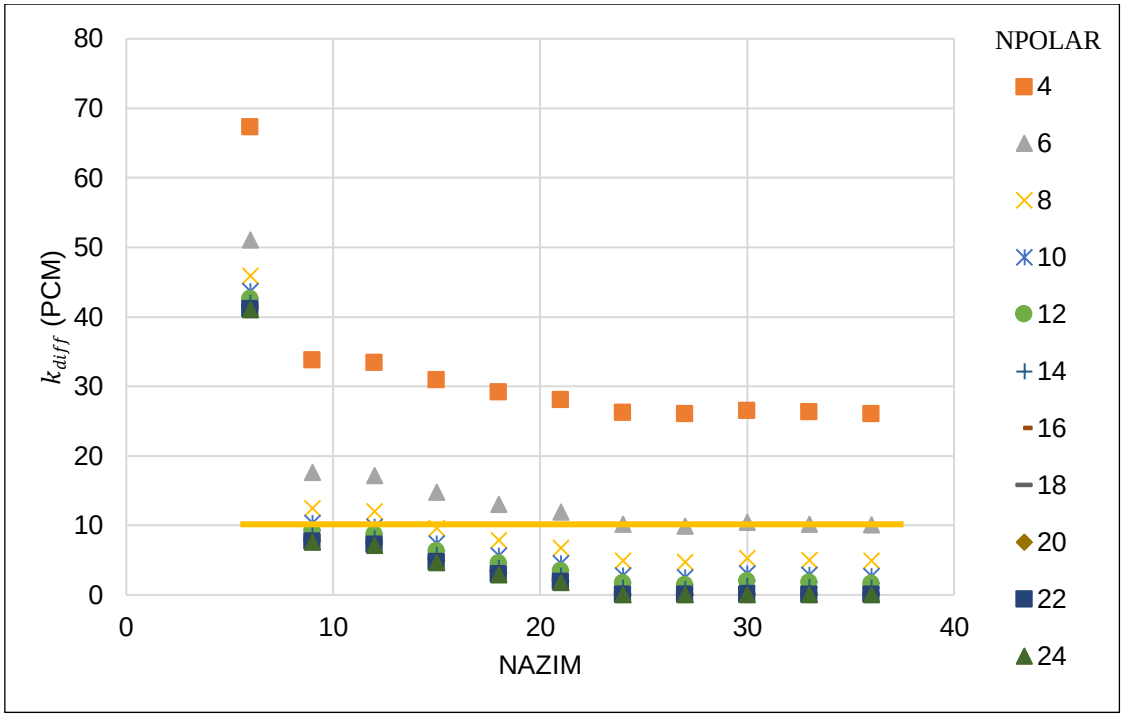

FIGURE 5-11: PQ SET RESULTS FOR FP

The difference in k_∞ of the various combinations for (NAZIM, NPOLAR) for both the FP and the FA are shown in Figure 5-11 and Figure 5-12 respectively. The reference k_∞ for these differences were 1.34877 and 1.34174 for the FP and the FA with (NAZIM, NPOLAR) = (36,24) and (36,20) respectively. Using the same modelling convergence criterion of 10 pcm the values of (NAZIM, NPOLAR) that can be used are those below the lines in Figure 5-11 and Figure 5-12. Since there are many possibilities for (NAZIM, NPOLAR) that satisfy the convergence criterion, a decision can then be made on the time taken for the calculation. Figure 5-13 shows the fractional time taken for each FP calculation. The fraction was calculated with reference to the calculation with (NAZIM, NPOLAR) = (12,10) which was chosen arbitrarily.

The choices for the FP are then (27,24), (24,14) and (18,12). These were chosen based on its convergences to be those below 10 pcm as can be seen in Figure 5-11 but also with reasonable computational time. A similar assessment with respect to calculation time could not be performed for the FA since many computers with different specifications were used. Calculating these results were not possible on one computer. Higher quadrature requires a lot of computer memory and too much computer time. However, the trend is expected to be the same. The difference in k_∞ between the LSQ and PQ calculations are 186 pcm and 43 pcm for the FP and the FA respectively when the optimized values of (NAZIM, NPOLAR) are used. The S_N value of 10 and 14 were used for FP and FA respectively. However, it should be noted that the LSQ were conducted with WBC and the PQ were conducted with RBC. Therefore, the PQ model should be run with WBC also at the optimized values to observe the effect of the boundary conditions. This is reserved as further work due to time and resource constraints.

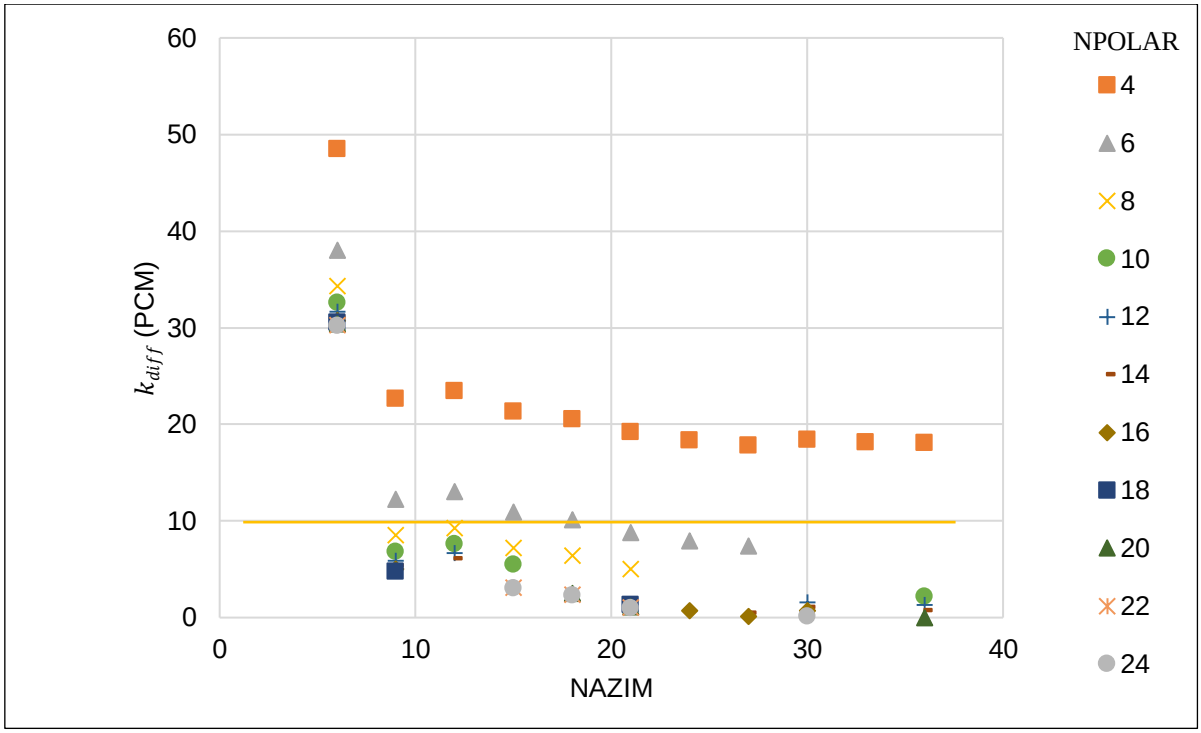

FIGURE 5-12: PQ SET RESULTS FOR FA

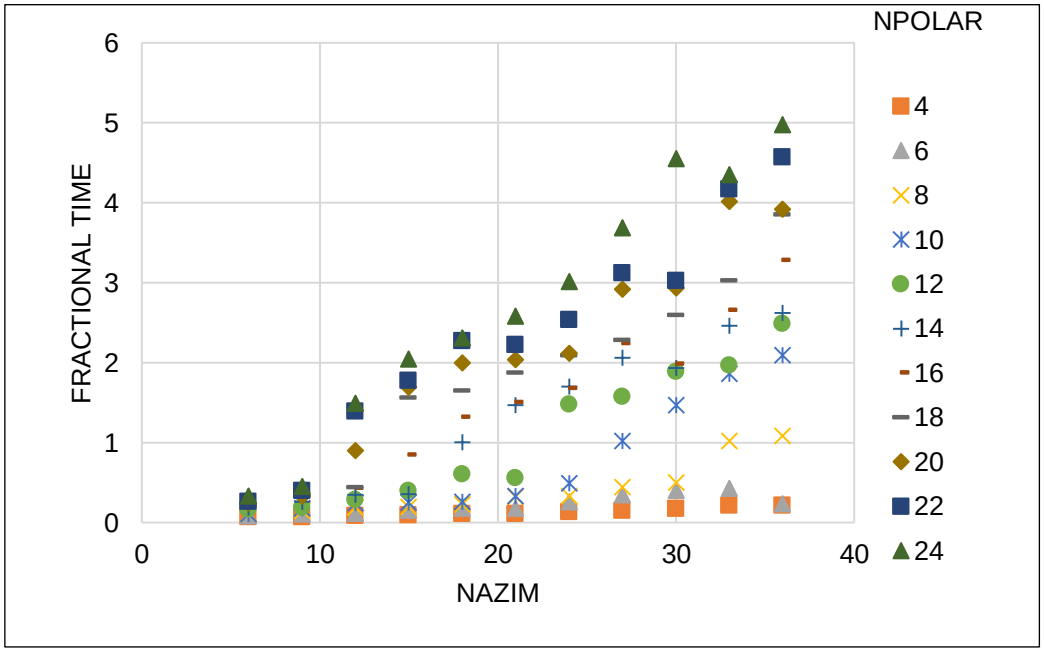

FIGURE 5-13: CPU TIME FOR FP

5.1.6 UNCERTAINTIES AND RANKING OF THE OPTIMISED PARAMETERS

Table 5-3 list the values of the XSProc and NEWT optimised parameters for both the FP and the FA respectively. The parameters were ranked accordingly using k_{diff} which is defined $k_i - k_{opt}$ where k_{opt} is the optimised results and i refers to all other possible values for the specific parameter.

For the calculations involving ISN, ITERP, SZF, DEMIN, ALUMP, DEMAX and IROPT, which is called set A for brevity, all the parameters were set at the default parameters except the parameter to be optimised. Set A were the parameters that were defined for the XSProc calculation. The parameters for NEWT were classified as set B. They were GD, S_N and NPOLAR/NAZIM.

The optimisation in set A was performed with set B parameters at default values; set B calculations were performed with the optimised values of set A. For all the parameters, a TSUNAMI-2D calculation was performed to obtain uncertainty in k ($\%\Delta k/k$) due to uncertainties in the nuclear data. The $\%\Delta k/k$ from all the parameters show little variations against each optimized parameter with the maximum and minimum being (0.57742, 0.57663) for the FP and (0.56484, 0.56462) for the FA. As a comparison, the $\%\Delta k/k$ for the corresponding TSUNAMI-3D of the FP and FA are 0.57642 and 0.56485 respectively. The TSUNAMI-3D calculations were performed with optimised XSProc parameters. These values correspond to the difference in Δk being less than 2 pcm (as seen in Column 7 of Table 5-3) with Δk calculated using Eq (63). The uncertainties in k ($\%\Delta k/k$) due to nuclear data for all the ranked parameters are similar with the $\%\Delta k/k$ for the default model, which is about 778 pcm when it is converted to Δk. When comparing the uncertainties due to the nuclear data ($\Delta k \approx$ 778 pcm) with that due to the modelling parameters (k_{diff}, Column 3 of Table 5-3), one notices that the difference due to the choice of ISN is comparable to the uncertainties due to the nuclear parameters (about 50%).

TABLE 5-3: OPTIMISED PARAMETERS RANKING FOR THE FP AND FA

Rank	**Parameter**	k_{diff} **(pcm)**	**Optim.Val**	$\%\Delta k/k$	Δk **(pcm)**	$\Delta k_{nom} - \Delta k_{opt}$
-	Default	-	-	0.57747	-	-
1	ISN	480	64	0.57713	777	0
2	GD	133	18	0.57710	777	0
3	NPOLAR	118	24	0.57663	778	-1
4	NAZIM	95	27	0.57663	778	-1
5	S_N	61	10	0.57714	777	0
6	ITERP	23	1	0.57710	777	0
7	SZF	19	0.3	0.57742	777	0
8	DEMIN	13	2×10^{-3}	0.57714	777	0
9	ALUMP	10	0.3	0.57712	777	0
10	DEMAX	4	2×10^{4}	0.57714	777	0
11	IROPT	3	1	0.57714	777	0
Fuel Assembly						
-	Default	-	-	0.56451	-	-
1	GRID	283	4/2	0.56473	758	-2
2	NPOLAR	79	18	0.56484	758	-2
3	NAZIM	32	24	0.56484	758	-2
4	S_N	71	14	0.56462	757	-1

From Figure 5-6, the value of k_∞ for ISN = 2 lies very far from the average of the rest. If this data point is neglected, then $k_{diff} = 200\ pcm$ will be obtained, which is still the largest contributor of the parameters studied.

The rest of the modelling parameters show differences that are less than 10% compared to those due to the nuclear data. This therefore suggests that, except for ISN, when assessing the uncertainties, those that arise from the modelling parameters as studied in this work are not as significant as the uncertainty due to the nuclear data.

The NEWT results compare well with its corresponding KENO-VI (MG) results when PQ sets were used with differences of 1 pcm and 10 pcm for the FP and FA respectively.

Despite the different methods used, the neutron-nuclide contributors contributing to Δk due to the nuclear data, across all the calculations are either identical or statistically indistinguishable. The largest top contributor is $^{235}U_{nubar}$ for all calculations.

5.2 SENSITIVITY ANALYSIS

This section presents the results of the sensitivity and uncertainty analysis of individual input data and modelling methods in terms of the KENO-VI calculations. The individual parameters are given in detail in Section 4.5. The results analysis is based on the multiplication factor (k_∞) accompanied by a standard deviation and both KENO-VI in multi-group (MG) and continuous energy (CE) mode were used. The k_∞ results were considered accurate and optimised when the statistical uncertainty of about $\sigma = 0.00011$ was obtained within a reasonable computational time. Running with $NPG = 40000$, $GEN = 1000$ and $NSK = 150$ yielded a small statistical uncertainty and practical computational runtime in all the calculations.

The uncertainty analysis was performed using the TSUNAMI-3D (MG/ CE) and the SAMPLER codes. All the required convergence tests were diligently analysed and were all confirmed to have been achieved. To assess the uncertainties in the results, nuclear data uncertainties, uncertainties of individual input data, correlations coefficients and scatter plots of uncertain input data and histogram of the k_∞ were obtained and analysed for the study. This analysis was performed on a fuel assembly (FA) model of the Kozloduy-6 VVER-1000 reactor system with spacer grids included. The reason for using spacer grids was to have a model that represents a real assembly to be able to assess all the individual uncertain parameters that are involved in this system.

5.2.1 3D BASE MODEL FOR VVER-1000 FUEL ASSEMBLY

The results were calculated using the available cross-sections library based on the ENDF/B-VII.0 evaluation. The k_∞ results produced using KENO-VI are given in Table 5-4, together with the

associated standard deviations for the model. The standard deviation is defined as the statistical uncertainty due to the use of Monte Carlo methods to compute k_∞. For the KENO-VI (MG), the XSProc parameters in Table 5-3 were used with their optimum values in this analysis.

A VVER-1000 FA neutronic calculation was performed on the results reported by Bratton (Bratton, et al., 2014) for the OECD/NEA benchmark. A $k_\infty = 1.31990$ is given in the report and this value is 917 pcm away from the current k_∞. It should be noted that a deterministic code, which assumes an infinite z-axis was used for the results by Bratton. The comparison of these results with the current study is therefore restrained.

TABLE 5-4: EIGENVALUE FACTOR FOR k_∞

	Hot Zero Power		**Hot Full Power**	
Parameter	k_n results	σ	k_n results	σ
KENO – VI (CE)	1.31073	0.00010	1.29570	0.00011
KENO – VI (MG)	1.30689	0.00010	1.29143	0.00010

The resulting k_∞ from KENO-VI (MG) is $k_{diff} = 0.00384$ and $k_{diff} = 0.00427$ away from the corresponding KENO-VI (CE) at HZP and HFP respectively. These results reveal that the change in k_∞ between the CE and MG is approximately 40 times the statistical standard deviation at both HZP and HFP. Although both CE and MG cross-section processing are based on an identical ENDF/B data evaluation, there are differences in the processing of the cross-section during the XSProc part of the calculation, and the reduction from a CE based model to an MG model with 238 energy groups, hence the differences in the results. The k_∞ estimation for criticality calculations done using a CE method is therefore assumed to have higher accuracy than a MG method (Pirouzmand & Mohammadhasni, 2016).

The results between HZP and HFP has a difference of about $k_{diff} = 0.01550$, which is expected, due to the difference in the temperatures at HZP and HFP states of the system.

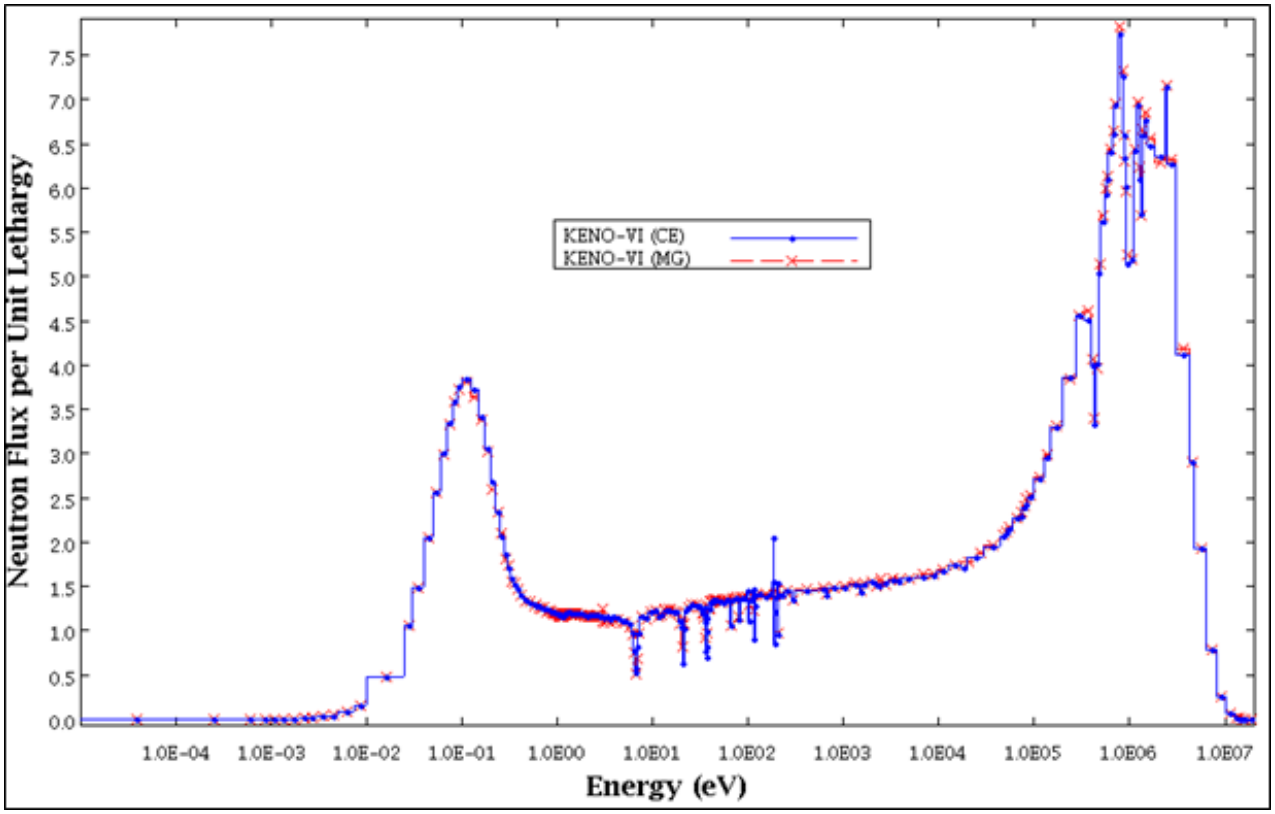

FIGURE 5-14: ENERGY DEPENDENT NEUTRON FLUX

The difference between the CE and MG calculation is further observed using the neutron flux distribution of the system as seen in Figure 5-14. The neutron energy flux spectrum is plotted as neutron flux per unit lethargy.

5.2.1.1 *Convergence of the fission source*

To provide confidence in the results of the KENO-VI calculations, the convergence of the Shannon entropy (H_{src}) of the fission source distribution and the multiplication factor (k) were evaluated and ensured. In terms of the fission source distribution, the KENO output file has an edit that indicates whether this parametric field is converged. By trial and error, a suitable choice of a sufficient number of initial skipped cycles and number of neutrons per generation where chosen to obtain convergence of the fission source. The convergence on k relied on the statistical accuracy required, and the appropriate number of active cycles were chosen to achieve this value. The output files were checked to analyse warning messages and to examine (analysis by plots) the behaviour of k_∞ and the Shannon entropy visually, as shown in Figure 5-15 and Figure 5-16 respectively.

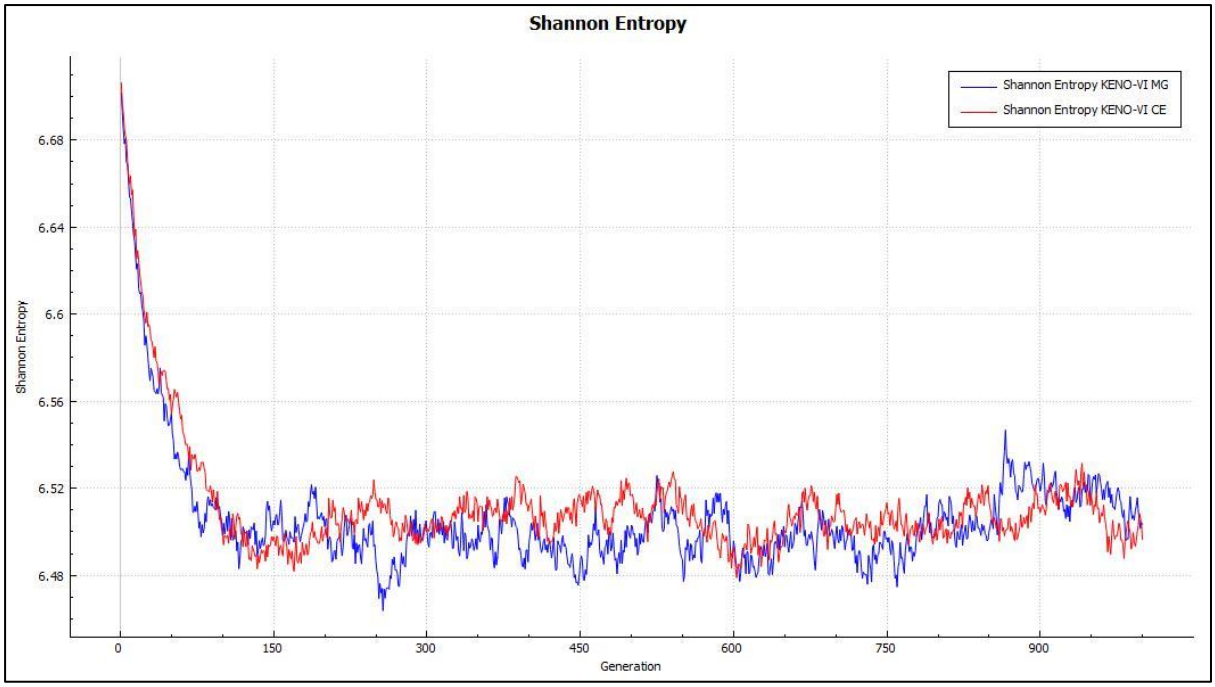

FIGURE 5-15: CONVERGENCE OF SHANNON ENTROPY

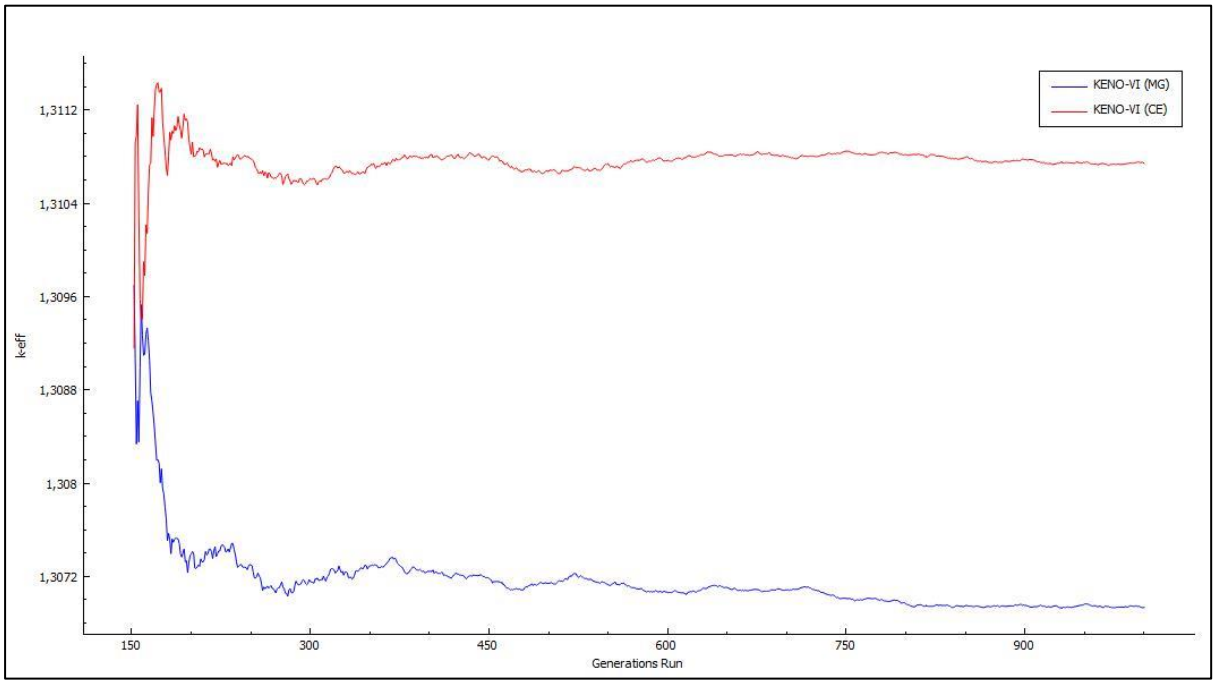

FIGURE 5-16: CONVERGENCE OF EIGENVALUE k

The three tests performed by KENO-VI to verify the fission source convergence were monitored in each KENO-VI calculation by examining the outputs as seen from Figure 5-17 to Figure 5-19. In each figure, each test states that it has passed to ensure that the source is converged.

Test 1: Is the final fission source converged? | *Test 1: passed*

Test 1 details:

Is the mean square posterior relative entropy < the center mean square Shannon entropy?

skipped	*msq*	*cmsq*
150	*1.20E-06*	*4.27E-05*
192	*1.18E-06*	*4.26E-05*
234	*1.16E-06*	*4.16E-05*
276	*1.16E-06*	*4.16E-05*
318	*1.17E-06*	*4.16E-05*
360	*1.17E-06*	*4.35E-05*
402	*1.17E-06*	*4.38E-05*
444	*1.17E-06*	*4.39E-05*
486	*1.17E-06*	*4.54E-05*
528	*1.17E-06*	*4.71E-05*
570	*1.19E-06*	*4.89E-05*
612	*1.19E-06*	*4.40E-05*
654	*1.21E-06*	*4.24E-05*
696	*1.14E-06*	*3.80E-05*
738	*1.13E-06*	*3.93E-05*
780	*1.09E-06*	*4.20E-05*
822	*1.13E-06*	*4.53E-05*
864	*1.06E-06*	*4.56E-05*
906	*1.11E-06*	*4.47E-05*
948	*9.58E-07*	*5.64E-05*

FIGURE 5-17: MSQ VS CMSQ

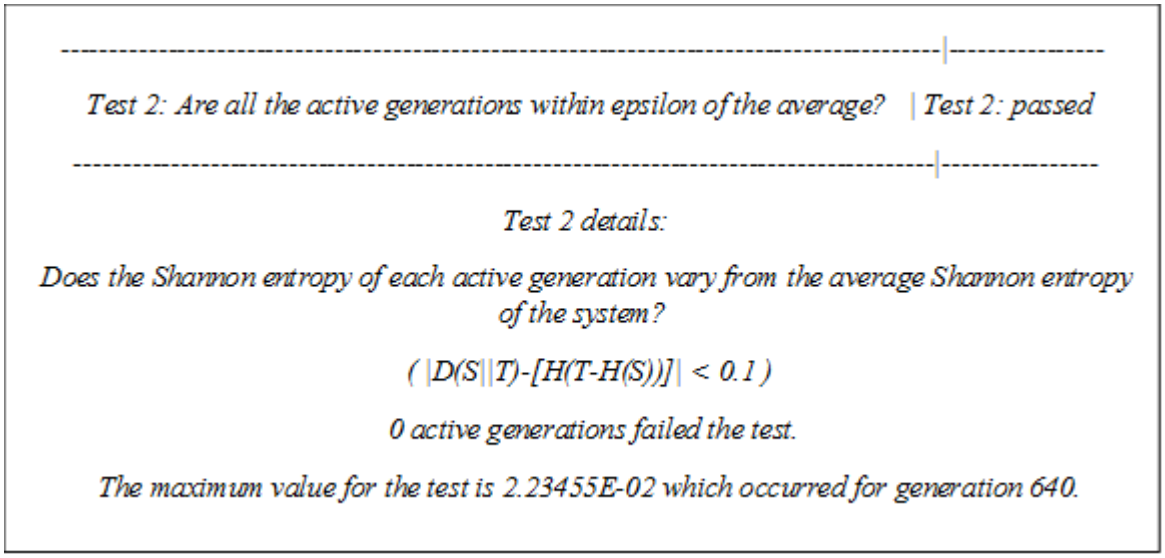

FIGURE 5-18: SHANNON ENTROPY OF EACH ACTIVE GENERATION

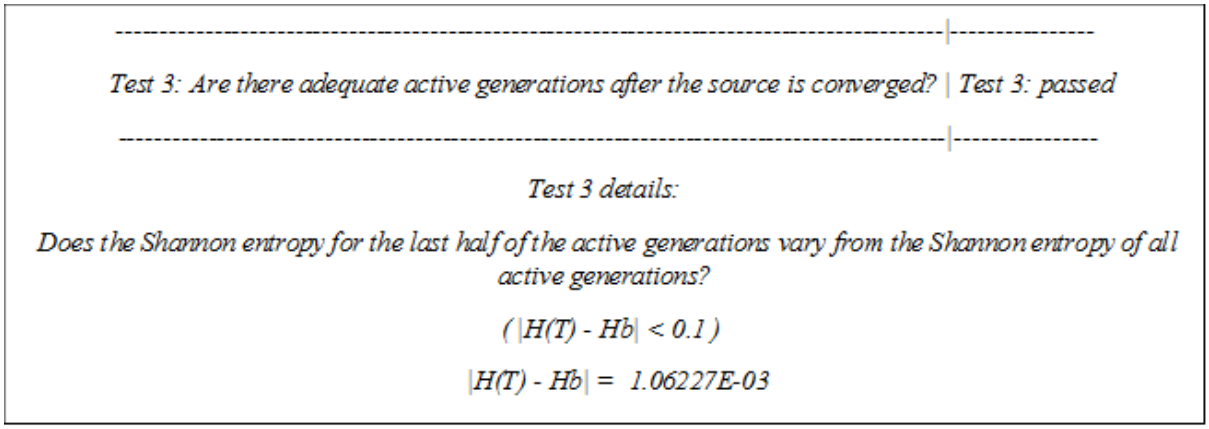

FIGURE 5-19: AVERAGE SHANNON ENTROPY

5.2.1.2 *Random number generations*

100 trials (individual KENO-VI calculations) were completed. The statistical uncertainty σ_i for each calculation was kept at about 0.00011, shown in column three of Table 5-5 for the first 10 calculations. The average of all these, calculated by summing all the individual KENO-VI calculations over 10 trials was 1.30677. Table 5-5 also lists the random number seeds, k_∞ and k_{diff} for the first 10 calculations. k_{diff} is calculated as the difference between the individual k_∞ values and the average k_∞ value. The consistency of the results of the individual calculation is displayed in Figure 5-20 by the frequency distribution plot of k_∞. The distribution is reasonably symmetrical and can be considered to approach a normal distribution for large N.

The average of $k_\infty = 1.30681$ was obtained for the 100 trials and the corresponding statistical uncertainty was calculated to be $\sigma = 0.00010$ using Eq (50). Using Eq (51), f was calculated to be 0.97. Since f was 0.97, it can therefore be seen that the statistical uncertainty due using different sequences of random number produces a value that equals the statistical uncertainty for the

individual calculations. Therefore, by keeping the individual statistical uncertainties low (around 10 pcm), the uncertainty due to the random number generation can be insignificant and therefore non-contributing to the uncertainty propagation.

TABLE 5-5: RESULTS FOR DIFFERENT RANDOM NUMBER SEEDS

Random number	k	σ_i	k_{diff}
F98B344A37F762A0	1.30669	0.00010	0.00017
C36D1611CB11116A	1.30671	0.00011	0.00030
510EA3859FE55D2E	1.30686	0.00013	0.00012
2F4C1E007FB91E67	1.30692	0.00010	0.00023
A60ECEF273A53FC3	1.30680	0.00010	0.00003
6E9F6F5F8939EFCE	1.30677	0.00010	0.00010
31B5A1E2910151E2	1.30659	0.00012	0.00020
7CA6FC5EF2FFB67D	1.30666	0.00010	0.00008
2FF85D32E5537687	1.30670	0.00011	0.00019
91A03F688CE610A7	1.30702	0.00010	0.00029

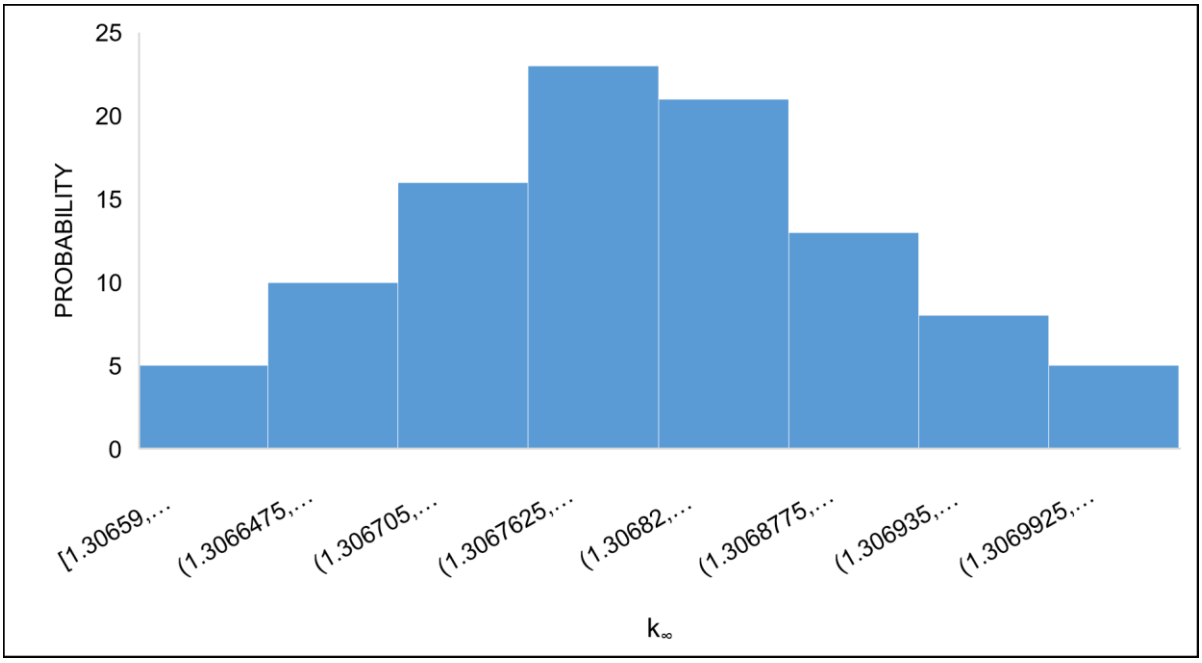

FIGURE 5-20: k FREQUENCY DISTRIBUTION OVER RANDOM NUMBERS

5.2.2 EVALUATION OF THE NUCLEAR DATA LIBRARIES

SCALE 6.2 is based on ENDF/B-VII.0 and ENDF/B-VII.1 cross-section libraries, therefore, a need to evaluate the cross-section libraries obtained from these two versions of ENDF/B-VII was seen. In addition to the ENDF/B-VII.0 libraries result, calculations with 56-, 252-group and CE libraries obtained from ENDF/B-VII.1 were therefore performed. Table 5-6 presents the k_∞ results obtained for the calculations with 56-, 252-MG and CE library that are based on the ENDF/B-VII.1 evaluation. When comparing the ENDF/B-VII.1 MG result with ENDF/B-VII.0 MG result, k_∞ becomes larger when the libraries from ENDF/B-VII.1 are used, leading to an underestimation of

the k_∞ results from ENDF/B-VII.0 results. The statistical uncertainty due to the use of Monte Carlo methods to compute k_∞, was 0.00010 in all the calculations.

TABLE 5-6: COMPARISON OF k_∞ RESULTS FOR NUCLEAR DATA LIBRARIES

Libraries	k_n results	MG ENDF/B-VII.0	CE ENDF/B-VII.0
56 MG -ENDF/B-VII.1	1.31002	313	71
252 MG -ENDF/B-VII.1	1.30858	169	215
CE -ENDF/B-VII.1	1.31065	376	8

As mentioned in Section 3.2, the MG libraries from ENDF/B-VII.1 provides a more detailed representation of the ^{238}U resonance structure and improved resonance self-shielding parameters to improve performance for light water reactor systems. Therefore, the results obtained using MG libraries from ENDF/B-VII.1 are expected to be more accurate than MG libraries from ENDF/B-VII.0. The results produced with 56-MG disagrees with the CE- ENDF/B-VII.0 k_∞ by 6 effective standard deviations and 252-group library differs by 20 effective standard deviations from the CE-ENDF/B-VII.0 k_∞ results. The k_∞ results from CE-ENDF/B-VII.1 compare much more favourably with the CE-ENDF/B-VII.0 results and is within a 1 standard deviation.

5.2.3 NUCLEAR DATA UNCERTAINTY ANALYSIS

The k_∞ uncertainties and sensitivities due to CE and MG cross-section libraries for nuclear data uncertainty propagation were performed using TSUNAMI-3D and SAMPLER. The uncertainties in k_∞ due to nuclear data from the ENDF/B-VII.0 cross-section libraries for the base case (both at HZP and HFP) given in Section 5.2.1 are provided in Table 5-7. The uncertainties were produced and compared between results from TSUNAMI-3D (CE), TSUNAMI-3D (MG) and SAMPLER (MG). This was done to compare uncertainty due to nuclear data obtained using a generalised perturbation theory-based method and statistical sampling-based methods described in Section 2.3.3.

For TSUNAMI-CE, the convergence of the $F^*(r)$ tallies are required before it can be applied to calculate the uncertainties. A $10 \times 10 \times 10$ mesh size with $NSK = 150$ was used as the parameters at which the $F^*(r)$ function over the scored tallies was converged. As it is seen in Figure 5-21, 0% $F^*(r)$ contains more than 50% uncertainty, therefore this confirms that the $F^*(r)$ tallies have converged and will accurately estimate the uncertainties due to nuclear data. The chosen mesh size was obtained from the recommendations given in a study by Sihlangu (Sihlangu, et al., 2018). It noted that the SCALE manual (Rearden & Jesse, 2016) also recommends a small mesh with skipped points between 50 and 100 NSK.

F(r) Convergence Statistics:*

WARNING: Of the 840 F(r) mesh intervals that scored tallies...*

21.79% of the F(r) tallies contain more than 5% uncertainty;*

1.90% of the F(r) tallies contain more than 10% uncertainty;*

0.36% of the F(r) tallies contain more than 20% uncertainty; and*

0.00% of the F(r) tallies contain more than 50% uncertainty.*

FIGURE 5-21: F*(R) CONVERGENCE

The impact of nuclear data uncertainties on the uncertainty in k_∞ using the individual methods ranges from 0.564%$\Delta k/k$ ($\Delta k = 740\,pcm$) to 0.576 %$\Delta k/k$ ($\Delta k = 753\,pcm$). The uncertainty in nuclear data for HZP and HFP calculations is in the same range. The uncertainties between the TSUNAMI-3D (CE), TSUNAMI-3D (MG) and SAMPLER (MG) codes appear to be in good agreement with each other. The results of Venturini (as shown in Section 5.1.2) was 670 pcm for the CZP FA. The equivalent results in Table 5-7 lies between 740 – 753 pcm. Possible reasons for this difference were discussed in Section 5.1.2.

TABLE 5-7: UNCERTAINTY IN $k_\infty(\%\Delta k/k)$

	Hot Zero Power		**Hot Full Power**	
Parameter	%Δk/k	Δk (pcm)	(%Δk/k)	Δk (pcm)
TSUNAMI-3D (CE)	0.56463	740	0.57071	739
TSUNAMI-3D (MG)	0.57586	753	0.58158	751
SAMPLER (MG)	0.57000	748	-	-

TABLE 5-8: TOP NEUTRON-NUCLIDE REACTION CONTRIBUTORS

	Hot Zero Power (HZP)		**Hot Full Power (HFP)**	
Nuclide	CE	238MG	CE	238MG
$^{235}U_{nubar}$	0.35023	0.35015	0.34941	0.34930
$^{238}U_{n,\gamma}$	0.29428	0.32236	0.30179	0.33135
$^{235}U_{n,\gamma}$	0.17138	0.17147	0.17132	0.17134
$^{235}U_{\chi}$	0.13951	0.14264	0.14390	0.14659
$^{235}U_{fission/n,\gamma}$	0.11577	0.11586	0.11557	0.11565
$^{56}Fe_{n,\gamma}$	0.10998	0.10133	0.11009	0.10147
$^{235}U_{fission}$	0.10072	0.10101	0.10297	0.10080
$^{238}U_{n,n'}$	0.09846	0.09158	0.10051	0.09221
$^{238}U_{nubar}$	0.06715	0.06727	0.06863	0.06880
$^{1}H_{n,\gamma}$	0.06330	0.06147	0.06202	0.06020

The TSUNAMI-3D results provide a ranking of important neutron-nuclide reaction contributors that contributes to the uncertainty due to nuclear data as seen in Table 5-8. SAMPLER does not present the neutron-nuclide reaction contributors. However, it can produce individual contributors due to

either the correlations between reactions of the same nuclide or correlations between different nuclides (Bostelmann, et al., 2017). These correlation results from SAMPLER are not presented in this study.

The two major neutron-nuclide reaction contributors to the result uncertainties are $^{235}U_{nubar}$ and $^{238}U_{n,\gamma}$ at the HZP and HFP state as found in Table 5-8. The neutron-nuclide reaction contributors were in the same order for all the calculations. The contributor ranked at 5 is between two different neutron-nuclide reaction contributors which are $^{235}U_{fissiom}$ and $^{235}U_{n,\gamma}$. This contributor pair is 3 times lower than the major contributor and can therefore be considered less important.

The $\%\,diff$ between the CE and MG neutron-nuclide reaction contributors is relatively small, except for the $^{238}U_{n,\gamma}$ (~9%). This difference may be due to the self-shielding treatment in the MG. It should be noted that neutron-nuclide reaction $^{238}U_{n,\gamma}$ is an important reaction in a thermal reactor system since the accuracy of the criticality results of a thermal nuclear system depends highly on this data for incident neutron energies from $0.0253\ eV$ to $25\ keV$.

Figure 5-22 shows the PDFs from 400 samples with k_∞ uncertainty due to nuclear data calculated with SAMPLER for the base model. The SAMPLER derived PDF shape resembles a normal distribution curve. The mean value of k_∞ was 1.30716 with a standard deviation of change in k_∞ of ~0.00745 (745 pcm) due to the nuclear data. This was equivalent to a $\%\Delta k/k$ of 0.57. The SAMPLER calculation was included for comparison purposes to quantify the precision of the TSUNAMI-3D estimation of the k uncertainty.

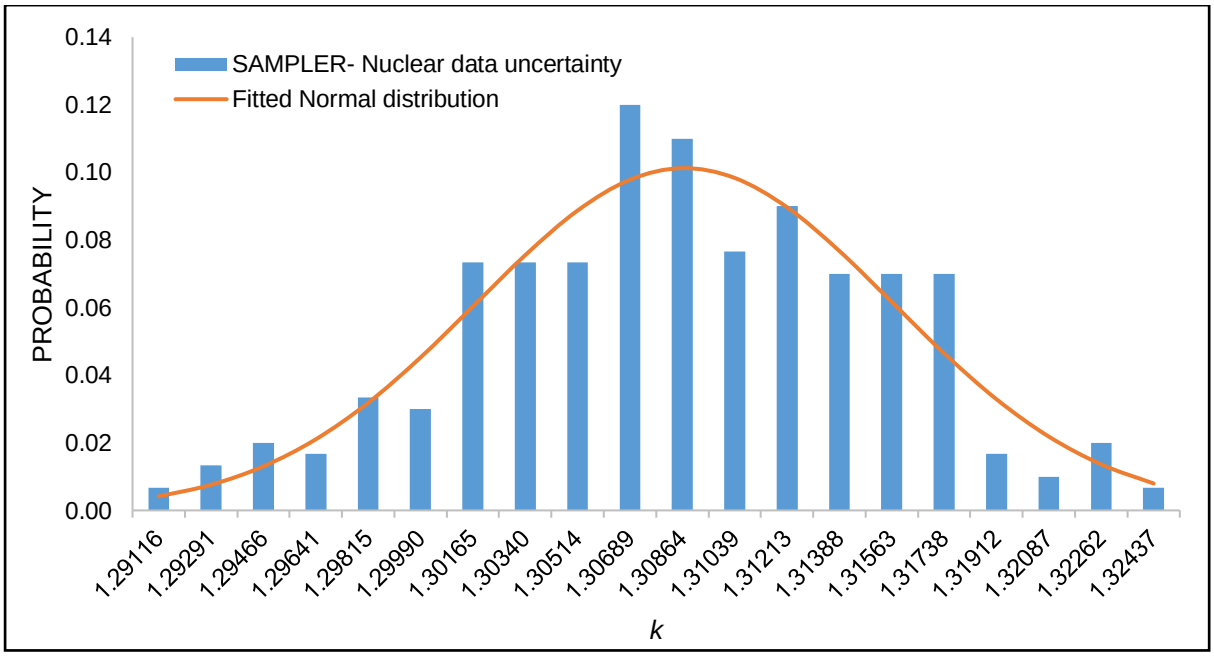

FIGURE 5-22: FREQUENCY PLOT FOR NUCLEAR DATA ANALSIS

To verify the accuracy and reliability of the 56- and 252-MG available cross-section libraries obtained from the ENDF/B-VII.1 evaluation, a further analysis was performed using TSUNAMI-3D. The uncertainty in k due to nuclear data provided by these libraries as well as the neutron-nuclide contributors are obtained. An uncertainty in k of about 0.575%$\Delta k/k$ (750 pcm) is obtained from the 56- and 252-MG available from ENDF/B-VII.1 library. This uncertainty compares well with the uncertainty of the cross-section libraries from ENDF/B-VII.0 which was about 0.568%$\Delta k/k$ (740 pcm) with a difference of about 10 pcm.

The results in Table 5-9 shows the ten neutron-nuclide reaction contributors that contribute to the uncertainty in k_∞ when each energy group set is used. When compared with results using the cross-section libraries from ENDF/B-VII.0 (Table 5-8), the neutron-nuclide reactions contributors have the same order of contribution.

TABLE 5-9: COMPARISON OF SCALE ENERGY GROUP LIBRARIES AT HZP

Nuclide	CE-ENDF/B-VII.1	56MG -ENDF/B-VII.1	252MG -ENDF/B-VII.1
$^{235}U_{nubar}$	0.35011	0.34997	0.35002
$^{238}U_{n,\gamma}$	0.29428	0.31810	0.30906
$^{235}U_{n,\gamma}$	0.17133	0.17107	0.17126
$^{235}U_{\chi}$	0.14104	0.14703	0.14012
$^{235}U_{fission/n,\gamma}$	0.11572	0.11584	0.11577
$^{56}Fe_{n,\gamma}$	0.10996	0.10130	0.10255
$^{235}U_{fission}$	0.10069	0.10092	0.10079
$^{238}U_{n,n'}$	0.09921	0.09090	0.08844
$^{238}U_{nubar}$	0.06750	0.06779	0.06757
$^{1}H_{n,\gamma}$	0.06325	0.06153	0.06172

Taking the neutron-nuclide reaction uncertainties calculated using MG-ENDF/B-VII.0, the $\%\ diff$ between the MG-ENDF/B-VII.0 and MG-ENDF/B-VII.1 of the neutron-nuclide reaction contributors' uncertainties are obtained and provided in Figure 5-23. The $\%\ diff$ between the MG-ENDF/B-VII.0 and MG-ENDF/B-VII.1 are relatively small, except for the $^{238}U_{n,\gamma}$ (~4%), $^{56}Fe_{n,\gamma}$ (~2%), $^{235}U_{\chi}$ (~3%), and $^{238}U_{n,n'}$ (~3). As can be seen in Table 5-8Figure 5-23, MG-ENDF/B-VII.0 produces large uncertainties due to $^{238}U_{n,\gamma}$ and $^{238}U_{n,n'}$ contributors and smaller uncertainties due to $^{235}U_{\chi}$ and $^{56}Fe_{n,\gamma}$ contributors than MG-ENDF/B-VII.1 libraries. However, considering the actual values in Table 5-8 and Table 5-9, these differences are not as significant as shown in Figure 5-23.

The energy-dependent sensitivity profiles of the top two neutron-nuclide reaction contributors obtained from the three available MG libraries used in TSUNAMI-3D calculations are shown in Figure 5-24.

Figure 5-24 compares the cross-section libraries' sensitivity profiles. The neutron-nuclide reaction sensitivities are closely identical across the three cross-section libraries. The 56-MG library has shorter and wider peaks in the energy interval between $0.1\,keV$ and $1.0\,keV$ due to the approximation of the broad group MG energy structure in the resonance range.

Similar accuracy with far fewer groups can lead to significant efficiency improvements for other computational procedures. Going forward, the 56 MG -ENDF/B-VII.1 and CE - ENDF/B-VII.1 will be used in the current study. In a later study, a transport depletion analysis is performed. A 56 MG -ENDF/B-VII.1 will therefore be appropriate for shorter execution time of these calculations.

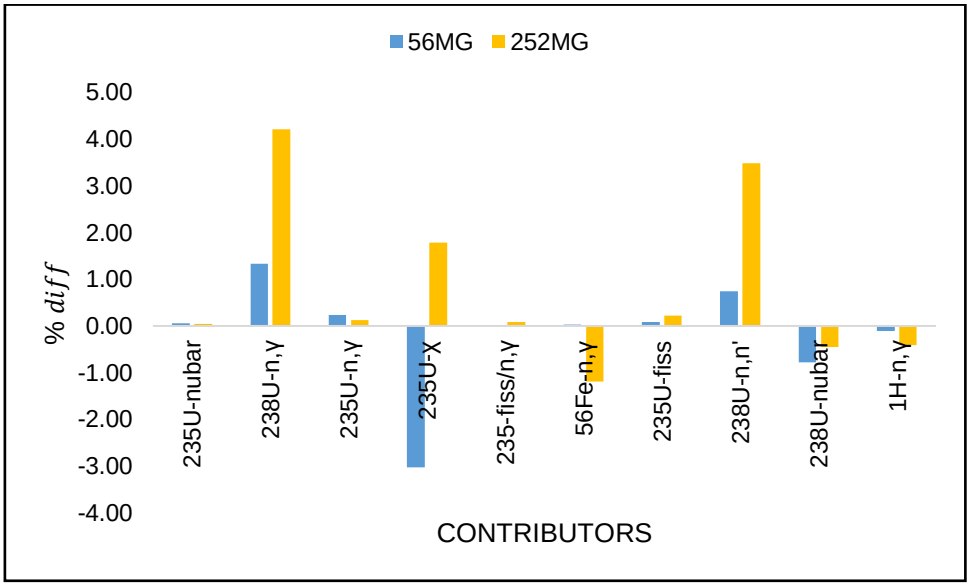

FIGURE 5-23: $\%\,diff$ OF THE CONTRIBUTORS BETWEEN DIFFERENT MG LIBRARY STRUCTURES

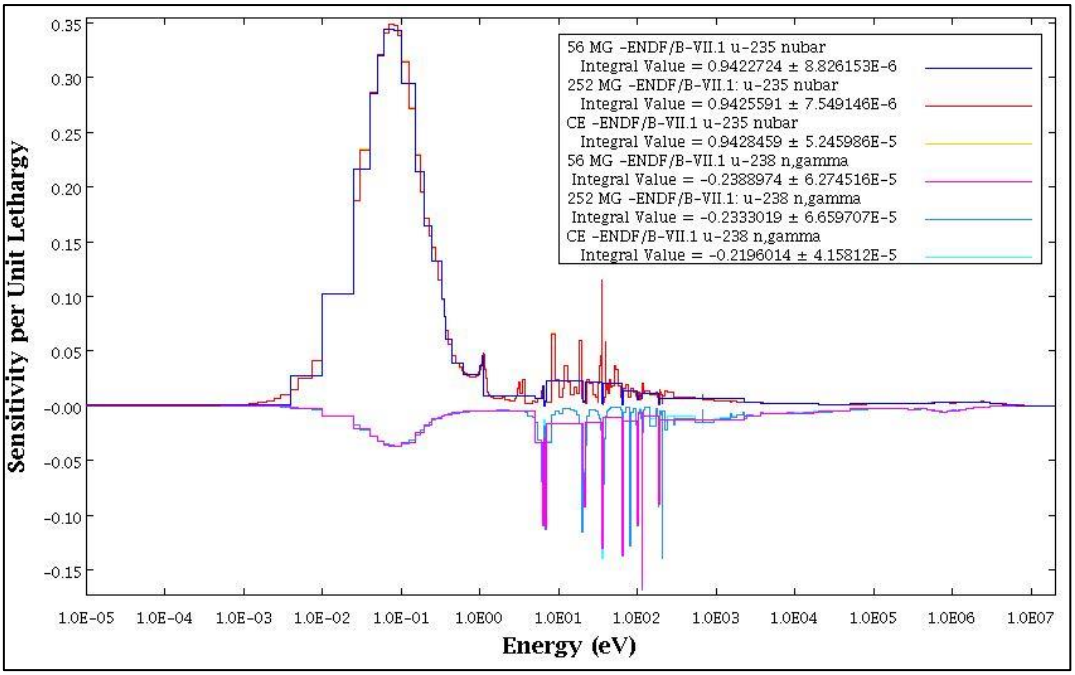

FIGURE 5-24: SDF PLOTS FOR $^{235}U_{nubar}$ AND $^{238}U_{n,gamma}$

5.2.4 GEOMETRY AND MATERIAL ANALYSES IN THE VVER-1000 MODEL

This section focuses on the geometry and material analyses of the spacer grids (SG). The results were performed using KENO-VI (CE) to accommodate analysis for a heterogeneous VVER-1000 FA model without the self-shielding treatment and group collapsing required in the KENO-VI (MG).

5.2.4.1 *Modelling of the spacer grid*

Table 5-10 shows the results of the HMB, HTB and HMA models of the SG in the FA. The HTB, HMA and HMB models were discussed in Section 4.5.3.1. The HTB model was analysed because, in an HTB calculation, the specification of materials and geometry of the model are treated accurately. Such treatment leads to accurate results for k_{∞}. Since the HMB model was used as a base model, to verify the accuracy of modelling the SGs in that manner, results of this base model and results obtained with HTB model were compared with each other.

TABLE 5-10: k RESULTS FOR SG MODELS

Parameter	k_n	k_{diff} (pcm)
HMB	1.31073	-
HTB	1.31084	11
HMA	1.30834	231

The difference in the results between the base model (HMB model) and the HMA model as given on Table 5-10 was at about 231 pcm and the difference with the HTB model was 11 pcm. The energy spectrum of the three models in Figure 5-25 shows that in the thermal region the peak is more pronounced for the HMA model. On the other hand, the HMB model is very close (by visual inspection, and also by the change in reported above) to the HTB model. A possible explanation

could be that the fast and epithermal neutrons are experiencing a higher absorption in the HTB and HMB models. This could be due to the lumping of the SGs in distinct bands. Since the HTB model is the closest representation to the physical system, this proves that the base model for modelling the SG is accurate. In the study by Tran and Pazirandeh described in Section 4.5.3.1, the difference of the k results between the HMB model with the HTB and HMA models were a bit larger compared to what they were in this study.

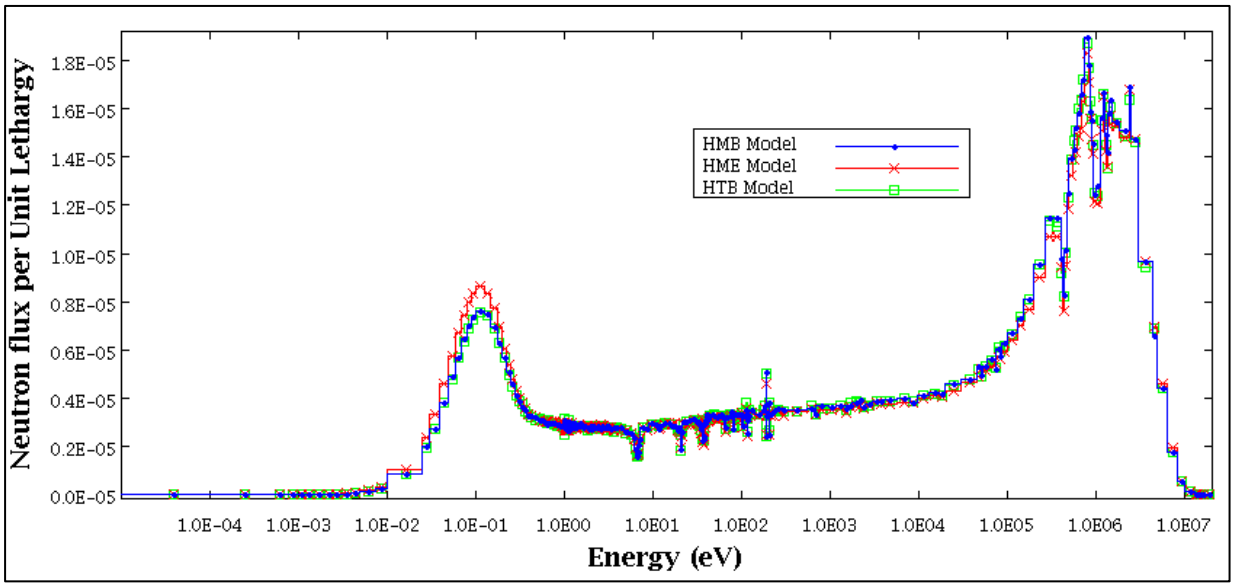

FIGURE 5-25: ENERGY DEPENDENT NEUTRON FLUX

The nuclide that is dominant in the SG materials is the ^{56}Fe. Since $^{56}Fe_{n,\gamma}$ is one of the top ten neutron-nuclide contributors that contributes to the uncertainties in the k as seen in Table 5-8, part of the uncertainties in k are also due to the presence of the spacer grid of the system. A TSUNAMI-3D calculation was therefore performed to obtain the impact of this neutron-nuclide reaction when each model is used. The uncertainties of this nuclide are given in units of $\%\Delta k/k$ from the TSUNAMI-3D output. To analyse them in pcm, $\%\Delta k/k$ was converted to Δk in pcm using Eq (63). The impact of $^{56}Fe_{n,\gamma}$ was around 140 pcm for the HTB and HMB model, while for HMA, the impact was around 160 pcm. The uncertainty in k due to this nuclide was a bit larger when the HMA model is used. This is further observed in the sensitivity coefficients data plot of this neutron-nuclide reaction as shown in Figure 5-26. The sensitivity of this neutron-nuclide reaction is most pronounced in the thermal to intermediate energy regions. Although the uncertainty due to ^{56}Fe is affected by the type SG modelling used, the difference in the total uncertainty is relatively small between the three models.

As can be seen above, the results for the HMA model are somewhat underestimated. However, for calculations that requires the use of a deterministic code, this model is appropriate. In a future study where the NEWT code results are desired, the HMA model will therefore be used to account for the SGs in the system.

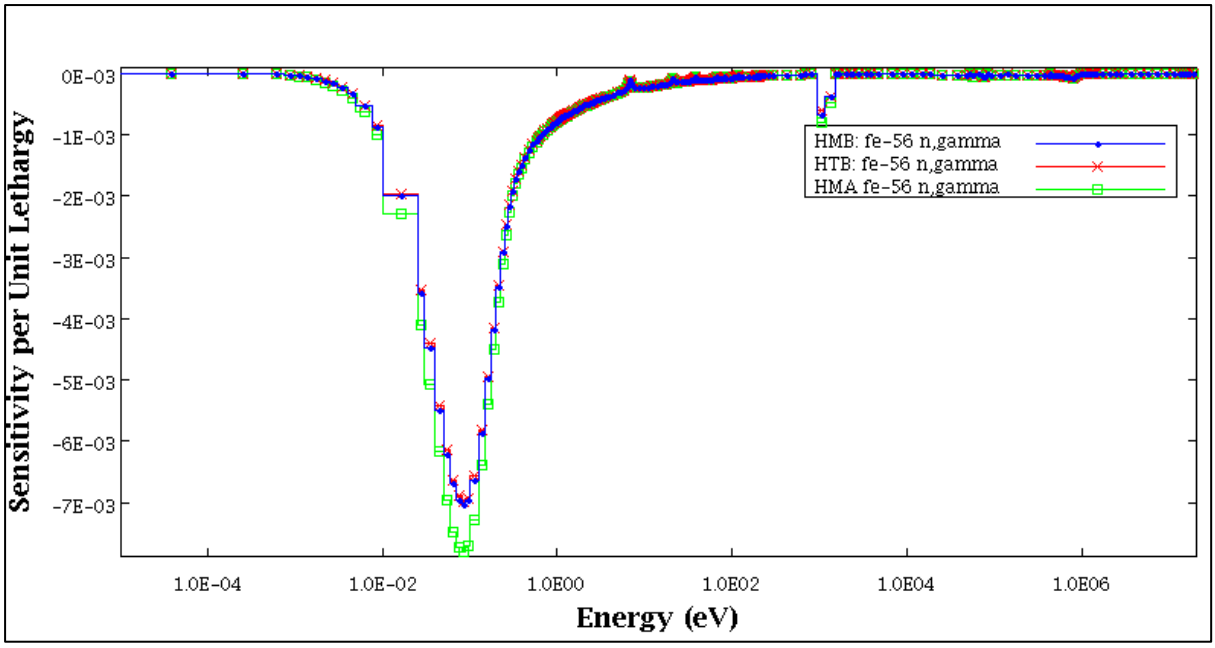

FIGURE 5-26: SDF PLOTS FOR $^{56}Fe_{n,\gamma}$

5.2.4.2 *Spacer grid dimensions*

A test to see the effect of varying the SG dimensions was performed on the HTB model to quantify the uncertainties of using a different value of the SG dimensions. The values for k are shown in Table 5-11 for the different SG heights tested.

TABLE 5-11: VARIATION OF THE SG HEIGHT

h (cm)	k	k_{diff} (pcm)
1.5	1.31308	150
2.5	1.31238	74
3.0	1.31084	0.0
3.5	1.30999	-85
4.5	1.30884	-115

The difference in k_∞ between consecutive data points ranged from 74 pcm to 150 pcm, with the difference between the end points being 424 pcm. The statistical uncertainty due to each calculation due to the Monte-Carlo method was about 15 pcm in each calculation. The choice of the SG height gives a significant difference in k_∞ compared to the statistical uncertainty and in all cases this is larger than 3σ. A change of k_∞ results that is not within a 3σ is normally taken to be the point at which deviations start to become significant. Assuming a normal distribution given by the function in Eq (66) of the results with the same statistical uncertainty, the distribution of the results is shown in Figure 5-27 and Figure 5-28.

$$f(x) = \frac{1}{\sqrt{2\pi\sigma}} e^{-\frac{(x-\mu)^2}{2\sigma^2}} \quad (66)$$

Figure 5-27 graphically reveals that the standard deviation of the change in k_∞ between the nominal, SGH=2.5 and SGH=3.4 cm cases is not within the <3σ. As the SG height is further decreased/ increased, the change in k_∞ becomes further outside of <3σ as seen in Figure 5-28.

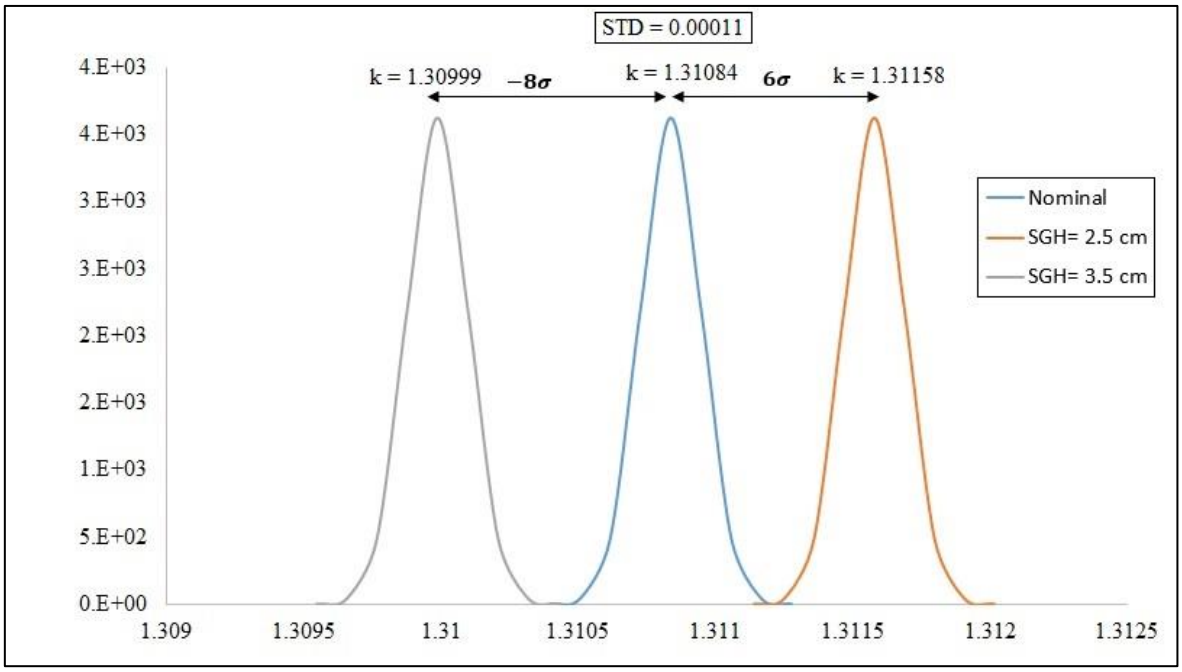

FIGURE 5-27: NORMAL DISTRIBUTION OF k FOR SG HEIGHTS

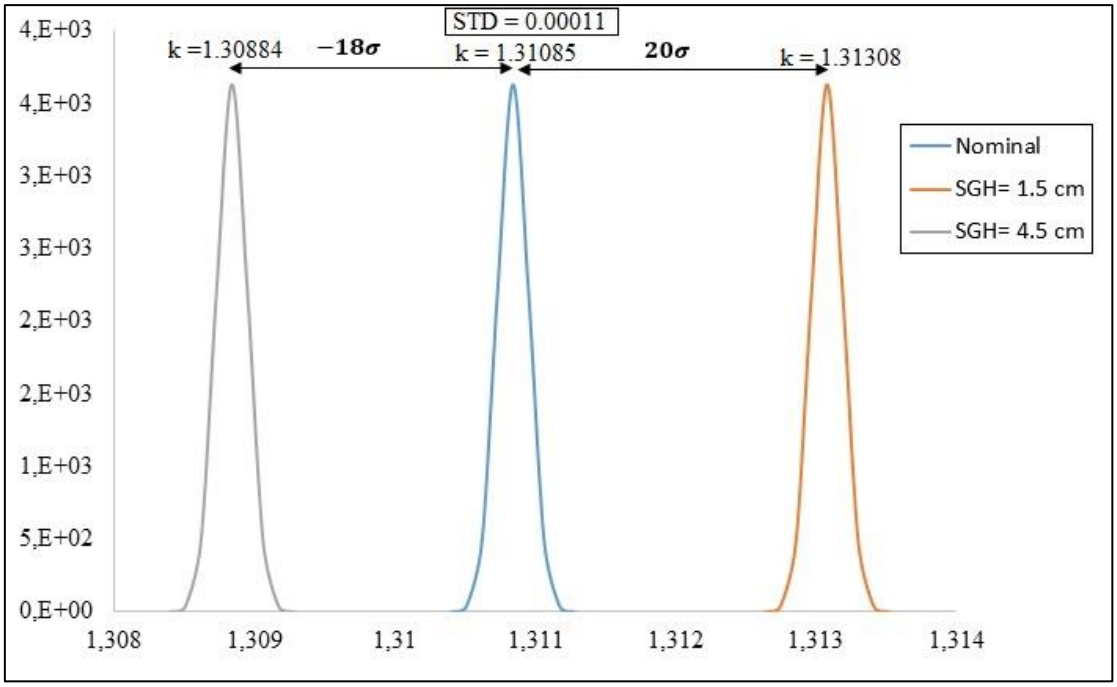

FIGURE 5-28: NORMAL DRISTRIBUTION OF k FOR SG HEIGHTS

Since varying the thickness of the spacer grids changes the level of heterogeneity of the system, the neutron means free paths are affected, and the criticality results will also be affected. This results in a significant effect in the thermal end of the spectrum, where the neutron mean free part

is short enough to distinguish the details of the geometry. The effect of the heterogeneity of the SG in the model is further displayed in Figure 5-29 which shows the sensitivity of the absorption rate as a function of energy over the two different SG-Heights.

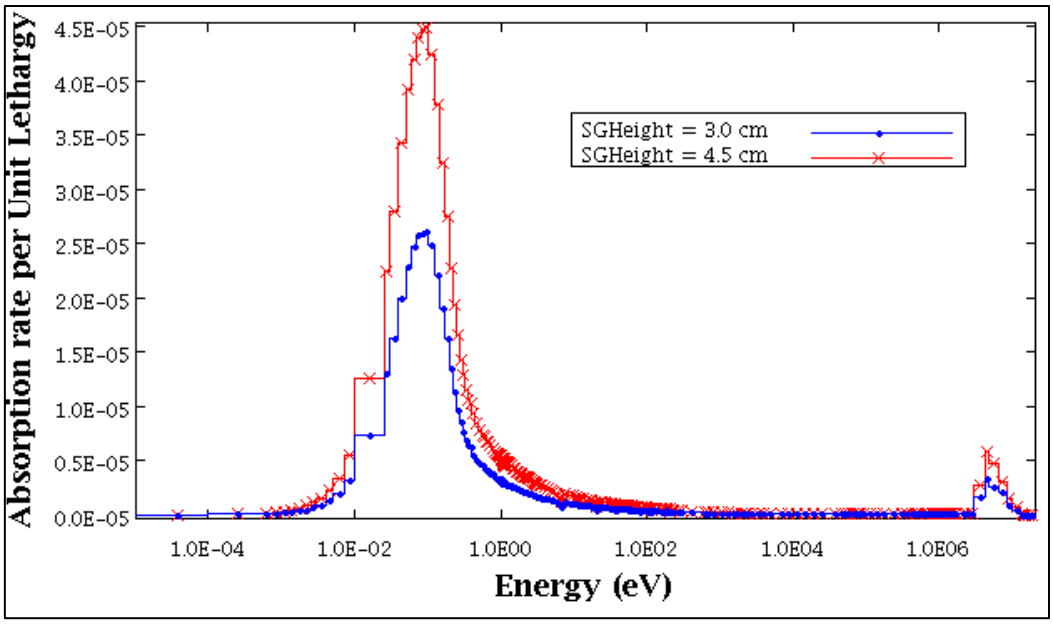

FIGURE 5-29: ENERGY DEPENDENT ABSORPTION RATE SPECTRUM

Figure 5-30 shows the difference in the $^{56}Fe_{n,\gamma}$ sensitivity coefficients between SG height at 3.0 cm and 4.5 cm. The impact of $^{56}Fe_{n,\gamma}$ in the results are 149 and 135 pcm for the SG height at 3.0 cm and 4.5 cm respectively. The differences in these uncertainties due to $^{56}Fe_{n,\gamma}$ between SG height at 3 cm and 4.5 cm were observed to be relatively small.

It is noted that this study on the spacer grid was performed because the SG height was not defined in the benchmark specification. It was therefore informative to compare the results using different heights. The analysis was not intended to verify the design of the VVER-1000 FA but to study the uncertainties that SGs introduces on the system.

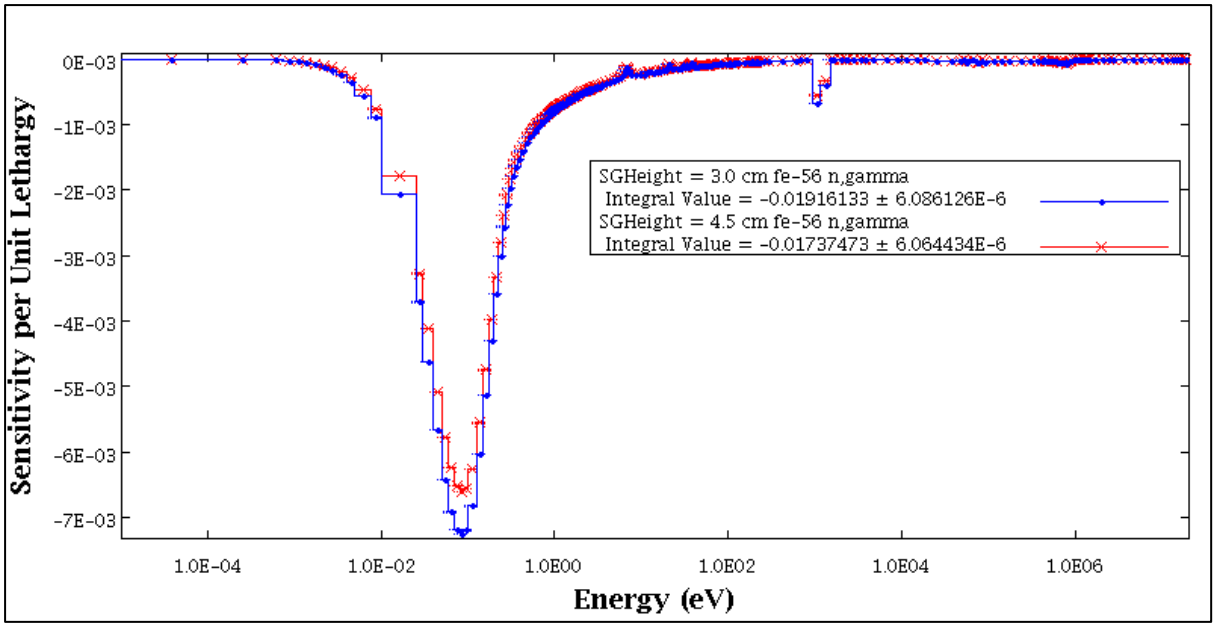

FIGURE 5-30: SDF PLOTS FOR $^{56}Fe_{n,\gamma}$

5.2.4.3 *Spacer grid material uncertainty*

The effects of the SG material are analysed in this section, by comparing results obtained from using either a stainless steel (SS), zirconium alloy or water as the SG material. Using water is the same as there being no SG present, and the input file retains its structure with the only change being the SG material definition. The k_∞ results were large for materials other than stainless steel. This is because certain important elements of water and zirconium-alloy elements have lower thermal absorption cross-sections than the stainless-steel alloy.

TABLE 5-12: POSSIBLE SG MATERIALS

Material	k_∞	k_{diff} **(pcm)**
SS-SG	1.31073	-
Water-SG	1.34010	2533
E110-SG	1.33468	1991

There is a difference in the energy spectra of the calculations with the different materials for the SG. The flux for the calculation with water as SG material has a higher peak in the thermal range than with the stainless steel and zirconium alloy material calculations. It is known that hydrogen in water serves as a better moderator than the heavier elements in the SG materials. Therefore, by replacing the SG with water will result in a higher peak in the thermal range.

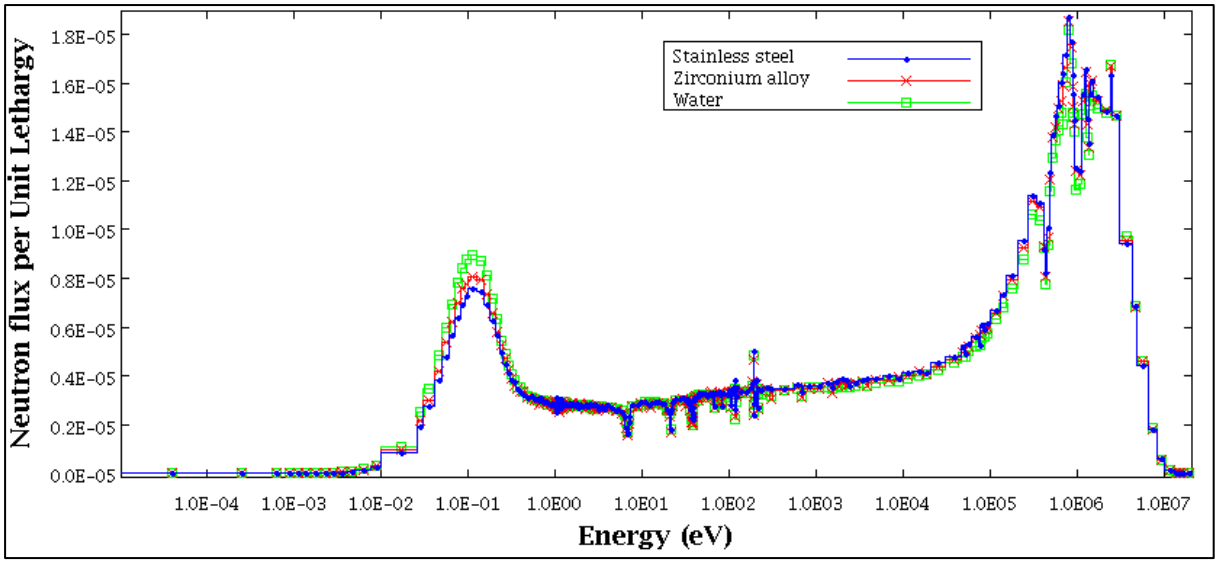

FIGURE 5-31: ENERGY DEPENDENT NEUTRON FLUX SPECTRUM

The nuclides that are dominant in these SGs materials are ^{56}Fe, ^{1}H and ^{90}Zr for stainless steel, water and E110 respectively. It must be noted that both $^{56}Fe_{n,\gamma}$ and $^{1}H_{n,\gamma}$ neutron-nuclide reactions are listed as part the top 10 contributors of the uncertainties in k.

Three individual TSUNAMI-3D calculations were performed, where, one had stainless steel, the second had no SG, meaning that the moderator occupied the location of the SGs and the last calculation had E110 material as a replacement for the stainless-steel material. This was done to obtain the impact of these dominant nuclides in each calculation to observe the uncertainty in changing SG material.

For the calculation where stainless steel (SS) is used as the SG material, the impact of $^{56}Fe_{n,\gamma}$ reaction was about 150 pcm, while for the cases where either moderator or E110 was used the impact was about 60 pcm. The impact of the $^{1}H_{n,\gamma}$ reaction was about 65 pcm in all three calculations.

The sensitivity coefficient data plots of the dominant nuclides of each of the SG materials are shown from Figure 5-32 to Figure 5-34. The following sensitivities were observed for each of the dominant nuclides in each calculation to see the change in the sensitivities as the system is altered. The sensitivity profiles (SDF plots) for $^{56}Fe_{n,\gamma}$ and $^{1}H_{n,\gamma}$ are most pronounced in the thermal to intermediate energy regions as can be seen in Figure 5-32 and Figure 5-33. The impact of the $^{90}Zr_{n,\gamma}$ reaction is very small (16 pcm) in all three calculations. Since zirconium isotopes have resonances in the medium energy range, the resonance absorption of these isotopes would be considered, even though absorption by zirconium isotopes is low. This can be observed in Figure 5-34.

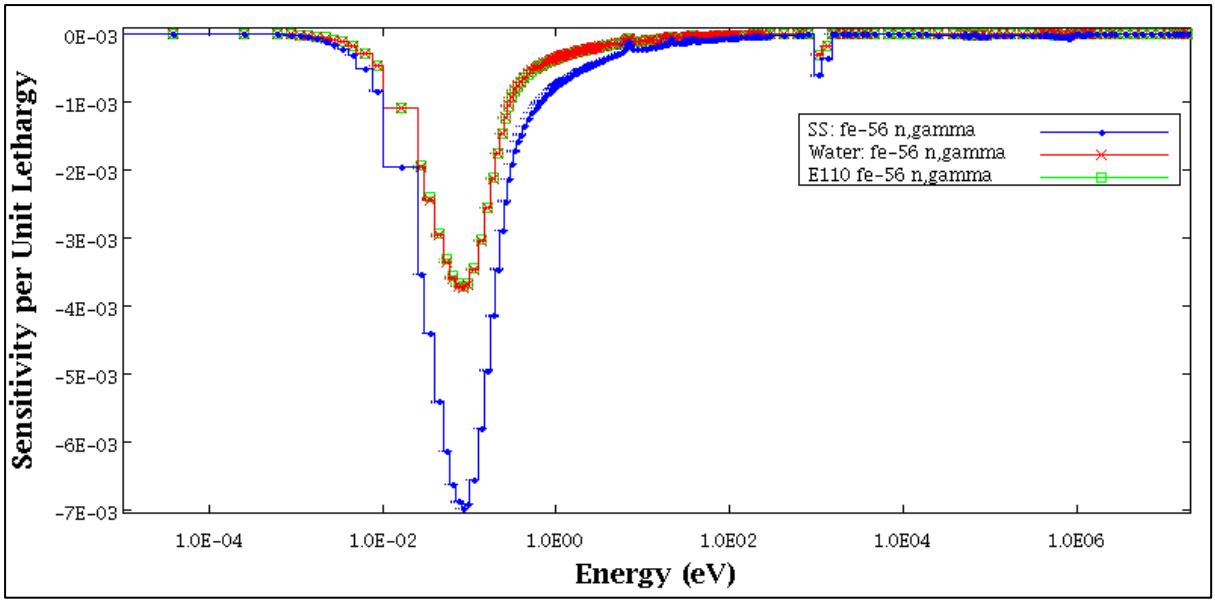

FIGURE 5-32: SDF PLOTS FOR $^{56}Fe_{n,\gamma}$

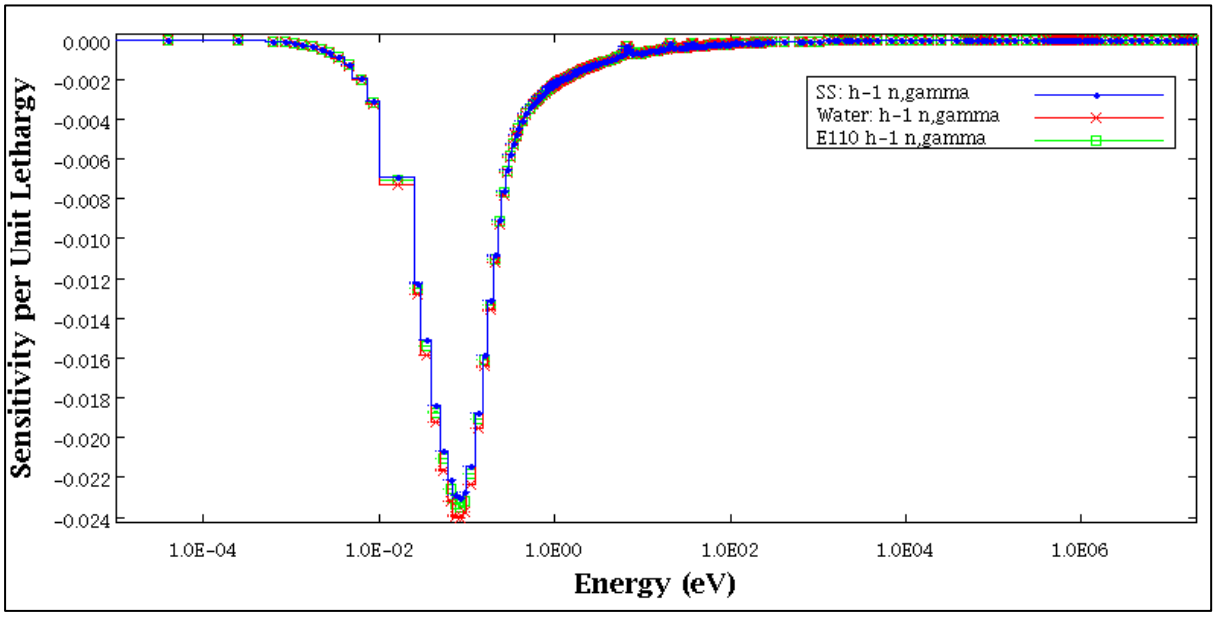

FIGURE 5-33: SDF PLOTS FOR $^{1}H_{n,\gamma}$

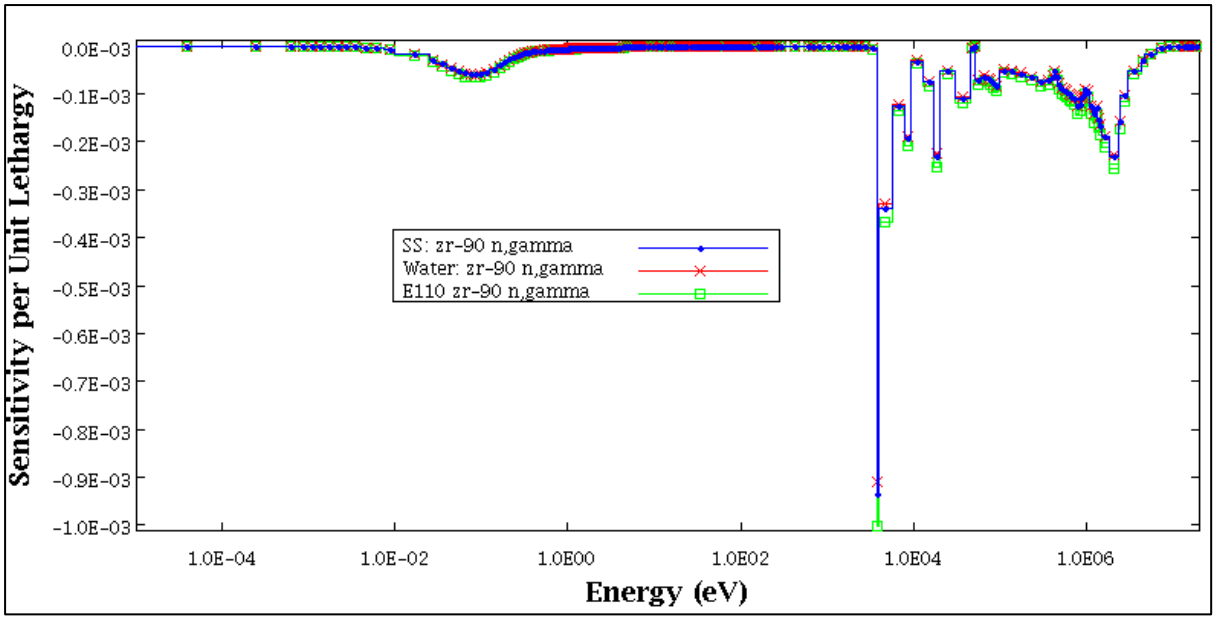

FIGURE 5-34: SDF PLOTS FOR $^{90}Zr_{n,\gamma}$

Nuclides such as Fe have many sharp resonances in the medium energy range and their resonance absorption effects should also be considered.

It was mentioned in Section 4.5.3.3 that both stainless steel and zirconium alloy were used as SG materials for different reactor designs of the VVER type. It was therefore informative to compare the results using stainless steel with those using Zr-alloy for the SG material. Since the OECD/NEA benchmark definition was clear in the definition of the SG material, i.e. stainless steel, this aspect of the study was not considered further.

5.2.5 SENSITIVITY DUE TO THE MANUFACTURING TOLERANCES ON THE RESULTS

Table 5-13 shows the sensitivity results due to the tolerance limits for the important parameters defined in Section 4.5.4.

The results were calculated for the lower and upper tolerance limits and are analysed by comparing the k_∞ results obtained from the individual parameters to the k_∞ of the base model results reported in Section 5.2.1 ($k_{diff} = k_i - k_b$). The last column of Table 5-13 ranks the parameters according to the change from the base model k_∞ results. The largest k_∞ sensitivity occurs for manufacturing tolerance of the clad OD and fuel ^{235}U enrichment. These variations have values of about 150 - 300 pcm.

The enrichment of ^{235}U (w/o) has proved to be the most sensitive parameter in terms of the results. The sensitivity of this parameter is observed to be even larger than the sensitivities that were obtained in the referenced study (Canuti, et al., 2012).

TABLE 5-13: SENSITIVITIES ON k_∞ RESULTS

Parameter	limits	k_{diff} (pcm)	Canuti	Rank
IHOD (cm)	+0.003	-36	80	6
ρ_{fuel} (g/cm^3)	+0.300	57	-151	5
FPOD (cm)	-0.003	-31	50	7
GOD (cm)	+0.006	-80	31	4
COD (cm)	-0.005	-178	-135	2
	+0.005	182	132	2
^{235}U w/o	-0.050	276	168	1
	+0.050	-292	173	1
^{235}U w/o	-0.050	93	-	3
	+0.050	-84	-	3
SG Height (cm)	-0.005	10	-	8
	+0.005	5	-	8

The sensitivity results for the clad OD have proved to be consistent with the results obtained from the referenced study as it can be seen in Table 5-13 (Canuti, et al., 2012). Because the clad OD introduced the second largest sensitivity to the results, the sensitivity of the clad OD was quantified using SAMPLER. However, each pin was perturbed individually, using a uniform distribution for each pin. The details of this rationale are given in Section 4.5.5.1. The uncertainty in k_∞ due to the perturbed clad OD was 14 pcm (0.01%) which is smaller than the value of 180 pcm given in Table 5-13. For the value given in Table 5-13, the clad OD were collectively considered to have a single tolerance range. Since the inner hole, fuel and gap diameter exhibited relatively small sensitivities, no further quantification was performed for these ODs. It was assumed that when considering each of these as individual elements, as was done for the clad OD, the uncertainty would be smaller than 14 pcm, which was found for the clad OD.

Table 5-14 shows the sensitivity results for the temperature and density of the moderator in the system. As was mentioned in Section 4.5.5.3, the nominal, upper and lower value of the temperature (±2K) each have a corresponding density, which in turn is also given a tolerance of ±0.002 (g/cm^3).

The k_{diff} in column 4 of Table 5-14 was calculated for the tolerance limits of the densities for the individual temperatures, by comparing the k results obtained from using the actual density ($k_{diff} = k_{actual} - k_{\rho_b}$).

The observations that were made from the moderator temperature/density analysis were that:

- The sensitivities in k_∞ due to the lower and upper limit of the temperature were -60 and 99 pcm respectively.

- Given a temperature, with a density that has a lower and upper limit, the sensitivity in k_∞ calculated at the lower and upper limit bound of the density is about ±40 pcm.
- Comparing the highest density to the lowest density within the temperature bounds gives a difference of about 233 pcm, which can be a significant effect.

TABLE 5-14: TEMPERATURE AND DENSITY SENSITIVITY

T (K)	ρ_{H_2O} limits	k_∞	k_{diff} (pcm)
550.15	Nominal	1.31129	
	-0.002	1.31088	+41
	+0.002	1.31169	-40
552.15	Nominal	1.31069	
	-0.002	1.31027	+42
	+0.002	1.31093	-24
554.15	Nominal	1.30970	
	-0.002	1.30936	34
	+0.002	1.31030	-60

Since the density is related to the temperature of the moderator as discussed in Section 4.5.5.3., the combined effect of the density and the temperature must be considered. The uncertainty that is due to both parameters must be propagated.

The FA system has more than one material, and the sensitivity due to the change in the density of the other available materials in the system was analysed. Table 4-3 shows a list of all the materials that are involved in this study. The sensitivity analysis was performed individually for each material and since their tolerances were not given in the OECD/NEA benchmark, the tolerance for the fuel was used for the other materials as well. The sensitivity results for the all the material densities in the system was less than 10 pcm, except for the water and fuel density.

The sensitivity due to the fuel density was 57 pcm. The referenced study reveals that the fuel density had an effect of about 151 pcm for a fuel calculation. The sensitivity appears to become small for the FA calculation, however.

From this manufacturing tolerance analysis, it was observed that, the parameters that introduce substantial difference in the result are ^{235}U w/o, UO_2 density and moderator temperature/density (T_{H_2O}/ρ_{H_2O}) and that these should therefore be quantified alongside with the nuclear data.

5.3 UNCERTAINTY QUANTIFICATION

To quantify the uncertainties in the Kozloduy-6 VVER-1000 system's criticality results, all the uncertain input data that have proved to contribute substantially to the results are propagated. SAMPLER/KENO-VI using the 56-MG library was used to propagate all the input data. Since the

propagated parameters includes axial geometry variation that can only be treated in a 3D code, NEWT was eliminated from this analysis. This is due to the restriction in the geometry definition in NEWT. Therefore, the parameters that were optimised for NEWT in Section 5.1 were not applicable in this section but will be relevant to the studies for the fuel depletion analysis and the UAM contribution. The optimised XSProc parameters are applicable in the current analysis since a multi-group library was used.

As shown in Table 4-8 in Chapter 4, the uncertain input data were divided into two groups. Because of the nature of the parameters in group one, this input data has specific values assigned to them and are mostly integers. This means that these parameters cannot be propagated by random sampling. Among the parameters in this group, the spacer grid height has shown a significant sensitivity. Two spacer grid heights were therefore chosen, one 3 cm (nominal) and the other 4cm. The other parameters in this group showed changes of less than 50 pcm in k_∞. Since these differences were small compared to the uncertainty due to nuclear data, their contribution to the uncertainty of k_∞ were not further considered. Only their optimal values were used.

Regarding group two, the sensitivities studies performed earlier in the study have shown that nuclear data, ^{235}U enrichment (w/o), UO_2 density (ρ_{fuel}) and moderator temperature/density (T_{H_2O}/ρ_{H_2O}) and are the most important parameters. The SZF and outer radius of the inner hole, fuel, gap and clad uncertainties were much less important and essentially insignificant. Therefore, these parameters do not need to be propagated. With regards to the random numbers, the effect of using a different number seed was less as well.

Two sets of SAMPLER calculations were performed using the two spacer grid heights. The first set of calculations had an SG height of 3 cm (reference height) and the second calculation with an SG height of 4 cm.

TABLE 5-15: k QUANTIFIED UNCERTAINTIES

Value	***SG=3.0***	***SG=4.0 cm***
Mean	1.31005	1.30111
Δk	0.00769	0.00767
Minimum	1.30236	1.29344
Maximum	1.31774	1.30878
$\%\Delta k/k$	0.58695	0.59018

Figure 5-36 shows the scatter plot for ^{235}U w/o over 300 samples. Over 300 samples, the perturbed values of the input data showed a good distribution between the limits set. This implies that the number of samples were enough to obtain good statistical analysis of the results. The running averages of ^{235}U w/o is shown in Figure 5-37 and can be considered to have stabilised

after 150 samples. This means that after 150 samples the perturbed values of the input data would also have shown a good distribution as when 300 samples were taken.

The total quantified uncertainty of the k_∞ results due to the overall input data uncertainty mentioned in Table 5-15 was 0.56%. The uncertainty was 769 pcm (0.587 $\%\Delta k/k$) and 767 pcm (0.590 $\%\Delta k/k$) at SG H = 3.0 cm and 4.0 cm respectively. This uncertainty compares well with the uncertainty of 730 pcm (0.56) due to nuclear data and this implies that the nuclear data uncertainty remains the large contributor to uncertainties in the neutronics results. Whilst the change in k due to using SGH = 3.0 and 4.0 cm was about 0.590$\%\Delta k/k$, no difference was reflected in the uncertainty of k when all the input uncertainties were propagated. One can therefore infer that the parameters listed in Group 1 of Table 4-8 does not significantly influence the propagated uncertainties. The parameters of Group 2 of Table 4-8, however, increase the uncertainty by 38 pcm.

The three parameters in Group 1 that were propagated were ^{235}U w/o, ρ_{fuel} and T_{H_2O}/ρ_{H_2O}. The maximum sensitivities using the tolerances as the limits were found to be 296, 57 and 233 pcm as shown in Section 5.2.5 for the three parameters respectively.

As a starting guess, one may assume that the total uncertainty be composed of a sum of the three individual uncertainties and the nuclear data uncertainty by Eq (67):

$$\Delta k = \sqrt{\Delta a^2 + \Delta b^2 + \Delta c^2 + \Delta d^2} \tag{67}$$

where a, b, c and d refer to the input parameters chosen for uncertainty propagation including nuclear data uncertainty.

However, since the uncertainties due to ^{235}U w/o, ρ_{fuel} and T_{H_2O}/ρ_{H_2O} were sampled using a uniform distribution, it can also be assumed arbitrarily that the individual contributions are a factor α of the given uncertainty, i.e. 197, 38 and 155 pcm respectively. Assuming $\alpha = \frac{2}{3}$, the total uncertainty will be:

$$\Delta k = \sqrt{730^2 + 197^2 + 38^2 + 155^2} = 773\ pcm \tag{68}$$

It is assumed that the uncertainty due to nuclear data yields the best value and there is no need to adjust this value by multiplying it with α.

If $\alpha = 1$, then the total uncertainty becomes:

$$\Delta k = \sqrt{730^2 + 296^2 + 57^2 + 233^2} = 823\ pcm \tag{69}$$

The following insights can be obtained from this exercise:

- Assuming that $\alpha = \frac{2}{3}$, the total uncertainty is well approximated using the simple sum of the individual uncertainties squared. Therefore, the total uncertainty approximated using a factor of $\alpha = 1$ is overestimated by 50 pcm. Instead of using $\alpha = \frac{2}{3}$ (0.667), a factor of $\alpha = 0.634$ can be used to obtain the uncertainty of 769 pcm which is equal to the uncertainty obtained by the SAMPLER simulation.

- If non-uniform distributions, like normal distributions were used to define the three parameters other than the nuclear data, then α might have a more mathematical basis.

- Even though the three parameters have relatively large contributions (296 pcm being the largest), the contribution to the total uncertainty only increases by the value of 39 pcm from the uncertainty due to nuclear data only.

- One possible method of propagating uncertainties would be to obtain the sensitivities of all the other parameters besides the nuclear data. If they are less than 300 pcm in magnitude, the final uncertainty can be calculated using Eq (67) once the uncertainty due to nuclear data has been individually propagated.

- Eq (67) is likely not valid since it is based on the equation that $k_\infty = a + b + c + d$. Given that the actual equation used to obtain k_∞ is the neutron transport equation, a more accurate equation would be necessary.

- Since improvements are constantly being made to the nuclear data libraries, it is quite possible that future releases of the libraries will have lower levels of uncertainty contribution. This then means that more careful attention must be paid to the other contributors, and to an alternate form of Eq (67) and also the underlying input parameters' probability distributions.

Uncertainty propagation using SAMPLER is time and resource consuming. If one can calculate the individual uncertainties given in Eq (67) using more efficient methods, then Eq (67) can be used to yield the final uncertainty. This method could then be more efficient. In this study for example, the uncertainty due to nuclear data can be obtained using TSUNAMI-3D which is more efficient than SAMPLER.

The histogram shown in Figure 5-35 can be fitted by a normal distribution. It is noted that all the input data uncertainties except the nuclear data uncertainties were modelled with uniform distributions. However, the nuclear data uncertainty was the largest contributor to the uncertainty and therefore the normal distribution observed is likely due to the distributions used to model the nuclear data uncertainties.

The running average of k_∞ in Figure 5-38 evaluates the convergence of the results over 300 samples. A good convergence of the results was after 150 samples. At least 150 samples can be used to obtain good results for the uncertainty quantification.

The uncertainty quantification of the individual input parameters is supported by a global sensitivity analysis. This global sensitivity analysis was based on correlation coefficients of the input and output as discussed in Section 2.3.3.3. The global sensitivity analysis provides a clearer picture of how the input uncertainties correlate to the output uncertainties.

Figure 5-39 gives the correlation coefficient of the propagated input parameters with respect to k_∞. Since these values are closer to 0 than -1 or 1, there is a weak correlation of these parameters with k_∞. At about 0.28, the parameter ^{235}U w/o has the highest correlation coefficient of all the parameters. A direct interpretation of this is that, if ^{235}U w/o increases, then k_∞ will also increase, since this is a fissile isotope.

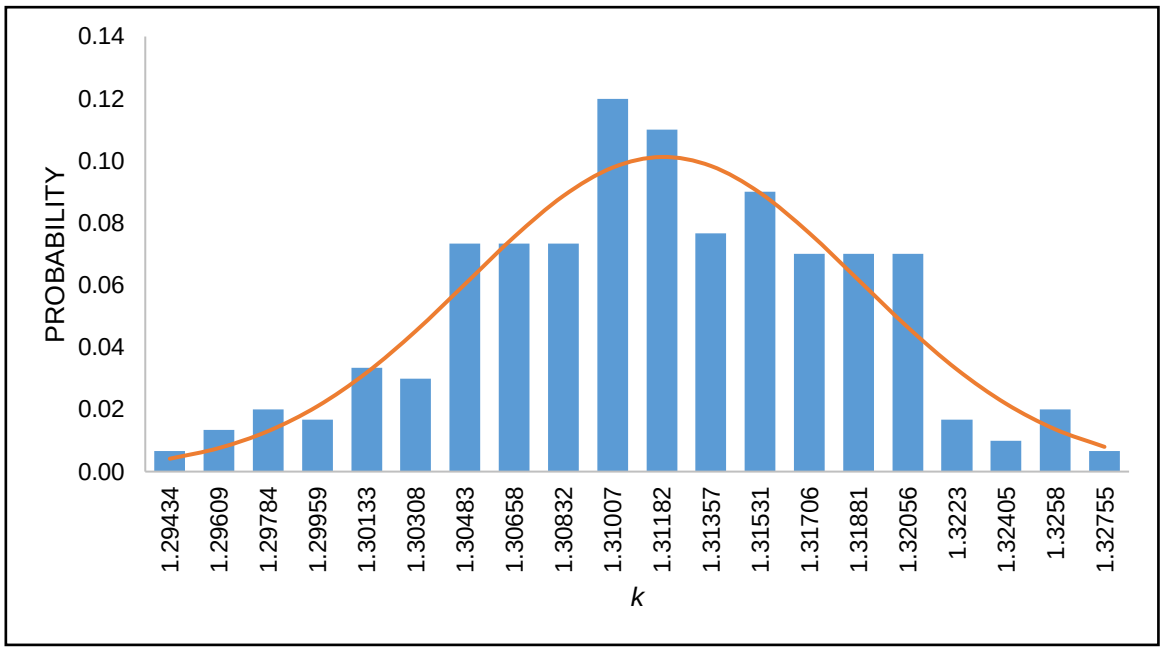

FIGURE 5-35: FREQUENCY PLOT FOR NUCLEAR DATA ANALYSIS

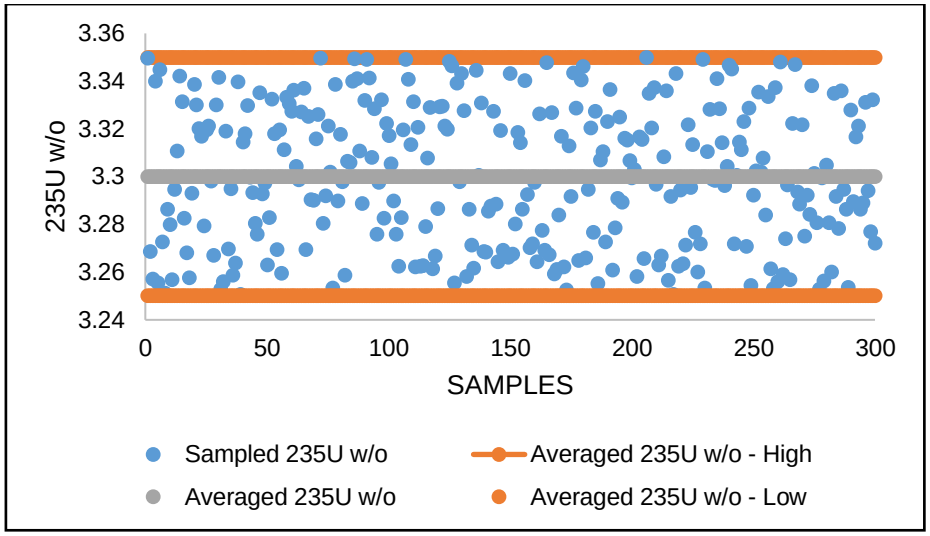

FIGURE 5-36: SCATTER PLOTS FOR ^{235}U W/O

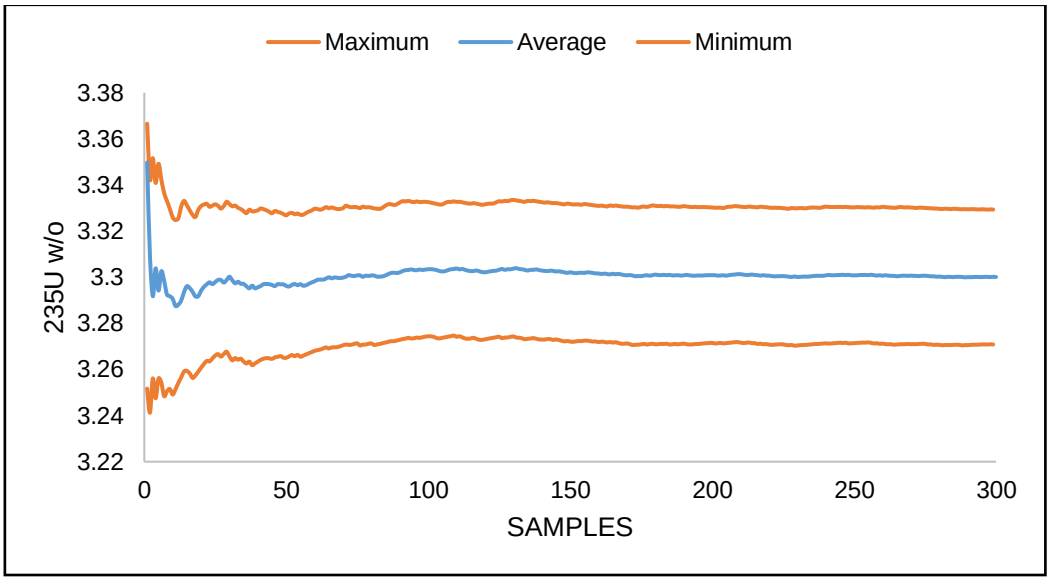

FIGURE 5-37: RUNNING AVERAGES ^{235}U W/O

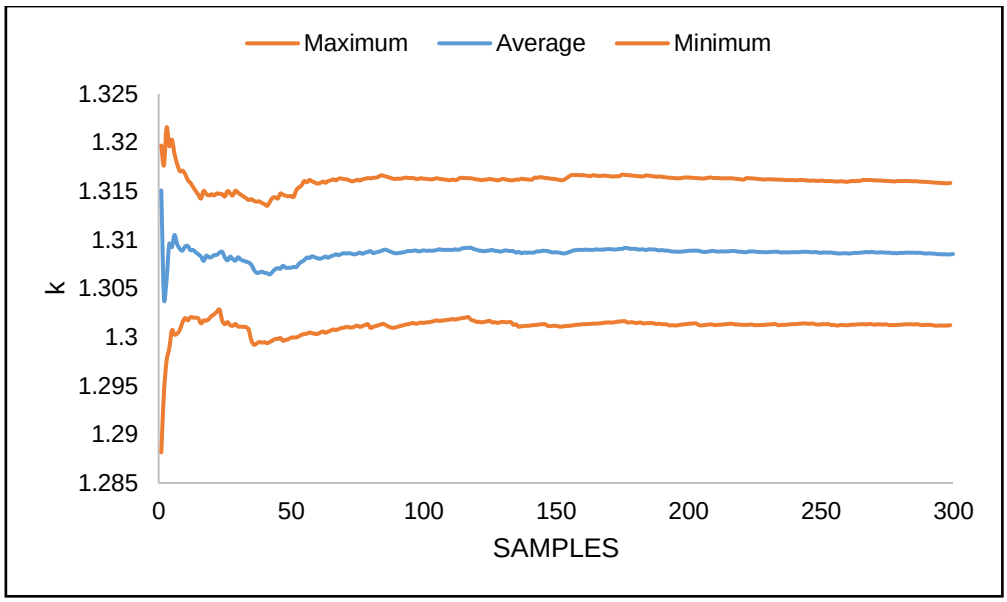

FIGURE 5-38: RUNNING AVERAGES FOR k_{∞} RESULTS

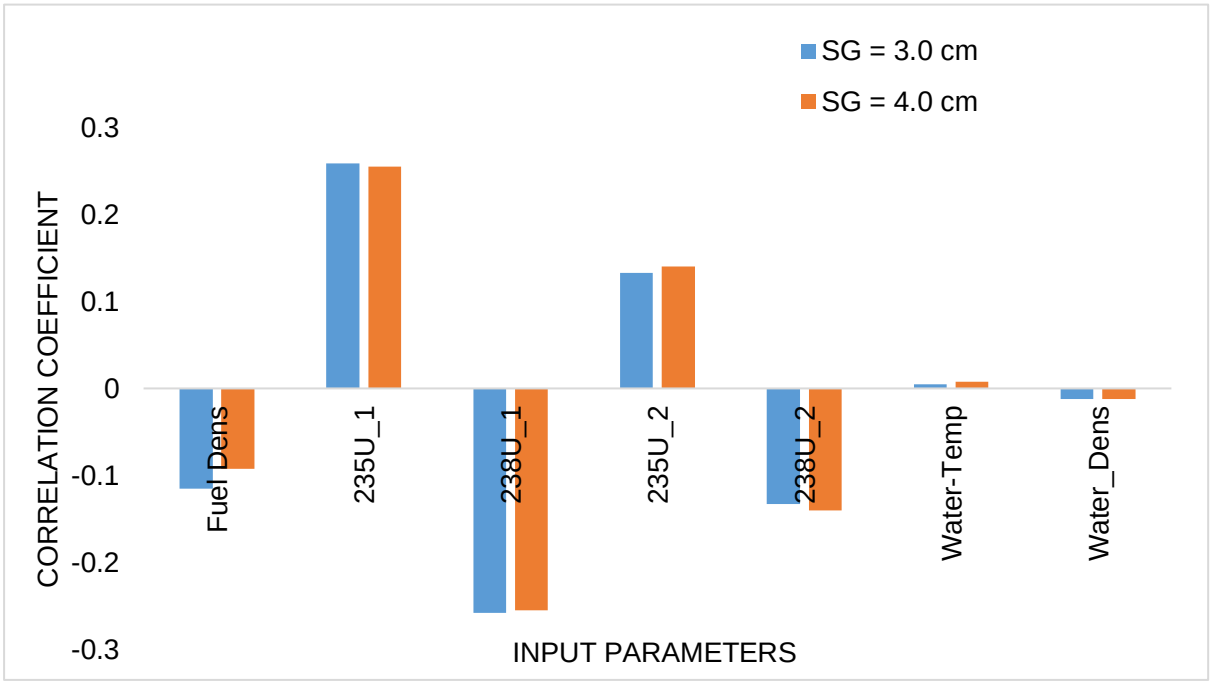

FIGURE 5-39: CORRELATION COEFFICIENTS OF PARAMETERS

5.4 FUEL DEPLETION ANALYSIS

In addition to the neutronics uncertainty analysis above, a fuel depletion calculation was obtained for the VVER-1000 fuel pin and fuel assembly. The following results demonstrates the difference in fuel depletion calculations performed with the TRITON/KENO-VI and the TRITON/NEWT code. A similar study was done on a typical VVER-1000 fuel assembly lattice design using one quadrant by Collins (Collins, et al., 2016). In the study, Collins compared the number densities of a number

of fission products calculated using TRITON/NEWT and NESTLE/ORIGEN calculations. NESTLE is a 3D diffusion code employing the nodal expansion method to solve a criticality problem and it is coupled to the latest version of the ORIGEN module of the SCALE suite to perform isotopic depletion analysis (Collins, et al., 2016). Depletion analysis with NESTLE/ORIGEN was shown to be consistent with the TRITON/NEWT depletion analysis.

5.4.1 CRITICALITY CALCULATION FOR FUEL BURN-UP

For the TRITON/NEWT results, the NEWT optimised parameters in Section 5.1 were used in this analysis. The parameters were the angular quadrature set (NPOLAR/NAZIM) and the grid discretisation (GD) for the fuel pin and the fuel assembly. As it was mentioned earlier, when KENO-VI is used, the statistical uncertainty due to the stochastic nature of KENO-VI must be small. For the results on each time step of the depletion calculation, the statistical uncertainty in TRITON/KENO-VI (MG) was confirmed to be less than 20 pcm. A reflective boundary condition (RBC) and the 56-MG library were used for both TRITON/NEWT and TRITON/KENO-VI (MG) calculations. To account for the spacer grids in the fuel assembly, the homogeneous model (HMA) defined in Section 4.5.3.1 was utilised. The time-steps that were used to obtain the k_∞ results were given in Table 4-9 in Chapter 4.

Figure 5-40 and Figure 5-41 respectively show the results of the fuel depletion for the fuel pin (FP) and the fuel assembly (FA). As expected, the k_∞ decreases as the fuel is depleted.

For the fuel assembly, two sets of calculations were performed for the fuel depletion calculation. One, used TRITON/NEWT and the second used TRITON/KENO-VI (MG). The TRITON/KENO-VI (MG) predicts higher k_∞ values in the burnup range of up to 12 GWd/MTU than the TRITON/NEWT. The difference of 180 pcm at BOC and 120 pcm at EOC are obtained between the TRITON/NEWT and TRITON/KENO-VI (MG) calculations.

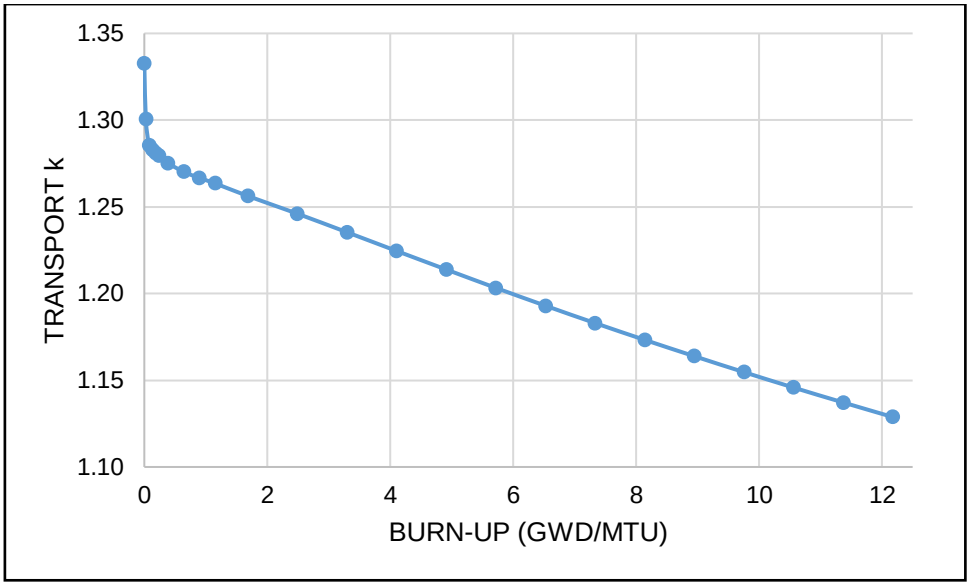

FIGURE 5-40: k RESULTS FOR BURN IN A FP

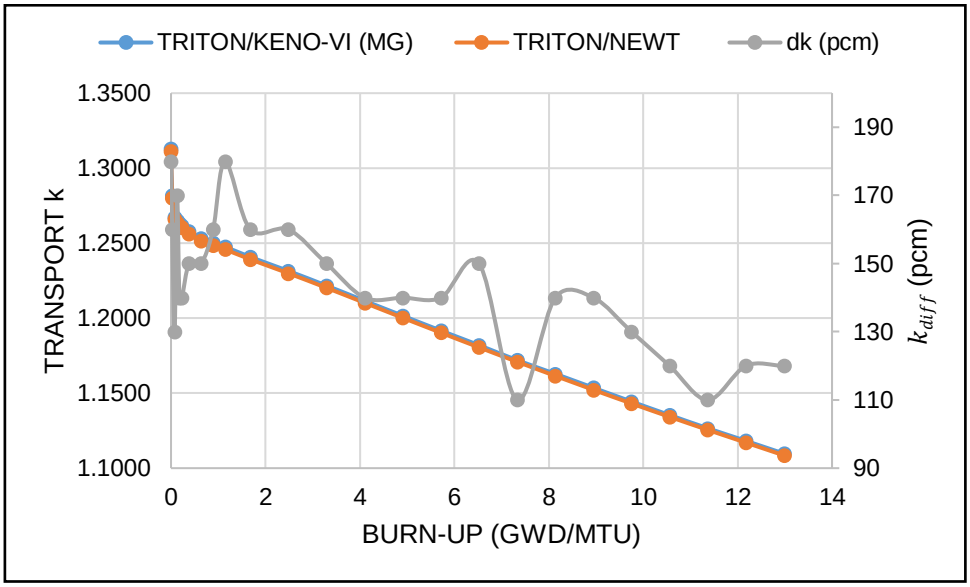

FIGURE 5-41: BURN-UP BETWEEN 2D AND 3D CODE

5.4.2 NUMBER DENSITIES OF THE IMPORTANT NUCLIDES

The concentrations of three fissile nuclides as calculated by TRITON/KENO-VI (MG) and TRITON/NEWT are shown in Figure 5-42 for the fuel pin. The main fissile isotope ^{235}U depletes as the fuel cycle progresses and some of the neutrons are absorbed by ^{238}U to procreate ^{239}Pu, which can also fission. The nuclide concentration of ^{239}Pu builds-up as the fuel depletes through the fuel cycle but remains below the concentration of ^{235}U. These two isotopes are important in a reactor since they contribute to the power of the reactor. The concentrations of the fissile nuclides calculated for the fuel assembly calculation are given in Figure 5-43. Figure 5-43 shows the nuclide concentrations calculated using TRITON/KENO-VI (MG) and TRITON/NEWT for the fuel assembly calculation. The $\%\ diff$ between the nuclide concentration predictions by TRITON/KENO-VI (MG)

and TRITON/NEWT was less than 1%. The results of the TRITON/NEWT and TRITON/KENO sequences are therefore in good agreement. This was expected since both codes used the same nuclear data library.

Figure 5-44 shows the $\%\ diff$ between the concentrations calculated for the fuel pin (FP) and for the fuel assembly (FA) of the three fissile nuclides. The build-up of ^{239}Pu and ^{241}Am concentration in the system as fuel material is depleted is higher in a fuel pin calculation than the fuel assembly calculation.

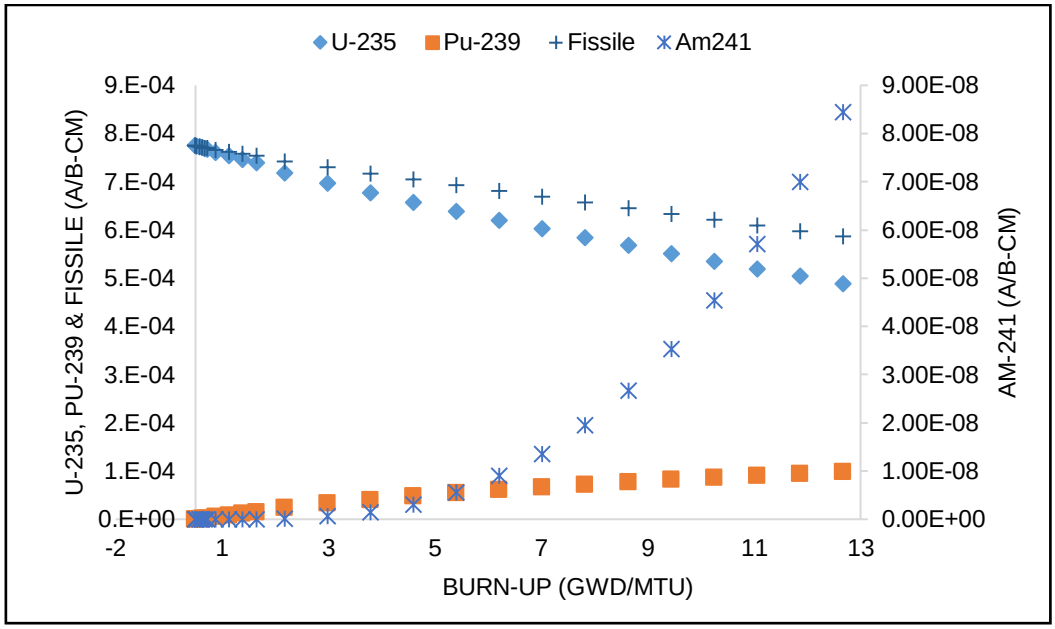

FIGURE 5-42: DEPLETION AND BULD-UP OF FISSILE ISOTOPES FOR FP

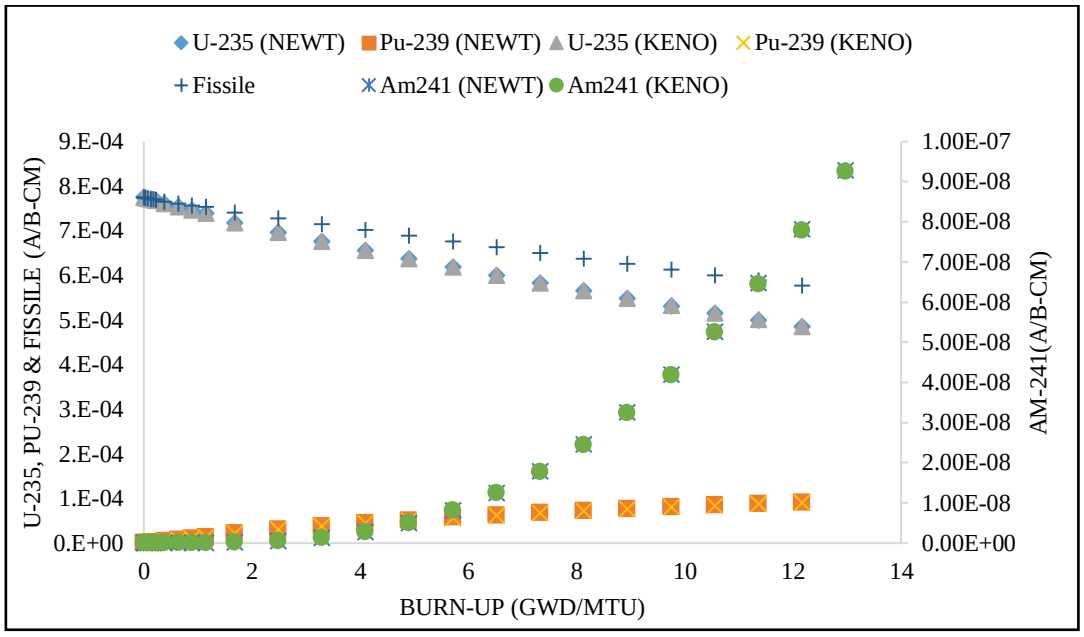

FIGURE 5-43: DEPLETION AND BULD-UP OF FISSILE ISOTOPES FA

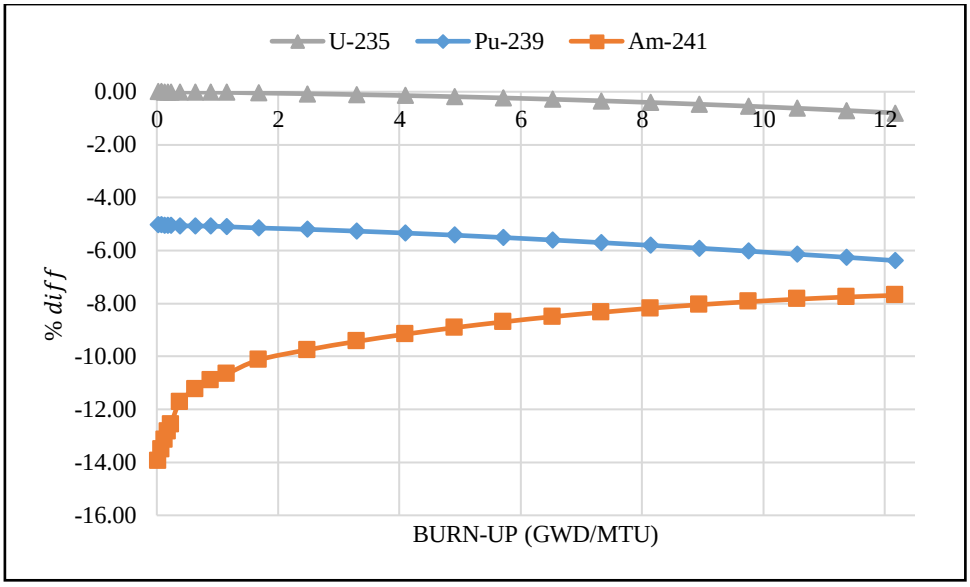

FIGURE 5-44: % $diff$ BETWEEN FP AND FA

5.4.3 UNCERTAINTY ANALYSIS OF THE DEPLETION CALCULATIONS

The above results are supplemented by an uncertainty analyses with respect to nuclear data and with respect to input data that are discussed in Section 5.3. This analysis was performed on a fuel pin using SAMPLER/T-DEPL for 200 samples.

In Figure 5-45, the uncertainty due to nuclear data only and the uncertainty due to all the uncertain parameters on the fuel depletion criticality calculations are shown. As expected, the uncertainty due to all uncertain input data has again proven to be larger than the uncertainty due to nuclear data only. The uncertainty in k given in $\%\Delta k/k$ is shown by the blue and orange curves and in terms of Δk is shown by the grey and yellow curves in Figure 5-45. The uncertainty in k in terms of Δk decreases with respect to the decrease in the k as shown by the grey and yellow plots in Figure 5-41. This quantity Δk is calculated using Eq (63). In terms of $\%\Delta k/k$, the uncertainty in k due to nuclear data decreases as the fuel is depleted up to 12 GWD/MTU. However, for the uncertainty due to all the uncertain input parameters shown by the orange curve, the uncertainty in terms of $\%\Delta k/k$ decreases to $4\ GWD/MTU$ burn-up and remains constant for the rest of the simulation. Considering the yellow curve (Δk), it can be observed that Δk decreases for the entire burn-up. Since the calculation of $\%\Delta k/k$ requires both Δk and k (shown in Figure 5-40), the levelling off of the orange curve ($\%\Delta k/k$) could just be the strengths of Δk and k in the product of Δk and k as a function of burn-up.

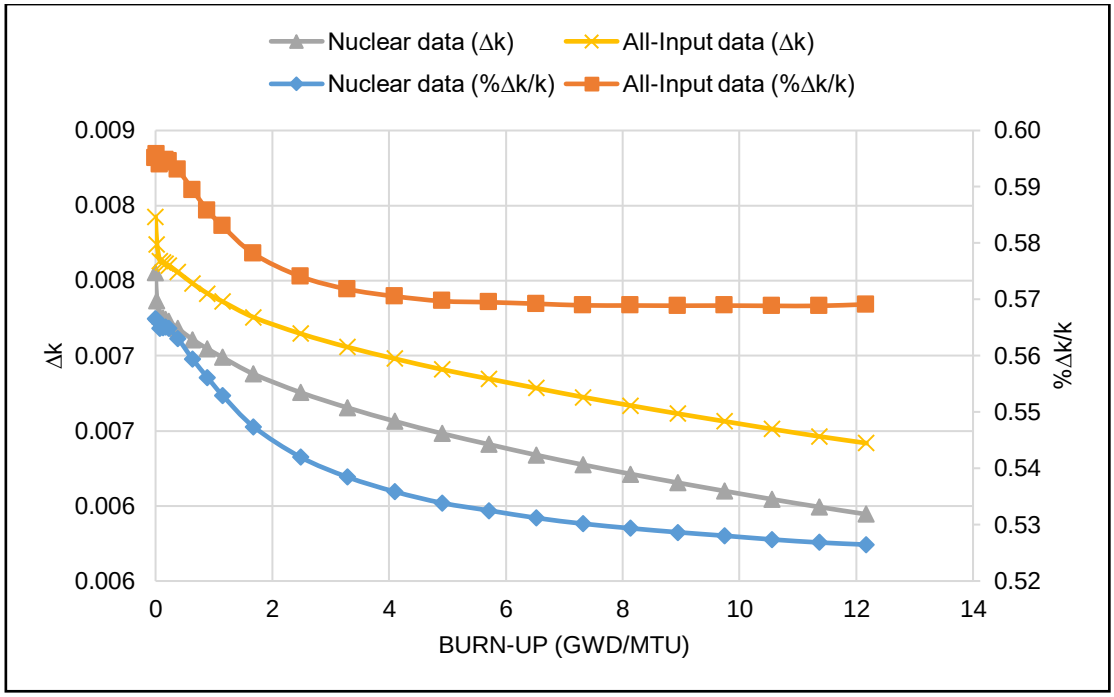

FIGURE 5-45: UNCERTAINTY IN k DUE TO INPUT DATA INCLUDING NUCLEAR DATA

The uncertainties in the calculated number densities (N) of the fissile nuclides ^{235}U, ^{239}Pu and ^{241}Am given for each burn-up step is given in Figure 5-46 to Figure 5-48 respectively, in terms of ΔN_i shown by the grey and yellow curves and in terms of $\Delta N_i/N$ shown by the blue and orange curves. The uncertainty due to all uncertain input data in the number densities (N) of the fissile nuclides ^{235}U, ^{239}Pu and ^{241}Am shown from Figure 5-46 to Figure 5-48 are also larger than the uncertainty due to nuclear data only.

It is instructive to first consider the burn-up calculation when only the nuclear data uncertainty is propagated. The burn-up calculation consists of a flux calculation at the start of the step and the end of the burn-up step. Also, the number density during the burn-up are calculated using the burn-up depletion equation as defined by Eq (42) discussed in Section 3.5. At the start of the depletion calculation where burn-up = 0, all the sample files will have identical number densities. Therefore ΔN and $\%\Delta N/N$ will be zero as observed in Figure 5-46.

However, due to the burn-up when the depletion is being performed, the nuclear data uncertainty will be propagated for the samples due to the uncertainty in the decay constants and other nuclear data of Eq (42). The number density at the end of the burn-up step will then show a distribution in values for all the N calculations. The situation changes for burn-up at step two, where a spread in the number density in the N calculation is presented. The effect of the uncertainty propagated when the depletion Eq (42) solved will be larger than for the first burn-up step. This effect, therefore gets compounded as the burn-up progresses. Therefore, as can be seen in Figure 5-46, the uncertainty in N starts at zero and steadily increases with the burn-up step.

The uncertainty due to all the input data in term of ΔN for N of ^{235}U decrease with burn-up. However, when one looks at the uncertainty in terms of $\%\Delta N/N$, one sees both the uncertainty with nuclear data and with all input data both behaves the same except for a vertical shift of about 1.160$\%\Delta N/N$. This was due to initial perturbation of ^{235}U enrichment and density.

The uncertainties in N of ^{239}Pu in terms of both ΔN and $\%\Delta N/N$ increases with the increase in N of ^{239}Pu in the system as shown in Figure 5-47. In terms of $\%\Delta N/N$, the uncertainty in N of ^{239}Pu represented in Figure 5-47 is small during the beginning of the burn-up process, however, this uncertainty increases as the process proceeds. The reason for this is because, in the beginning of the cycle, ^{239}Pu is not present, and it builds up slowly during the first few burn-ups. However, it builds up more rapidly as the fuel is depleted in the system.

The uncertainties in the number densities of ^{241}Am increases with the increase in its number density in the system in terms of ΔN. Although N increases during the fuel cycle process, the rate of increase is slow. The uncertainty in terms $\Delta N/N$ is therefore expected to decrease.

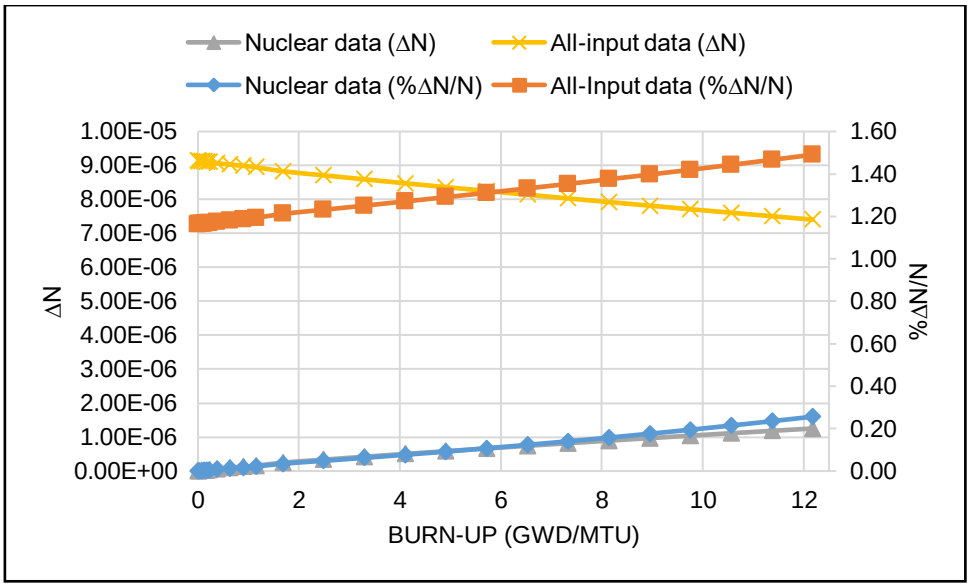

FIGURE 5-46: UNCERTAINTY IN ^{235}U NUMBER DENSITY

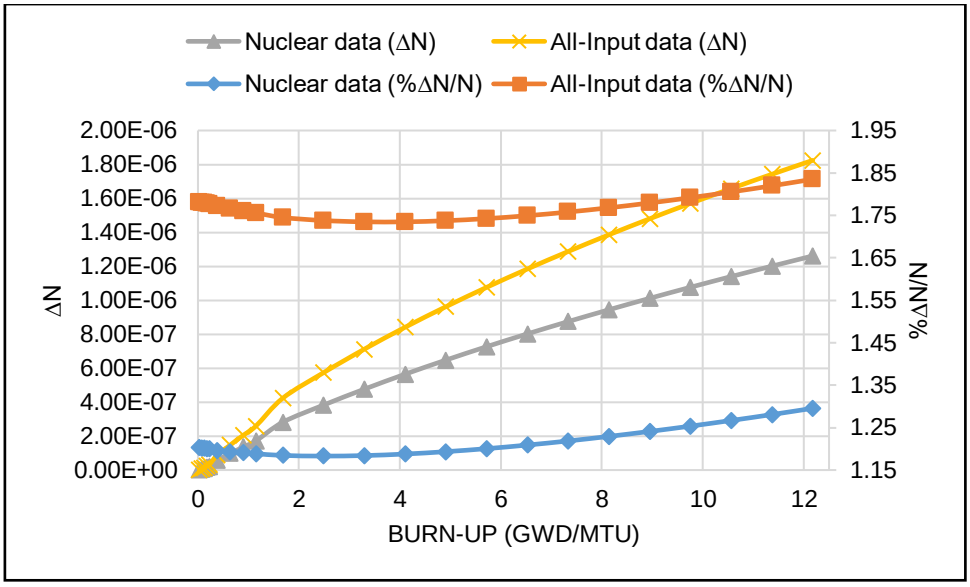

FIGURE 5-47: UNCERTAINTY IN ^{239}Pu NUMBER DENSITY

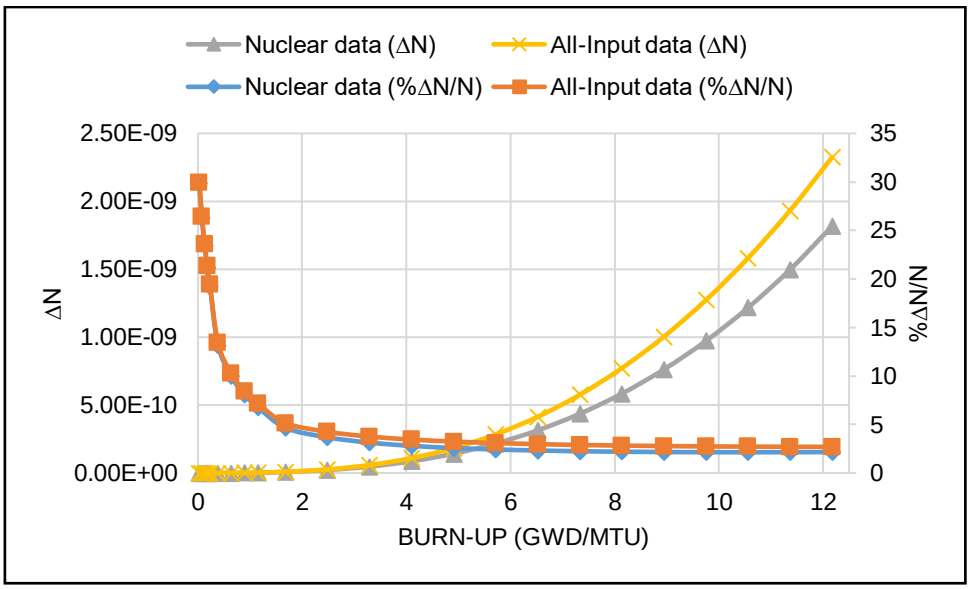

FIGURE 5-48; UNCERTAINTY IN ^{241}Am NUMBER DENSITY

5.5 UAM CONTRIBUTION RESULTS

The results in this section were submitted as part of a contribution by the author to the OECD/NEA benchmark for LWRs systems. The results submitted were for Exercises I-1a, I-1b and, I-2a of the OECD/NEA benchmark on the Kozloduy-6 VVER-1000 system. The Exercises I-1a and I-2a were analysed at hot zero power (HZP) and reflective boundary condition (RBC) were utilised for every exterior surface. Exercise I-1b results are the fuel depletion results for the fuel pin and were performed at hot full power (HZP) with RBC. These exercises of the benchmark involve the assessment of uncertainties for a VVER-1000 lattice configuration. The FA being analysed is un-rodded and has spacer grids treated using the homogeneous model (HMA) defined in Section 4.5.3.1. The presented results were calculated using the SAMPLER/NEWT and TSUNAMI-2D

codes. The optimised parameters of XSProc and NEWT codes from Section 5.1.6 are used. KENO-VI calculations were not necessary in this analysis.

All the results that are provided in this section are as per the OECD/NEA UAM team's request, which is required from each participant that are part of the OECD/NEA benchmark. The uncertainties obtained in these results were due to nuclear data only as it was requested in the OECD/NEA benchmark for these sets. No full core calculations were performed in this section.

5.5.1 EXERCISE I-1: CRITICALITY, CROSS-SECTION RESULTS AND THE ASSOCIATED UNCERTAINTIES

The results given in Table 5-16 are the eigenvalue and its absolute uncertainty based on the multi-group covariance matrices used. The number of samples used for the SAMPLER calculations were 200 for the fuel pin. The microscopic absorption and fission cross-sections and their uncertainties are also represented in Table 5-16 for ^{235}U and ^{238}U, together with the corresponding macroscopic absorption and fission cross-sections for the fuel region. The un-collapsed macroscopic cross-section of reaction x was obtained as the sum of the product of the number density of nuclide i and microscopic cross-section of reaction x as Eq (70):

$$\Sigma_x = \sum N_i \sigma_x \tag{70}$$

The uncertainties of the k_∞ due to nuclear data in the fuel pin was about $\%\Delta k/k = 0.55$, which is about 750 pcm when converted to Δk in pcm. The fourth column of the Table 5-16 are the uncertainties of each cross-section value and ranges between 1% and 5% with the highest uncertainty value for σ_f^{238}. Eq (70) is obtained directly from the OECD/NEA benchmark specification and is applied only to the uranium in the fuel. It neither includes the oxygen in the fuel, nor the clad, gap moderator cross-sections.

In the report written by Bratton (Bratton, et al., 2014), similar results were reported for the VVER-1000 as part of the OEC/NEA benchmark contribution. In the report, the k_∞ was 1.34590 and this value is 283 pcm away from the current k_∞. The uncertainty in the k is larger in the referred report with its uncertainty being 867 pcm ($0.644\%\Delta k/k$) and the difference compared to current uncertainty being 119 pcm.

The $\%\, diff$ between the referred results and the calculated results were less than 2%, except for the absorption cross-section of ^{235}U which had a $\%\, diff$ of about 23%. When comparing the uncertainties in the calculated cross-sections, the uncertainties in the referred report were lower.

The calculations of the referred report study were performed using SCALE-6.0 with 44-group covariance library data as opposed to the SCALE-6.2.1 with 56-group covariance library data. The

difference in k_∞ may be due to the different version of SCALE and the difference in the uncertainties may be due to the covariance library. The uncertainties are given in $\%\Delta x/x$, where x represents each parameter in Table 5-16.

TABLE 5-16: EXERCISE I-1 RESULTS

Output	Value	Abs STD	$\%\Delta x/x$	Bratton	$\%\Delta x/x$	$\%diff$
k_∞	1.34874	0.00748	0.555	1.34590	0.644	-
σ_a^{235}	59.181	0.73494	1.241	47.00	0.707	22.94
σ_a^{238}	1.001	0.01021	1.015	0.98	0.750	2.12
σ_f^{235}	48.532	0.61118	1.259	48.50	0.720	0.07
σ_f^{238}	0.0944	0.00479	5.072	0.0958	2.645	-1.47
Σ_a	0.0684	0.00069	1.005	-	-	-
Σ_f	0.0397	0.00038	0.953	-	-	-

Figure 5-49 provides the top five neutron-nuclide reactions contributing to the uncertainty of k. The neutron-nuclide contributor uncertainties are given in units of $\%\Delta k/k$ obtained from TSUNAMI-2D. In the referred report, the neutron-nuclide contributors were obtained for the VVER-1000 fuel pin. The order of the neutron-nuclide contributors between the referred report and the current study are not the same as can be seen in the ranking table in Table 5-17. The first three contributors were the same in both the referred report and the current study and those were $^{238}U_{n,\gamma}$, $^{235}U_{nubar}$ and $^{235}U_{n,\gamma}$. However, the first contributor in the referred report was the second contributor in the current study and vice versa as observed in Table 5-17. The third contributor was the same for both studies. The fourth and the fifth contributors were different as observed in Table 5-17.

TABLE 5-17: RANKING OF THE TOP CONTRIBUTORS

Ranking	SCALE-6.2.1	Bratton
1	$^{235}U_{nubar}$	$^{238}U_{n,\gamma}$
2	$^{238}U_{n,\gamma}$	$^{235}U_{nubar}$
3	$^{235}U_{n,\gamma}$	$^{235}U_{n,\gamma}$
4	$^{238}U_{\chi}$	$^{238}U_{fission}$
5	$^{238}U_{fission/n,\gamma}$	$^{238}U_{elastic}$

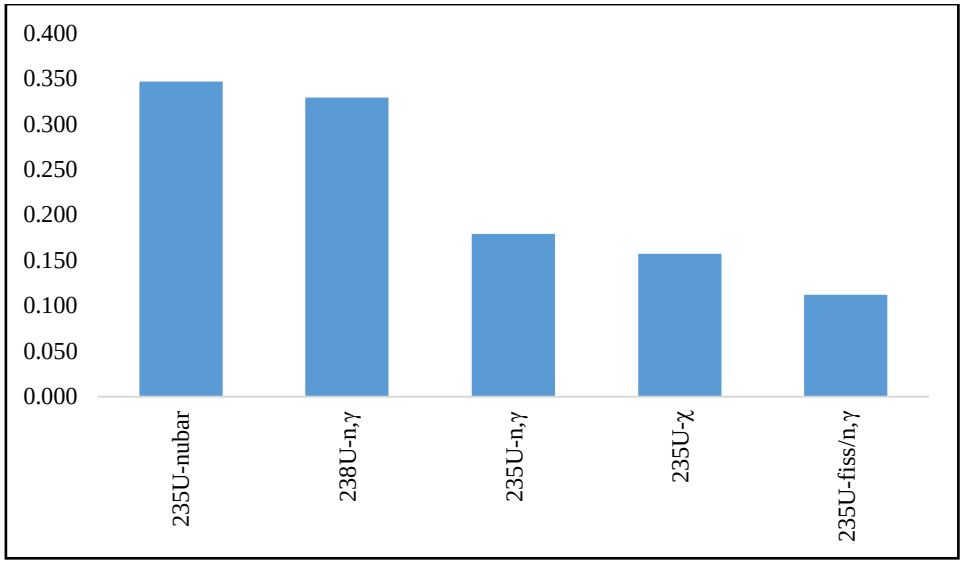

FIGURE 5-49: TOP FIVE UNCERTAINTY CONTRIBUTORS

The sensitivity data plots of the first three neutron-nuclide reaction is given in Figure 5-50. For $^{235}U_{nubar}$, the sensitivities of k have higher peaks in the thermal region. For $^{238}U_{n,gamma}$ and $^{235}U_{n,gamma}$ the sensitivities have higher peaks in the epithermal region although the peak in the thermal region is wider as seen in Figure 5-50. In addition, the correlation coefficients matrix for the values given in Table 5-16 are given in Figure 5-51. These correlation coefficients were calculated using Eq (39) defined in Section 2.3.3.3.

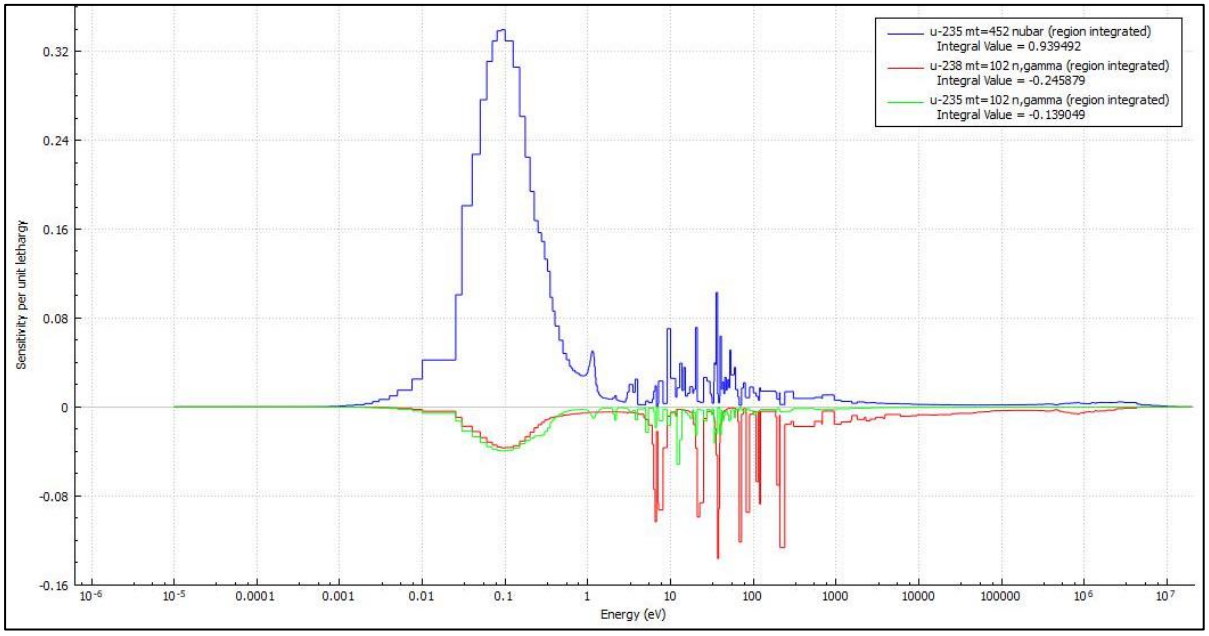

FIGURE 5-50: SDF PLOTS FOR THE FIRST THREE NUCLIDE REACTIONS

	k	σ_a^{235}	σ_a^{238}	σ_f^{235}	σ_f^{238}	Σ_a	Σ_f
k	1.000						
σ_a^{235}	-0.207	1.000					
σ_a^{238}	-0.591	0.370	1.000				
σ_f^{235}	-0.092	0.978	0.340	1.000			
σ_f^{238}	0.336	-0.935	-0.450	-0.910	1.000		
Σ_a	-0.368	0.951	0.639	0.923	-0.923	1.000	
Σ_f	-0.019	0.958	0.298	0.993	-0.855	0.893	1.000

FIGURE 5-51: CORRELATION COEFFICIENTS

5.5.2 EXERCISE I-2: CRITICALITY, TWO-GROUP PARAMETERS AND THE ASSOCIATED UNCERTAINTIES

Exercise I-2 consists of the propagation of input uncertainties through lattice physics simulations to obtain output uncertainties in evaluated lattice-average parameters. Two energy groups were used, with the first energy group cutting off at $0.625eV$. The output presented in Table 5-18 are the assembly k_{inf}, homogenised two-group macroscopic cross-section, diffusion coefficients $(D\ in\ cm)$, fluxes $(\phi\ in\ 1/cm^2s)$, inverse neutron velocity $(v^{-1}\ in\ s/m)$, lambda $(\lambda\ in\ s^{-1})$ for delayed neutrons and the assembly discontinuity factor (ADF). The homogenised two-group macroscopic cross-sections in units of (cm^{-1}) are:

- Absorption,
- Fission,
- Up-scattering and down-scattering,
- Transport, and
- Nubar*fission (n-f).

Nubar*fission (n-f) is defined as the product of the fission cross-section and the number of neutrons produced per fission (Rearden & Jesse, 2016).

All the parameters are given with their corresponding uncertainties. As it is observed in Table 5-18, the uncertainties associated with each parameter is higher in the first energy group for most of the parameters. In the report by Bratton (Bratton, et al., 2014), the k_∞ results for the fuel assembly was 1.31990 and this value is 1023 pcm away from the current k_∞. As stated above, calculations of the referred report study were performed using SCALE-6.0 with 44-group covariance library data as opposed to the SCALE-6.2.1 with 56-group covariance library data. The difference in the k may be due to the different version of SCALE. The referenced report did not provide any information about the modelling of spacer grids. Therefore, the treatment of spacer grids in the fuel assembly

may also be contributing to difference in k. The difference in the uncertainties may be due to the covariance library.

TABLE 5-18: EXERCISE I-2 RESULTS FROM NEWT

Parameter	Value	Abs STD	$\%\Delta x/x$	Bratton	$(\%\Delta x/x)$
k	1.30967	0.00728	0.554	1.31990	0.512
Σ_{a-1}	0.00925	0.00009	0.922	0.00930	0.780
Σ_{a-2}	0.08396	0.00023	0.274	0.08340	0.297
Σ_{f-1}	0.00256	0.00002	0.599	0.00259	0.758
Σ_{f-2}	0.05602	0.00017	0.306	0.05630	0.258
Σ_{s1-1}	0.52986	0.00512	0.966	0.53600	0.720
Σ_{s1-2}	0.00134	6.4E-06	0.482	0.01990	1.128
Σ_{s2-1}	0.01781	0.00025	1.389	0.00089	0.260
Σ_{s2-2}	1.27520	0.00299	0.233	1.27000	0.161
Σ_{to-1}	0.55689	0.05425	0.973	0.56900	0.816
Σ_{to-2}	1.36050	0.00301	0.220	1.54000	0.125
Σ_{tr-1}	0.22892	0.00573	2.511	0.22600	2.415
Σ_{tr-2}	0.91100	0.00279	0.306	0.91400	0.174
D_1	1.45611	0.03695	2.526	1.45000	1.434
D_2	0.36589	0.00112	0.306	0.33800	0.175
$nu * f_1$	0.00652	0.00006	0.900	0.00656	0.888
$nu * f_2$	0.13651	0.00067	0.492	0.13700	0.408
ϕ_1	0.07752	0.00092	1.188	-	-
ϕ_2	0.01619	0.00007	0.457	-	-
v_1^{-1}	5.9E-08	8.0E-10	1.357	5.8E-08	1.239
v_2^{-1}	2.5E-06	1.0E-09	0.041	2.5E-06	0.035
λ_1	0.01248	0.00002	0.161	0.01250	0.015
λ_2	0.03075	0.00006	0.192	0.03070	0.012
λ_3	0.11433	0.00138	1.216	0.11300	0.058
λ_4	0.30896	0.00319	1.038	0.30500	0.043
λ_5	1.22252	0.02223	1.836	1.18000	0.052
λ_6	3.26936	0.86070	2.669	3.14000	0.073
ADF_1	0.97958	0.00022	0.022	-	
ADF_2	1.16200	0.00064	0.057	-	

Figure 5-52 shows the top five neutron-nuclide contributors, which contribute the most to uncertainties of k, obtained using TSUNAMI-2D code. The neutron-nuclide reaction contributors were observed to be in the same order as the one obtained in Section 5.2.3. the report did not provide any contributors for Exercise I-2 (VVER-100 FA). In addition to the uncertainty analysis results above for the fuel assembly, the correlation coefficient matrix of the individual two-group parameters is given in Figure 5-53.

This correlation matrix gives the correlation between two parameters. As was discussed in Section 2.3.3.3 for the correlation coefficients, a value that is moving towards +1 indicates that two parameters increase together, while a value moving towards -1 indicates that two parameters tend to move in opposite directions. Moving in opposite directions means that, if one parameter increases, the other parameter will decrease (anticorrelated).

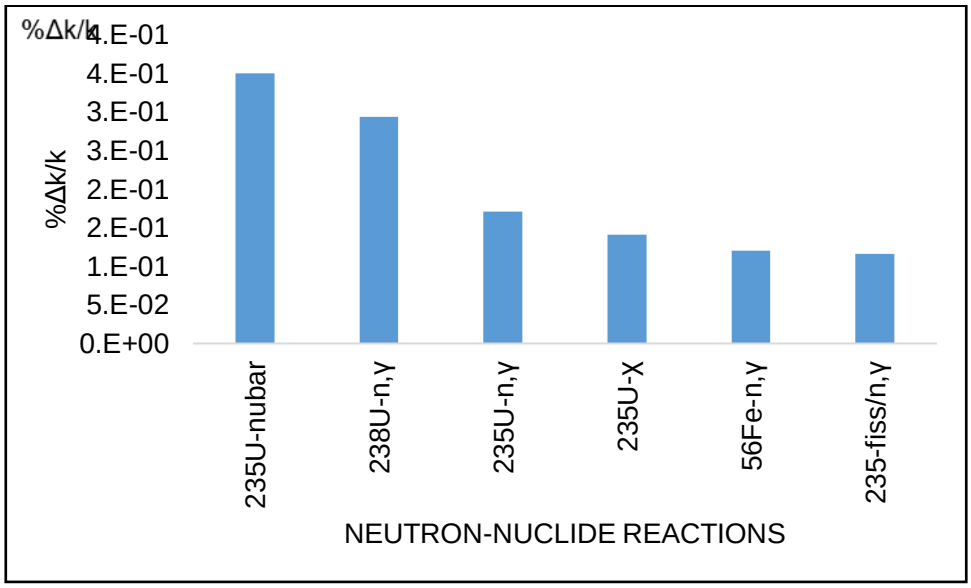

FIGURE 5-52: TOP FIVE UNCERTAINTY CONTRIBUTORS FOR EXI-2

	k	Σ_{a-1}	Σ_{a-2}	Σ_{f-1}	Σ_{f-2}	Σ_{s1-1}	Σ_{s1-2}	Σ_{s2-1}	Σ_{s2-2}	Σ_{to-1}	Σ_{to-2}	Σ_{tr-1}	Σ_{tr-2}	D_1	D_2	$n\text{-}f_1$	$n\text{-}f_2$	ϕ_1	ϕ_2	AD_1	AD_2
k	1.000																				
Σ_{a-1}	-0.475	1.000																			
Σ_{a-2}	-0.410	0.275	1.000																		
Σ_{f-1}	0.395	-0.465	-0.019	1.000																	
Σ_{f-2}	0.369	0.061	0.228	0.126	1.000																
Σ_{s1-1}	-0.236	0.782	0.069	-0.569	0.109	1.000															
Σ_{s1-2}	-0.189	0.269	0.515	0.020	0.186	0.364	1.000														
Σ_{s2-1}	-0.207	0.769	0.012	-0.603	0.101	0.939	0.102	1.000													
Σ_{s2-2}	0.107	0.171	-0.001	0.062	0.075	0.418	0.692	0.191	1.000												
Σ_{to-1}	-0.240	0.789	0.070	-0.573	0.108	1.000	0.353	0.944	0.406	1.000											
Σ_{to-2}	0.075	0.192	0.076	0.060	0.093	0.422	0.731	0.192	0.997	0.410	1.000										
Σ_{tr-1}	-0.235	0.788	0.028	-0.517	0.110	0.939	0.238	0.937	0.221	0.942	0.222	1.000									
Σ_{tr-2}	0.076	0.181	0.028	0.052	0.089	0.424	0.791	0.174	0.979	0.411	0.979	0.243	1.000								
D_1	0.237	-0.789	-0.030	0.518	-0.107	-0.939	-0.239	-0.937	-0.220	-0.942	-0.222	-0.999	-0.243	1.000							
D_2	-0.076	-0.181	-0.028	-0.052	-0.089	-0.424	-0.791	-0.174	-0.979	-0.411	-0.979	-0.243	-1.000	0.243	1.000						
$n\text{-}f_1$	0.485	-0.473	-0.021	0.915	0.040	-0.615	0.007	-0.643	0.052	-0.618	0.050	-0.577	0.043	0.577	-0.043	1.000					
$n\text{-}f_2$	0.675	0.068	0.211	0.067	0.611	0.091	0.180	0.065	0.159	0.090	0.175	0.054	0.152	-0.052	-0.152	0.170	1.000				
ϕ_1	0.293	-0.864	-0.083	0.609	-0.093	-0.941	-0.146	-0.986	-0.189	-0.947	-0.195	-0.940	-0.178	0.940	0.178	0.642	-0.068	1.000			
ϕ_2	0.373	-0.066	-0.776	-0.247	-0.073	0.373	-0.389	0.481	0.079	0.373	0.018	0.396	0.037	-0.394	-0.037	-0.283	-0.107	-0.358	1.000		
AD_1	0.089	-0.690	0.151	0.481	-0.057	-0.860	-0.034	-0.903	-0.160	-0.864	-0.148	-0.882	-0.149	0.883	0.149	0.510	-0.066	0.887	-0.539	1.000	
AD_2	-0.306	0.307	0.700	-0.031	0.246	0.274	0.590	0.185	0.267	0.272	0.321	0.216	0.306	-0.214	-0.306	-0.078	0.138	-0.223	-0.439	0.155	1.000

FIGURE 5-53: CORRELATION COEFFICIENTS OF THE FA SYSTEM

5.5.3 FUEL DEPLETION CALCULATIONS AND ASSOCIATED UNCERTAINTIES

The objective of this analysis is to evaluate criticality results k_∞, fission and capture rates and nuclide concentrations. In addition to these results, collapsed macroscopic cross-sections, nubar and diffusion coefficients $(D\ in\ cm\ )$ were obtained. This fuel depletion analysis was performed on Exercise 1b, for the fuel pin of the VVER-1000 system using TRITON/NEWT. TRITON/NEWT uses the method in Section 2.2.3.3 to obtain collapsed parameters. The fuel pin is burnt through a single

irradiation cycle at HFP operating conditions. The capture and fission reaction rates densities are reported for ^{235}U , ^{238}U , ^{239}Pu, ^{240}Pu, and ^{241}Pu. The two-group collapsed burn-up dependent macroscopic cross-sections reported in this work are the absorption and fission cross-sections.

The evaluated results from Figure 5-54 to Figure 5-56 are given from 0 to $60\ GWd/MTU$ burnups. Figure 5-55 shows the results for the parameters collapsed in Group 1 and Figure 5-56 shows Group 2 parameter results. The results from Figure 5-54 to Figure 5-56 shows a good relative agreement with the results reported in Bratton (Bratton, et al., 2014) for the Three Mile Island fuel pin. This comparison assists in verifying the results of the VVER-1000 pin-cell since there were no results reported on the VVER-1000 system. Both TMI pin-cell and VVER-1000 pin-cell are a pressurised water reactor system.

As observed from Figure 5-54 to Figure 5-56, the results decrease, as the fuel is depleted in the system, except for the absorption cross-section, which increases. The diffusion coefficient for group one increases during the first few burn-ups, up to about 12 GWd/MTU, however it then decreases up to the end of the burn-up cycle.

The k_∞ results in Figure 5-54 are accompanied by its associated uncertainties due to nuclear data shown in Figure 5-57. The uncertainty data given in units of $\%\Delta k/k$ is shown by the blue curve in Figure 5-57. This value first decreases and then increases as the fuel is depleted. However, k decreases as burnup increases as shown in Figure 5-54. Since boron is not added to compensate for the decrease in k, the behavior of the blue curve can be expected. Considering Δk, as shown by the orange line in Figure 5-57 the uncertainty in k due to nuclear data decrease up to 30 GWd/MTU. Then it remains fairly constant until the final burn-up. A clear indication of the trend in the uncertainty with burnup is therefore observed. This trend on the uncertainty in k is a bit different from the trend that was observed in Figure 5-45 in Section 5.4.3. That is because the burn-up in Figure 5-45 was only up to $12\ GWd/MTU$.

Figure 5-58 and Figure 5-59 represent the reaction rates for the fissile and fertile materials obtained during burn-up. The reaction rate results are presented for $60\ GWd/MTU$. The nuclide concentration of the major actinides and fissile products are given from Figure 5-60 to Figure 5-62.

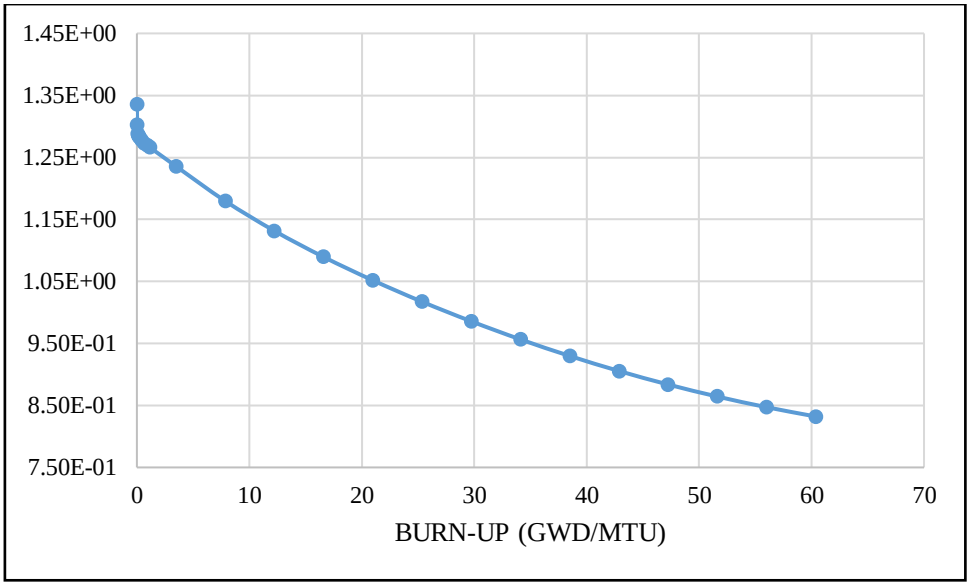

FIGURE 5-54: k_{∞} RESULTS FOR FUEL PIN

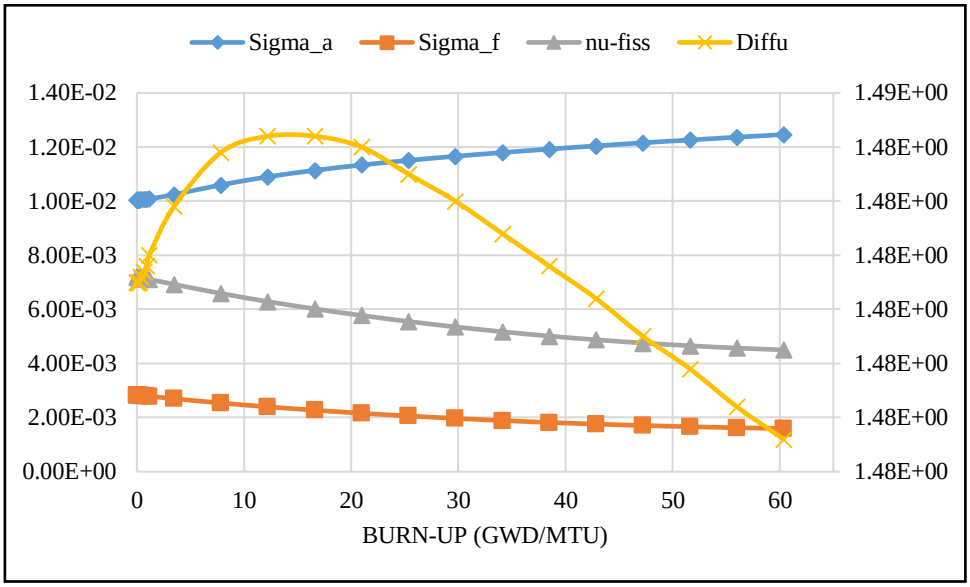

FIGURE 5-55: GROUP ONE CROSS-SECTIONS, NUBAR AND DIFFUSION

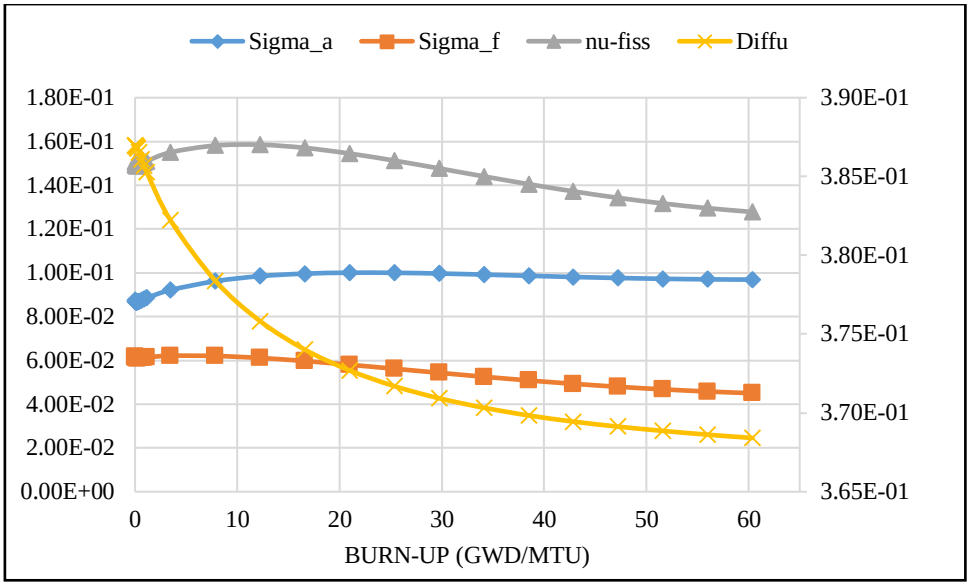

FIGURE 5-56: GROUP TWO CROSS-SECTIONS, NUBAR AND DIFFUSION

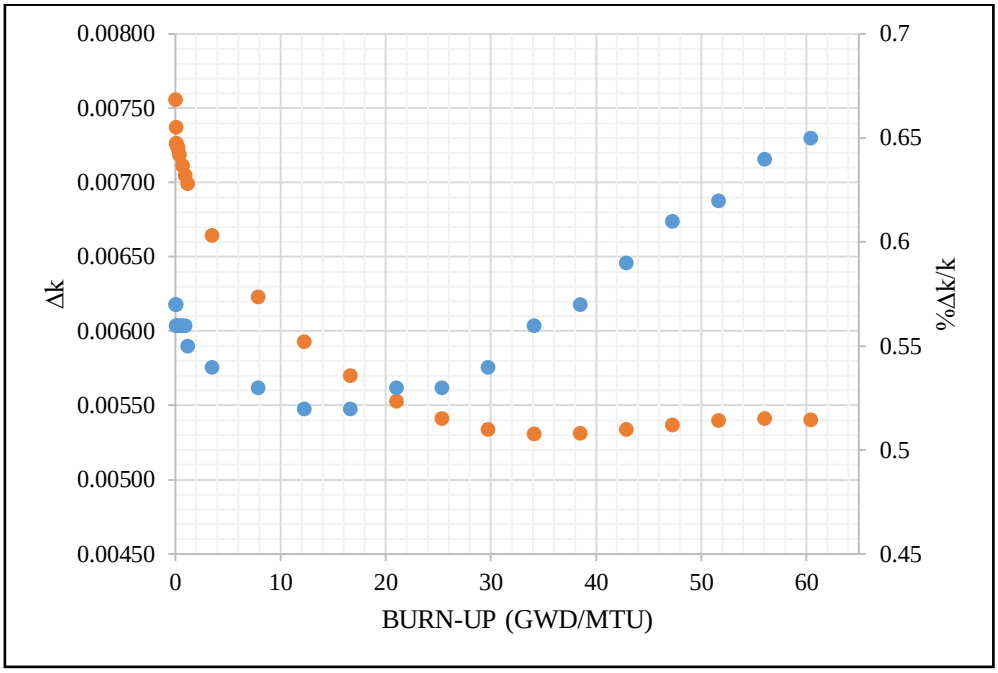

FIGURE 5-57: UNCERTAINTY IN k DUE TO NUCLEAR DATA

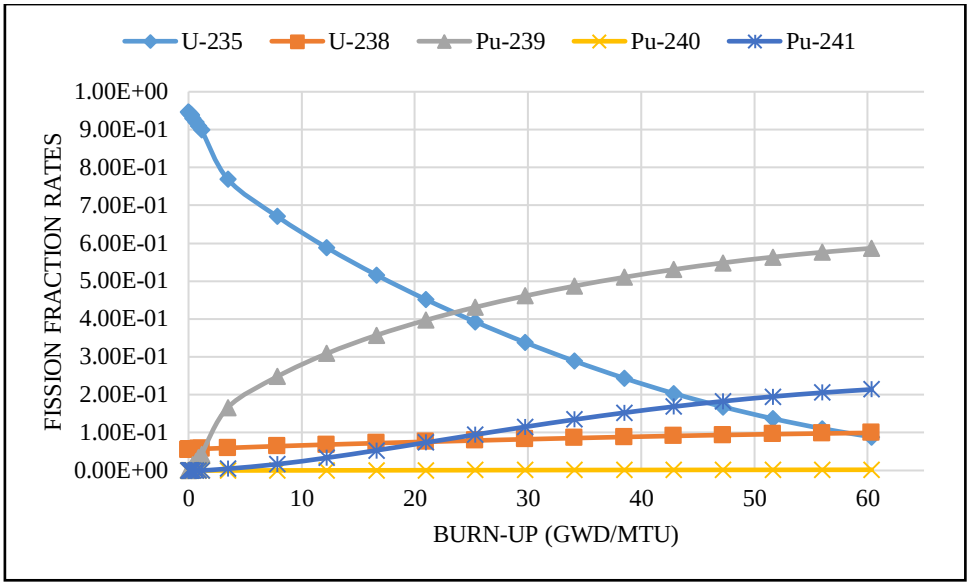

FIGURE 5-58: FISSION FRACTION RATES

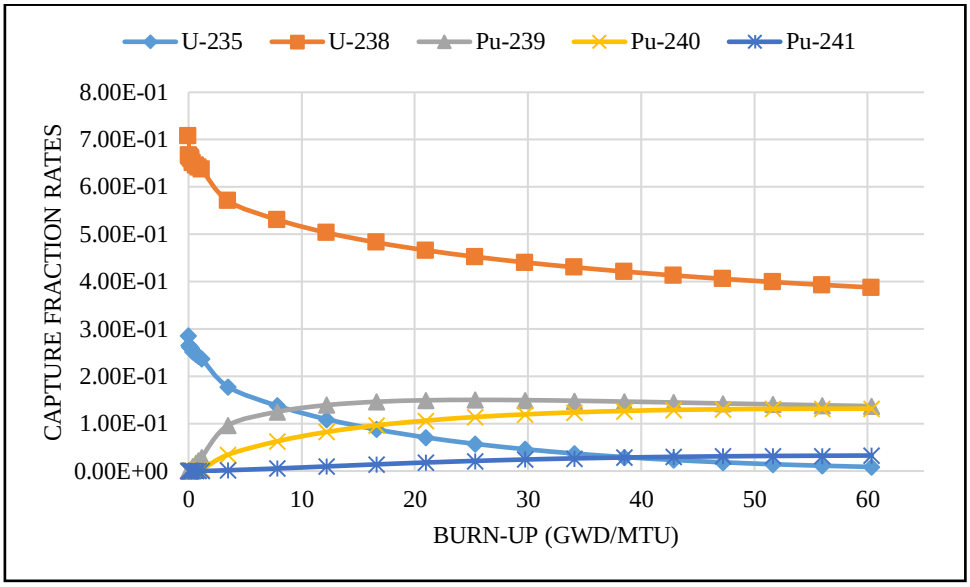

FIGURE 5-59: CAPTURE REACTION RATES

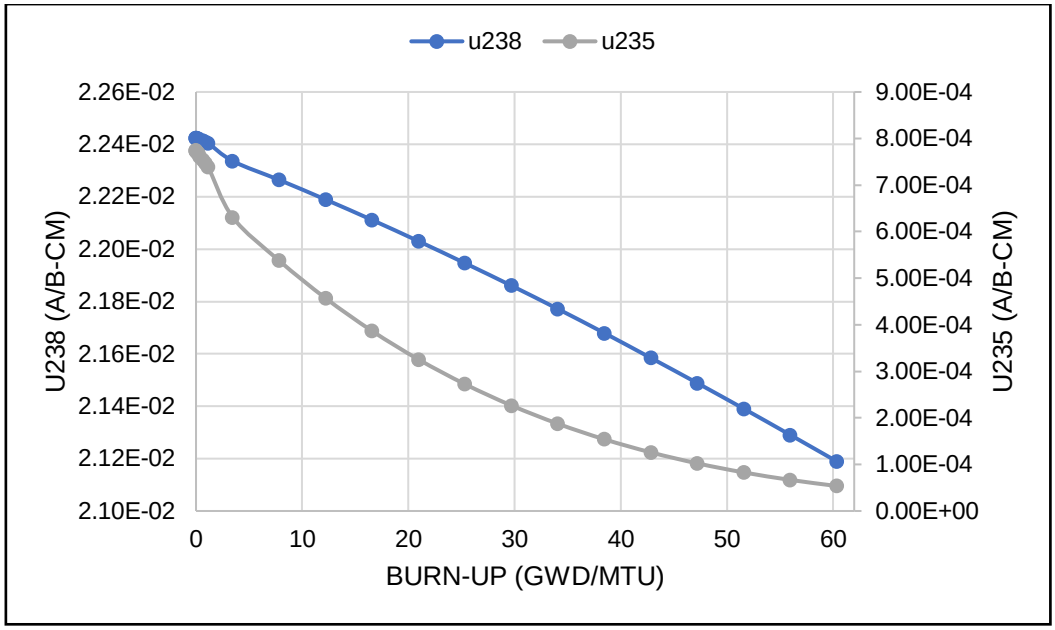

FIGURE 5-60: NUCLIDE CONCENTRATIONS

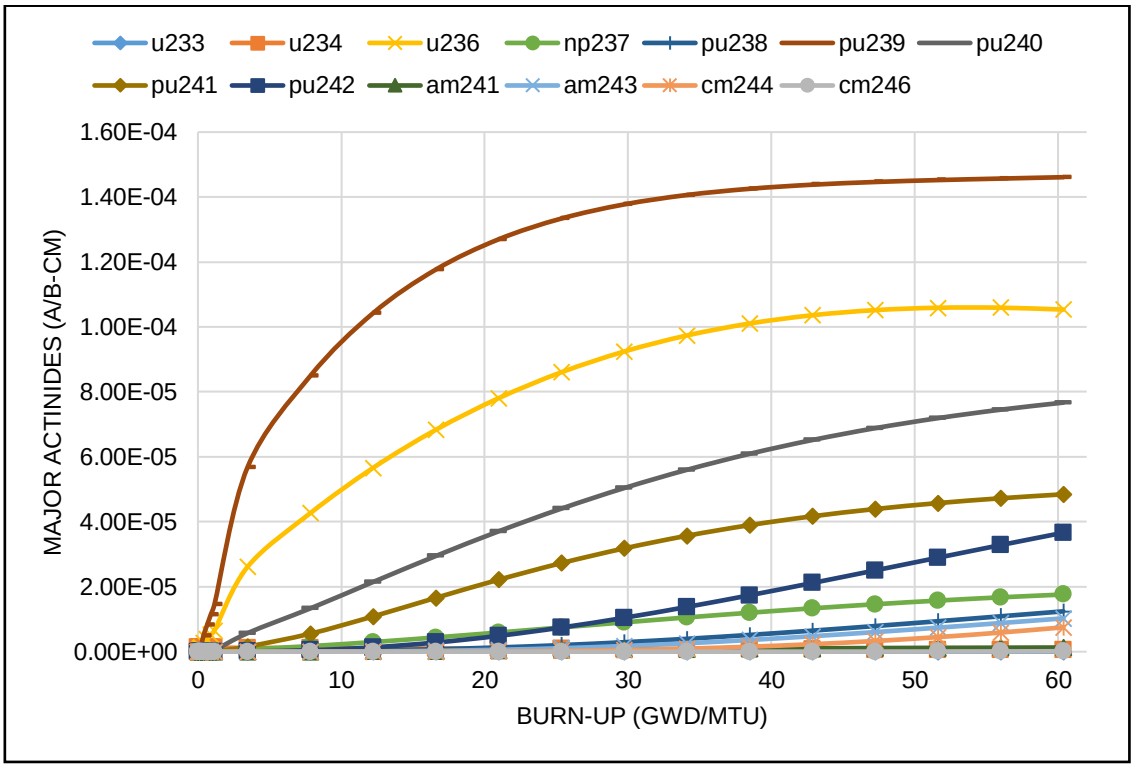

FIGURE 5-61: MAJOR ACTINIDES NUCLIDE CONCENTRATION

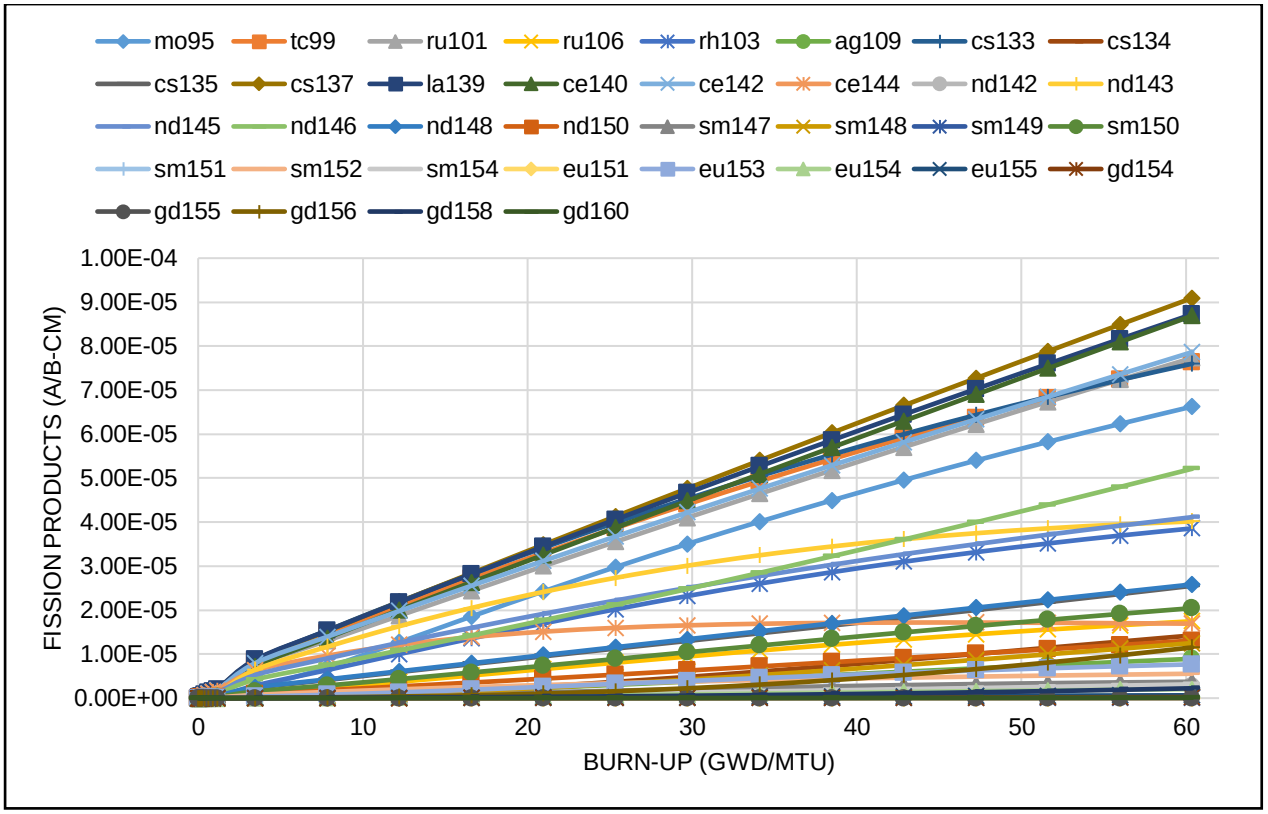

FIGURE 5-62: FISSION PRODUCTS NUCLIDE CONCENTRATIONS

5.6 CLOSING DISCUSSION

The uncertainty analysis of the VVER-1000 system was successfully done in 5 sections. In accordance with the objectives of the study, the following was provided in this chapter:

- The Kozloduy-6 VVER-1000 fuel pin and fuel assembly were built and the neutronics results were obtained using NEWT and KENO-VI.
- The sensitivity analysis due to the input data of the VVER-1000 system was performed and the parameters that showed a largely change in the neutronics results were established.
- Propagation of the uncertain input data was performed.
- Fuel depletion analysis was performed, together with an uncertainty analysis on the fuel pin and fuel assembly.
- The contribution results to the OECD/NEA benchmark were prepared and analysed as part of this study and submitted to be included in the final benchmark document.

Section 5.1 presented the results for the optimisation of the XSProc and NEWT code parameters. For the XSProc parameters, the difference in the results using the least optimal value and optimised value for SZF, IROPT, ITERP, ALUMP and DEMAX and DEMIN was less than 23 pcm and for ISN, the difference was 200 pcm. For the NEWT parameters, the difference in the results

for each parameter tested is less than 140 and 283 pcm for the FP and FA results respectively. The difference in k_∞ between KENO-VI and NEWT when using PQ sets were 1 pcm and 10 pcm for the FP and FA respectively.

The uncertainty due to nuclear data for the nominal cases were 780 and 760 pcm for the fuel pin and fuel assembly respectively. For each parameter, an uncertainty analysis due to nuclear data was performed for the least optimal value and optimised value. The optimisation of the parameters did not contribute significantly to the uncertainty that is due to nuclear data. When comparing the uncertainties due to nuclear data with that due to the modelling parameters, the uncertainty in the multiplication factor due to nuclear data uncertainty was larger than that due to modelling uncertainties.

Section 5.2 presented results using KENO-VI to obtain the uncertainties propagated due to nuclear data uncertainties, method and modelling uncertainties, and manufacturing tolerances. The uncertainties due to the statistical nature of the KENO-VI code were less than 15 pcm. This was achieved by defining adequate number of neutrons per generation and the number of skipped and active cycles. This was further verified by means of the random number generation analysis. The analysis was performed for 100 trials using a different random number seeds in each trial to produce a statistical uncertainty that was in good agreement with the statistical uncertainty in one KENO-VI calculation.

KENO-VI calculations using, first, MG-ENDF/B-VII.0 and a CE-EDNF/B-VII.0 nuclear data libraries and secondly, using MG-ENDF/B-VII.0 and MG-ENDF/B-VII.1 were performed for comparison. There are differences in the k_∞ results between calculations done using ENDF/B-VII.0 and ENDF/B-VII.1. However, a reasonable agreement was observed for calculations between the 56-MG-ENDF/B-VII.1 and the CE-ENDF/B-VII.1 nuclear data libraries.

With regard to the SGs modelling, the heterogeneous and the homogeneous band models were in good agreement in k_∞, while the entire homogenised model was different from the first two models. Therefore, the heterogeneous model has verified that the homogeneous band model was defined accurately and can be used in place of the heterogeneous model. However, the choice of SG modelling in the neutronics calculations depends on the neutron transport solution method desired. For MC methods, all the SG modelling methods are applicable. It was also seen that the choice of the SG height has a significant influence on the difference in k_∞ and should be considered carefully.

Nuclear data introduces uncertainties of about 730 pcm (~0.57 $\%\frac{\Delta k}{k}$) to the k_∞ results. The top five nuclide reactions that contributes to this uncertainty were: $^{235}U_{nubar}$, $^{238}U_{n,\gamma}$, $^{235}U_{n,\gamma}$, $^{235}U_{\chi}$ and $^{235}U_{f}/^{235}U_{n,\gamma}$. In terms of using different nuclear data libraries, the total uncertainty due to nuclear

data were in good agreement. However, the uncertainties due to the individual contributors were larger for most of the contributors when the 238 MG nuclear data library was used in a TSUNAMI-3D simulation.

During the study of the sensitivity of spacer grids, it was found that the presence of the spacer grid in the system contributes to the uncertainty due to nuclear data. This contribution was observed via the neutron-nuclide reaction contributors. The dominant nuclide ^{56}Fe of the spacer grid material was contributing to the uncertainty in a form of $^{56}Fe_{n,\gamma}$ with an impact of about 150 pcm.

In terms of the manufacturing tolerances, the highest contributors to the uncertainty in k ^{235}U enrichment (w/o) (~292 pcm), UO_2 (ρ_{UO_2}) density (~57 pcm) and moderator (T_{H_2O}/ρ_{H_2O}) temperature/density (~233 pcm). These were the parameters that were required that were propagated alongside the nuclear data uncertainty. The contribution from the rest of the parameters were less than 10 pcm.

Section 5.3 presented the results for the propagation of the input data uncertainties in the Kozloduy-6 VVER-1000 system. These input data were those that yielded uncertainties larger than 50 pcm in the individual sensitivity studies. The input data of which the uncertainties were propagated were the nuclear data, ^{235}U w/o, ρ_{UO_2} and moderator T_{H_2O}/ρ_{H_2O}. The SG height was set to 3 cm and the uncertainty was 769 pcm ($0.587\%\Delta k/k$). Although the SG height was an important contributor in terms of k_∞, the change in the uncertainty was insignificant, being 767 pcm (0.590%Δk/k) when the height was set to 4 cm.

In comparing the uncertainty due to nuclear data only to the uncertainty due to nuclear data and the other parameters as mentioned above, the change in the uncertainty was 39 pcm. Further analysis regarding this was discussed in the text in Section 5.3.

In Section 5.4, the results for fuel depletion were presented for TRITON/NEWT and TRITON/KENO-VI (MG). The computation of the number densities of the important nuclides in TRITON/NEWT was verified to be consistent with the TRITON/KENO-VI (MG) calculations. The uncertainty of the fuel depletion calculations due to nuclear data and due to all other uncertain parameters was also observed. The uncertainty in k_∞ decreases during the first burn-up steps and remains constant for the rest of the burn-up calculation.

Section 5.5 presented the results for Exercise I-1a, I-1b and I-2a of Phase 1 of the OECD/NEA benchmark. As per the OECD/NEA benchmark team's request, the uncertainty results in this section was based only on the nuclear data uncertainty for the results of the VVER-1000. The results obtained for Exercise I-1a and Exercise I-2a were submitted to the benchmark and the results for Exercise I-1b are still to be sent. The results were calculated using SAMPLER/NEWT and TSUNAMI-2D codes and the optimised parameters that were obtained in Section 5.1 were

applied in this calculations. Full core calculations were considered to be out of the scope of this study. The results that were obtained for this section were the criticality, cross-sections and burn-up results. These results were accompanied by their associated uncertainties, and where available, were compared to results that were submitted by other benchmark team members.

For Exercise I-1 of the benchmark, the criticality was calculated and was larger by 283 pcm from the referred study. However, the uncertainty due to nuclear data $\left(\%\,{}^{\Delta k}/_{k}\right)$ from the reference study was smaller by 119 pcm. The difference between the calculated cross-sections and the referenced cross-sections ranges from 1% to 23% and the uncertainties in the cross-sections from the reference were lower. These differences may be due to the different version of SCALE and the covariance library. The neutron-nuclide reaction contributors were the same between the two studies, however, the other is different.

For Exercise I-2 of the benchmark, the criticality was smaller by -1023 pcm from the reference study. The referred study does not explain or show that spacer grids were models in their calculations as it was in the current study. Therefore, this might be the contributing factor to the difference in the results, in addition to the fact that the SCALE versions and covariance library are also different.

The fuel depletion analysis presented in this section covers several aspects of the depletion calculations. There were no results previous submitted in the benchmark for the VVER fuel depletion analysis. Therefore, these results were compared with the results for the Three Mile Island fuel pin PWR results and they showed good agreement.

6 DESCRIPTION OF THE VALIDATION MODEL

In this chapter, the model that was used for the validation of neutronics calculation using KENO-VI and the techniques of the TSUNAMI-3D sequence is defined. The method used for the verification of this model is defined in this chapter as well.

6.1 THE VVER PHYSICS EXPERIMENTS: THE LR-0 REACTOR

6.1.1 INTRODUCTION

The system chosen for validation was the experiment zero-power reactor LR-0 located at the Nuclear Research Institute Rez plc in the Czech Republic. It is an experimental facility suitable for determining neutronic characteristics of a VVER reactor core. The LR-0's continuous maximal nominal power is 1 kW with a neutron thermal flux density of about 10^{13} $n.m^{-2}s^{-1}$. The LR-0 key feature allows for the possibility to achieve criticality by adjustments of the water level. The main aim of the VVER physics experiment was the assessment of the capability of simulation codes to predict the power and flux for neutronics calculations. The objective of the experiment is to create the experimental data bases, which could be utilised for validation of criticality codes and libraries used for neutronic calculations in safety analyses of criticality of cores. The VVER-1000 LR-0 system is a good system for testing the methodology being developed in terms of the uncertainty quantification.

Because of the nature of this reactor, the 3D computer code KENO-VI of SCALE-6.2.1 is used. The models used to generate eigenvalue and uncertainty results are based on the models defined in earlier chapters for the cases given in the LR-0 benchmark specification. The results obtained using KENO-VI will further be compared against MCNP4a results provided from the VVER physics experiment specification. In addition to the KENO-VI validation, the TSUNAMI-3D sequence will be validated by quantifying the nuclear data induced uncertainties in the eigenvalue of the system. This is done by evaluating neutronics similarity between different systems, in this case, the OECD/NEA benchmark and the LR-0 benchmark.

6.1.2 THE VVER PHYSICS EXPERIMENT DESCRIPTION

The LR-0 reactor fuel inventory consists of 67 shortened VVER-1000 type dismountable fuel assemblies that are placed inside an aluminium cylindrical tank with an inner diameter of 350 cm. The wall of the tank is 1.6 cm thick and the tank is located in a massively heavy concrete shielding. The fuel assemblies are placed on a plate called the standard supporting plate to allow the change of the fuel assemblies' pitch in the triangular lattice. The core level above the standard supporting plate is filled with moderator of demineralised water with dilute boric acid up to a given moderator height. The area above the moderator is filled with air. The general view of the reactor is given in

Figure 6-1. Each fuel assembly contain 312 fuel pins with enrichments, 18 cluster tubes, 1 central tube and five spacer grids to hold the control-cluster tubes and fuel pins together.

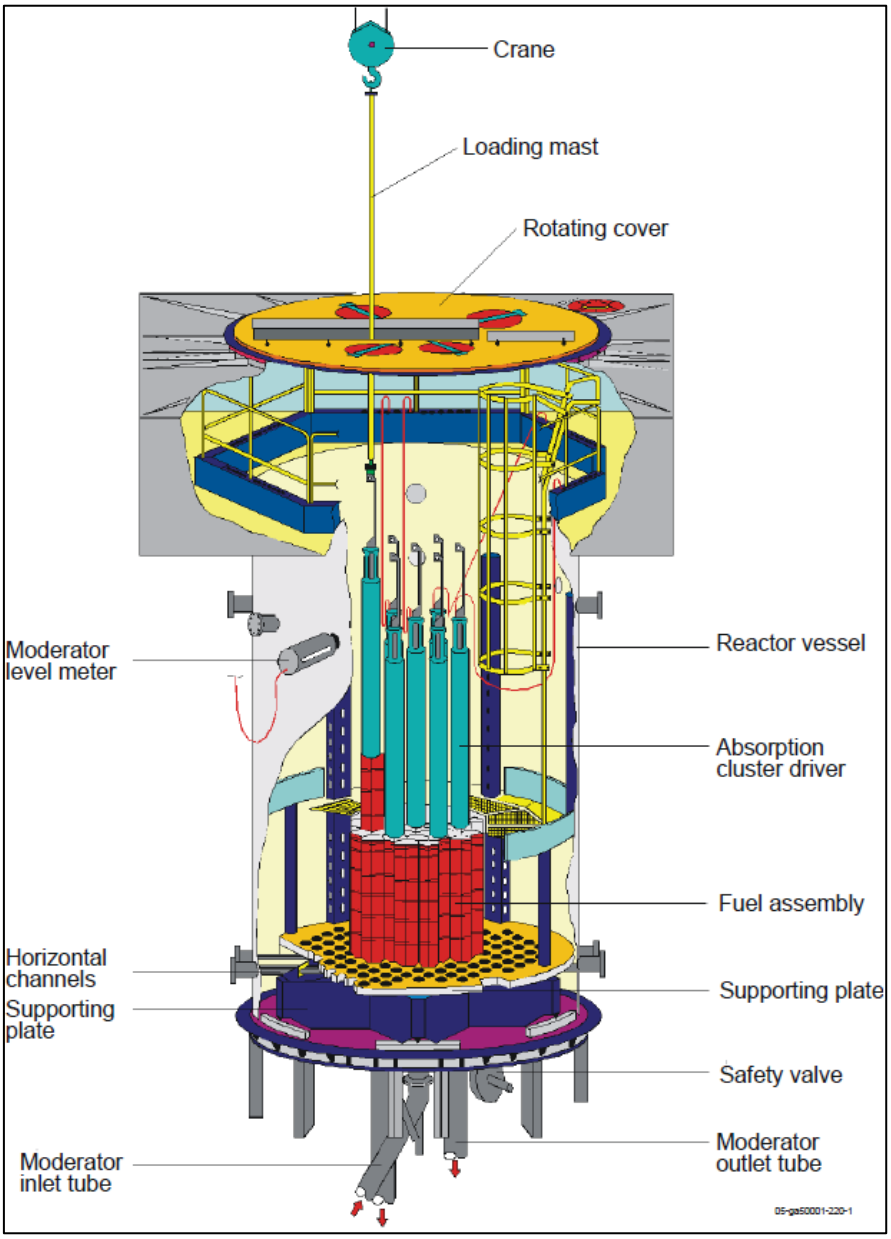

FIGURE 6-1: SCHEMATIC DESCRITPITON OF THE LR-0 REACTOR

There are 10 experiments that were evaluated in the LR-0 reactor in 1998 for criticality results, and those experiments were accepted as LR-0 benchmarks. The experiments consisted of 6 fuel assemblies surrounding a fuel assembly at the centre of the core and three emergency cluster assemblies. The ^{235}U enrichments of the centre fuel assembly could be 2 $wt.\%$, 3.0 $wt.\%$, 3.3 $wt.\%$, 3.6 $wt.\%$ and 4.4 $wt.\%$ and was differed in each experiment. The ^{235}U enrichment of the surrounding fuel assemblies was kept at 4.4 $wt.\%$ for the first five experiments and at 3.6 $wt.\%$ for the remaining five experiment (Kyncl, et al., 2005). The specific details of the fuel assemblies and core structures such as the materials and geometry of each component are given in Section 6.1.3.

Although the neutronics validation analysis and uncertainty quantification is based mainly on the first experiment, criticality calculations for the 10 experiments will be given for comparison with the results in the LR-0 benchmark. The following Section 6.1.3 will provide specifications for all the other nine experiments.

6.1.3 MODELLING OF THE LR-0 REACTOR SYSTEM

In order to be able to model the LR-0 reactor, a detailed 3D KENO-VI model was developed following the specifications that were provided in the LR-0 benchmark experiment's document. Although a 3D KENO-VI model gives one of the best representations of a real system, there are components in a reactor system that are peculiar and can be difficult to model in a computer code. In this instance, the model must be developed such that simplifications are made on these peculiarities. In the specification document of the experiment, a model was developed with simplifications made on the core and fuel assembly details (Kyncl, et al., 2005). These simplifications are considered to have small influence on the criticality results. One of the simplifications were on the geometry of the fuel assemblies and the fuel rods, where certain parameters such as the plenum volumes and springs were ignored altogether. In this section, the model of the LR-0 benchmark is given in detail including all the assumptions that were defined in the LR-0 benchmark.

The core shown in Figure 6-2 consists of ten assemblies, six which are fuel assemblies surrounding one centre assembly and three of which are emergency cluster assemblies. The simplified form of the core is shown axially in Figure 6-3. The core has three reflectors below the fuel assemblies which are a special plate, benchmark plate and standard plate. They all consist of steel and water mixtures. The moderator below the last reflector as can be seen in Figure 6-3 is fixed with a height of 14.8 cm and is made of demineralised water with diluted boric acid.

TABLE 6-1: CORE DIMENSIONS

Diameters	Value (cm)
Core diameter	120.00
Core height	149.02
Special plate height	5.50
Benchmark plate height	7.00
Standard plate height	6.20
Water reflector height	14.80

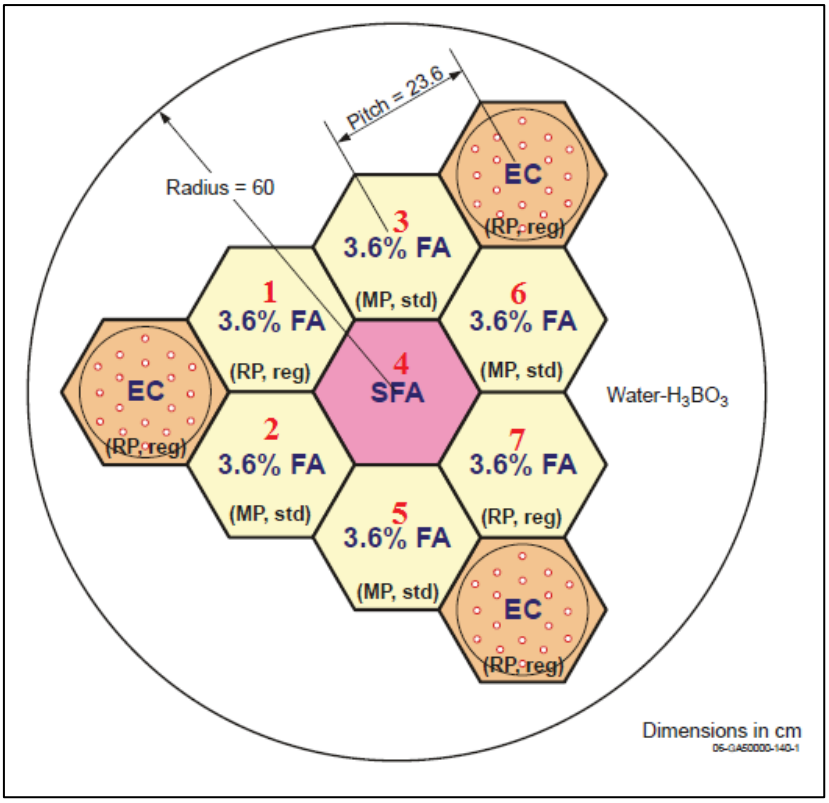

FIGURE 6-2: LR-0 REACTOR TOP LAYOUT

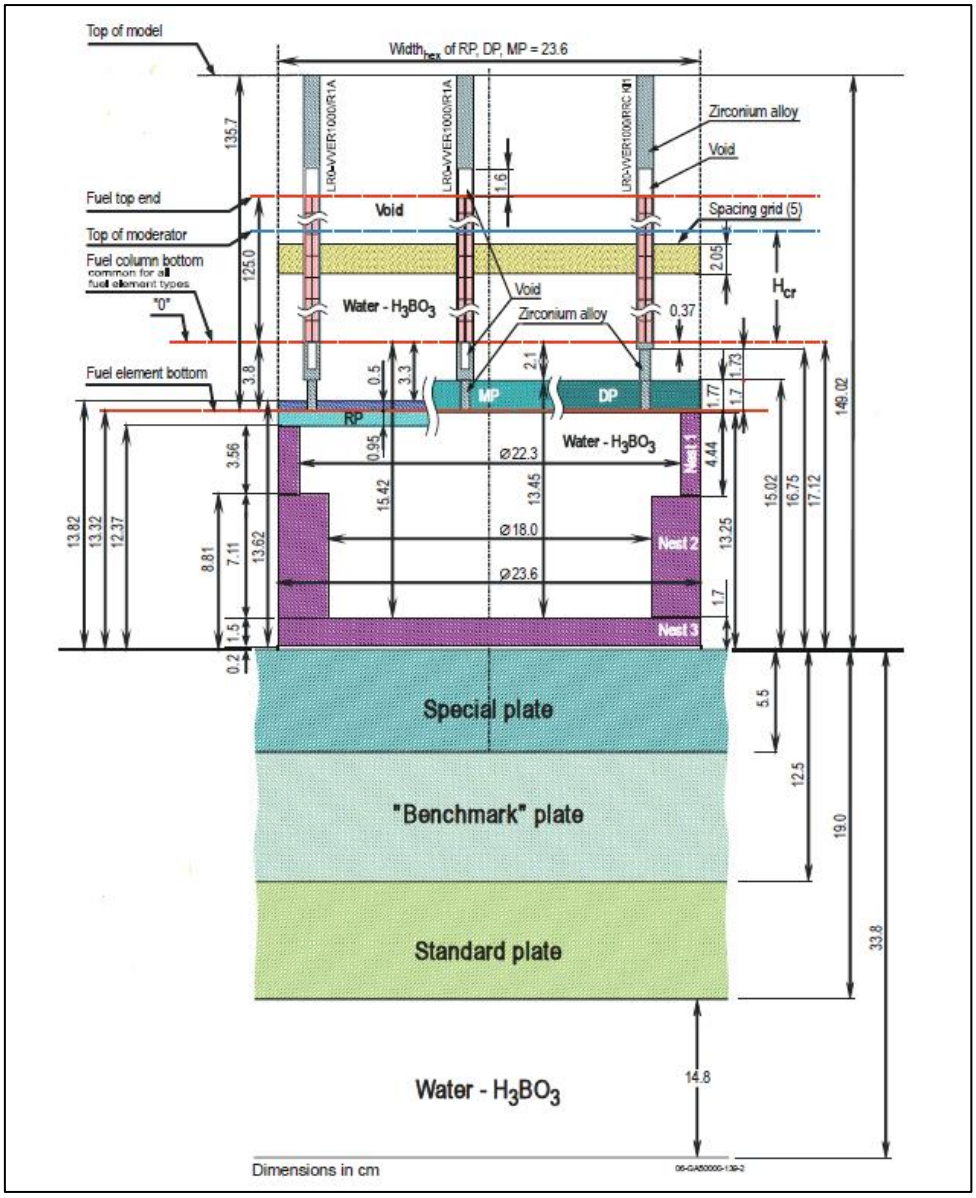

FIGURE 6-3: HORIZONTAL VIEW OF THE REACTOR

6.1.3.1 *The fuel assembly specifications*

As it has been mentioned earlier, each fuel assembly contains 312 fuel rods, 18 guide tubes, one instrumentation tube and five spacer grids. The fuel assembly has a height of 149.02 cm and a pitch of 23.6 cm. There are two ways of distinguishing each fuel assembly in the core. The first way is by the arrangement of the cluster tubes. The cluster tubes can be arranged in either a standard (std) or a regular (reg) arrangement as shown in Figure 6-4. The layout in the core is shown in Figure 6-2. The emergency clusters are arranged in a regular arrangement.

The second way to distinguish the fuel assembly is by the base plate. There are three different types of the base plates and those are a regular plate (RP), milled plate (MP) and drilled plate (DP) as can be seen in Figure 6-3 and marked as RP, MP and DP. The three types of the base plate have a lower and upper part, with both parts made up of stainless steel and demineralised water

diluted with boric acid. Because of the complexity of the structure of the base plates, the lower and upper parts of each base plate types were simplified by homogenising the materials that defines those structures. The base plate can be seen in Figure 6-3.

The arrangement of each fuel assembly in the core for each case is given in Table 6-2. The positions 1 to 7 that appear in the third row are shown in Figure 6-2 and “CENTER” is Position 4 in Figure 6-2.

The height of the moderator for each case is different as can be seen in Table 6-3.

TABLE 6-2: FUEL ASSEMBLY ARRANGEMENT

	Fuel assembly number						
Experiment	1	2	3	CENTRE	5	6	7
Case 1	RP, std	RP, std	RP, std	RP, std	RP, std	RP, std	RP, std
Case 2	RP, std	RP, std	RP, std	RP, reg	RP, std	RP, std	RP, std
Case 3	RP, std	RP, std	RP, std	DP, std	RP, std	RP, std	RP, std
Case 4	RP, std	RP, std	RP, std	RP, reg	RP, std	RP, std	RP, std
Case 5	RP, std	RP, std	RP, std	RP, reg	RP, std	RP, std	RP, std
Case 6	RP, reg	MP, std	MP, std	RP, reg	MP, std	MP, std	RP, reg
Case 7	RP, reg	MP, std	MP, std	RP, std	MP, std	MP, std	RP, reg
Case 8	RP, reg	MP, std	MP, std	DP, std	MP, std	MP, std	RP, reg
Case 9	RP, reg	MP, std	MP, std	RP, reg	MP, std	MP, std	RP, reg
Case 10	RP, reg	MP, std	MP, std	RP, reg	MP, std	MP, std	RP, reg

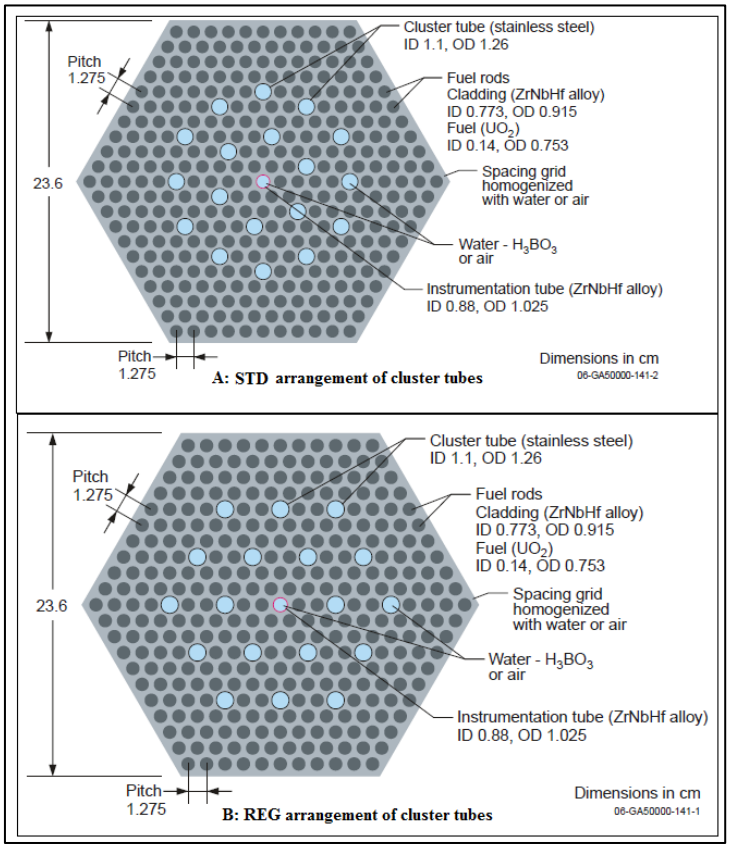

FIGURE 6-4: FA – (A) STD; AND (B) REG ARRANGEMENT

TABLE 6-3: CRITICAL MODERATOR HEIGHT

Experiment	Moderator H (cm)
Case 1	40.210
Case 2	43.872
Case 3	45.861
Case 4	47.856
Case 5	63.033
Case 6	56.227
Case 7	48.379
Case 8	60.484
Case 9	65.292
Case 10	113.680

6.1.3.2 *The rod dimensions*

The fuel pins (FP), guide tubes (GT) and instrumentation tube (IP) have hexagonal symmetry with a pitch of 1.275 cm. The rods in the current analysed system is modelled the same way as OECD/NEA benchmark discussed in Chapter 4. The FP is modelled as a concentric cylinder of inner hole, fuel, gap and clad while the GT and IP are modelled as two concentric cylinders of moderators and clad surrounded by moderator. The outer (OD) and inner (ID) diameter of the cylinders are given in Table 6-4. The height of each fuel pin is 135.7 cm, of which 3.8 cm is the bottom, 125.0 cm is the active length and 6.9 cm is the height of the top end of the fuel pin. The height of the GT and IP is 135.7 cm with no bottom or top ends.

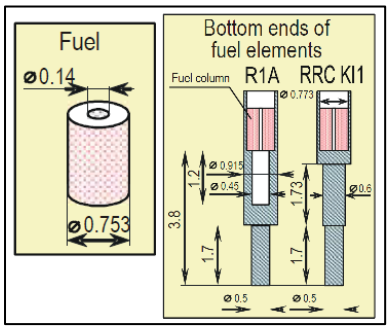

FIGURE 6-5: BOTTOM ENDS

Geometrically, there are two types of FP and can be differentiated at the bottom ends as shown in Figure 6-5. The choice of the type of the FP type depends on the choice of the base plate type in each fuel assembly, as it is demonstrated in Figure 6-3. The top ends are the same for the two types of FP.

TABLE 6-4: LR-0 RODS DIAMETERS

Diameters	Value (cm)
Inner Hole OD	0.140
Fuel Pin OD	0.753
Gap OD	0.773
Clad OD	0.915
Guide tube ID	1.100
Guide tube OD	1.260
Instru. tube ID	0.880
Instru. tube OD	1.025

6.1.3.3 *Materials specifications*

The main materials of the LR-0 system are UO_2, zirconium alloy, stainless steel and demineralised water with boric acid. The fuel pins consist of UO_2 pellets with an inner hole filled with dry air, and an outside gap filled with helium, and is enclosed by a zirconium alloy cladding. The guide tubes are made up of stainless steel and the instrumentation tube is made of zirconium alloy. The moderator up to the critical height is demineralised water with boric acid and the area above the critical moderator height is considered to be filled with dry air.

Table 6-5 and Table 6-6 shows the respective enrichment and densities of UO_2 of each assembly, in each experiment. The enrichment in the centre fuel assemblies are different in each case. For the surrounding assemblies, the enrichment was considered to be slightly different for each assembly. The method to obtain these enrichments and densities was provided in the LR-0 benchmark (Kyncl, et al., 2005).

TABLE 6-5: FUEL ENRICHMENTS (w/o)

	Fuel assembly number						
Experiment	1	2	3	CENTRE	5	6	7
Case 1	4.4168	4.3689	4.3422	4.3498	4.3749	4.3415	4.4589
Case 2	4.4168	4.3689	4.3422	3.5945	4.3749	4.3415	4.4589
Case 3	4.4168	4.3689	4.3422	3.2968	4.3749	4.3415	4.4589
Case 4	4.4168	4.3689	4.3422	3.0119	4.3749	4.3415	4.4589
Case 5	4.4168	4.3689	4.3422	2.0148	4.3749	4.3415	4.4589
Case 6	3.6028	3.5959	3.5962	3.5945	3.5941	3.5942	3.5945
Case 7	3.6028	3.5959	3.5962	4.3498	3.5941	3.5942	3.5945
Case 8	3.6028	3.5959	3.5962	3.2987	3.5941	3.5942	3.5945
Case 9	3.6028	3.5959	3.5962	3.0113	3.5941	3.5942	3.5945
Case 10	3.6028	3.5959	3.5962	2.0154	3.5941	3.5942	3.5945

TABLE 6-6: FUEL DENSITIES (g/cm^3)

	Fuel assembly number						
Experiment	1	2	3	CENTRE	5	6	7
Case 1	10.0712	10.0388	10.0666	10.0531	10.0785	10.0614	10.1405
Case 2	10.0712	10.0388	10.0666	10.3011	10.0785	10.0614	10.1405
Case 3	10.0712	10.0388	10.0666	10.3378	10.0785	10.0614	10.1405
Case 4	10.0712	10.0388	10.0666	10.4057	10.0785	10.0614	10.1405
Case 5	10.0712	10.0388	10.0666	10.3199	10.0785	10.0614	10.1405
Case 6	10.3112	10.2997	10.3203	10.3011	10.3007	10.3376	10.3011
Case 7	10.3112	10.2997	10.3203	10.0531	10.3007	10.3376	10.3011
Case 8	10.3112	10.2997	10.3203	10.3487	10.3007	10.3376	10.3011
Case 9	10.3112	10.2997	10.3203	10.4021	10.3007	10.3376	10.3011
Case 10	10.3112	10.2997	10.3203	10.3014	10.3007	10.3376	10.3011

The compositions and densities of the zirconium alloy, stainless steel and demineralised water with boric acid are given in Table 6-7. The boric acid has a boron concentration of 4.59 g/kg which is equivalent to 803.25ppm.

TABLE 6-7: MATERIAL COMPOSITIONS

Material	**Composition**	**Density (g/cm^3)**
Zirconium alloy	Zr-99.97%, Nb-1.00%, Hf-0.03%	6.45
Stainless steel	Fe-69.33%, Ni-11.00%, Cr-18.00%, Si-0.40%, Mn-1.00%, C-0.04%, Ti-0.20%, P-0.018%, S-0.01%	7.9
Demineralised	$H_2O + H_3BO_3$	0.99798

All the materials of the complex structures of the system were treated as homogenised materials of stainless steel and water. Table 6-8 shows the homogenised materials together with their associated densities for the materials required for the model.

The volume fractions of the individual components for the homogenised materials are shown in columns two and three of Table 6-8. The final densities of the homogenised materials are derived from summing up the product of the volume fraction and densities of each component in the volume being homogenised. In the case of the spacer grids, above the moderator height, the spacer grids are homogenised with air using the same volume fraction as the stainless steel and water fraction.

TABLE 6-8: HOMOGENISED MATERIALS

Components	Water	Stainless steel	Densities
Spacer grid	0.82608	0.17392	2.19988
RP Lower part	0.03740	0.96260	7.64193
RP Upper part	0.01792	0.98208	7.77635
MP Lower part	0.47094	0.52906	4.65042
MP Upper part	0.35845	0.64155	5.42662
DP Lower part	0.67986	0.32014	3.20883
DP Upper part	0.61177	0.38823	3.67866
Artificial layer	0.89530	0.10470	1.72225
Benchmark plate	0.74684	0.25316	2.74665
Standard plate	0.95314	0.04686	1.32314

6.2 CRITICALITY BASE MODEL

As it has been discussed earlier, a KENO-VI criticality calculation is achievable when a nuclear data library, geometry and materials of the system modelled are specified. In this analysis, a KENO-VI model was developed based on the methods given in Section 3.7. The nuclear data libraries considered for this study were the CE-ENDF/B-VII.1 and the 56MG-ENDF/B-VII.1. For the MG library, the parameters that were used for the XSProc processing of the cross-section are obtained in Table 5-3 of Chapter 5. The geometry and materials are defined based on the specification given in Section 6.1.3. To ensure a negligible statistical uncertainty due to KENO-VI methods, the number of inactive cycles, NSK, was set to 150, the number of active cycles, GEN, was set to 1000 and the number of source generations, NPG, was set to 40000.

6.3 MCNP CODE FOR CRITICALITY CALCULATIONS

Using the specifications given in Section 6.1.3, MCNP4a was used to model several of the scenarios. The nuclear libraries were ENDF/B-VI (60.c) and ENDF/B-V. MCNP (Monte Carlo N-Particle code) is a worldwide code that uses the Monte Carlo stochastic technique to attain the solutions of the neutronics simulations. The theory behind MCNP was briefly discussed in Section 2.2.2 and the random walk of the neutrons are modelled similarly to the way in which they are modelled in KENO-VI. The difference is in the way the multiplication factor k is calculated. MCNP can model a three-dimensional geometry and run in parallel mode.

There are two calculations that were performed for Case 1 of the experiments. One calculation was using the nuclear data library ENDF/B-V and the other was using ENDF/B-VI (60.c). Using nuclear data library ENDF/B-VI (60.c) will give results that are 150 pcm smaller than with nuclear data library ENDF/B-V, with the k being 1.00080 and 1.00230 respectively (Kyncl, et al., 2005). This has proven that changing the nuclear data library affects the criticality results.

For this analysis, an additional calculation of the LR-0 benchmark experiment was performed using MCNP6 to obtain the criticality results. This was done to verify the results of the MCNP4b and to assist with the validation of the KENO-VI code. The nuclear cross-sections for these codes are both obtained from the evaluated nuclear data file (ENDF). The advantage of using the MCNP6 alongside of the KENO-VI is that ENDF/B-VII.0 and ENDF/B-VII.1 are available in both codes.

6.4 VERIFICATION OF THE MODELS BY NWURCS CODE

The North-West University Reactor Code Suites (NWURCS) is a Fortran compiled sets of codes used to generate input files for codes such as MCNP, SCALE and RELAP. In terms of SCALE, the input files are generated for the modules NEWT and KENO. The models discussed thus far in this chapter and the preceding chapters were developed by the author of this work without the use of NWURCS. However, a few models were also developed using NWURCS. These were the validation models. Therefore, the agreement of the first set of models with those generated using NWURCS serves to verify the first set of models. Version 1 of NWURCS had already been used successfully to build a full core VVER-1000 model (Nyalunga, et al., 2016).

However, NWURCS is still under development, and is currently in Version 2. An important change has been to model axial layers independently. Then there is no longer any distinction between the layers being in the core or in the bottom or top axial reflectors is no longer a distinction. Version 1 of NWURCS required three sets of axial regions, the core and the upper and lower reflectors. A second change was to change the definition of the volumes in the input for NWURCS from complex surfaces to simple surfaces as defined in both MCNP and KENO-VI (Naicker, 2018). Therefore, an agreement between the author's models with those generated by NWURCs serves to verify the changes made in NWURCS going from Version 1 to Version 2.

6.5 SENSITIVITY AND UNCERTAINTY ANALYSIS

Following the methodology for the uncertainty propagation of the exercises in the OECD/NEA benchmark as shown in the previous chapters, the sensitivity and uncertainty analysis of the LR-0 benchmark was divided into two parts. In the first part, the sensitivities due to the individual parameters, based on the experience gained in the earlier chapters, were studied. The sensitivities studied were separated in to the following categories:

- Sensitivity due to the geometry modelling methods;
- Sensitivity due to materials; and
- Sensitivity due to manufacturing tolerances.

In parallel with results of the OECD/NEA benchmark, the geometry and material sensitivities were performed in terms of the spacer grid geometric modelling and choice of spacer grid material. The three modelling methods defined in Section 4.5.3.1 to treat the spacer grids in the VVER-1000 system were used.

In the specifications of the LR-0 benchmark, the spacer grids were homogenised using the banded homogenisation model (HMB). A comparison using a heterogeneous model (HTB) was carried out to verify the HMB simplification.

TABLE 6-9: PARAMETER'S TOLERANCE LIMITS

Parameter	Actual value	Tolerance limit
ρ_{fuel} (g/cm^3) central	10.05310	+0.300
ρ_{fuel} (g/cm^3) drive	10.07620	+0.300
C_b (g/kg)	4.59000	+0.060
H_{cr} (cm)	40.21000	-0.058
^{235}U w/o central FA	4.40000	-0.054
^{235}U w/o drive FA	4.40000	-0.054
Hf content in clad	0.30000	-0.300
Nb content in clad	1.00000	+0.050
ρ_{H_2O} (g/cm^3)	0.99798	+0.003
T_{H_2O} (K)	291.000	+2.000

To evaluate the sensitivities due to the manufacturing tolerances, the limits of the parameters of interest is given in the Table 6-9. These limits were obtained from the benchmark experiments specifications. For this analysis there are parameters that are added, which were not available in the quantification of the OECD/NEA benchmark uncertainty. These parameters were not part of the OECD/NEA benchmark analysis since the model either did not have them defined in the system or they were not specified in the OECD/NEA benchmark specifications of the tolerance limits. They were however in the LR-0 benchmark specifications, and are also considered.

Some parameters, which were observed in Chapter 5 are not included in this section, since they were proven to be insignificant on the results in Chapter 5. These parameters are the diameters of the fuel inner hole, fuel pellet, gap as well as the fuel clad. When each clad diameter pin is perturbed individually using a uniform distribution, the uncertainty was 14 pcm, equivalent to 0.01%. This was then assumed for the other diameters of the fuel rod as it was also done in Section 5.2.5. Hence, in this analysis, the diameters of these components were not included as part of the sensitivities of the tolerance limits.

Once the high uncertainty contributing parameters were identified, the uncertainties of these parameters were then propagated in the calculation to get the final uncertainty in the criticality results.

6.6 SUMMARY

This chapter has defined the modelling methods for the VVER-1000 validation core

7 VALIDATION AND UNCERTAINTY ANALYSIS OF THE LR-0 REACTOR CORE

The neutronics results for the uncertainty quantification and validation analyses of the VVER-1000 LR-0 are summarised and evaluated in this chapter. The first part of the results is the nominal results of the LR-0 reactor criticality results performed on Case 1 of the LR-0 benchmark experiment. These results are accompanied by a convergence analysis of the model result. The second part of the results is the verification of the model by comparing results between a manually defined input and the input generated using NWURCS. Section 7.2.1 of the results discusses the validation results by comparing results obtained from SCALE-6.2.1 code with the measured results, as well as the results obtained using MCNP6. The third section of this chapter evaluates the results of cases 2 - 10. The fourth sections provide results of the uncertainty in k_{eff} due to nuclear data. The fifth and sixth section provides results for the sensitivity analysis. The last section gives the uncertainty quantification results and concludes this chapter. The verification and validation analyses are presented by starting with the multiplication factor k_{eff}, accompanied by its statistical uncertainty. Then, the UQ of these results is evaluated by analysing the nuclear data, method and modelling uncertainties, and manufacturing tolerances.

7.1 NOMINAL CRITICALITY RESULTS

The results analysis is based on the multiplication factor (k_{eff}) for KENO-VI (CE) calculation. The KENO-VI (CE) k_{eff} results were considered accurate and optimised when the statistical uncertainty was about $\sigma = 0.00015$. The nuclear data library that was used for this calculation was the CE-ENDF/B-VII.1. The uncertainty in the k_{eff} due to nuclear data for this model is provided alongside the k_{eff} as can be seen in Table 7-1. The result for k_{eff} was 1.00429 and this value is larger than the criticality value of 1.0000 by 429 pcm. In this chapter, the factors that may be contributing to this difference will be analysed from Section 7.1.1 to 7.2.5.

The uncertainty of k and those due to the neutron-nuclides reaction contributors are given in Table 7-1. These results were obtained with the use of the TSUNAMI-3D code. The impact of nuclear data uncertainties to the k results in terms of Δk was about 580 pcm (equivalent to 0.57674 $\%\Delta k/k$ seen in Table 7-1). The highest neutron-nuclide reaction contributor was $^{235}U_{nubar}$ with an impact of about 350 pcm and the 11th neutron-nuclide reaction contributor was $^{56}Fe_{n,\gamma}$ with an impact of about 67 pcm (it will be discussed later that $^{56}Fe_{n,\gamma}$ appeared as the 5th contributor for the OECD/NEA benchmark).

TABLE 7-1: NEUTRON-NUCLIDE CONTRIBUTORS

k_{eff}	$\%\Delta k/k$
1.00429	0.57674

Contributors	$\%\Delta k/k$
$^{235}U_{nubar}$	0.34947
$^{238}U_{n,n'}$	0.26621
$^{238}U_{n,\gamma}$	0.20055
$^{235}U_{\chi}$	0.18277
$^{235}U_{n,\gamma}$	0.16176
$^{235}U_{fission/n,\gamma}$	0.11696
$^{235}U_{fission}$	0.11017
$^{16}O_{elastic}$	0.92052
$^{1}H_{elastic}$	0.88956
$^{1}H_{n,\gamma}$	0.69673
$^{56}Fe_{n,\gamma}$	0.66226

7.1.1 CONVERGENCE OF THE MODEL

7.1.1.1 *Fission source and* k

The input code parameters, $NSK = 150$ (inactive cycles), $GEN = 1000$ (active cycles) and $NPG = 40000$ (number of source generation) of KENO-VI were taken from the calculations in Section 5. Although, the model in this section is a full core calculation, and the model in Section 5 was an FA calculation, the chosen numbers of the specified input code parameters have shown to produce converged results. To verify this statement, the Shannon Entropy plot in Figure 7-1 and k_{eff} distribution plot in Figure 7-2 were evaluated for the LR-0 models.

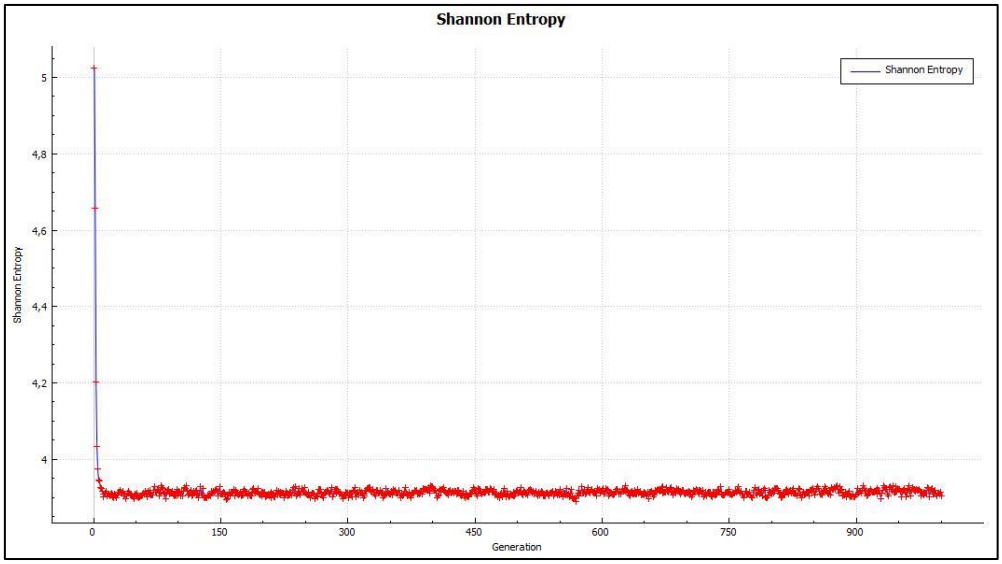

FIGURE 7-1: FISSION SOURCE DISTRIBUTION

The Shannon Entropy is automatically produced in the KENO-VI calculations. Figure 7-1 shows that the Shannon Entropy of the fission source distribution decreases during the first few cycles, then becomes constant from these few cycles to the last cycles. To further check the convergence of the fission source distribution, the results of the three-tests described in Section 3.8.1 were checked in the output file. All the tests were passed with a similar trend as from Section 5.2.1.1.

For each cycle, KENO-VI computes k_{eff}, and Figure 7-2 shows the convergence of the k_{eff} distribution over the entire cycle. k_{eff} starts to converge from 250 cycles. However, due to statistical noise in the random walk of the neutrons in each cycle, it is not clear when the k_{eff} converges. Since the fission source reached convergence at an earlier cycle, the number of active cycles required was therefore based on the statistical uncertainty in the k_{eff} required, which was chosen to be $\sigma < 0.00020$.

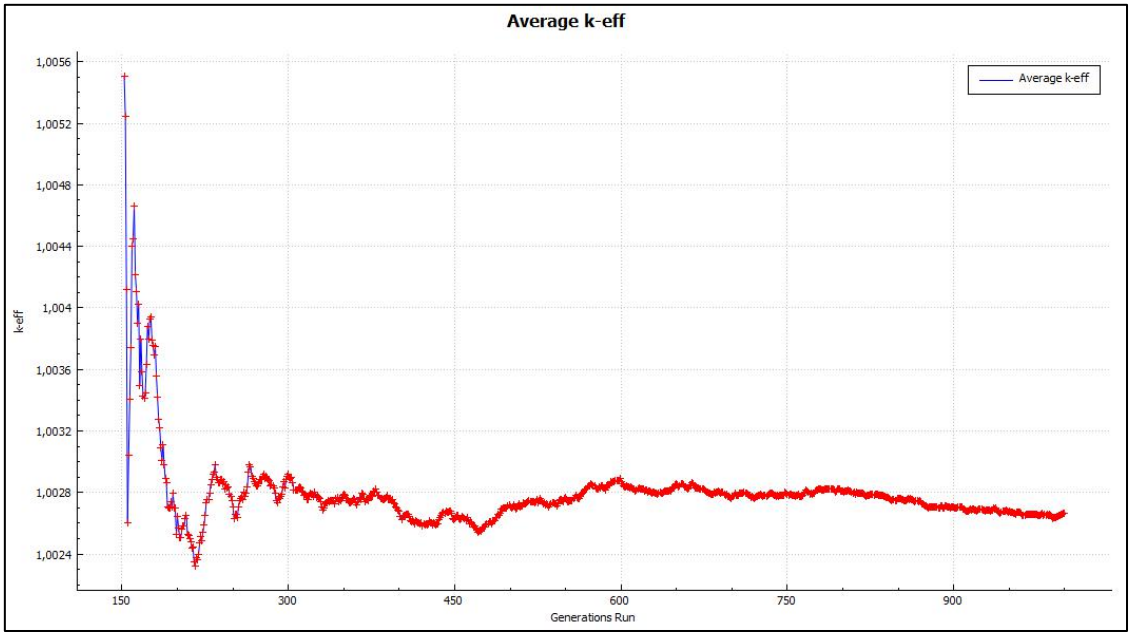

FIGURE 7-2: k_{eff} DISTRIBUTION

7.1.1.2 *Random number generations*

Table 7-2 shows the results for the random number analysis. The calculations were performed for the same input model but with the different random number seeds provided in Table 7-2. The analysis of this results is observed based on the method defined in Section 3.8.3 of Chapter 3. The statistical uncertainty σ_i for each calculation was kept at about 0.00017. See the third column of Table 7-2 for 10 calculations. The term k_{diff} was calculated as the difference between the individual k_{eff} values with their individual random number and the average k_{eff} value. In Section 5.2.1.2 of Chapter 5, 100 trials were completed for 100 different random numbers. An average of k was obtained for the first 10 trials and 100 trials, and the k_{diff} between k averages taking over

the first 10 trials and 100 trials was about 0.00004. Therefore, an analysis of the random number analysis done over 10 trials can be considered to be a solid analysis.

In this analysis, the k average, calculated by summing all the individual KENO-VI calculations over 10 trials was 1.00458 and the corresponding statistical uncertainty was $\Delta k = 0.00010$ using Eq (50). The k_{diff} remains below 0.00015 for all the 10 trials. By keeping the individual statistical uncertainties low (around 15 pcm), the uncertainty due to the random number generation is therefore insignificant and not contributing to the uncertainty propagation.

TABLE 7-2: RANDOM NUMBER ANALYSIS ON THE LR-0 SYSTEM

Random number	k	σ	k_{diff}
F98B344A37F762A0	1.00444	0.00016	0.00014
C36D1611CB11116A	1.00453	0.00016	0.00005
510EA3859FE55D2E	1.00448	0.00015	0.00010
2F4C1E007FB91E67	1.00469	0.00015	0.00011
A60ECEF273A53FC3	1.00471	0.00017	0.00013
6E9F6F5F8939EFCE	1.00462	0.00015	0.00004
31B5A1E2910151E2	1.00460	0.00016	0.00002
7CA6FC5EF2FFB67D	1.00443	0.00015	0.00015
2FF85D32E5537687	1.00468	0.00015	0.00010
91A03F688CE610A7	1.00461	0.00015	0.00003

7.1.1.3 *F*(r) convergence*

As it was discussed earlier, the convergence of the $F^*(r)$ tallies are required before it can be applied to calculate the uncertainties. A $5 \times 5 \times 5$ mesh size with $NSK = 150$ was used as the parameters at which the $F^*(r)$ function over the scored tallies was converged. As it is seen in Figure 5-21, 3% of the $F^*(r)$ tallies contain more than 50% uncertainty. With this low number, it was assumed that the $F^*(r)$ tallies have converged and will accurately estimate the uncertainties due to nuclear data. The recommendations given in a study by Sihlangu (Sihlangu, et al., 2018) was used to form this mesh. The SCALE manual (Rearden & Jesse, 2016) also recommends a small mesh.

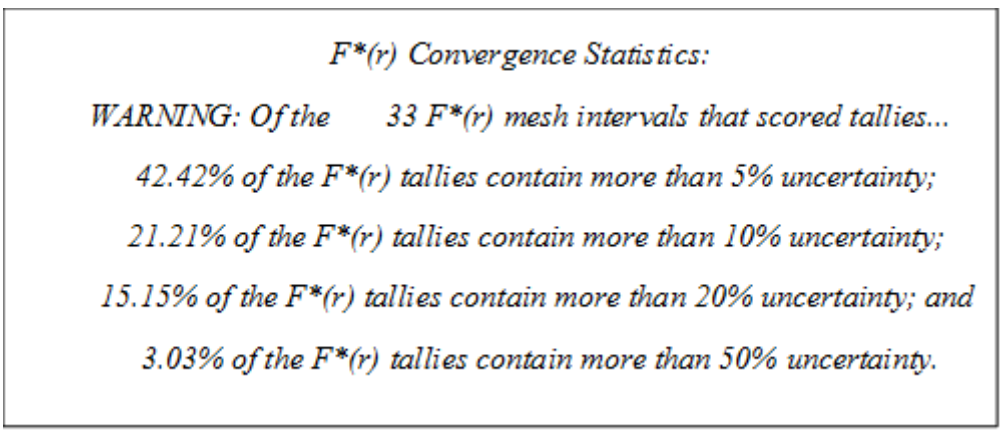

FIGURE 7-3: F*(R) SCORED TALLIES

7.1.2 VERIFICATION OF LR-0 SYSTEM CALCULATIONS

To verify the results in this section, two KENO-VI input files were compared. One was hand-written (HDW) and the second one was generated using the NWURCS code. The verification of this model was based on the material number densities and the geometry defined for this model.

7.1.2.1 *Verification of material definition*

To verify the number densities of the material used in the model, a comparison of the number densities between NWURCS generated data and LR-0 benchmark data was done to obtain a $\%\ diff$. The comparison between two number density data has shown a good agreement, with a slight $\%\ diff$ that is <0.5% as can be seen in Table 7-3. In Table 7-3, only UO_2 and demineralised water with boric acid were given for the verification. The difference in all the material number densities for the system were <0.5%. The reason for this slight difference may be due to slight differences in either the molar masses or weight fractions used.

TABLE 7-3: $\%\ diff$ OF THE NUMBER DENSITIES

Isotopes	NWURCS	LR-0 Benchmark	$\%\boldsymbol{diff}$
h-1	6.6799E-02	6.6781E-02	0.03
h-2	7.6827E-06	7.6807E-06	0.03
o-16	3.3457E-02	3.3382E-02	0.23
o-17	1.2752E-05	1.2716E-05	0.28
b-10	8.8797E-06	8.9023E-06	-0.25
b-11	3.5742E-05	3.5833E-05	-0.25
o-16	4.4998E-02	4.4842E-02	0.35
o-17	1.7151E-05	1.7081E-05	0.41
u-235	9.8730E-04	9.8757E-04	-0.03
u-238	2.1436E-02	2.1442E-02	-0.03

Using the number densities provided in Table 7-3, two criticality calculations were performed to observe the effect of using NWURCS or the LR-0 benchmark number densities on the results. The difference between the two results was 25 pcm. This implies that material number densities differences contribute 25 pcm towards the overall difference between the NWURCS numbers and LR-0 benchmark numbers. Within the context of this study, the $\%\ diff$ between the number densities is considered minimal and the effect of these number densities is negligible.

Since the generation of the nuclear data processing depends on the material information given in the input, complimentary TSUNAMI-3D calculations were performed to obtain the uncertainties due to nuclear data. This was done to see the influence of the number densities on the nuclear data uncertainties. The uncertainties in the results due to nuclear data were $\%\Delta k/k = 0.57674$ $(\Delta k = 580\ pcm)$ and 0.57920 $(\Delta k = 582\ pcm)$ for HDW and NWURCS calculations respectively. This verifies that the slight change in the material number densities does not influence the nuclear data uncertainties.

7.1.2.2 *Verification of geometry definition*

In Figure 7-4, the schematic illustration of the full core (FC) geometry obtained from HDW (A) and NWURCS input (B) is given. The geometry was defined, such that it matches the specification given in the LR-0 benchmark experiment. The colours of the two systems are different because the program randomly selects the colour for each input. To complete the geometry verification, the two input files were run, and the results were differed by about 9 pcm. Except for the differences in colour of the two models, they are identical.

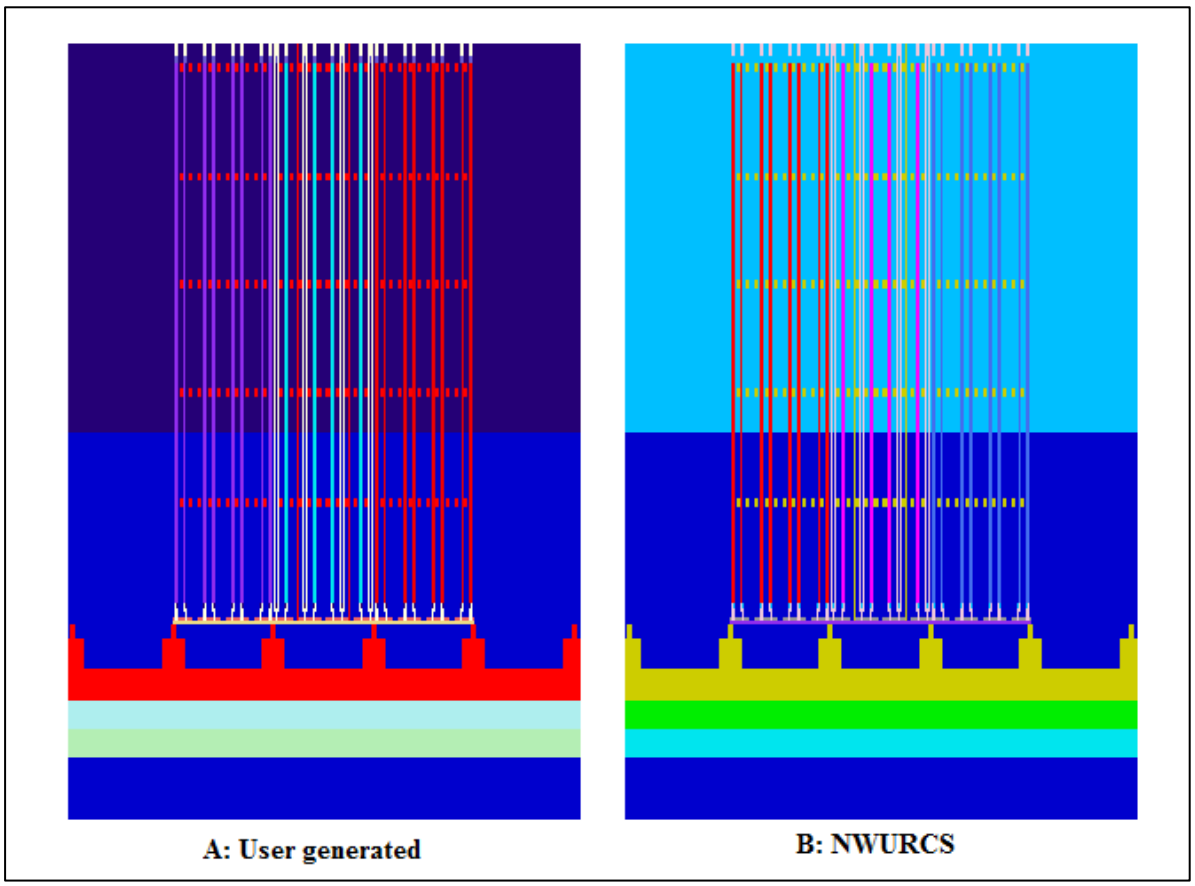

FIGURE 7-4: GEOMETRY VERIFICATION

7.2 NEUTRONICS VALIDATION RESULTS

7.2.1 RESULTS COMPARISON OF DIFFERENT CODES

As a first assessment of the validation results, the comparison between KENO-VI (CE/MG), MCNP6 and MCNP4a is given in terms of the multiplication factor and the results are reported in Table 7-4. The reported results were obtained for Case 1 of the LR-0 benchmark only. In Table 7-4, the results reported for MCNP4a were obtained from the LR-0 benchmark specifications, and the results reported for KENO-VI (CE/MG) and MCNP6 were calculated. The results based on KENO-VI (CE) of the SCALE code are taken as the base case. In Section 5.2.3 of Chapter 5, it

was recommended that, for desired KENO-VI (MG) results, the 56 MG library be used. Therefore, in this analysis, all the results calculated with KENO-VI (MG) will use the 56 MG library.

The difference between KENO-VI (CE) and MCNP4a is around -349 pcm with the statistical uncertainty of 25 pcm. This implies that k_{eff} is over-estimated by 0.4% and the difference is not within 3 standard deviations. This is due to the difference in the versions of the cross-section libraries used to provide the nuclear data in each code calculation. The results between KENO-VI (CE) and MCNP6 were in good agreement with both having good acceptable statistical uncertainty. The results performed with KENO-VI (MG) shows a discrepancy of 59 pcm, and the change in k_{∞} between the CE and MG is approximately 4 times the statistical standard deviation (slightly outside 3 standard deviations). Because this difference is slightly outside 3 standard deviations, this comparison can also be considered to be a good agreement.

TABLE 7-4: CASE 1 MCNP AND SCALE EIGENVALUE COMPARISON

Code	k_{eff} results
KENO-VI (CE)	1.00429 (0.00015)
MCNP4a	1.00080 (0.00040)
MCNP6 (ENDF-7.1)	1.00401 (0.00013)
KENO-VI (MG)	1.00370 (0.00013)

To further verify that the older versions of the cross-section libraries results in high discrepancies, an extra calculation using cross-section data obtained from ENDF-7.0 of MCNP6 was performed. The difference in the results between the ENDF-7.0 and ENDF-7.1 of the MCNP6 code is about 150 pcm which is 0.1 in % difference. This was expected, since it has been shown in several studies that discrepancies of about 1% are most likely to be obtained in the k results using different cross-section libraries (Leppanen, 2003).

7.2.2 CRITICALITY RESULTS OF CASE 2 – 10

Since the LR-0 benchmark is based on 10 experiments (10 cases), the criticality results for the other 9 cases were also obtained using KENO-VI (CE) and compared with the results provided in the LR-0 benchmark specifications. The results in the LR-0 benchmark were obtained with MCNP4a for all cases. The specifications for the 10 cases can be obtained in Section 6.1.3. As per Figure 7-5, the results among the codes clearly differ. As mentioned above, the large discrepancies between the LR-0 benchmark results and the calculated results could be attributed to the choice of the version of the nuclear data library. The profile of the calculated results from Case 2 to Case 10 is consistent with the profile of the LR-0 benchmark results as observed in Figure 7-5. The consistency in the discrepancy and the consistency in the profile therefore indicates that the models were accurately defined.

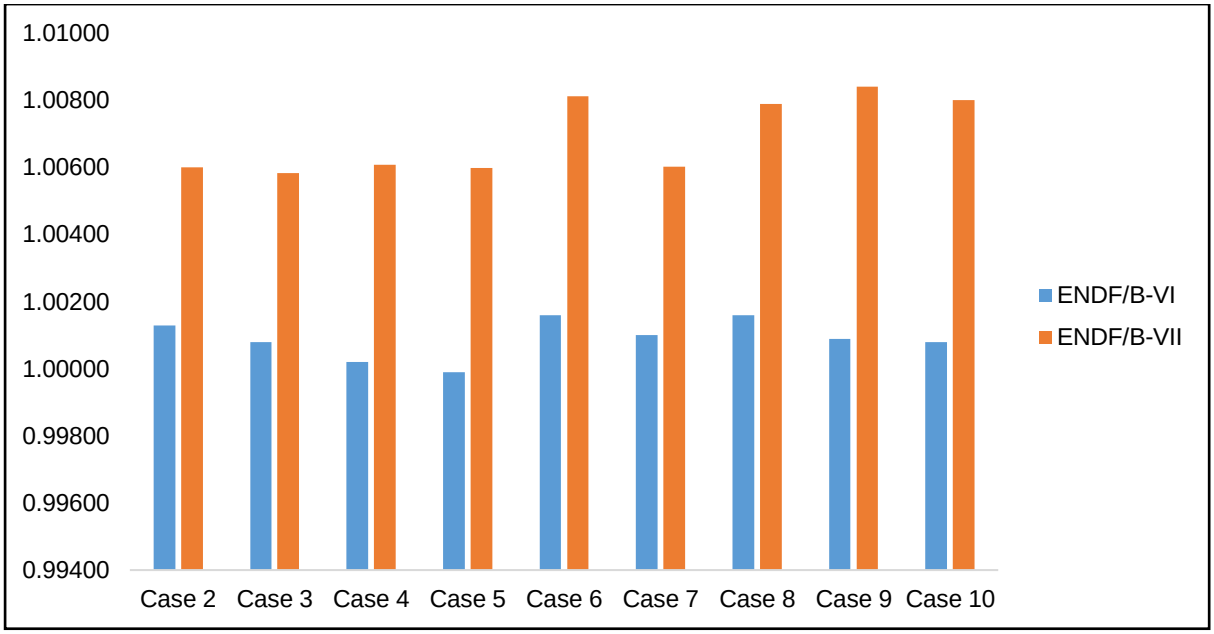

FIGURE 7-5: COMPARISON OF k RESULTS BETWEEN ENDF/B-VI AND ENDF/B-VII

7.2.3 NUCLEAR DATA UNCERTAINTY ANALYSIS

The results reported in this section are the uncertainties in k_{eff} due to nuclear data for the LR-0 Case 1 benchmark. The results were obtained using TSUNAMI-3D of the SCALE-6.2.1 code. In Table 7-5, the uncertainty in k obtained using CE ENDF/B-VII.1 and MG ENDF/B-VII.1 are shown and compared to each other. No uncertainty analysis due to nuclear data were calculated with MCNP6.

TABLE 7-5: UNCERTAINTY IN k DUE TO NUCLEAR DATA

Code	k_{eff}	$\%\,\Delta k/k$	Δk (pcm)
CE ENDF/B-VII.1	1.00429 (16)	0.57674 (58)	580
MG ENDF/B-VII.1	1.00370 (14)	0.59594 (40)	598

The uncertainties due to nuclear data is 18 pcm larger for the MG ENDF/B-VII.1 model. The results in Table 7-6 of the significant neutron-nuclide reaction contributors are given for CE ENDF/B-VII.1 and MG ENDF/B-VII.1 model. The order of the neutron-nuclides reaction contributors between the models are the same, but the magnitude of the uncertainties is different.

The highest neutron-nuclide reaction contributor was $^{235}U_{nubar}$ with an impact of about 350 pcm for both the CE ENDF/B-VII.1 and MG ENDF/B-VII.1. The last neutron-nuclide reaction contributor shown in the list is $^{238}U_{nubar}$ and has an impact of about 63 pcm.

The $\%\,diff$ between these uncertainties are given in the last column of Table 7-6. The large $\%\,diff$ between CE ENDF/B-VII.1 and MG ENDF/B-VII.1 model are seen for contributors $^{238}U_{n,n'}$, $^{238}U_{n,\gamma}$, $^{235}U_{\chi}$, $^{16}O_{\text{elastic}}$, $^{1}H_{n,\gamma}$ and $^{56}Fe_{n,\gamma}$.

TABLE 7-6: NEUTRON-NUCLIDE REACTION CONTRIBUTORS

Nuclide reaction	CE ENDF/B-VII.1	MG ENDF/B-VII.1	$\%diff$
$^{235}U_{\ nubar}$	0.34947	0.35015	-0.19
$^{238}U_{\ n,n'}$	0.26621	0.28967	-8.44
$^{238}U_{\ n,\gamma}$	0.20055	0.21581	-7.33
$^{235}U_{\ \chi}$	0.18277	0.19862	-8.31
$^{235}U_{\ n,\gamma}$	0.16176	0.16176	0.00
$^{235}U_{\ \mathrm{fission}/n,\gamma}$	0.11696	0.11733	-0.32
$^{235}U_{\ \mathrm{fission}}$	0.11017	0.11045	-0.25
$^{16}O_{\mathrm{elastic}}$	0.09205	0.08704	5.60
$^{1}H_{\mathrm{elastic}}$	0.08896	0.08809	0.97
$^{1}H_{n,\gamma}$	0.06967	0.06188	11.85
$^{56}Fe_{n,\gamma}$	0.06623	0.06242	5.92
$^{238}U_{\ nubar}$	0.06378	0.06282	1.52

7.2.3.1 *Sensitivity profiles for the first three contributors*

The following sensitivity profiles are plotted for the first three contributors obtained in Table 7-6 for the CE ENDF/B-VII.1 and MG ENDF/B-VII.1 models. The difference in the contributors between the CE ENDF/B-VII.1 and MG ENDF/B-VII.1 calculations are also observed from Figure 7-6 and Figure 7-8 for the three contributors.

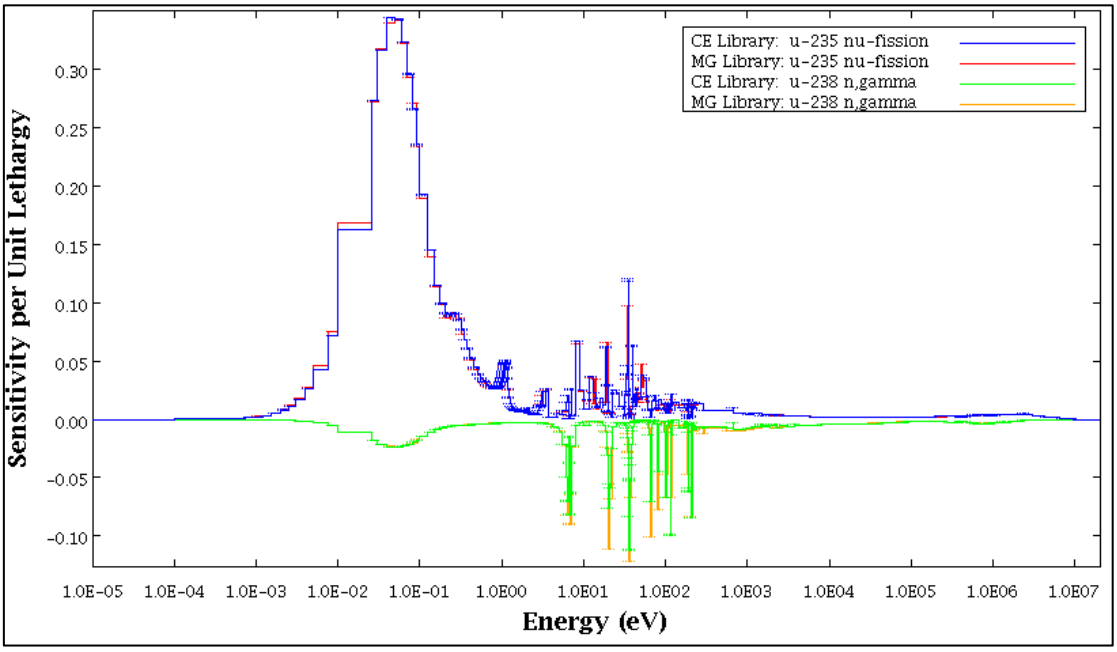

FIGURE 7-6: SDF PLOTS OF $^{235}U_{\ nubar}$ AND $^{238}U_{\ n,\gamma}$ REACTIONS

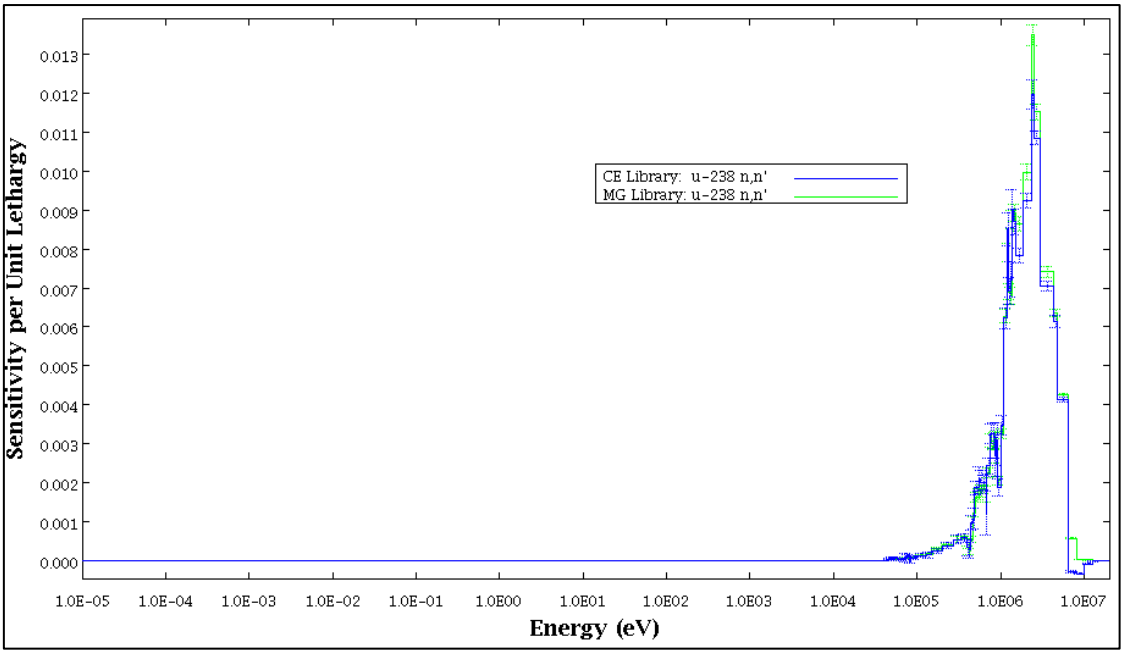

FIGURE 7-7: SDF PLOTS OF $^{238}U_{n,n'}$ REACTION

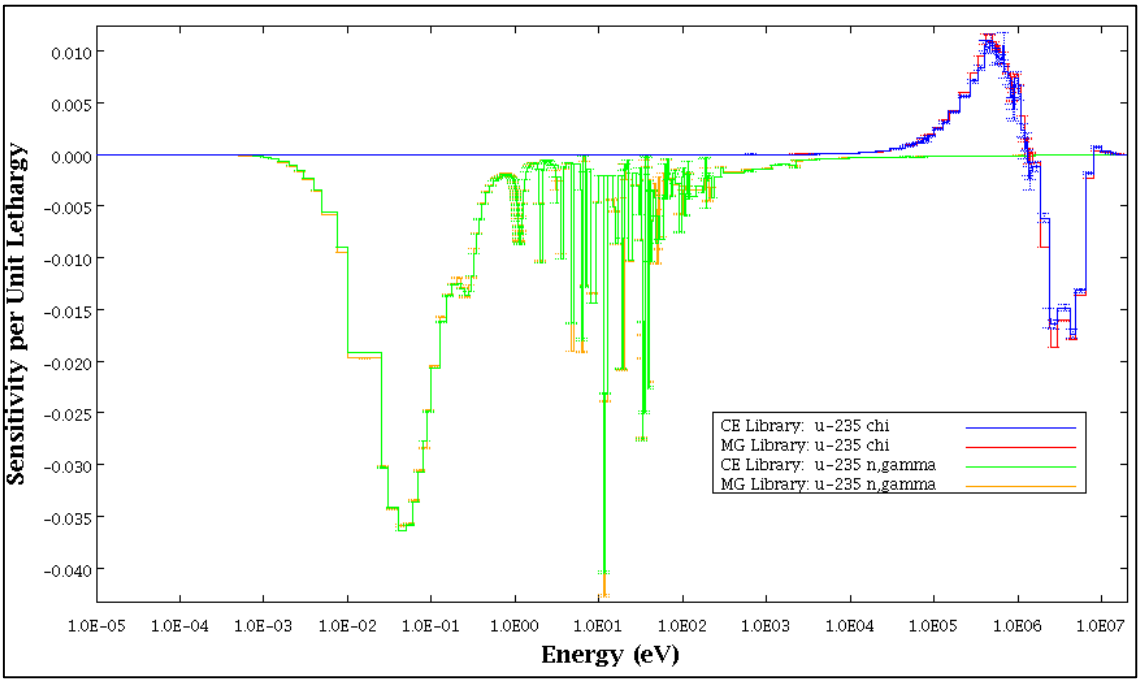

FIGURE 7-8: SDF PLOTS OF $^{235}U_{\chi}$ AND $^{235}U_{n,\gamma}$ REACTIONS

7.2.3.2 *Comparison of nuclear data uncertainty between the two benchmarks*

The uncertainty due to nuclear data was about 760 pcm for the OECD/NEA benchmark and in this model, it was 580 pcm. The difference is therefore about 200 pcm between the two models. The reason for obtaining this uncertainty could be due to the size of the model and the materials involved in each system. Since the uncertainties of the OECD/NEA benchmark were obtained for a fuel assembly calculation, a TSUNAMI-3D calculation was performed for the LR-0 fuel assembly for a fair comparison of these uncertainties. The uncertainties in the LR-0 fuel assembly were 590

pcm, which is still less as compared to the OECD/NEA benchmark uncertainties. The generation of cross-sections for a criticality results requires the definition of material and geometry. With this analysis, it can therefore be concluded that the uncertainty also depends on the size, material and geometry of the system defined.

Table 7-7 depicts the effect on k due to the neutron-nuclide reaction contributors of two systems, with the LR-0 having models for a fuel assembly and full core. According to the results in Table 7-7, the neutron-nuclide reaction contributor order differs for all the models. However, the top contributor remains $^{235}U_{nubar}$ for the three models.

Since the order of the contributors was different, Table 7-7 has been represented using a colour coding, where each contributor is allocated a specific colour. This was done to be able to identify each contributor and analyse its uncertainty within the three rows.

In Table 7-7, the uncertainties due to the neutron-nuclide contributors ranges from 400 pcm to 10 pcm for the three models. Most of the neutron-nuclide contributors have different uncertainties when compared amongst the three models. In comparison the following observations were made:

- The highest neutron-nuclide contributor $^{235}U_{nubar}$ was the same and their uncertainties were also close for the three models.
- The order of appearance of the other contributors was different for the three models.
- Although the order of the contributors was not the same for the three models, some contributors had uncertainties that were close to each other and those were: $^{235}U_{n,\gamma}$, $^{235}U_{fiss/n,\gamma}$, $^{235}U_{fiss}$, $^{238}U_{nubar}$, and $^{1}H_{n,\gamma}$.
- The uncertainties of the other contributors were quite different for the three models and those contributors were: $^{238}U_{n,n'}$, $^{238}U_{n,\gamma}$, $^{235}U_{\chi}$, $^{235}U_{n,n'/ela}$, $^{1}H_{elastic}$, $^{16}O_{elastic}$, $^{56}Fe_{n,\gamma}$, $^{238}U_{ela}$, $^{91}Zr_{n,\gamma}$, $^{92}Zr_{n,\gamma}$, $^{90}Zr_{ela}$, $^{238}U_{ela/n,\gamma}$, $^{238}U_{fiss}$ and $^{238}U_{\chi}$.

In Figure 7-9, the $\%\ diff$ of the uncertainties for each contributor was calculated between the three systems. The highest differences are mostly between the LR-0 FC and the OECD-FA models. Between the OECD-FA and LR-0 FA, the difference is quite small for most of the contributors as compared to the differences with the LR-0 FC and OECD-FA. However, as can be seen in the scatter in the colours, it is difficult to find any definite trend, except perhaps for the first three rows. However, even in this comparison, the $^{238}U_{n,n'}$ does not fit. Whilst for the LR-0 FC, its contribution is 0.2662 $\%\Delta k/k$, for the OECD FA and the LR-0 FA the values are 0.0992 and 0,0178 respectively.

TABLE 7-7: $\%\Delta k/k$ DUE TO NEUTRON-NUCLIDE REACTION FOR THREE SYSTEMS

LR-0 FC	$\%\Delta k/k$	OECD	$\%\Delta k/k$	LR-0 FA	$\%\Delta k/k$
$^{235}U_{nubar}$	0.3495	$^{235}U_{nubar}$	0.3501	$^{235}U_{nubar}$	0.3434
$^{238}U_{n,n'}$	0.2662	$^{238}U_{n,\gamma}$	0.2943	$^{238}U_{n,\gamma}$	0.2178
$^{238}U_{n,\gamma}$	0.2006	$^{235}U_{n,\gamma}$	0.1713	$^{235}U_{n,\gamma}$	0.1751
$^{235}U_{\chi}$	0.1828	$^{235}U_{\chi}$	0.1410	$^{235}U_{fission/n,\gamma}$	0.1142
$^{235}U_{n,\gamma}$	0.1618	$^{235}U_{fission/n,\gamma}$	0.1157	$^{235}U_{fission}$	0.1058
$^{238}U_{n,n'/elastic}$	-0.1531	$^{56}Fe_{n,\gamma}$	0.1100	$^{238}U_{nubar}$	0.0670
$^{235}U_{fission/n,\gamma}$	0.1170	$^{235}U_{fission}$	0.1007	$^{56}Fe_{n,\gamma}$	0.0665
$^{235}U_{fission}$	0.1102	$^{238}U_{n,n'}$	0.0992	$^{1}H_{n,\gamma}$	0.0607
$^{1}H_{elastic}$	0.0921	$^{238}U_{nubar}$	0.0675	$^{235}U_{\chi}$	0.0604
$^{16}O_{elastic}$	0.0890	$^{1}H_{n,\gamma}$	0.0632	$^{91}Zr_{n,\gamma}$	0.0346
$^{238}U_{nubar}$	0.0697	$^{91}Zr_{n,\gamma}$	0.0414	$^{1}H_{elastic}$	0.0330
$^{56}Fe_{n,\gamma}$	0.0662	$^{92}Zr_{n,\gamma}$	0.0358	$^{92}Zr_{n,\gamma}$	0.0297
$^{1}H_{n,\gamma}$	0.0638	$^{238}U_{elastic/n,\gamma}$	0.0326	$^{238}U_{elastic}$	0.0261
$^{238}U_{elastic}$	0.0494	$^{238}U_{elastic}$	0.0237	$^{238}U_{elastic/n,\gamma}$	0.0208
$^{91}Zr_{n,\gamma}$	0.0339	$^{238}U_{n,n'/elastic}$	0.0236	$^{238}U_{n,n'/elastic}$	0.0202
$^{92}Zr_{n,\gamma}$	0.0295	$^{238}U_{\chi}$	0.0219	$^{238}U_{\chi}$	0.0178
$^{90}Zr_{elastic}$	0.0274	$^{16}O_{elastic}$	0.0186	$^{238}U_{n,n'}$	0.0178
$^{238}U_{elastic/n,\gamma}$	0.0196	$^{238}U_{fission}$	0.0154	$^{238}U_{fission}$	0.0168
$^{238}U_{fission}$	0.0188	$^{1}H_{elastic}$	0.0146	$^{90}Zr_{elastic}$	0.0134
$^{238}U_{\chi}$	0.0178	$^{90}Zr_{elastic}$	0.0026	$^{16}O_{elastic}$	0.0112

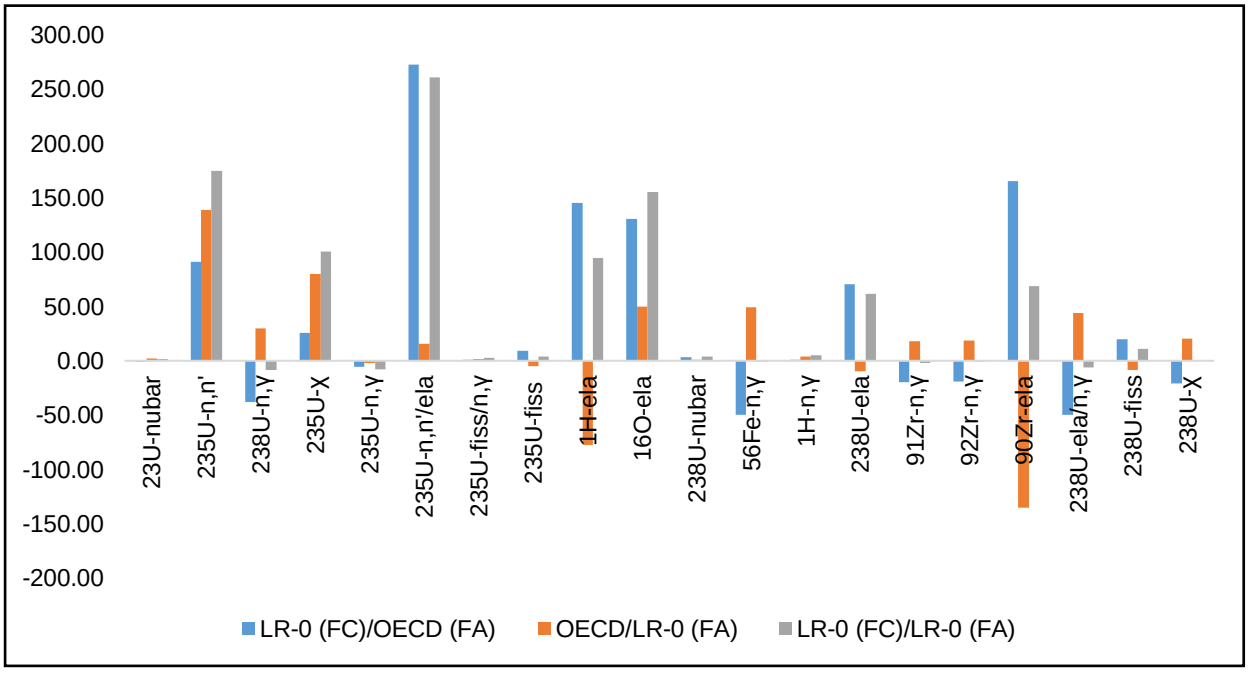

FIGURE 7-9: $\%\ diff$ OF THE UNCERTAINTIES OF THE CONTIBUTORS

7.2.4 SENSITIVITY DUE TO SPACER GRID MODELLING

In the LR-0 benchmark specification, the method of modelling of the spacer grids used was the homogeneous band (HMB) model. Three types of modelling methods were defined in Chapter 5. Those were the heterogeneous band (HTB), homogeneous band (HMB) and homogeneous (HMA) models. The HTB and HMB models produced results that were in good agreement, but results were large for the HMA model. Since these are the three available methods for defining the spacer grid in a reactor system, a test was done in this section to see the effects of the spacer grid modelling. This analysis was done for three reasons:

- To verify the methods that were used to define the HTB and HMB models;
- To verify the model definition for the LR-0 reactor; and
- To observe the contribution of the $^{56}Fe_{n,\gamma}$ contributor in the uncertainty of k_{eff} for a larger system.

In terms of the last point above, in Chapter 5 it was discovered that one of the contributors to the uncertainty was $^{56}Fe_{n,\gamma}$ with a contribution of about 150 pcm. Additional calculations were performed to test the spacer grids presence by using a different material other than the one provided in the specifications for the spacer grids.

7.2.4.1 *Spacer grid modelling*

Table 7-8 represents the results and the difference in the results that were obtained for the three SG models. The differences k_{diff} given in Table 7-8 were obtained between the base model (HMB model) and the two available modelling methods (HTB and HMA). The difference between an HMB model and a HTB model was about 37 pcm, while the difference between an HMB and HMA model was about 211 pcm. These results have shown the same trend as the results that were obtained in Section 5.2.4.1. Therefore, the defined methods for defining the spacer grids in a reactor system, can be considered to be accurate.

TABLE 7-8: SG MODELLING METHODS

Model	k_{eff}	k_{diff} (pcm)
HMB	1.00429	-
HTB	1.00466	37
HMA	1.00218	211

Three complimentary uncertainty calculations were performed using TSUNAMI-3D to observe the changes in the uncertainties due to nuclear data between the three models. The total uncertainty due to nuclear data between the three models was consistent, with an uncertainty of about 580 pcm (0.577%Δk/k), with the difference between the models bounded by 2 pcm.

In terms of the contribution of $^{56}Fe_{n,\gamma}$ to the uncertainty in the results, Table 7-7 shows that the impact of $^{56}Fe_{n,\gamma}$ was about 66 pcm for the LR-0 reactor system, which is about half the impact that was obtained in the OECD/NEA benchmark (150 pcm) in Chapter 5. The impact of $^{56}Fe_{n,\gamma}$ in the LR-0 benchmark was similar for the three methods.

Since the impact of $^{56}Fe_{n,\gamma}$ was compared between for the LR-0 FC model and the OECD/NEA FA model, three additional calculations were performed for the LR-0 FA model, for the three modelling methods. This was done to further verify these observations. The difference k_{diff} between the modelling methods for the LR-0 FA model also had the same trend as the OECD/NEA benchmark and the LR-0 FC model.

The uncertainty due to nuclear data was 587 pcm (0.493%Δk/k), which is only 7 pcm larger than the uncertainty obtained for the LR-0 FC model. The contribution of $^{56}Fe_{n,\gamma}$ to the uncertainty in the LR-0 FA model was about 80 pcm. This uncertainty was consistent between the three models for the LR-0 FA model. The difference in the $^{56}Fe_{n,\gamma}$ uncertainty between the LR-0 FA and LR-0 FC models is about 15 pcm. This uncertainty is still small compared to the one that was obtained for the OECD/NEA FA.

7.2.4.2 *Spacer grid materials*

Considering other materials for spacer grids, the following results were obtained as can be seen in Table 7-9. The k_{eff} results together with their differences are given and for the model without spacer grids (called moderator) the difference is larger. The difference with the result obtained for zirconium alloy as the SG material was 521 pcm. These differences are much lesser than the differences that were obtained in the OECD/NEA benchmark results in Table 5-12 of Chapter 5.

The uncertainty due to nuclear data calculated using TSUNAMI-3D for the three models, each with a different material was similar within the three models with a value of about 580 pcm (0.577%Δk/k). The contribution of $^{56}Fe_{n,\gamma}$ to the uncertainty was also observed for the three models. Since the other two possible spacer grids materials, water and E110 have ^{1}H and ^{90}Zr respectively as their dominant nuclides, their contributions to the uncertainties were also observed for the three models.

In the OECD/NEA benchmark results, the uncertainty due to $^{56}Fe_{n,\gamma}$ decreases depending on the choice of spacer grid material. The same was observed in this analysis as it can be seen in the sensitivity profile in Figure 7-10.

The uncertainties due to $^{1}H_{n,\gamma}$ and $^{90}Zr_{n,\gamma}$ contributors were about 72 and 14 pcm respectively. These uncertainties were also similar between the three models as can be seen in Figure 7-11 and Figure 7-12.

These observations were also seen in the LR-0 FA model. Therefore, the choice of spacer grid material in the LR-0 models contributes small uncertainties than in the OECD/NEA benchmark.

TABLE 7-9: MATERIALS FOR SG

Code	k_{eff}	k_{diff} (pcm)
Stainless steel	1.00429	-
Moderator	1.01248	819
Zirconium ally	1.00950	521

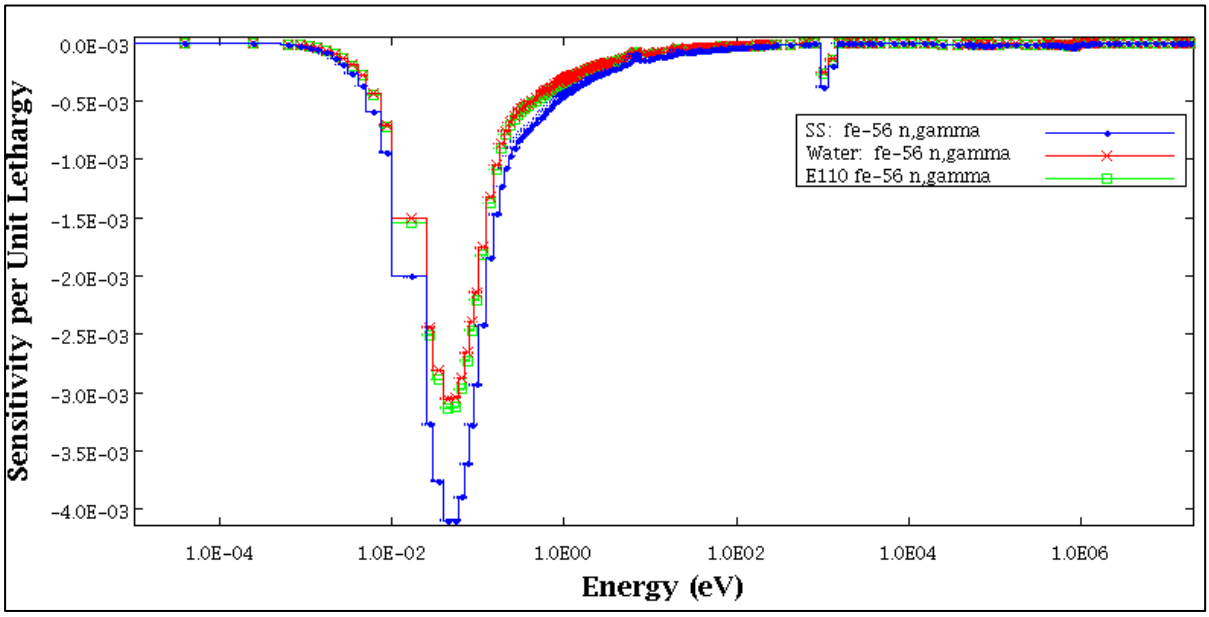

FIGURE 7-10: SDF PLOTS FOR $^{56}Fe_{n,\gamma}$

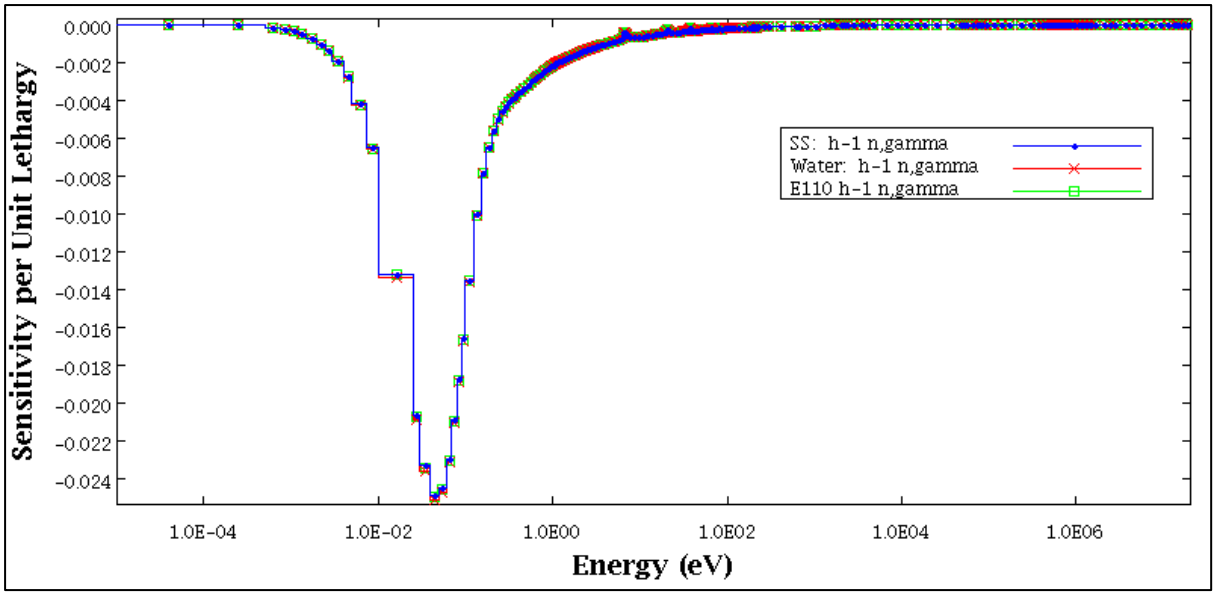

FIGURE 7-11: SDF PLOTS FOR ${}^{1}H_{n,\gamma}$

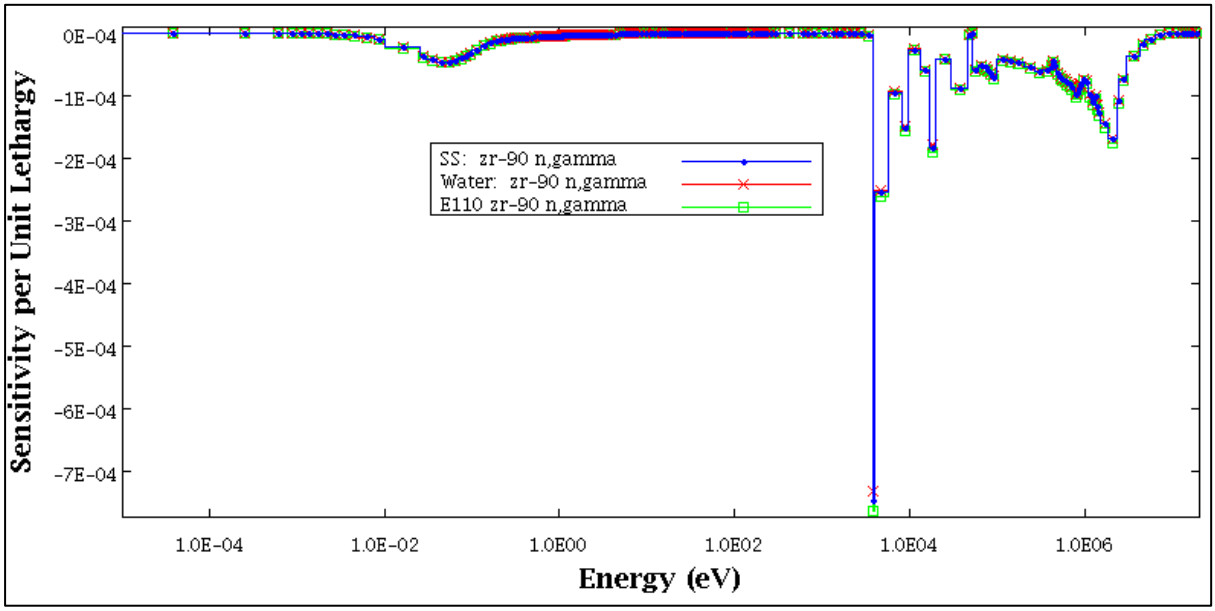

FIGURE 7-12: SDF PLOTS FOR ${}^{90}Zr_{n,\gamma}$

7.2.5 SENSITIVITY DUE TO MANUFACTURING TOLERANCES

A sensitivity study was performed to demonstrate the effect of variations in the input parameters other than the nuclear data. The sensitivity analysis was performed using KENO-VI with CE ENDF/B-VII.1 as in the previous calculations. The parameters in Table 7-10 were varied within tolerance ranges obtained from the model specifications.

The results were obtained for the lower and upper tolerance limits and are analysed by comparing k obtained from the individual parameters to k_{eff} of the nominal results reported in Section 7.1 ($k_{diff} = k_i - k_b$). The parameters are ranked in the last column of Table 7-10. The sensitivity due to the manufacturing tolerances of the parameters listed in Table 7-10 varies from about 5 to

380 pcm. The largest k_{eff} sensitivity occurs for manufacturing tolerance of the ^{235}U enrichment (w/o), UO_2 density, boric acid concentration C_b (g/kg) and Hf content in clad.

TABLE 7-10: MANUFACTURING TOLERANCE SENSITIVITY RESULTS

Parameter	Tolerance	k_{diff} (pcm)	LR-0	%Δk/k	Rank
ρ_{fuel} (g/cm^3) Central FA	+0.300	167		0.57365	4
ρ_{fuel} (g/cm^3) Drive FA	+0.300	382	-	0.57644	1
C_b (g/kg)	+0.060	93	30	0.57964	5
H_{cr} (cm)	-0.058	-5	-60	0.57873	10
^{235}U w/o Central FA	-0.054	-62	-	0.57942	6
^{235}U w/o drive FA	-0.054	-142	200	0.57789	3
Hf content in Clad	-0.03	-249	-220	0.58148	2
Nb content in Clad	+0.05	-20	-30	0.57989	8
ρ_{H_2O} (g/cm^3)	0.003	-49	-70	0.57769	7
T_{H_2O} (K)	+2	-30	Negligible	0.57639	9

The geometry dimensions of the system, such as the diameters of the fuel pin were excluded from this analysis. When varying the cladding outer diameter as a single number, the change in k was 163 pcm. Since this was similar to the results found in Chapter 5, the assumption was that varying this parameter individually per fuel pin as performed in Chapter 5 will yield values of k_{diff} less than 50 pcm. It was also assumed that differences in the uncertainty propagated will be negligible.

The parameters that has shown a sensitivity that is above 50 pcm on the results are: ^{235}U w/o, UO_2 density, C_b (g/kg) and Hf content in clad, with the highest being the UO_2 density. The other parameters of Table 7-10 were not considered for any further analysis in terms of the uncertainty.

For each of these parameters listed in Table 7-10, an individual TSUNAMI-3D (CE) calculation was performed to obtain the uncertainty due to nuclear data when the limit bounds of these parameters are used. The total uncertainty due to nuclear data for these parameters was consistent, with an uncertainty of about 0.577%Δk/k (580 pcm) and a different of about ±2 pcm.

Therefore, the parameters that will be propagated along with nuclear data in Section 7.3 were ^{235}U w/o, UO_2 density, C_b (g/kg) and Hf content in Clad.

7.3 UNCERTAINTY QUANTIFICATION ANALYSIS

To quantify the uncertainties in the LR-0 reactor core, SAMPLER/KENO-VI using 56 MG-ENDF/B-VII.1 was used. It is noted that the uncertainty propagated using nuclear data uncertainties on the upper and lower bounds of the tolerances of these parameters were about 0.577%Δk/k (580 pcm).

The uncertainties of the input parameters that were considered to be contributing the most (>50 pcm) to the uncertainty of the system's results listed in Table 7-10 will be propagated through the calculation together with the nuclear data. Those parameters were ^{235}U enrichment (w/o), UO_2 density, boric acid concentration (C_{boric}), as well as the Hf content in clad. The XSProc parameters that were listed in Section 5.1.6 were used since these were the optimised values and were assumed to still apply. The number of calculations were specified to be 300 samples.

To check the adequacy of the sampling, a scatter plot for one of the inputs ($^{235}U\ w/o$) is given in Figure 7-13. Over the 300 samples, the sampled values of the input data showed a good distribution. Therefore, this verifies that enough samples were used to obtain converged results. To further support this, Figure 7-14 shows the running average plots of the sampled values of the input data for the ^{235}U w/o.

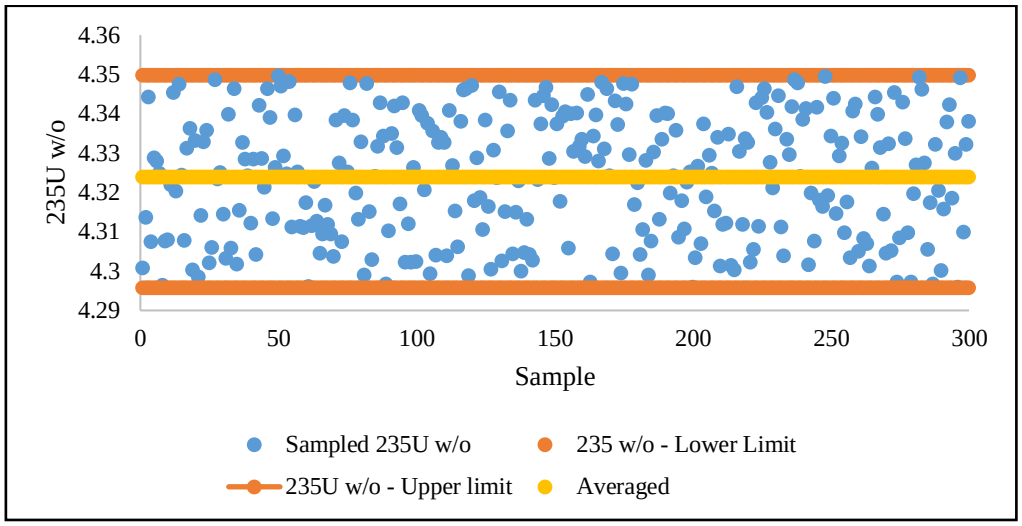

FIGURE 7-13: SCATTER PLOTS FOR ^{235}U W/O

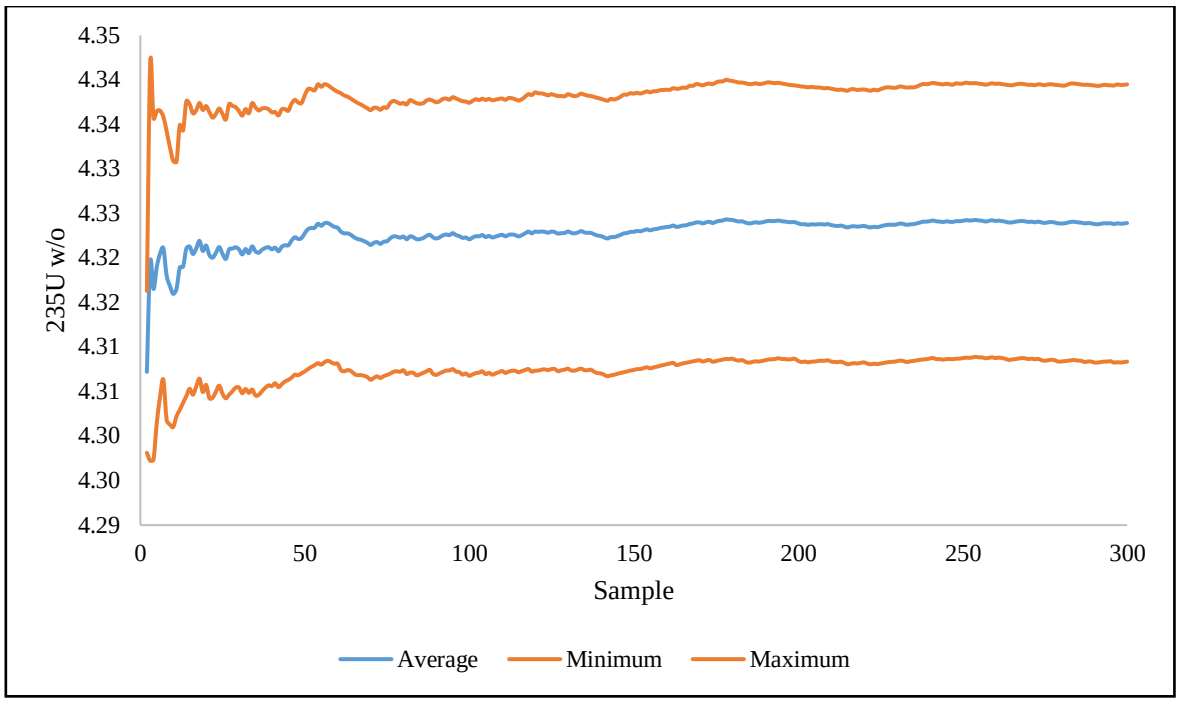

FIGURE 7-14: RUNNING AVERAGES ^{235}U W/O

TABLE 7-11: k QUANTIFIED UNCERTAINTIES

Value	***Calc 1***	***Calc 2***
Mean k	1.00553	1.00491
Δk	0.00644	0.00640
Minimum	0.99909	0.99851
Maximum	1.01197	1.01131
$\%\Delta k/k$	0.64045	0.63674

Figure 7-15 shows the k_{eff} results from the 300 calculations and it is clear that a normal distribution provides a reasonable representation of the results. The running average of k_{∞} in Figure 7-16 evaluates the convergence of the results over 300 samples. A good convergence of the results was observed after 150 samples. Therefore, at least 150 samples can be used to obtain good results for the uncertainty quantification.

The total uncertainty of the k_{eff} obtained for calculation one (Calc 1) was 644 pcm ($\%\Delta k/k$ = 0.640) as it can be seen in Table 7-11. The difference between this uncertainty and that due to the nuclear data uncertainties of 580 pcm ($\%\Delta k/k$ = 0.577) was 64 pcm. The difference between these two uncertainties was due to ^{235}U w/o, UO_2 density, C_{boric}, and Hf content uncertainties.

A second calculation two (calc 2) was performed for the parameter uncertainties using only the parameter uncertainties that were propagated in the OECD/NEA benchmark in Section 5.3. This was carried to identify the effect of the inclusion of other parameters in the uncertainties, viz: the contributions due to the uncertainties of the boric acid concentration and Hf content in the clad.

Since the moderator ρ_{H_2O}/T_{H_2O} did not show sensitivities above 50 pcm, it was not included for the propagation of uncertainties.

The total uncertainty in k_{eff} obtained for calculation two was 640 pcm (%$\Delta k/k$ = 0.637) as it can be seen in Table 7-11. The difference between this uncertainty the uncertainty obtained for calculation one is 4 pcm and due to the nuclear data uncertainties only about 56 pcm.

Using the assumption that was made in Section 5.3 that the total uncertainty is composed from a sum of the four individual uncertainties and the nuclear data by Eq (67), the obtained uncertainty can be approximated. Considering the parameters propagated in calculation one, the maximum sensitivities using the tolerances as limits for the four parameters, ^{235}U w/o, UO_2 density, C_{boric}, and the Hf content were found to be 142, 382, 93 and 249 pcm respectively.

By assuming that the individual contributions are a factor α of the given uncertainty, i.e. 95, 255, 62 and 166 pcm respectively, with $\alpha = \frac{2}{3}$, then the total uncertainty becomes:

$$\Delta k = \sqrt{580^2 + 95^2 + 255^2 + 62^2 + 166^2} = 657\ pcm \tag{71}$$

This uncertainty was 14 pcm larger than the uncertainty calculated by SAMPLER. When $\alpha = 0.57$, the uncertainty becomes the same as the one obtained with SAMPLER as seen in Eq (72)

$$\Delta k = \sqrt{580^2 + 82^2 + 220^2 + 53^2 + 143^2} = 644\ pcm \tag{72}$$

If $\alpha = 1$, the uncertainty becomes overestimated by about 110 pcm as given in Eq (73).

$$\Delta k = \sqrt{580^2 + 142^2 + 382^2 + 93^2 + 249^2} = 757\ pcm \tag{73}$$

Considering calculation two where $\alpha = \frac{2}{3}$ and α= 1, the uncertainty were obtained to be 641 and 709 pcm as shown by Eq (74) and Eq (75) respectively.

$$\Delta k = \sqrt{580^2 + 95^2 + 255^2} = 641\ pcm \tag{74}$$

$$\Delta k = \sqrt{580^2 + 142^2 + 382^2} = 709\ pcm \tag{75}$$

With these results, when $\alpha = \frac{2}{3}\ (0.667)$ was used, the uncertainty estimated using Eq (67) was almost the same as the uncertainty obtained through SAMPLER with a difference of 1 pcm. For $\alpha = 0.664$, the uncertainty was exactly 640 pcm and this value of $\alpha = 0.664$ is very close to $\alpha = \frac{2}{3}$. When $\alpha = 1$ was used for calculation two, the uncertainty was smaller than the uncertainty obtained for calculation one by a difference of 48 pcm.

Therefore, if $\alpha = \frac{2}{3}$, the total uncertainty can be well approximated using the simple sum of the individual uncertainties squared. As in Section 5.3 this implies that a possible method of propagating uncertainties would be to obtain the sensitivities of all the other parameters besides nuclear data. If they are less than 300 pcm in magnitude, the final uncertainty can be calculated using Eq (67) after the uncertainty due to nuclear data has been propagated.

It is also observed that the α values used to calculate the total uncertainty to be exactly that of the propagated total uncertainty is not the same for all the different models. This also then hints that Eq (67) might not be valid as it was discussed in Section 5.3. Therefore, a more accurate equation would be required, if possible.

The uncertainty quantification of the individual input parameters was supported by correlation coefficients. Figure 7-17 shows the correlation between the k_{eff} results and each input parameter besides the nuclear data. The correlations between the input parameters and the results were weak as can be seen in Figure 7-17.

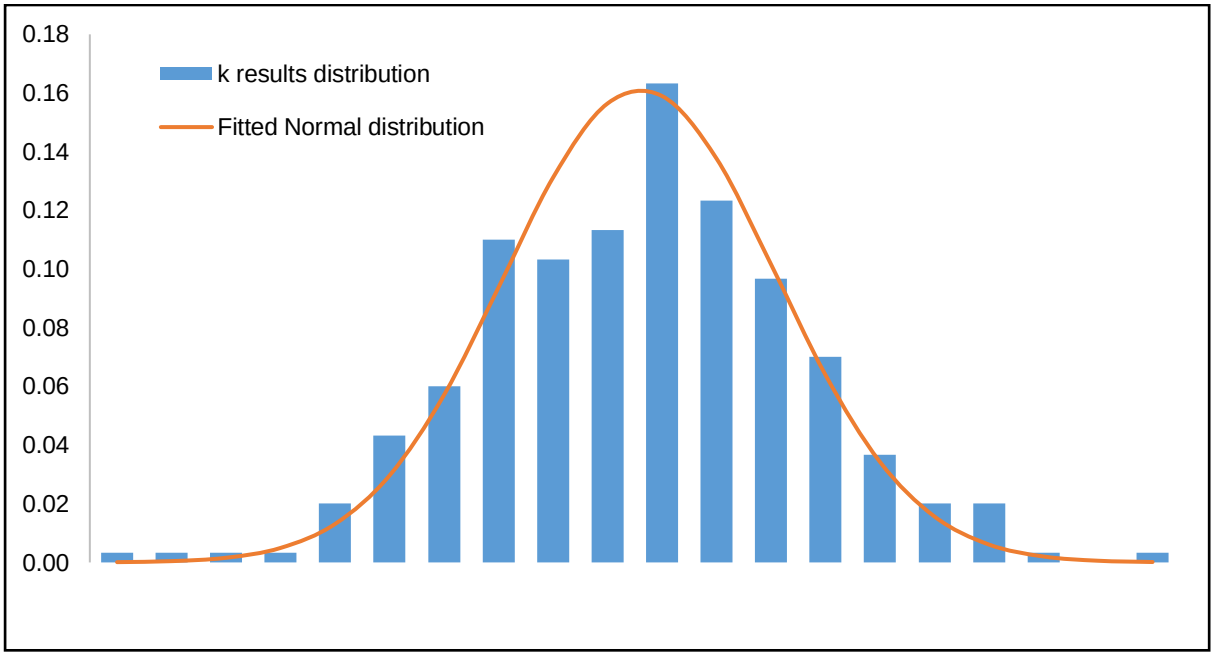

FIGURE 7-15: FREQUENCY PLOT FOR NUCLEAR DATA ANALYSIS

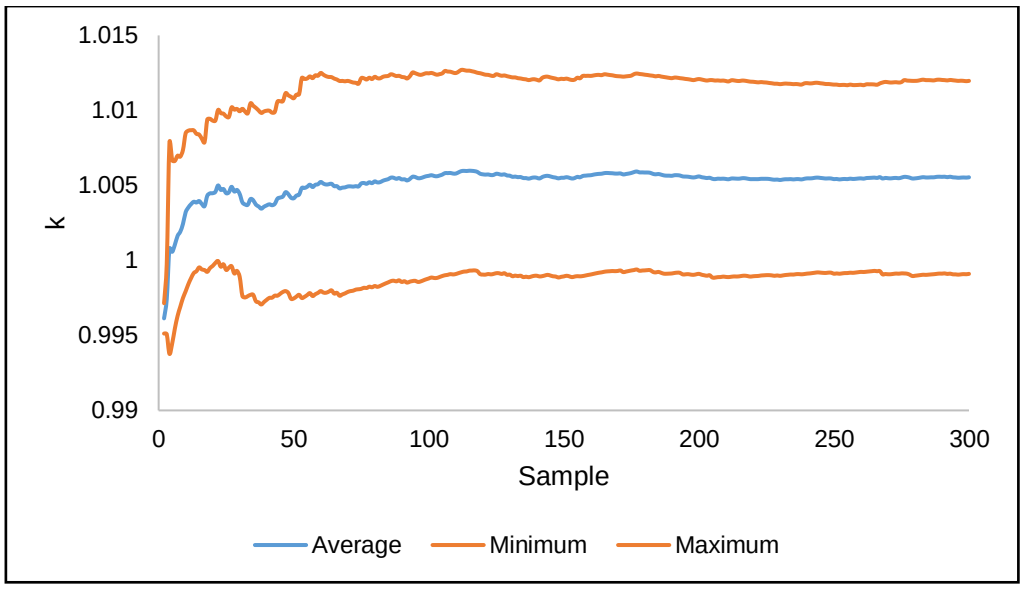

FIGURE 7-16: RUNNING AVERAGES FOR k_{∞} RESULTS

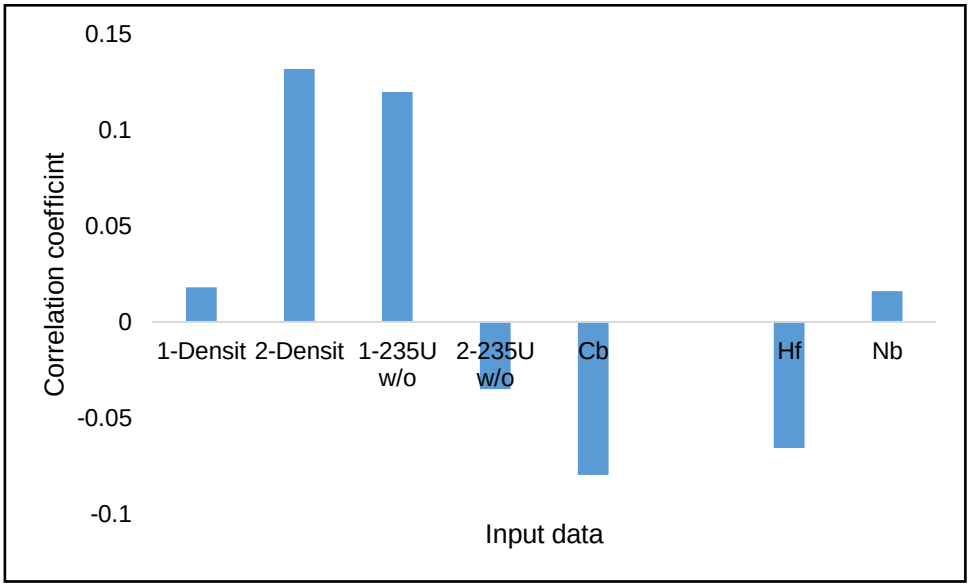

FIGURE 7-17: CORRELATION COEFFICIENTS OF PARAMETERS

7.4 CLOSING DISCUSSION

This chapter validates the neutronics results using the BE estimate code KENO-VI on the LR-0 reactor core. This was successfully performed in the following steps:

- Verification of the model
- Comparison of results between different criticality codes
- Nuclear data uncertainty evaluation
- Comparison of nuclear data uncertainties for various systems
- Sensitivity analysis
- Uncertainty quantification

The verification of the model was successfully done by comparing the material number densities and the geometry between a NWURCS and hand-written input. The difference between the hand-written and NWURCS model was 25 pcm. The material number densities calculated by NWURCS was not the same as the HDW values, having at most a difference of about 1%. When identical material number densities definitions were used for both HDW and NWURCS, the difference was 9 pcm. This was then considered to be the result from the statistical nature of KENO-VI.

The results for k_{eff} obtained using KENO-VI (CE) was 1.00429, which was 349 pcm larger than the results that was reported in the LR-0 benchmark specification. Deviations between the computed results and the LR-0 benchmark measure results are mainly due to the different data library used and partially to the different statistics adopted in the two codes. There was an overall good and consistent agreement between the latest version of MCNP6 and KENO-VI of SCALE-6.2.1 for the calculation.

The uncertainty due to the nuclear data provided by the library was about 580 pcm. The neutron-nuclide reaction contributors that were observed to produce more than 100 pcm were $^{235}U_{nubar}$, $^{238}U_{n,n'}$, $^{238}U_{n,\gamma}$, $^{235}U_{\chi}$, $^{235}U_{n,\gamma}$, $^{235}U_{fission/n,\gamma}$ and $^{235}U_{fission}$.

In comparing this uncertainty to the uncertainty obtained for the OECD/NEA FA benchmark in Section 5.3, the uncertainty due to nuclear data was larger for the OECD/NEA benchmark. The difference was about 150 pcm. The impact of the neutron-nuclide reaction contributors differed for each system. Therefore, it was concluded that the size, material and geometry of the system have an influence on the nuclear data uncertainties.

Sensitivities of the results were further tested by considering the modelling methods of the SGs as described in Section 4.5.3. In this analysis, the method that provided in the specification for modelling the SGs was verified through a heterogeneous model. The homogeneous model (HMA) was larger by 211 pcm and this was the same observation that was obtained in Section 5.2.4. In Section 5.2.4, the presence of the spacer grid contributed to the uncertainty of the results. This contribution was observed via the neutron-nuclide reaction contributors, where $^{56}Fe_{n,\gamma}$, which was the dominant nuclide of the SG material, contributed an uncertainty of about 150 pcm. The LR-0 model contribution of $^{56}Fe_{n,\gamma}$ was about 70 pcm.

In terms of the manufacturing tolerances, the highest contributors to the uncertainty in k were: ^{235}U enrichment (~142 pcm), fuel density (~382 pcm), boric acid concentration (C_{boric}), and Hf content in clad. These were the parameters whose uncertainty required propagation alongside with the nuclear data uncertainty. The contribution from the rest of the parameters were less than 10 pcm.

After the propagation of uncertainties of all input parameters together with the nuclear data uncertainty, the total uncertainty was 644 pcm. This uncertainty was about 60 pcm larger than that due to the nuclear data only, which can may mean that the other parameters only contributed 60 pcm to the uncertainty. Using the arguments that were made in Section 5.3, it can still hold that the magnitude of the nuclear data uncertainty can suppress the uncertainties due to the other parameters even if these parameters yield a large uncertainty on k when propagated individually. Hence, the overall uncertainty will be closer to the nuclear data uncertainties.

8 CONCLUSIONS AND RECOMMENDATIONS

This chapter gives the conclusions that were made as well as recommendation for future studies. The conclusions given in this section provides the results that were performed prior to quantification of the uncertainties of the VVER-1000 system using codes obtained in SCALE 6.2.1.

8.1 CONCLUSIONS

The following conclusions are given according to the six analyses that was performed in this study. The five analyses were:

- The optimisation of XSProc and NEWT parameters for better criticality results;
- Sensitivity and uncertainty analysis of input data of the complex VVER-1000 system;
- Fuel depletion criticality calculations as well as uncertainty quantification of all input data;
- Results contribution of the OCED/NEA benchmark; and
- The verification and validation of the neutronics calculations using the LR-0 system.

The fuel pin and fuel assembly models of the Kozloduy-6 VVER-1000 system were developed using NEWT and KENO-VI (MG/CE). A 3D full core model of the LR-0 reactor was developed successfully for KENO-VI (MG/CE) and MCNP6 which are both high fidelity codes. These models were verified in terms of input generation for criticality calculations. These models were used as reference models to propagate the uncertainties in the Kozloduy-6 VVER-1000 system and the LR-0 reactor core.

In terms of the optimization of XSProc and NEWT, for the parameters tested for XSProc, the highest sensitivity was about 200 pcm, while for the NEWT parameters tested this was about 283 pcm. The uncertainty due to nuclear data uncertainties was not affected significantly by the change in the code parameters in the optimisation tests.

A good agreement between NEWT results with optimised parameters and the KENO-VI results was obtained. The KENO-VI model assisted in finding confidence in the accuracy of the optimised parameters.

Further models of the VVER-1000 FA were developed using KENO-VI code to obtain insight of the complexity of the geometry. This was done by choosing to study the sensitivity due to the spacer grid parameters in the system. The presence of the spacer grids was found to contribute about 150 pcm to the uncertainty due to nuclear data when only the nuclear data uncertainties were propagated. This was found from the neutron-nuclide contributor, $^{56}Fe_{n,\gamma}$, which was produced

from the dominant nuclide of the SG material. When the material of the SG was altered, the uncertainty due to $^{56}Fe_{n,\gamma}$ became smaller.

Other large uncertainty contributors to the uncertainty in the VVER-1000 system beside the nuclear data uncertainty were ^{235}U enrichment, UO_2 density and moderator temperature/density. These parameters had uncertainties of 292, 57 and 233 pcm on the k results.

The total uncertainty when propagating all the considered input parameters in the Kozloduy-6 VVER-1000 fuel assembly analysis was 769 pcm. With the contribution from the nuclear data being 730 pcm as calculated in a model in which only the nuclear data was perturbed. The nuclear data is the largest contributor to the total uncertainty propagated.

For the LR-0 models, the total uncertainty was 644 pcm. When only the nuclear data uncertainty was propagated the uncertainty was 580 pcm.

With all these analyses, it was concluded that for a VVER-1000 system, nuclear data was the input parameter that contributed the most to the uncertainty in the results. Although this is the case, the uncertainty due to a few other parameters when propagated individually was also significant. This is important, since it is possible that the nuclear data uncertainties might decrease in future releases of nuclear data files, and therefore the other contributors would become important in reactor system safety analysis.

Regarding burn-up, the system studied was the fuel pin of the Kozloduy-6 VVER-1000 reactor system. The uncertainty parameters Δk and $\%\Delta k/k$ displayed different behaviours as a function of burn-up. Δk starts of with about 750 pcm, decreases to about 550 pcm at about $15\ GWd/MTU$ burnup, and then increases steadily, reaching a maximum of about 730 pcm at $60\ GWd/MTU\ burnup$. This behaviour correlated well with the depletion of ^{235}U and the build-up of ^{239}Pu and ^{241}Am. In terms of $\%\Delta k/k$, this parameter decreased in an exponential like behaviour until about $30\ GWd/MTU$ and then starts to increase up to about $55\ GWd/MTU$ and then decreases at $60\ GWd/MTU$. This behaviour is not surprising since k decreases with the burnup, therefore the product of Δk with $1/k$ would not be that straight forward.

8.2 RECOMMENDATIONS FOR FUTURE STUDY

In this study there are other aspects that were not investigated, some of which were due to scope and time constraints. These studies would supplement the current study. These were:

- The FA uncertainty quantification showed all the important parameters in the system that were studied. It is suggested that the uncertainty quantification be done on a full core

Kozloduy-6 VVER-1000 reactor system to obtain the full core uncertainty. The core fuel assemblies have different enrichments.

- In addition to the above, the new version of NWURCS can be further verified by modelling the full core VVER-1000 reactor system.

The next step following from this work in the development of the uncertainty quantification for the reactor cores would be the uncertainties related to heat transfer and thermal-hydraulics since the coupling of neutronic and thermal-hydraulics analysis of a reactor system is crucial for safety analysis. Since thermal-hydraulic studies have already been started at the NWU, it is suggested that future research consider continuing with the current study to include coupling with thermal-hydraulics and heat transfer of the reactor core.

Finally, it is possible that other institutions might contribute results to the OECD/NEA benchmark in terms of the exercises that were completed in this study towards the benchmark. It would then be instructive to compare all the results, in part further verifying the results presented in this work.

REFERENCES

Abbasi, F., 2016. *Monte Carlo based modelling and simulation of neutron flux distribution and activity map of the German Reasearch Reactor FRJ-2,* Aachen, Germany: RWTH Aachen University, Dissertation.

Abe, A., Giovedi, C., Gomes, D. & Silva, A., 2014. Revisiting stainless steel as PWR fuel rod cladding after Fukushima Daiichi accident. *Journal of Energy and Power Engineering, Vol. 8,* pp. 973-980.

Ade, B., 2012. *SCALE/TRITON Primer: A primer for light water reactor lattice physics calculations,* Oak Ridge, United State: United State Nuclear Regulatory Commission.

Alhassan, E., 2014. *Nuclear data uncertainty propagation for a lead-cooled fast reactor: Combining TMC with criticality benchmarks for improved accuracy,* Sweden: Uppsala Universitet, Thesis..

Alhassan, E., 2015. *Nuclear data uncertainty quantification and data assimilation for a lead-cooled fast reactor,* Uppsala, Sweden: Acta Universitatis Upsaliensis, Thesis.

Alpan, A. & Haghighat, A., 2000. *IPEN - Nuclear and Energy Research Institute.* [Online] Available at: https://www.ipen.br/biblioteca/cd/physor/2000/physor/232.pdf

Arkuszewski, J., 1973. *New spatial differencing for the neutron transport equation,* Switerland: EIR Switzerland.

Ball, M., 2011. *Uncertainty in lattice reactor physics calculations,* Hamilton, Ontario, Canada: McMaster University, Thesis..

Barkauskas, V., Plukiene, R., Plukis, A. & Remeikis, V., 2017. Generation of RMBK-1500 spent nuclear fuel one-group cross-section libraries and their evaluation against experimental data. *Lithuanian Journal of physics, Vol. 57, No. 1,* pp. 42-53.

Blakely, C., 2018. *Uncertainty quantification and sensitivity analysis of multiphysics environments for application in pressurized water reactor design,* Utah, United State: Utah State University.

Blanchet, D., Mikityuk, K., Coddington, P. & Chawla, R., 2007. *An uncertainty assessment methodology for materials behaviour in advanced fast reactors.* Karlsruhe, Germany., SMINS, Workshop proceedings.

Blyth, T., 2012. *Fuel performance code benchmark for uncertainty analysis in Light Water Reactor modelling,* Pennsylvania, United States: The Pennsylvania State University.

Bostelmann, F. et al., 2017. *SCALE multi-group libraries for Sodium-cooled fast reactor systems.* Jeju, Korea, M&C 2017.

Bratton, R., Avramova, M. & Ivanov, K., 2014. OECD/NEA benchmark for uncertainty analysis in modelling (UAM) for LWRs - Summary and discussion of neutronics cases (Phase 1). *Nuclear engineering and technology, Vol. 46,* pp. 313-342.

Briesmeister, J., 2000. *MCNP - A general Monte Carlo N-Particle transport code, version 4C,* California, US: Los Alamos National Laboratory.

Cai, L., 2014. *Condensation and homogenization of cross sections for the deterministic transport codes with,* Paris, France: Universite Paris Sud.

Canuti, E., Petruzzi, A., Auria, F. & Kozlowski, T., 2012. Sensitivity studies for the exercise I-1 of the OECD/UAM benchmark. *Hindawi publishing corporation: Science and Technology of nulcear installations.*

Cardoso, F. et al., 2015. *Preliminary uncertainty analysis of OECD/UAM benchmark for the TMI-1 reactor.* Sao Paulo, Brazil, Associacai Brasileira de Energia Nuclear - ABEN.

Chapman, B., 2010. *Diagnostics of source distribution and particle population in Monte Carlo source iteration methods,* Mexico: Univeristy of New Mexico, Thesis.

CNSC, 2003. *Reactor physics,* Canada: Canadian Nuclear Safety Commission.

Collins, P., Luciano, N. & Maldonado, G., 2016. Modernization and expansion of isotopic depletion capabilities within the NESTLE 3D nodal simulator. *Transactions - American Nuclear Society..*

Czakoj, T., Frybort, J. & Lovercky, M., 2018. *Calculation uncertainties in spent fuel inventory determination.* Prague, Czech Technical University, pp. 14 - 20.

DeHart, M., 2006. *Advancements in generalized-geometry discrete ordinates transport for lattice physics calculations,* United State: American Nuclear Society - ANS.

DeHart, M. et al., 2015. *NEAMS-Funded University Research in support of TREAT modelling and simulation, FY15,* United States: Idaho National Laboratory.

du Toit, M., 2017. *Analysis of specific design aspects of a thorium-uranium fuelled European Pressurised Reactor ,* North West, Potchefstroom, South Africa: North-West University, Thesis.

Duerigen, S., 2013. *Neutron transport in hexagonal reactor cores modeled by trigonal-geometry diffusion and simlified P3 nodal methods,* Karlsruhe, Germany: Karlsruhe Institute of technology (KIT).

Dunn, M., Greene, N. & Petrie, L., 2004. *Point KENO V.a: A continuous-energy Monte Carlo code for transport applications.* Chicago, Illinois, American Nuclear Society - ANS.

Ferrer, R., Rhodes, J. & Smith, K., 2012. *CASMO5/TSUNAMI-3D spent nuclear fuel reactivity uncertainty analysis.* Knoxville, Tennsessee, American Nuclear Society.

Fisher, H., 1989. *A nuclear cross-section data handbook,* New Mexico: Los Alamos National Laboratories.

Frosio, T., Bonaccorsi, T. & Blaise, P., 2017. Manufacturing data uncertainties propagation method in burn-up problems. *Hindawi: Science and technology of nuclear installations.*

Gabrielli, F., 2011. *Models for transient analyses in advanced test reactors,* Stuttgart, Germany: Universitat Stuttgart, Dissertation.

Ghasbyan, L., 2013. *Use of Serpent Monte-Carlo code for development of 3D full-core models of Gen-IV fast-spectrum reactors and preparation of group constants for transient analyses with PARCS/TRACE coupled system,* Stockholm, Sweden: Royal Institute of Technology (KTH), Thesis.

Goluoglu, S. et al., 2007. *Generation and testing of the ENDF/B-VI continuous-energy cross-section library for use with contonuous-energy versions of KENO.* St. Petersburg, Russia, Oak Ridge National Laboratory.

Goncalves, I., Martinho, E. & Salgado, J., 2001. Monte Carlo calculations of epithermal neutron resonance self-shielding factors in wires of different materials. *Applied radiation and isotopes,* pp. 447-451.

Grgic, D., Jecmenica, R. & Pevec, D., 2010. *Spectral codes pin power prediction comparison.* Slovenia, Russia, Proceedings of the International conference Nuclear energy for new Europe 2010.

Hamilton, S. et al., 2016. *Hot Zero Power reactor calculations using the insilico code,* Oak Ridge, USA: Oak Ridge National Laboratory.

Hartmann, C., 2016. *Advanced methodology to simulate Boiling Water Reactor Transient using coupled Thermal-Hydraulic/Neutron-Kinetic codes,* Germany: Karlsruher Institut für Technologie (KIT), Dissertation.

Helgesson, P., 2013. *UO-2 vs MOX: Propagated nuclear data uncertainty with burnup using Fast Total Monte Carlo,* Sweden: Uppasa Universitat.

Helton, J., Johnson, J., Sallaberry, C. & Storlie, C., 2006. *Survey of sampling-based methods for uncertainty and sensitivity analysis,* Albuquerque, New Mexico: Sandia National Laboratories.

Herman, B., 2009. *Cross section generation strategy for high conversion light water reactors,* Cambridge, USA: Massachusetts Institute of Technlogy.

Herman, M. & Trkov, A., 2009. *ENDF-6 format manual,* Upton, United State: Brookhaven National Laboratory.

IAEA., 2015. *Quality and reliability aspects in nuclear power reactor fuel engineering,* Vienna, Austria: International Atomic Energy Agency.

IAEA, 2008. *Best-estimate safety analysis for nuclear power plants: uncertainty evaluation,* Vienna, Austria: International Atomic Energy Agency.

IAEA, 2008. *Thermophysical properties of materials for nuclear engineering: A tutorial and collection of data,* Vienna, Austria: International Atomic Energy Agency.

Ivanov, K. et al., 2013. *Benchmark for uncertainty analysis in modelling (UAM) for design, operation and safety analysis of LWRs,* s.l.: OECD Nuclear Energy Agency.

Jarrel, J. & Adams, M., 2011. *Discrete-ordinates quadrature sets based on linear discontinuous finite elements.* Rio de Janeiro, Brazil, Latin American Section (LAS) / American Nuclear Society.

Kriangchaiporn, N., 2006. *Transport model based on 3-D cross-section generation for TRIGA core analysis,* Pennsylvania, United State: The Pennsylvania State University, Thesis.

Kyncl, J. et al., 2005. *VVER physics experiment: Hexagonal lattices (1.275 cm pitch) of low-enriched U(3.6, 4.4 WT.% 235U)O2 fuel assemblies in light water with H3BO3,* Czech: MTI Czech Republic project No.1H-PK/20, 2005, NEA/NSC/DOC/(95)03IV.

Leal, L., 2016. *Role of nuclear data in response to practical applications,* Paris, France: Universite Paris-Sud.

Leppanen, J., 2003. *Cross sections library based discrepancies in MCNP criticality calculations.* Portoroz, Slovenia, s.n.

Leppanen, J., 2017. *PHYS-E0562 Nuclear engineering advanced course: Lecture 3 - Monte Carlo Simulation,* Espoo, Finland: Aalto University, School of Science.

Liu, Y., 2015. *A full core ronance self-shielding method accounting for temperature-dependent fuel subregions and resonance interference,* Michigan, United State: University of Michigan.

Mesado, C., 2017. *Uncertainty quantification and sensitivity analysis for cross sections and thermahydraulic parameters in lattice and core physics codes.,* Valencia, Spain: Universitata Politecnica Valencia, Thesis.

Moghrabi, A. & Novog, D., 2018. Determination of the optimal few-energy group structure for the Canadian Super Critical Water-cooled reactor. *Annals of nuclear energy,* pp. 27-38.

Mulatier, C., 2016. *A random walk approach to stochastic neutron transport,* Paris, France: Universite Paris-Saclay.

Naicker, V., 2018. *NWURCS user guide,* Potchefstroom: North-West University.

Naicker, V. et al., 2016. *Quantification of the SCALE 6.1 eigenvalue uncertainty due to cross-section uncertainties for exercise I-1 of the IAEA CPR on HTGR uncertainties.* Sun Valley, United State, American Nuclear Society - ANS, pp. 2358-2370.

NEI, 2017. *Guidance for performing criticality analyses of fuel storage at light water reactor power plants,* Washington D.C.: Nuclear Energy Institute.

Nyalunga, G., 2016. *Developing a fresh core neutronic model at 300K for a VVER-1000 reactor type using MCNP6,* Potchefstroom, South Africa: North-West University, Dissertation..

Nyalunga, G., Naicker, V. & du Toit, M., 2016. Developing skills for neutronic modelling of nuclear power reactors in South Africa. *Journal of energy in Southern Africa, Vol.27 ,* pp. 64-76.

Nyalunga, G., Naicker, V. & Ivanov, K., 2018. *Optimisation of code parameters on the multiplication eigenvalue with its associated uncertainty for the Kozloduy-6 VVER-1000 fuel assembly.* Lucca, Italy, BEPU, ANS.

Oberle, P., Broeders, C. H. M. & Dagan, R., 2006. *Burnup calculations with SCALE 50/TRITON other burnup codes and experimental results,* United State: American Nuclear Society - ANS..

Okumura, K., Oka, Y. & Ishiwatari, Y., 2014. *Springer.* [Online] Available at: www.springer.com/cda/content/document/cda_downloaddocument/9784431548973-c1.pdf?SGWID=0-0-45-1460909-p176580799

Pazirandeh, A., Ghaseminejad, S. & Ghaseminejad, M., 2011. Effects of various spacer grid modeling on the neutronic parameters. *Annal of nuclear energy, Vol. 38,* pp. 1978-1986.

Pelowitz, D., 2013. *MCNP6 user's manual, version 1.0,* United State: Los Alamos National Laboratory.

Perfetti, C. & Rearden, B., 2016. Development of a generalized perturbation theory method for Sensitivity analysis using continuous-energy Monte Carlo methods. *Nuclear science and engineering, Vol. 182,* p. 354–368.

Perko, Z., 2015. *Sensitivity and uncertainty analysis of coupled reactor physics problems - Method development for multi-physics in reactors,* Delft, The Netherlands: Delft Universit of Technology, Thesis.

Pirouzmand, A. & Mohammadhasni, F., 2016. *A comparative study of probabilistic and deterministic methods for multi-group diffussion constants generation.* Bushehr, Iran, PENPP2016.

Pounders, J., 2006. *Stochastically generated multi-group diffusion coefficients,* Georgia, United State: Georgia Institute of Technology, Thesis.

Rearden, B., 2004. Perturbation theory eigenvalue sensitivity analysis with Monte Carlo techniques. *Nuclear science and engineering,* pp. 367-382.

Rearden, B. & Jesse, M., 2016. *SCALE code system ,* Oak Ridge, United State: Oak Ridge National Laboratory .

Reed, D. et al., 2014. *SCALE/TSUNAMI sensitivity data for ICSBEP evaluations,* Oak Ridge: Oak Ridge National Laboratory.

Sabouri, P., 2013. *Application of perturbation theory methods to nuclear data uncertainty propagation using the collision probability method,* Grenoble, France: Institut National Polytechnique.

Sanchez, R., Mao, L. & Santandrea, S., 2002. Treatment of boundary conditions in trajectory-based deterministic. *Nuclear science and engineering: 140,* p. 23–50.

Sihlangu, S., Naicker, V., Hou, J. & Reitsma, F., 2018. *Uncertainty quantification in the MHGTR-350 fuel compact and block using TSUNAMI-3D CLUTCH method and SAMPLER.* Lucca, Italy, BEPU-2018.

Stacey, W., 2007. *Nuclear reactor physics.* Weinheim, Germany: Wiley-VCH Verlag GmBh & Co. KGaA.

Taavitsainen, A., 2016. *CFENSS-SRS method for he uncertainty analysis of nuclear fuel and neutronics,* Espoo, Finland: Aalto University, Thesis.

Taylor, J., Knott, D. & Baratta, A., 2007. *A method of characteristics solution to the OECD/NEA 3D neutron transport benchmark problem.* Monterey, Carlifornia, American Nuclear Society.

Tran, X. & Cho, N., 2016. A study of neutronics effects of the spacer grids in a typical PWR via Monte Carlo calculation. *Nuclear engineering and technology, Vol. 48,* pp. 33-42.

Tuttelberg, K., 2014. *STORM in Monte Carlo reactor physics calculations,* Stockholm, Sweden: KTH Royal Institute of Technology, Thesis.

Ueki, T., Brown, F., Parsons, D. & Korneich, D., 2003. Autocorrelation and dominance ration in Monte Carlo criticality calculations. *Nuclear science and engineering: The Journal of the American Nuclear Society,* pp. 279-290.

Venturini, A., 2014. *Neutronic investigations of MOX and LEU fuel assemblies for the VVER reactors,* Pisa, Italy: Università degli studi di Pisa.

Wagner, J., Redmond II, E., Palmtag, S. & Hendricks, J., 1994. *MCNP: Multi-group / Adjoint Capabilities,* New Mexico: Los Alamos National Laboratory.

Wang, Y., 2009. *Adaptive mesh refinement solution techniques for the multigroup SN transport equation using a higher-order discontinuous finit element method ,* Texas, United State : Texas A&M University, Dissertation.

Willert, J., Kelley, C., Knoll, D. & Park, H., 2013. Hybrid deterministic / Monte Carlo neutronics. *Society for industrial and applied mathematics,* pp. S62 - S83.

Wyant, T., 2012. *Numerical study of error propagation in Monte Carlo depletion simulations,* Georgia, United State: Georgia Institute of Technology.

Young, M., 2016. *Orthogonal-mesh, 3-D Sn with embedded 2-D method of characteristics for whole core, pin-resolved reactor analysis,* Michigan, United State: University of Michigan, Dissertation.

APPENDICES

APPENDIX A. MATERIAL PROPERTIES

In the following appendix, the material number densities for the OECD benchmark has been provided. All the number densities were calculated using the material information in Table 4-3 and Eq (43).

TABLE A-1: NUMBER DENSITIES (ATOM/B-CM)

H_2O - HZP	
H	5.12787E-02
O	2.56394E-02
H_2O - HFP	
H	5.03093E-02
O	2.51547E-02
UO_2 - 3.3% w/o	
U-234	1.27377E-06
U-235	7.04633E-04
U-238	2.24941E-02
O	4.64014E-02
UO_2 - 3.0% w/o	
U-234	1.27377E-06
U-235	7.04633E-04
U-238	2.24941E-02
O	4.63998E-02
Zircaloy	
O	3.08176E-04
Cr	7.58615E-05
Fe	1.48329E-04
Zr	4.19923E-02
Nb	4.24567E-04
Sn	4.81807E-04
E110	
H	3.85384E-05
C	1.61697E-04
N	1.94121E-05
O	1.21388E-04
Al	1.15169E-05
Si	6.91510E-05
Ti	5.68032E-06
Fe	3.47773E-05
Ni	1.65448E-05
Zr	4.20354E-02
Nb	4.18085E-04
Hf	4.24614E-04

Stainless Steel	
C	3.16876E-04
Si	1.35515E-03
P	5.37590E-05
S	2.96740E-05
Ti	5.96339E-04
Cr	1.64695E-02
Mn	1.73195E-03
Fe	5.83260E-02
Ni	8.10567E-03

APPENDIX B. NUCLEAR REACTIONS

The reaction types analysed in this study are described in this appendix. The reaction types are identified by an integer number described as MT numbers in various input (Rearden & Jesse, 2016).

MT1 ---------- Neutron total cross-section
MT2 ---------- Elastic scattering cross-section for incident particles (elastic)
MT3 ---------- Inelastic neutron cross-section (n, n')
MT4 ---------- Production of a neutrons (n, elastic)
MT18 ---------- Fission cross-section
MT27 ---------- Absorption cross-section
MT101 ---------- Neutron disappearance (n, γ)
MT102 ---------- Radiative capture (n, γ)
MT452 ---------- Average total number of neutrons released per fission ($nubar$)
MT458 ---------- Energy released in fission for incident neutrons
MT1452 ---------- Product of average neutrons times the fission cross-section
MT1018 ---------- Fission spectrum (χ)

APPENDIX C. INPUT SAMPLES

In this appendix, the examples of the layout of input files for NEWT, KENO-VI, TSUNAMI and SAMPLER are presented. These input files contain the input for the fuel pin of the OECD Kozloduy-6 VVER-1000 criticality calculations. The input files are built and edited using a basic text editor. The SCALE-6.2.1 allows the use of the FULCRUM command for building and editing the input file. This command is convenient, since it can also provide visual images of the input file being built to verify the model and an option to run the input file for the desired sequence. The layout of the input files is shown in Figure C-1.

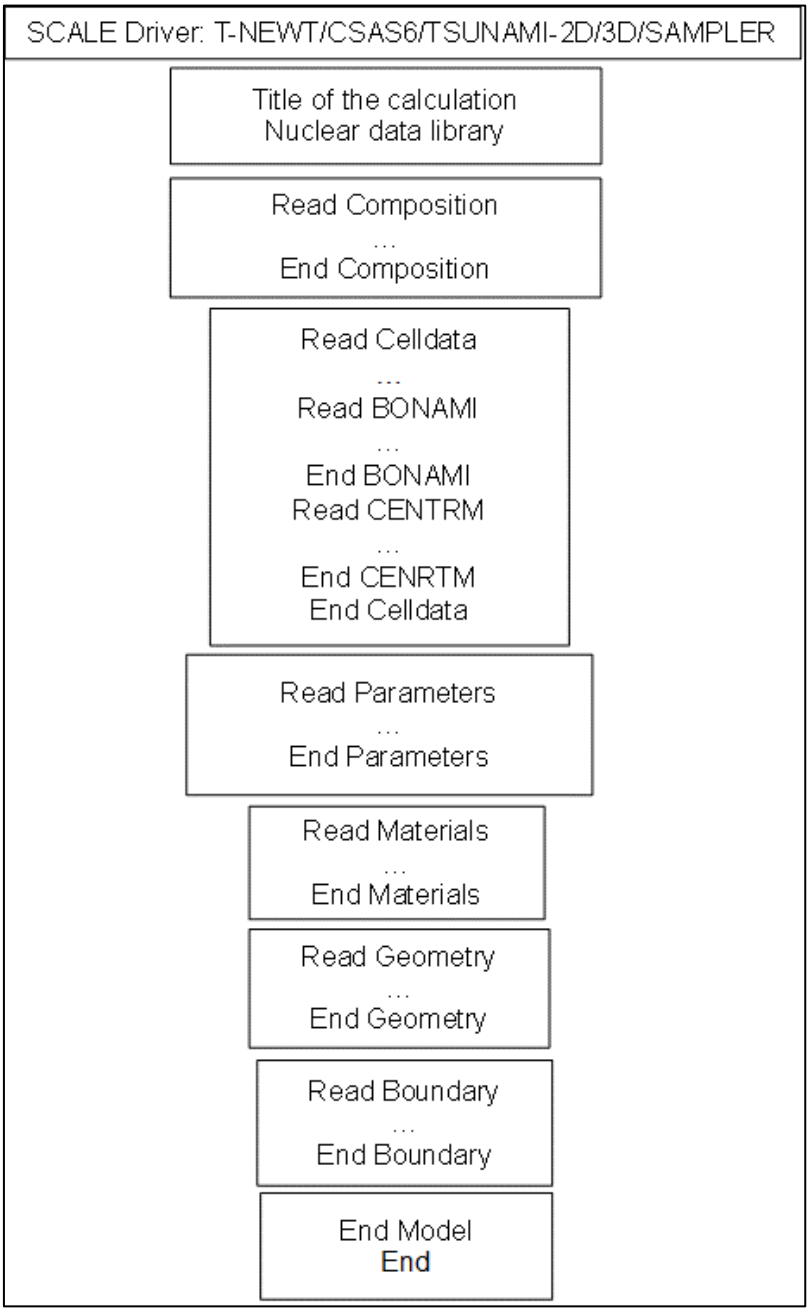

FIGURE C-1: STRUCTURE OF A SCALE-6.2.1 INPUT FILE

The first few lines of the input file are the same for NEWT, KENO-VI and TSUNAMI-2D/3D sequence as seen Figure C-2, but different for the SAMPLER file as can be seen in Figure C-3. In Figure C-2, the code is specified together with the title of the calculation and the nuclear data library. In a SAMPLER input, the type of input that requires perturbation and sample size is required to start the simulation before specification of the code and nuclear data library as in Figure C-3.

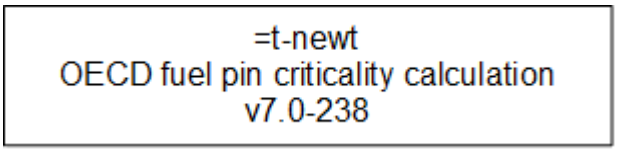

FIGURE C-2: CODE SPECIFICATION AND LIBRARY

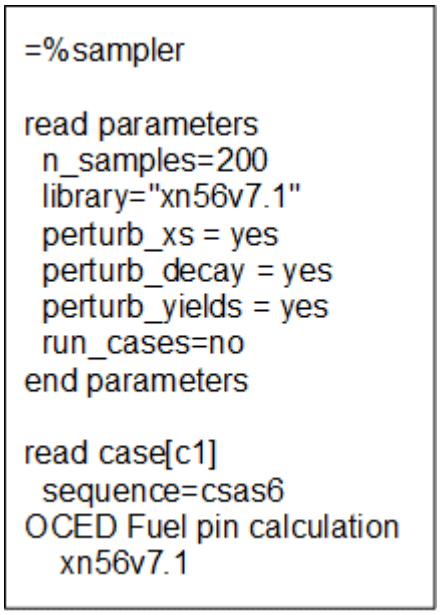

FIGURE C-3: CODE SPEFICICATION AND LIBRARY

The block that follows after the nuclear data library definition is the composition block. The compositions of the materials in the desired system are defined in the same format for all the above-mentioned codes.

```
read comp
'1:central void
    n  1  0 4.07494E-05  900.00   end
    o  1  0 9.51401E-06  900.00   end
'
'2: fuel - 3.3%U235
    uo2  2  den=10.4 1  900.00  92238 96.6946
         92235 3.3 92234 0.0054 end
'
'3: Helium
    he 3  0 2.46747E-11  750.00   end
'4: Clad
    o   4  0 3.08058E-04  600.00   end
    cr  4  0 3.29618E-06  600.00   end
    fe  4  0 8.66985E-06  600.00   end
    nb 4  0 4.24567E-04  600.00   end
    sn 4  0 4.67353E-06  600.00   end
'
'5:Pitch
    h2o  5 den=0.7525   1  560.00   end
end comp
```

FIGURE C-4: MATERIAL COMPOSITION EXAMPLE

The CELLDATA definition is only required for multi-group calculations and follows the structure in Figure C-5 in an input file. This block also includes the XSProc parameters definition defined under read MORE or read CENTRM.

```
read celldata
    latticecell atriangpitch
          imodr=0.0700 1
          fuelr=0.3780 2
    gapr=0.386 3
          cladr=0.4550 4
          hpitch=0.6375 5 end
  MORE data BONAMIEPS=1e-08
    szf=0.3
    IROPT=1 end MORE
  CENTRM data isn=24
    ITERP=1
    EPS=1e-08
    kernel=1
    ALUMP=0.3
    DEMAX=2e4
    DEMIN=5e-3 end CENTRM
 end celldata
```

FIGURE C-5: CROSS-SECTION PROCESSING

For a NEWT calculation, an additional material block is required and can be defined as it is shown in Figure C-6.

```
read materials
    mix=1 pn=1 com="central void"  end
    mix=2 pn=1 com="fuel - 3.6%"   end
    mix=3 pn=1 com="Helium"        end
    mix=4 pn=1 com="clad"          end
    mix=5 pn=2 com="H2O"           end
 end materials
```

FIGURE C-6: ADDITIONAL MATERIAL BLOCK FOR NEWT

The following Figure C-7 gives the structure for specifying parameters that are required for NEWT and KENO. In the NEWT calculation, parameters such as output of the calculation of cross-sections can be specified under this block. For the KENO-VI, parameters such as the number of neutrons per generation, number of skipped cycles and number of active cycles are specified.

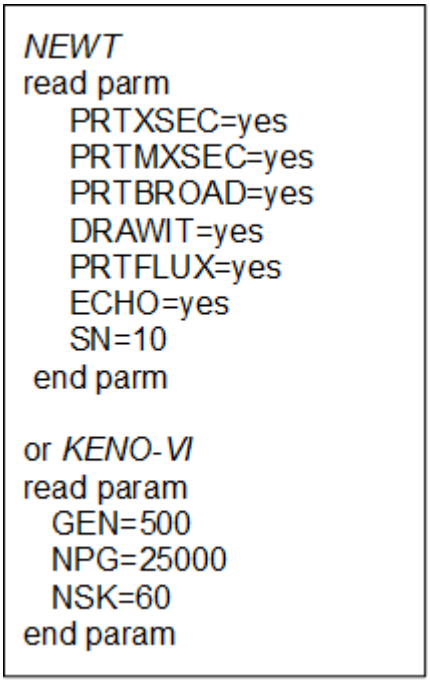

FIGURE C-7: PARAMETER BLOCK

The following geometry block gives a 3D geometry and a 2D geometry as can be defined in the input file.

```
NEWT
read geom
  global unit 1
    cylinder   10 .0700
    cylinder    20 .3780
    cylinder    30 .3860
    cylinder    40 .4550
    hexprism  50 .6375
 media 1 1 10
 media 2 1 20 -10
 media 3 1 30 -20
 media 4 1 40 -30
 media 5 1 50 -40
    boundary  50 24 24
 end geom

Or KENO-VI
read geom
  global unit   1
    cylinder   10 .0700  11.25  0.0
    cylinder   20 .3780  11.25  0.0
    cylinder   30 .3860  11.25  0.0
    cylinder   40 .4550  11.25  0.0
    hexprism 50 .6375  11.25  0.0
 media 1 1 10
 media 2 1 20 -10
 media 4 1 30 -20
 media 3 1 40 -30
 media 5 1 50 -40
   boundary 50
end geom
```

FIGURE C-8: GEOMETRY DEFINITION

The boundary conditions of the system being modelled are specified using the following block. Also, in this Figure C-9, the closing statement of the calculation is given. In terms of KENO-VI, end data is used while in NEWT end model is used.

```
read bounds
     all=mirror
 end bounds

end model/data
end
```

FIGURE C-9: BOUNDARY CONDITION

In terms of TSUNAMI the calculations of the sensitivity coefficients and uncertainty of the results is calculated when the SAMS block is specified. The SAMS block only applies in a multi-group calculation. For a TSUNAMI-3D CE calculation, three additional parameters are required under the read PARAMETER block and also a read GRIDGEOMETRY block shown in Figure C-11 is required. The first parameter is CET, which specify the use of the CLUTCH method, second parameter is CFP which specifies the number of latent generation and the last parameter is CGD that specify grid block number in Figure C-11.

```
read sams
makeimp
pltp
prtgeom
prtimp
usemom
end sams
```

FIGURE C-10: SAMS BLOCK

```
read gridGeometry 11
    title="Mesh for collecting fission
source distribution"
          tolerance=1E-006
          xlinear 10 -1.4722 1.4722
          tolerance=1E-006
          ylinear 10 -0.6375 0.6375
          tolerance=1E-006
          zlinear 10 -0.00000 400.200
 end gridGeometry
```

FIGURE C-11: F*(R) BLOCK

APPENDIX D. THE DEPENDENCE OF UO_2 DENSITY

The density of UO_2 and the enrichment of ^{235}U have been analysed to see if the change in the enrichment have an effect on the density. This was done following the method below.

Consider only mass m_0^u of uranium with the enrichment e_0 of ^{235}U in UO_2 with e_0 expressed in w/o. The mass of each isotope of the uranium, ^{234}U, ^{235}U and ^{238}U can be obtained as:

$$m^{234} = \frac{f}{100} m_0^u \tag{76}$$

$$m^{235} = \frac{e_0}{100} m_0^u \tag{77}$$

$$m^{238} = m_0^u - m^{234} - m^{235} = m_0^u \left(1 - \frac{f}{100} - \frac{e_0}{100}\right) \tag{78}$$

where $f = 0.0054$ remains constant. In terms number densities N^i for each i isotope this becomes:

$$N^{234} = \frac{m^{234} N_A}{MM^{234}} \tag{79}$$

$$N^{235} = \frac{m^{235} N_A}{MM^{235}} \tag{80}$$

$$N^{238} = \frac{m^{238} N_A}{MM^{238}} \tag{81}$$

where MM is the molar mass of each isotope and N_A is Avogadro's number. Then, the number density of the uranium atoms is therefore:

$$\begin{aligned} N^U &= \frac{m^{234} N_A}{MM^{234}} + \frac{m^{235} N_A}{MM^{235}} + \frac{m^{238} N_A}{MM^{238}} \\ &= \frac{f}{100} \frac{m_0^u N_A}{MM^{234}} + \frac{e_0}{100} \frac{m_0^u N_A}{MM^{235}} + \frac{100 - f - e_0}{100} \frac{m_0^u N_A}{MM^{238}} \end{aligned} \tag{82}$$

The corresponding number density of the oxygen in UO_2 is:

$$N^O = 2 \times \left(\frac{f}{100} \frac{m_0^u N_A}{MM^{234}} + \frac{e_0}{100} \frac{m_0^u N_A}{MM^{235}} + \frac{100 - f - e_0}{100} \frac{m_0^u N_A}{MM^{238}} \right) \tag{83}$$

With the mass calculated as:

$$m^O = 2 \times \left(\frac{f}{100} \frac{m_0^u N_A}{MM^{234}} + \frac{e_0}{100} \frac{m_0^u N_A}{MM^{235}} + \frac{100 - f - e_0}{100} \frac{m_0^u N_A}{MM^{238}} \right) \times \frac{MM^O}{N_A} \tag{84}$$

$$= \frac{2m_0^u}{100} \left(\frac{f}{MM^{234}} + \frac{e_0}{MM^{235}} + \frac{100 - f - e_0}{MM^{238}} \right) \times MM^O$$

Then, the total mass of UO_2 becomes:

$$m^T = m_0^u \left(1 + \frac{2}{100} \left(\frac{f}{MM^{234}} + \frac{e_0}{MM^{235}} + \frac{100 - f - e_0}{MM^{238}} \right) \times MM^O \right) \tag{85}$$

Given the density ρ_0, the corresponding volume of UO_2 can be calculated as:

$$V^T = \frac{m_0^u}{\rho_0} \left(1 + \frac{2}{100} \left(\frac{f}{MM^{234}} + \frac{e_0}{MM^{235}} + \frac{100 - f - e_0}{MM^{238}} \right) MM^O \right) \tag{86}$$

Given another enrichment e_1, with the volume assumed to remain constant, the following can be obtained:

$$V^T = \frac{m_1^u}{\rho_1} \left(1 + \frac{2}{100} \left(\frac{f}{MM^{234}} + \frac{e_1}{MM^{235}} + \frac{100 - f - e_1}{MM^{238}} \right) MM^O \right) \tag{87}$$

Equating Eq (86) and Eq (87), the following is obtained:

$$\frac{m_0^u}{\rho_0} \left(1 + \frac{2}{100} \left(\frac{f}{MM^{234}} + \frac{e_0}{MM^{235}} + \frac{100 - f - e_0}{MM^{238}} \right) MM^O \right) \tag{88}$$

$$= \frac{m_1^u}{\rho_1} \left(1 + \frac{2}{100} \left(\frac{f}{MM^{234}} + \frac{e_1}{MM^{235}} + \frac{100 - f - e_1}{MM^{238}} \right) MM^O \right)$$

For a specific case, assume that m_0^u is 100 g. if the enrichment is 3.0 or 3.5, then m^{235} will be 3.0 g or 3.5 g, and m^{234} will be 0.0054 g and m^{238} will be 96.9946 g or m^{234} will still be 0.0054 g and m^{238} will be 96.4946 g.

Generalising this then means that $m_0^u = m_1^u$, therefore, Eq (88) will be:

$$\rho_1 = \rho_0 \frac{\left(1 + \frac{2}{100} \left(\frac{f}{MM^{234}} + \frac{e_1}{MM^{235}} + \frac{100 - f - e_1}{MM^{238}} \right) MM^O \right)}{\left(1 + \frac{2}{100} \left(\frac{f}{MM^{234}} + \frac{e_0}{MM^{235}} + \frac{100 - f - e_0}{MM^{238}} \right) MM^O \right)} \tag{89}$$